



HAL
open science

Neutrino propagation in dense astrophysical environments: beyond the standard frameworks

Amélie Chatelain

► **To cite this version:**

Amélie Chatelain. Neutrino propagation in dense astrophysical environments: beyond the standard frameworks. Physics [physics]. Université Sorbonne Paris Cité, 2018. English. NNT : 2018US-PCC224 . tel-02466847

HAL Id: tel-02466847

<https://theses.hal.science/tel-02466847>

Submitted on 4 Feb 2020

HAL is a multi-disciplinary open access archive for the deposit and dissemination of scientific research documents, whether they are published or not. The documents may come from teaching and research institutions in France or abroad, or from public or private research centers.

L'archive ouverte pluridisciplinaire **HAL**, est destinée au dépôt et à la diffusion de documents scientifiques de niveau recherche, publiés ou non, émanant des établissements d'enseignement et de recherche français ou étrangers, des laboratoires publics ou privés.

THÈSE DE DOCTORAT DE L'UNIVERSITÉ SORBONNE PARIS CITÉ

Préparée à l'Université Paris Diderot

École doctorale des Sciences de la Terre et de l'Environnement et Physique de l'Univers,
Paris - ED 560

Laboratoire ASTROPARTICULES ET COSMOLOGIE (APC) - Groupe théorie

Neutrino propagation in dense astrophysical environments: beyond the standard frameworks

THÈSE DE DOCTORAT - SPÉCIALITÉ : PHYSIQUE THÉORIQUE

présentée par

Amélie CHATELAIN

dirigée par

Maria Cristina VOLPE

et soutenue publiquement le 13 décembre 2018 à Paris devant un jury composé de :

Présidente du jury	Danièle Steer	Professeure	Université Paris Diderot
Rapporteur	Carlo Giunti	Professeur	Università di Torino et INFN
Rapporteuse	Gail McLaughlin	Professeure	North Carolina State University
Examinatrice	Sacha Davidson	DR-CNRS	Université de Montpellier
Directrice de thèse	Maria Cristina Volpe	DR-CNRS	Université Paris Diderot

Neutrino Propagation in dense astrophysical environments: beyond the standard frameworks

ABSTRACT

Since the discovery of neutrino oscillations in vacuum, it has been shown that the presence of a matter background can greatly modify the flavor evolution. The inclusion of neutrino self-interactions in the studies of neutrino flavor conversions in dense astrophysical environments has triggered an intense theoretical activity. This thesis enters into this context by going beyond usual approaches. In our first project, we explore analytically and numerically the so-called helicity coherence, using for the first time a detailed astrophysical simulation of binary neutron star merger remnants. This study shows that helicity coherence cannot lead to conversions and, by doing so, strengthens the validity of the usually-employed mean-field equations in dense media. It also brought a better understanding of the nonlinear feedback mechanism. Having done so, we examine in a second part the role of nonstandard matter-neutrino interactions in the same astrophysical setting. We find that the presence of such interactions creates another MSW-like resonance, called the inner resonance, which can have an interesting interplay with the matter-neutrino resonance, and leads to flavor conversions very close to the central object. We also analyze the mechanism of such a resonance and show that it can be met as a synchronized resonance in the presence of a strong self-interaction potential. Finally, our last study is more formal, as it focuses on the fundamental question of decoherence by wave-packet separation in the presence of strong gravitational fields. We use the density matrix formalism for the neutrino wave packet in the Schwarzschild metric and derive the expression of the coherence length. This work provides with the first study in the description of decoherence in curved space-time.

Keywords: neutrinos, astrophysics, binary neutron stars, helicity coherence, nonstandard, wave packets.

Depuis la découverte des oscillations de neutrinos dans le vide, il a été démontré que la présence d'un environnement de matière peut avoir une grande influence sur les changements de saveurs. L'inclusion des termes d'interactions neutrino-neutrino dans les études des conversions de saveurs dans les environnements astrophysiques denses a créé une activité théorique très intense. Cette thèse entre dans ce cadre en allant au-delà des approches usuelles. Dans notre premier projet, nous explorons analytiquement et numériquement le rôle de la cohérence d'hélicité, en nous basant pour la première fois sur une simulation astrophysique détaillée d'un rémanent de fusion de système binaire d'étoiles à neutrons. Cette étude montre que la cohérence d'hélicité n'engendre pas de conversions, et par ce fait, renforce la validité des équations de champs moyens

habituellement utilisées dans les milieux denses. Elle apporte également une meilleure compréhension du mécanisme de nonlinear feedback. Après cela, nous examinons dans une seconde partie le rôle des interactions non-standards entre matière et neutrinos dans le même contexte astrophysique. Nous trouvons que la présence de telles interactions peut créer une nouvelle résonance de type MSW, appelée la résonance "inner", qui peut avoir un couplage intéressant avec la résonance matière-neutrino, et provoque des conversions de saveurs très proches de l'objet central. Nous analysons également le mécanisme d'une telle résonance, et montrons qu'elle se manifeste comme une résonance synchronisée en présence d'un potentiel d'interaction neutrino-neutrino fort. Enfin, notre dernière étude est plus formelle et se focalise sur la question fondamentale de la décohérence par séparation de paquets d'ondes en présence de champs gravitationnels forts. Nous utilisons le formalisme de la matrice densité pour le paquet d'onde du neutrino dans la métrique de Schwarzschild, et dérivons l'expression de la longueur de cohérence. Ce travail constitue la toute première étude dans la description de la décohérence en espace-temps courbe.

Mots clés : neutrinos, astrophysique, systèmes binaires d'étoiles à neutrons, cohérence d'hélicité, non-standard, paquets d'ondes.

Acknowledgments

I would like to thank all the people who accompanied me during this journey.

My first thought goes to Cristina, who accepted me as a Ph.D. student despite not looking for one. She introduced me and guided me to the fascinating field of neutrino physics and was always there to help. I am infinitely grateful for her help and moral support in particular during the past few months, without which this would not have been possible. I feel privileged to have had the opportunity to work with her over the past three years.

I also would like to thank Gail Mclaughlin and Carlo Giunti for agreeing to be my referees, and my jury members Sacha Davidson and Daniele Steer, some of whom traveled for attending my defense.

Working in the theory group at APC was a pleasure for me, and I would like to thank all its staff and members for welcoming me there. I value the fun times I spent with the Ph.D. students I got to know during my stay, in particular, Cyrille, Félix, Frédéric, Gabriel, Jan, Leandro, Makarim, Maxime, Pierre and Theodoros. I also would like to express my appreciation to my friends Damien, Mathilde and Yasin for making my life easier and more enjoyable during the course of this thesis.

Finally, I would like to express my gratitude to my family whose support has been invaluable to me. There are not enough words to thank you enough.

Amélie

Contents

1	GENERAL INTRODUCTION	4
2	THEORY OF NEUTRINO OSCILLATIONS	10
2.1	Introduction to neutrino physics	11
2.1.1	Neutrinos in the standard model	11
2.1.2	Massive neutrinos and mixing	13
2.1.3	Neutrino oscillations in vacuum	17
2.2	Describing neutrino propagation in dense media	20
2.2.1	Most general equations in the mean-field approximation	20
2.2.2	Deriving the effective Hamiltonian in the mean-field approximation	24
2.2.3	Homogeneous system in the ultra-relativistic limit	32
2.3	Neutrino propagation in matter: the MSW effect	35
2.4	Neutrino oscillations: experimental status	39
2.4.1	Solar neutrinos	39
2.4.2	Neutrino oscillation parameters	43
2.4.3	Future progress	44
3	NEUTRINO PROPAGATION IN DENSE ASTROPHYSICAL ENVIRONMENTS	48
3.1	Introduction	48
3.2	Neutrinos in core-collapse supernovae	50
3.2.1	General description of core-collapse Supernovae	50
3.2.2	Neutrino flavor evolution in supernovae	56
3.2.3	Recent developments	59
3.3	Neutrinos in binary neutron star merger remnants	60
3.3.1	General description of binary neutron star merger remnants	60
3.3.2	Neutrino flavor evolution in binary neutron star merger remnants	65
3.3.3	Recent developments	68
4	HELICITY COHERENCE IN BINARY NEUTRON STAR MERGERS AND NONLINEAR FEEDBACK	71
4.1	Introduction	72
4.2	Theoretical framework	73
4.2.1	Mean-field evolution equations with mass contributions	73
4.2.2	The Majorana case with $N_f = 2$	77
4.2.3	The Dirac case with $N_f = 2$	79
4.2.4	Our schematic model based on neutron star mergers simulations	79
4.3	Results	84
4.3.1	Resonance conditions for helicity coherence	84
4.3.2	Numerical results on flavor evolution	87
4.4	Nonlinear feedback mechanisms	94
4.4.1	Nonlinear feedback in the MNR	94
4.4.2	Nonlinear feedback in a one-flavor model	96
4.4.3	Nonlinear feedback and helicity coherence	97
4.5	Conclusions	99

5	NEUTRINO PROPAGATION IN BINARY NEUTRON STAR MERGERS IN PRESENCE OF NONSTANDARD INTERACTIONS	101
5.1	Introduction	102
5.2	The model	103
5.2.1	Neutrino evolution equations in presence of nonstandard interactions	103
5.2.2	Two-neutrino flavor evolution in binary neutron star mergers	104
5.3	Impact of nonstandard interactions on neutrino flavor evolution	106
5.3.1	New conditions for the I resonance	107
5.3.2	NSI, the MNR and the I resonance	114
5.4	Discussion and conclusions	117
6	DECOHERENCE OF NEUTRINOS IN CURVED SPACE-TIME	119
6.1	Introduction	119
6.2	Neutrino wave packets	121
6.2.1	Describing neutrinos as wave packets	121
6.2.2	Neutrino wave packets in astrophysical environments	122
6.2.3	Coherence length: a heuristic approach	124
6.3	Evolution equation for the neutrino WP in flat space-time	127
6.3.1	Evolution of the neutrino state vector	127
6.3.2	Vacuum oscillations in flat space-time	129
6.4	Evolution equation for the neutrino WP in curved space-time	132
6.4.1	Evolution of the neutrino state vector and covariant phase	132
6.4.2	Vacuum oscillations in Schwarzschild metric	133
6.5	Discussions and conclusions	138
7	CONCLUSIONS	141
	APPENDIX A SPINOR PRODUCTS	145
	APPENDIX B EXTENDED EVOLUTION EQUATIONS WITH MASS CONTRIBUTIONS : DIRAC CASE	147
	APPENDIX C GEOMETRIC FACTOR IN THE CONTEXT OF BINARY NEUTRON STAR MERGER REMNANTS	149
	APPENDIX D ADIABATICITY	153
	REFERENCES	164

1

General introduction

The existence of neutrinos was first proposed in 1930 by Wolfgang Pauli, in order to explain the continuous spectra of beta particles emitted in beta decay. The word "neutrino" itself was introduced to the scientific community by Enrico Fermi in two conferences —Paris, in July 1932 and the Solvay conference in October 1933—, to differentiate this new, neutral particle from the heavier neutron. In 1934, Fermi postulated his theory on beta decay, in which four fermions, including the neutrino, were interacting with one another. This work was first submitted to Nature which rejected it, judging it "too remote from reality to be of interest to the reader". Today, we know that Fermi's theory corresponds to the low-energy limit of the weak interaction.

However, it was only in 1956 that neutrinos were detected for the first time. Cowan, Reines, Harrison, Kruse and McGuire [1] announced the first detection of reactor electron antineutrinos through inverse beta decay. The produced neutrons are captured on nuclei while the produced positrons annihilate with electrons, both processes emitting photons that could be detected. Later, the first muon neutrino was detected in 1962 by Lederman, Schwartz, and Steinberger, hence showing that more than one type of neutrino exists. The third lepton flavor, tau, was discovered in 1975 at the Stanford Linear Acceleration Center and assumed to have an associated neutrino. However, it was directly measured only in 2000 by the DONUT collaboration at Fermilab.

In the late 60s, the Homestake experiment, headed by Davis detected and counted neutrinos emitted by nuclear reactions in the Sun [2]. They observed a discrepancy in the number of neutrinos detected, with the measured flux being about one-third of the flux predicted by Bahcall, creating the so-called solar neutrino

problem. This problem remained unsolved for about thirty years, triggering numerous experiments and lead to the discovery of neutrino oscillations in 1998 [3]. In 1957, Pontecorvo introduced first the idea of neutrino-antineutrino conversions by analogy with kaon oscillations [4]. After the existence of muon neutrinos was established, Maki, Nakagawa and Sakata introduced in 1962 the notion of flavor mixing [5], leading to $\nu_e \leftrightarrow \nu_\mu$ and $\bar{\nu}_e \leftrightarrow \bar{\nu}_\mu$ oscillations. Pontecorvo further elaborated on those oscillations in 1967. After the discovery of the solar neutrino problem, Gribov and Pontecorvo published the first modern treatment of neutrino oscillations, introducing neutrino masses in an article called "Neutrino astronomy and lepton charge" [6]. The Homestake measurement of solar neutrinos and the first detection of supernova neutrinos in 1987 were two milestones for the field of neutrino astronomy.

The discovery of neutrino oscillations by the SuperKamiokande (1998) [3] and SNO (2001) [7] experiments has proven that neutrinos are elementary massive particles with mixing, that is the mass (or propagation) basis and the flavor (or interaction) basis do not coincide. Since then, precision measurements have determined most of the fundamental neutrino oscillation parameters. Crucial open questions remain, in particular, the nature of neutrinos (Majorana or Dirac), the neutrino mass ordering, the existence of sterile neutrinos and of CP violation in the lepton sector. It is also still unknown how neutrino masses are generated.

As neutrinos are very light and interact only through weak interactions, they also make wonderful messengers of the universe. Expanding the work of Wolfenstein [8], Mikheev and Smirnov noted in 1985 [9] that neutrino oscillations could be drastically modified in the presence of a matter background. In particular, they showed the existence of the so-called Mikheev-Smirnov-Wolfenstein (MSW) resonance that could be met in the Sun. It is now well-established that the MSW phenomenon is at the origin of the high-energy ^8B solar neutrinos deficit.

Flavor evolution in dense astrophysical environments, such as core-collapse supernovae or compact binary objects, has turned out to be a complex problem. Indeed, the presence of neutrino self-interactions in such environments makes the study of neutrino evolution a nonlinear problem [10]. The inclusion of self-interaction terms [11] has triggered more than a decade of intense theoretical investigations, and models of increasing complexity are used to unravel new flavor instabilities and mechanisms such as collective conversion phenomena. Such studies are necessary to assess the actual impact of neutrino oscillations on the physics of the environment, in particular, on the dynamics of supernovae, on the nucleosynthetic r process abundances as well as for future observations of supernova neutrinos and of the diffuse supernova neutrino background. Understanding the mechanism for the explosion of massive stars and identifying the sites where heavy elements are produced (r process) are two key longstanding open questions in astrophysics.

The recent observation of gravitational waves from a binary neutron star merger event GW170817 [12] coincidentally with a short gamma-ray burst and a kilonova constitute the first direct evidence for r process nucleosynthesis in such sites. Moreover, recent works have shown that a significant part of the r process elements is likely to be produced in the so-called neutrino-driven winds. Therefore, fully understanding neutrino flavor conversions in this type of environment, as well as their role in nucleosynthesis is primordial.

The main goal of the present thesis is to investigate neutrino flavor conversions in dense astrophysical environments beyond the standard frameworks. We do so in three respects, encompassing the exploration of the role of helicity coherence which is usually neglected, the effects of nonstandard interactions and neutrino decoherence by wave packet separation.

The first project of this thesis is a study of the so-called helicity coherence correlators, which appear as nonrelativistic corrections to our neutrino evolution equations. The corresponding contributions, proportional to the absolute mass of neutrinos, create a coupling between active and sterile neutrino components ("wrong helicity" components) in case of Dirac neutrinos, or between neutrinos and antineutrinos in case of Majorana neutrinos. While one first study of these terms has been done in a very simple model with one Majorana neutrino flavor [13], no study was ever made on the effect of this new coupling in a realistic scenario. In the first toy model, the authors found that the presence of helicity coherence coupling could create a MSW-like resonance between neutrinos and antineutrinos, which could be amplified by a nonlinear feedback, created by the nonlinear nature of the equations, inducing strong flavor conversions. Our goal in this thesis is to investigate the possible effects of helicity coherence coupling neutrinos to antineutrinos in a realistic framework with two Majorana neutrino flavors, based on detailed astrophysical simulations of a binary neutron star merger remnants. After re-deriving the most general equations for neutrino propagation in the mean-field approximation, we numerically explore a large number of trajectories as well as a large parameter range. We find that MSW-like resonance conditions between neutrinos and antineutrinos can be met in this detailed astrophysical scenario. We also analyze analytically our results in the light of nonlinear feedback, discussing general conditions for multiple MSW-like resonances that would increase the adiabaticity. Our results also shed light more generally on nonlinear feedback mechanisms, which are observed in binary neutron star mergers simulations such as the one associated with a flavor phenomenon called the matter-neutrino resonance. The work presented in this thesis constitutes the first realistic investigation considering helicity coherence and allows to assess the validity of the usual mean-field equations used in flavor evolution studies.

The second project of this thesis is focused on the role of possible nonstandard matter-neutrino interactions (NSI) in binary neutron star merger remnants. Indeed, experimental constraints on matter-neutrino

nonstandard interactions, obtained with scattering and oscillation experiments, are still rather loose. The presence of NSI would modify the interpretation of oscillation experiments and may explain observed anomalies. Studies of these interactions in core-collapse supernovae [14, 15, 16, 16] have shown that they can alter neutrino flavor conversions, in particular by creating a new MSW resonance called the Inner (I) resonance extremely close to the neutrino emission surface. Because of its location, this new resonance could have a strong effect on r process nucleosynthesis. We explore for the first time the role of NSI in binary neutron star merger remnants through numerical simulations and show that the I resonance condition can also be met, creating strong flavor conversions very close to the neutrino emission surface. Moreover, we shed a new light on its mechanism and show that it can be interpreted as a synchronized MSW resonance in the presence of a significant self-interaction potential. This aspect of the I resonance has been overlooked in previous studies of NSI in core-collapse supernovae. Flavor conversions due to NSI such as the I resonance can have a strong impact on the electron fraction —the proton-to-baryon ratio, which is a key parameter for r process nucleosynthesis— as they are occurring very close to the central object, and could modify the abundances of the elements produced through r process in the neutrino-driven winds. We discuss the potential impact of NSI on the electron fraction in this environment.

The third project of the thesis goes towards a more fundamental direction with respect to the previous two. In fact, it focuses on the investigation of decoherence by wave-packet separation on neutrino flavor conversions, and in particular the effects of curved space-time. Indeed, as neutrinos are described by wave packets rather than plane waves, it is possible for them to separate, leading to a damping of the oscillation terms. After discussing the wave-packet description in dense astrophysical environments, we rederive consistently the coherence length in flat space-time using the density matrix formalism and discuss the inclusion of adiabatic matter effects. Then, we investigate the differences arising when considering the propagation of neutrinos in strong gravitational fields. This is still an ongoing project for which final results have not been included yet because of lack of time.

The thesis is organized as follows. First, we present the current understanding of neutrino physics in Chapter 2. We discuss both the theoretical aspects of neutrino propagation in dense astrophysical environments and the current status in neutrino physics. In Chapter 3, we describe the astrophysical scenarios of core-collapse supernovae and binary neutron star merger remnants, as well as the neutrino emissions and key features of their propagation in these environments. The following chapters are dedicated to the original work developed in the course of this thesis, studying neutrino propagation in dense astrophysical environments beyond the standard frameworks. The role of helicity coherence correlators and nonlinear feedback mechanisms are explored in Chapter 4 in the context of binary neutron star merger remnants. In Chapter 5,

we present a study of the effects of nonstandard interactions on neutrino propagation in the same astrophysical setting. The numerical results presented in Chapters 4 and 5 have been obtained using a FORTRAN (90/95) developed during the course of this thesis. Decoherence by wave-packet separation in vacuum and in the presence of gravitational fields is discussed in Chapter 6. In order to maintain the readability of this manuscript, some calculations are detailed in the Appendices while only their main results are discussed in the text. Our Conclusions are presented at the end of the manuscript.

The results obtained have made the object of two publications

- [17] A. Chatelain and M.C. Volpe, *Helicity coherence in binary neutrino star mergers and nonlinear feedback*, Phys.Rev.D95 (2017) no.4, 043005.
- [18] A. Chatelain and M.C. Volpe, *Neutrino propagation in binary neutron star mergers in the presence of nonstandard interactions*, Phys.Rev.D97 (2018) no.2, 023014.

Unless specified otherwise, we adopt the following conventions and notations

- Natural units are used $\hbar = c = k_B = G = 1$,
- The signature of the metric is chosen to be $(-, +, +, +)$,
- Greek indices μ, ν, \dots run from 0 to 3.
- $\eta_{\mu\nu} = \eta^{\mu\nu} = \text{diag}(-1, +1, +1, +1)$ is the Minkowskian metric,
- γ^μ denotes one the usual gamma matrices, satisfying the Clifford algebra $\{\gamma^\mu, \gamma^\nu\} = 2\eta^{\mu\nu}$ and γ_5 is defined as $\gamma_5 \equiv i\gamma^0\gamma^1\gamma^2\gamma^3$,
- Feynman slash notation is used: $\not{\phi} = a_\mu\gamma^\mu$,
- Flavor neutrinos are specified by $\alpha, \beta, \gamma, \dots$, while massive neutrinos are specified by i, j, k, \dots

2

Theory of neutrino oscillations

Contents

2.1	Introduction to neutrino physics	II
2.1.1	Neutrinos in the standard model	II
2.1.2	Massive neutrinos and mixing	13
2.1.3	Neutrino oscillations in vacuum	17
2.2	Describing neutrino propagation in dense media	20
2.2.1	Most general equations in the mean-field approximation	20
2.2.2	Deriving the effective Hamiltonian in the mean-field approximation	24
2.2.3	Homogeneous system in the ultra-relativistic limit	32
2.3	Neutrino propagation in matter: the MSW effect	35
2.4	Neutrino oscillations: experimental status	39
2.4.1	Solar neutrinos	39
2.4.2	Neutrino oscillation parameters	43
2.4.3	Future progress	44

IN THIS CHAPTER, we will review the bases of neutrino physics. In Section 2.1.1, we start by introducing neutrinos as elementary particles in the standard model. We present the minimal extension to the standard

model, in which neutrinos get a mass, and introduce the notion of mixing. We discuss the differences between Majorana and Dirac neutrinos and show a first derivation of neutrino oscillation probabilities in vacuum. In Section 2.2, we derive the most general evolution equations for the neutrino density matrix in media in the mean-field approximation and the element of the Hamiltonian involved in those equations. We discuss the limit of a homogeneous system and ultra-relativistic neutrinos. In Section 2.3, we use the equations derived above to study the propagation of neutrinos in matter and show that the coupling to matter gives rise to a resonance phenomenon called the Mikheev-Smirnov-Wolfenstein effect. Finally, in Section 2.4, we present a brief overview of the experimental status of the domain.

2.1 INTRODUCTION TO NEUTRINO PHYSICS

2.1.1 NEUTRINOS IN THE STANDARD MODEL

IN THE STANDARD MODEL (SM) OF PARTICLE PHYSICS, neutrinos are introduced as massless particles subject only to the weak interaction. Neutrinos are fermions (intrinsic spin $1/2$ particles), which exist in three leptonic flavors: the electron neutrino, the muon neutrino, and the tau neutrino[†].

The fermionic free Lagrangian density is given by [20]

$$\mathcal{L}_0(x) \equiv -\bar{\psi}(x) (\not{\partial} + m) \psi(x), \quad (2.1)$$

where m is the mass of the fermion, created through a Yukawa-type coupling between the fermionic field and the Higgs boson. The fermionic field ψ can be expressed

$$\psi(x) = \int \frac{d^3\vec{q}}{(2\pi)^{3/2}} \sum_{\sigma=\pm 1/2} (u(\vec{q}, \sigma) e^{iqx} a(\vec{q}, \sigma) + v(\vec{q}, \sigma) e^{-iqx} b^\dagger(\vec{q}, \sigma)), \quad (2.2)$$

where σ is the spin, p the four-momentum vector, u and v are four-component Dirac spinors, and a and b are, respectively, the standard particle and antiparticle annihilation operators. The equal-time anti-commutation relations are

$$\{a(\vec{q}, \sigma), a^\dagger(\vec{q}', \sigma')\} = \{b(\vec{q}, \sigma), b^\dagger(\vec{q}', \sigma')\} = \delta_{\sigma, \sigma'} \delta^{(3)}(\vec{q} - \vec{q}'), \quad (2.3)$$

$$\{a(\vec{q}, \sigma), a(\vec{q}', \sigma')\} = \{b(\vec{q}, \sigma), b(\vec{q}', \sigma')\} = 0. \quad (2.4)$$

To describe massless fermions, we introduce the projectors $P_L = \frac{1-\gamma_5}{2}$ and $P_R = \frac{1+\gamma_5}{2}$. In the SM of particle physics, neutrinos are supposed to be massless fermions interacting only through their left-handed

[†]This introduction is adapted from Ref. [19].

component $\psi_L = P_L\psi$ through Charged Current (CC) and Neutral Current (NC) interactions, with the Lagrangian densities respectively given by

$$\mathcal{L}_{CC} = \frac{ig}{2\sqrt{2}} \sum_{\alpha=e,\mu,\tau} \bar{\psi}_{\nu_\alpha} \gamma^\mu (1 - \gamma_5) \psi_\alpha W_\mu + h.c. \equiv \frac{ig}{2\sqrt{2}} j_W^\mu W_\mu + h.c., \quad (2.5)$$

$$\mathcal{L}_{NC} = \frac{ig}{2 \cos \theta_W} \sum_{\alpha=e,\mu,\tau} (\bar{\psi}_{\nu_\alpha} \gamma^\mu (c_v^{\nu_\alpha} - c_a^{\nu_\alpha} \gamma_5) \psi_{\nu_\alpha} + \bar{\psi}_\alpha \gamma^\mu (c_v^\alpha - c_a^\alpha \gamma_5) \psi_\alpha) Z_\mu \equiv \frac{ig}{2 \cos \theta_W} j_Z^\mu Z_\mu, \quad (2.6)$$

where $g \equiv \frac{e}{\sin \theta_W}$ is the electro-weak coupling constant, e being the electric charge and θ_W the *Weinberg* angle, ψ_x denotes the fermionic field of the particle x , and c_v^x, c_a^x are the vector and axial coupling constants of the particle x , related to its isospin and its charge. W and Z are two bosonic vector fields, respectively the charged and neutral weak interaction gauge boson fields, of masses m_W and m_Z .

It is interesting to notice that the masses of the vector bosons W and Z are of the order of 100 GeV, which is much larger than the energy involved in the phenomena considered here. Therefore, the propagators of the massive bosons Z and W can be simplified (for example, for W)

$$\frac{-i}{(2\pi)^4} \frac{\eta^{\mu\nu} + \frac{p^\mu p^\nu}{m_W^2}}{p^2 + m_W^2} \xrightarrow{|p|^2 \ll m_W^2} \frac{-i}{(2\pi)^4} \frac{\eta^{\mu\nu}}{m_W^2}, \quad (2.7)$$

where p is the momentum carried by the boson. The interaction can be considered as a contact interaction, as depicted in figure 2.1 for the CC process. Defining the *Fermi constant* $\frac{G_F}{\sqrt{2}} = \frac{g^2}{8m_W^2} = \frac{g^2}{8 \cos^2 \theta_W m_Z^2}$, the CC and NC Lagrangians can be rewritten

$$\mathcal{L}_{CC} = \frac{-G_F}{\sqrt{2}} j_W^\mu j_{W\mu}^\dagger, \quad (2.8)$$

$$\mathcal{L}_{NC} = \frac{-G_F}{\sqrt{2}} j_Z^\mu j_{Z\mu}^\dagger. \quad (2.9)$$

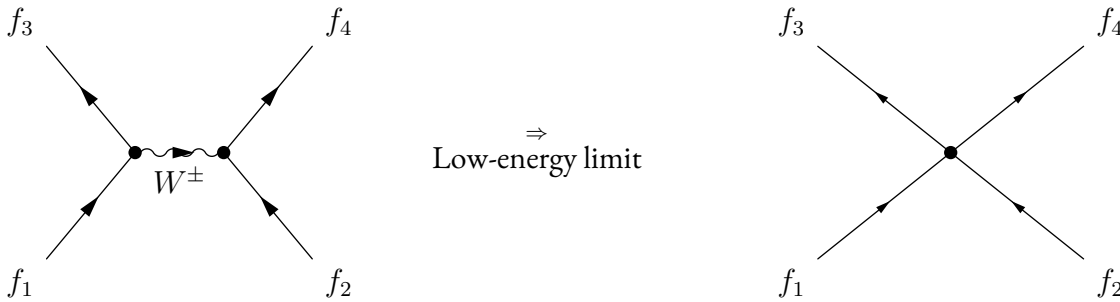


Figure 2.1: In the low-energy limit, the CC (or NC) interaction involving the propagation of a vector boson W (or Z) becomes a contact interaction.

In the SM, neutrinos are massless. On the other hand, there is no symmetry in the SM imposing the

masslessness of neutrinos. Yet, the discovery and experimental confirmation of neutrino oscillations [3] imply the existence of massive neutrinos and mixings. Thus, to have a more complete understanding of neutrinos, it is necessary to extend the SM. In the next section, we will introduce the *minimally extended Standard Model*, in which right-handed neutrinos exist.

2.1.2 MASSIVE NEUTRINOS AND MIXING

DIRAC NEUTRINOS

Neutrinos are neutral leptons, and since their charged-leptonic partners e, μ, τ are Dirac fermions, it is natural to consider them as such. In the minimal extension of the SM, Dirac fermions, namely leptons and quarks, acquire their mass through the Higgs mechanism. The Dirac mass term reads, for a fermion of mass m_D

$$\mathcal{L}_{\text{mass}}^D = -m_D \bar{\psi} \psi = -m_D \bar{\psi}_R \psi_L + h.c.. \quad (2.10)$$

However, the mass term and the CC interaction term are not necessarily diagonal in the same basis: neutrinos with a definite mass are not necessarily neutrinos with a definite flavor. This phenomenon is known as *neutrino mixing* and is responsible for neutrino oscillations.

From now on, we will denote by ν_k a neutrino with a definite mass m_k , and ν_α a neutrino with a definite flavor α : the basis $|\nu_k\rangle$ is called the *mass basis*, while $|\nu_\alpha\rangle$ is called the *flavor basis*. These two bases are related by a 3×3 unitary matrix U , called the *Pontecorvo - Maki - Nakagawa - Sakata* (PMNS) matrix

$$|\nu_\alpha\rangle = \sum_k U_{\alpha k}^* |\nu_k\rangle. \quad (2.11)$$

Rewriting the weak leptonic current in the mass basis $j_W^\mu = \sum_{\alpha=e,\mu,\tau} \sum_{k=1}^3 U_{\alpha k}^* \bar{\psi}_{\nu_k} \gamma^\mu (1 - \gamma_5) \psi_\alpha$, it becomes obvious that flavor eigenstates, created through weak interactions, are a mixture of massive eigenstates. A $n \times n$ unitary matrix has n^2 real independent parameters which can be parametrized by $\frac{n(n-1)}{2}$ angles and $\frac{n(n+1)}{2}$ phases. However, because of the invariance of the Lagrangian under global phase transformations, $2n - 1$ phases can be eliminated. Therefore, in the case of three Dirac neutrinos, the PMNS matrix depends on three mixing angles, $\theta_{12}, \theta_{23}, \theta_{13}$ and one CP-violating phase, δ , and can be parametrized as

$$U = \begin{pmatrix} 1 & 0 & 0 \\ 0 & c_{23} & s_{23} \\ 0 & -s_{23} & c_{23} \end{pmatrix} \begin{pmatrix} c_{13} & 0 & s_{13} e^{-i\delta} \\ 0 & 1 & 0 \\ -s_{13} e^{i\delta} & 0 & c_{13} \end{pmatrix} \begin{pmatrix} c_{12} & s_{12} & 0 \\ -s_{12} & c_{12} & 0 \\ 0 & 0 & 1 \end{pmatrix}, \quad (2.12)$$

where $c_{ij} = \cos \theta_{ij}$ and $s_{ij} = \sin \theta_{ij}$ ($i, j = 1, 2, 3$).

MAJORANA NEUTRINOS

In 1937, Majorana suggested that the left-handed and right-handed component of the neutrino field, ψ_L and ψ_R , are not independent [21]. Let us define the charge-conjugate of a field ψ , $\psi^c = \mathcal{C}\bar{\psi}^\top$, where $\mathcal{C} = i\gamma^2\gamma^0$ is the charge-conjugation matrix and \top the transpose [19]. Then, one may notice that ψ_L^c is right-handed, namely $P_L\psi_L^c = 0$. It is also possible to check that ψ_L^c transforms as ψ_L under a Lorentz transformation. As a consequence ψ_L and ψ_L^c can, in principle, form a mass term, called the Majorana mass term

$$\mathcal{L}_{\text{mass}}^L = -\frac{1}{2}m\bar{\psi}_L^c\psi_L + h.c., \quad (2.13)$$

where the factor $1/2$ comes from the fact that ψ_L and ψ_L^c are not independent.

A Majorana field is therefore a field that satisfies the Majorana condition $\psi_R = \psi_L^c$, which can also be re-expressed $\psi = \eta\psi^c$ (where η is a phase) by defining $\psi = \psi_L + \eta\psi_L^c$. This condition requires the Majorana field to be neutral, and neutrinos are (currently) the only known neutral fermions.

In terms of annihilation and creation operators, a Majorana fermionic field has a similar expression to the Dirac field (2.2), but with the additional relation $b(\vec{q}, \sigma) = a(\vec{q}, \sigma)$, namely

$$\psi_{\nu_i}^M(x) = \int \frac{d^3\vec{q}}{(2\pi)^{3/2}} \sum_{\sigma=\pm 1/2} \left(u_i(\vec{q}, \sigma)e^{iqx} a_i(\vec{q}, \sigma) + v_i(\vec{q}, \sigma)e^{-iqx} a_i^\dagger(\vec{q}, \sigma) \right). \quad (2.14)$$

By convention, left-handed neutrinos are called neutrinos while right-handed neutrinos are called anti-neutrinos.

It is worthwhile to note that a Majorana neutrino has half as many degrees of freedom as a Dirac neutrino (see figure 2.2). Indeed, from CPT invariance and Lorentz invariance, there are four possible helicity states for a Dirac neutrino of a given momentum: ν_L , ν_R , $\bar{\nu}_L$ and $\bar{\nu}_R$. However, as a Majorana field is self-charge conjugated, a CPT transformation only modifies its helicity, hence there are only two possible states for a Majorana neutrino of a given momentum ν_L and ν_R .

The presence of neutrino mixing doesn't depend on the nature of neutrinos. There exists a mixing matrix U such that $|\nu_\alpha\rangle = \sum_k U_{\alpha k}^* |\nu_k\rangle$. However, there is a major difference between Dirac and Majorana neutrinos. In the case of massive Dirac neutrinos, $2n - 1$ phases of the mixing matrix are eliminated because of the invariance of the Lagrangian under global phase transformations, but for Majorana neutrinos, the mass term is not invariant: if $\psi_{\nu_k, L} \rightarrow \psi'_{\nu_k, L} = e^{i\phi_k}\psi_{\nu_k, L}$, then $\bar{\psi}_{\nu_k, L}^c \rightarrow \psi'_{\nu_k, L} = e^{i\phi_k}\bar{\psi}_{\nu_k, L}^c$ and the lepton number is violated. As a consequence, only n phases, corresponding to the re-phasing of the charged lepton fields, can be eliminated. Therefore, in the case of three flavors, if neutrinos are Majorana particles, there are two additional phases in the PMNS mixing matrix.

Experimentally, a signature of the Majorana nature of neutrinos would be the observation of neutrinoless double beta decay $(A, Z) \rightarrow (A, Z + 2) + 2e^-$, where (A, Z) is a nucleus with A nucleons and Z pro-

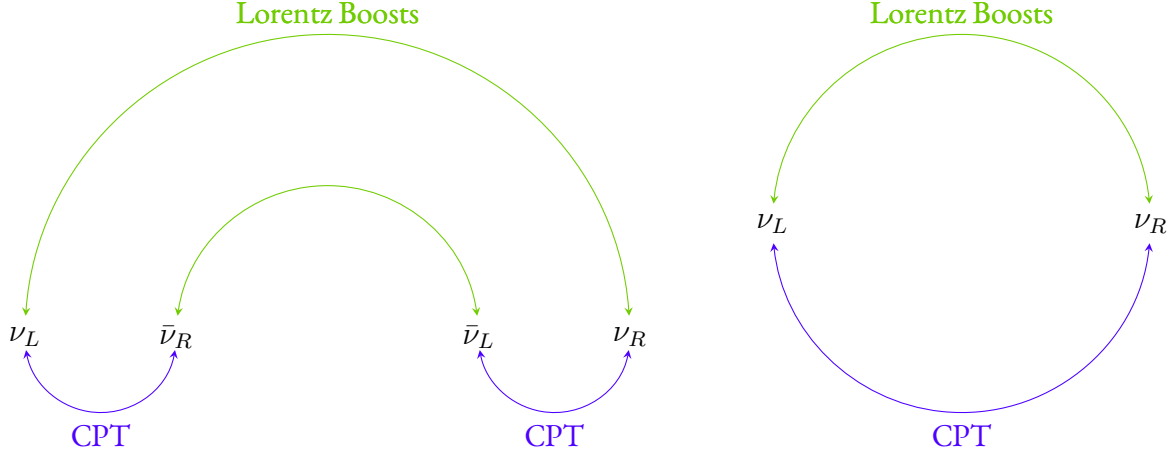


Figure 2.2: Dirac (left) and Majorana (right) degrees of freedom.

tons, that is a double beta decay process with the emission of two electrons. This lepton-number-violating phenomenon can occur only if a right-handed antineutrino emitted at a vertex can be reabsorbed at another vertex as a left-handed neutrino, which would imply neutrinos are Majorana particles. This process is yet to be detected.

It is, therefore, possible to describe massive neutrinos with a single chiral component. Another Majorana mass term can be introduced in extended versions of the SM as $\mathcal{L}_{\text{mass}}^R = -\frac{1}{2}m\bar{\psi}_R^c\psi_R + h.c.$, where ψ_R describes a sterile, right-handed neutrino field. The so-called *seesaw* mechanism relies on the existence of this mass term. This mechanism, proposed in the seventies, explains the lightness of the left-handed active neutrinos with the presence of very heavy, sterile, right-handed neutrinos. It assumes that neutrino masses are described by the Dirac and Majorana mass term, which is the most general mass term for Majorana neutrinos, involving both left-handed and right-handed neutrinos. In the following, we describe the main idea of this mechanism.

We consider here the simplest case in which only one generation of neutrino exists, with two neutrino fields ν_L and ν_R . The Dirac and Majorana mass term can be written in the matrix form

$$\mathcal{L}_{\text{mass}}^{D+M} = -\frac{1}{2}\bar{n}_L M n_L^c + h.c., \quad (2.15)$$

where n_L is a vector

$$n_L = \begin{pmatrix} \nu_L \\ \nu_R^c \end{pmatrix}, \quad (2.16)$$

and M is the mass matrix

$$M = \begin{pmatrix} m_L & m_D \\ m_D & m_R \end{pmatrix}. \quad (2.17)$$

We assume here CP invariance so that m_L, m_R, m_D are real parameters. This matrix can be diagonalized by

a unitary matrix U so that (see e.g. Ref. [22])

$$U^\dagger M U = \begin{pmatrix} m_1 & 0 \\ 0 & m_2 \end{pmatrix}, \quad (2.18)$$

with the eigenvalues m_1, m_2 given by

$$m_1 = \frac{1}{2} \left| m_R + m_L - \sqrt{(m_R - m_L)^2 + 4m_D^2} \right|, \quad (2.19)$$

$$m_2 = \frac{1}{2} \left| m_R + m_L + \sqrt{(m_R - m_L)^2 + 4m_D^2} \right|. \quad (2.20)$$

The mass term (2.15) can then be rewritten

$$\mathcal{L}_{\text{mass}}^{D+M} = -\frac{1}{2} \sum_{i=1,2} m_i \bar{\nu}_i \nu_j, \quad (2.21)$$

where the fields ν_1 and ν_2 describe Majorana particles of definite masses

$$\begin{pmatrix} \nu_1 \\ \nu_2 \end{pmatrix} = U^\dagger n_L + (U^\dagger n_L)^c. \quad (2.22)$$

The matrix U can be parametrized [19] as

$$U = \begin{pmatrix} \cos \theta & \sin \theta \\ -\sin \theta & \cos \theta \end{pmatrix} \begin{pmatrix} e^{i\lambda} & 0 \\ 0 & 1 \end{pmatrix}, \quad (2.23)$$

with $\theta \in [0, \frac{\pi}{2}]$ and $\lambda \in [0, 2\pi]$. Using Eq. (2.18), we find for those parameters the relations

$$\tan 2\theta = \frac{2m_D}{m_R - m_L}, \quad (2.24)$$

and $\tan 2\lambda = 0$, as we assumed m_L, m_R, m_D are real parameters.

The main assumptions of the seesaw mechanism presented here are the following

1. Assume that the Majorana mass term is null, that is $m_L = 0$. This is a natural assumption, as the presence of such a term is forbidden by the symmetries and renormalizability of the SM (see Ref. [19]).
2. Assume that the Dirac mass m_D is generated through a standard Higgs mechanism, and is therefore of the same order as the electroweak scale.
3. Assume that the lepton number is violated by m_R at a scale much larger than the electroweak scale:

$$m_R \gg m_D.$$

With these assumptions, the eigenvalues (2.19-2.20) become

$$m_1 \sim \frac{m_D^2}{m_R} \ll m_D, \quad (2.25)$$

and

$$m_2 \sim m_R \gg m_D. \quad (2.26)$$

Therefore, m_1 is very light compared to other leptons, while m_2 is very heavy. The parameter θ (2.24) becomes very small: ν_1 is mostly composed of active ν_L while ν_2 is mostly composed of sterile ν_R . This is the so-called seesaw mechanism: a very heavy right-handed neutrino is responsible for the lightness of the left-handed neutrino.

The suppression factor, $\frac{m_D}{m_R}$, depends on the scale on which the lepton number is violated. Note that if we take $m_D \approx 10^2$ GeV, and if we consider m_R to be of the order of the grand-unification scale $m_D \approx 10^{14} - 10^{16}$ GeV, then we find $\frac{m_D}{m_R} \approx 10^{-14} - 10^{-12}$: the seesaw mechanism would explain why neutrino masses are so small compared to other leptons.

As described above, the inclusion of neutrino mass terms and mixing make it possible for neutrinos to change their flavors, leading to the phenomenon of neutrino oscillations. In the section below, we discuss the simplest case of neutrino oscillations in vacuum.

2.1.3 NEUTRINO OSCILLATIONS IN VACUUM

Neutrinos are produced through CC interaction processes and are therefore produced as flavor eigenstates which are superpositions of mass eigenstates. Because the mass eigenstates have non-zero and non-degenerate masses, and because of mixing, the superposition detected after propagation is not necessarily the same as the initially produced one: the neutrino detected may have changed its flavor. This phenomenon, first introduced by Bruno Pontecorvo in 1957 [4, 23], has been discovered by the SuperKamiokande and SNO experiments [3, 24]. In this section, we will present the standard derivation of the neutrino oscillation probabilities.

Let us assume that a neutrino of flavor α and momentum \vec{q} is created through a CC weak process at the instant $t = 0$. As we have seen before, it is created as a pure flavor state and can be written as

$$|\nu_\alpha\rangle = \sum_k U_{\alpha k}^* |\nu_k\rangle. \quad (2.27)$$

Note that the number of massive neutrinos is not limited: its minimum is three, but it may be larger than three. If so, the additional neutrinos in the flavor basis would be *sterile*, namely, they would not participate in any interaction except gravity. Therefore, the number of massive neutrinos will not be specified in the following general derivation. We consider orthonormal massive neutrino states: $\langle \nu_l | \nu_k \rangle = \delta_{kl}$, and since U is unitary, $\langle \nu_\alpha | \nu_\beta \rangle = \delta_{\alpha\beta}$.

In a Schrödinger-like picture, the massive neutrino states are eigenvalues of the Hamiltonian \mathcal{H} of the system: $\mathcal{H} |\nu_k\rangle = E_k |\nu_k\rangle$ where $E_k^2 = \vec{q}_k^2 + m_k^2$, and we consider that all neutrinos have equal momenta $\vec{q}_k = \vec{q}$. Therefore, they evolve according to the Schrödinger equation as $|\nu_k(t)\rangle = e^{-iE_k t} |\nu_k\rangle$. Using this equation and $|\nu_k\rangle = \sum_\alpha U_{\alpha k} |\nu_\alpha\rangle$, we find

$$|\nu_\alpha\rangle = \sum_\beta \sum_k U_{\alpha k}^* U_{\beta k} e^{-iE_k t} |\nu_\beta\rangle. \quad (2.28)$$

The transition probability is then given by

$$P_{\nu_\alpha \rightarrow \nu_\beta}(t) = |\langle \nu_\beta | \nu_\alpha(t) \rangle|^2, \quad (2.29)$$

$$= \sum_{k,j} U_{\alpha k}^* U_{\beta k} U_{\alpha j} U_{\beta j}^* e^{-i(E_k - E_j)t}, \quad (2.30)$$

$$\approx \sum_{k,j} U_{\alpha k}^* U_{\beta k} U_{\alpha j} U_{\beta j}^* e^{-i \frac{\Delta m_{kj}^2 L}{2E}}, \quad (2.31)$$

where we considered ultra-relativistic neutrinos detected at a distance $L \approx t$, with equal momenta \vec{q} such that $E_k - E_j \approx \frac{\Delta m_{kj}^2}{2E}$, where $\Delta m_{kj}^2 = m_k^2 - m_j^2$ and $E = |\vec{q}|$. It is easy to verify that the transition probability does not depend on the (possible) Majorana phases of the mixing matrix U . The antineutrino transitions $\bar{\nu}_\alpha \rightarrow \bar{\nu}_\beta$ have different probabilities than neutrino transitions $\nu_\alpha \rightarrow \nu_\beta$ in the presence of a non-zero Dirac CP-violating phase δ . The first evidence of neutrino oscillations was provided by the pioneering experiment Super-Kamiokande [3]. In 1998, they observed an azimuthal asymmetry in the number of atmospheric muon detected (see figure 2.3). This can be explained by the fact that muon neutrinos converted into ν_τ that were not detected. The experimental evidence of neutrino oscillations are discussed in more detail in Section 2.4.

An interesting special case is the one of *two-neutrino* mixing. In this approximation, we consider only two massive neutrinos out of three. While this simplifies greatly the oscillation formulas, it is also well justified as most experiments are not sensitive to the influence of three-neutrino mixing. Therefore, we consider two neutrino flavors ν_α and ν_β , which can be either pure flavor neutrinos or a linear combination of pure flavor neutrinos. The mixing matrix U is reduced to a 2×2 matrix, which is a rotation matrix in the Dirac case, but includes an additional phase in case neutrinos are Majorana particles. However, it is easy to see in the equations above that such a phase does not play any role [22]. In the Dirac case, the matrix U can be

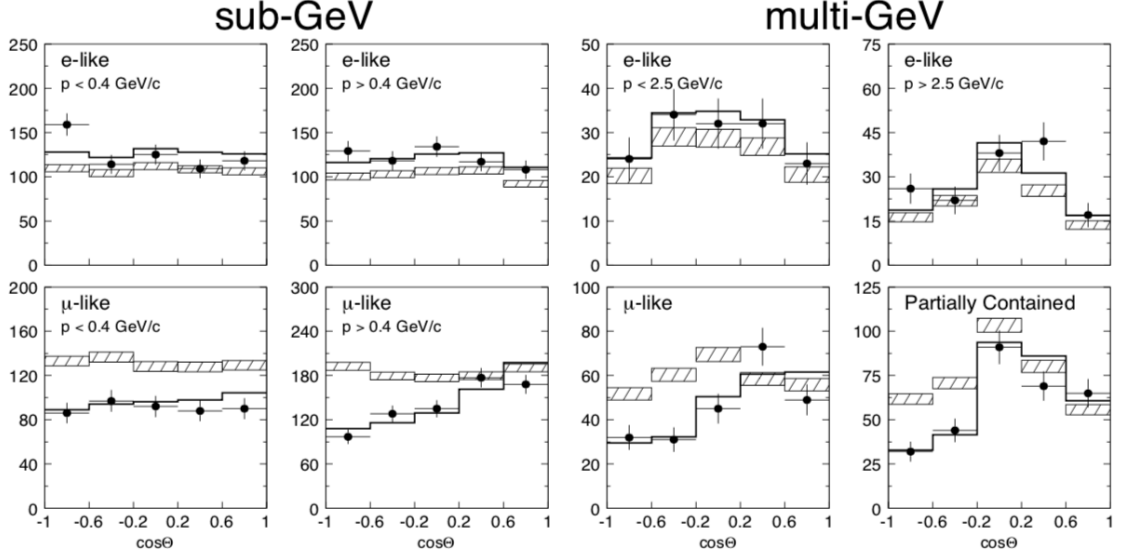


Figure 2.3: Zenith angle distributions of μ -like and e -like events for sub-GeV and multi-GeV data sets. Upward-going particles have $\cos \theta < 0$ and downward-going particles have $\cos \theta > 0$. Sub-GeV data are shown separately for $p < 400$ MeV/c and $p > 400$ MeV/c. Multi-GeV e -like distributions are shown for $p < 2.5$ GeV/c and $p > 2.5$ GeV/c and the multi-GeV μ -like are shown separately for FC and PC events. The hatched region shows the Monte Carlo expectation for no oscillations normalized to the data live-time with statistical errors. The bold line is the best-fit expectation for $\nu_\mu \leftrightarrow \nu_\tau$ oscillations with the overall flux normalization fitted as a free parameter. Figure and caption adopted from Ref. [3].

parametrized as

$$U = \begin{pmatrix} \cos \theta & \sin \theta \\ -\sin \theta & \cos \theta \end{pmatrix}, \quad (2.32)$$

where θ is the effective mixing angle, and the appearance and survival probabilities take the simple forms

$$P_{\nu_\alpha \rightarrow \nu_\beta}(L, E) = \sin^2 2\theta \sin^2 \left(\frac{\Delta m^2 L}{4E} \right) \quad (\text{for } \alpha \neq \beta), \quad (2.33)$$

$$P_{\nu_\alpha \rightarrow \nu_\alpha}(L, E) = 1 - \sin^2 2\theta \sin^2 \left(\frac{\Delta m^2 L}{4E} \right), \quad (2.34)$$

where $\Delta m^2 \equiv \Delta m_{21}^2$. Using different source-to-detector distances and different energy ranges enable to explore different values of the parameters Δm^2 and θ . The amplitude of the oscillations is controlled by the value of the mixing angle θ , while the *oscillation length*, $L_{\text{osc}} = \frac{4\pi E}{\Delta m^2}$ depends only on the energy of the neutrino and on the difference of the squared masses of the massive neutrinos. Note that the oscillation probabilities in vacuum do not depend on the sign of Δm^2 . Therefore, neutrino oscillation experiments give us access only to the absolute value of such a parameter.

2.2 DESCRIBING NEUTRINO PROPAGATION IN DENSE MEDIA

WHEN NEUTRINOS ARE PROPAGATING IN DENSE ENVIRONMENTS, their flavor evolution can be drastically modified because of the interactions with the particles composing the medium.

In this section, we derive the equations describing neutrino evolution in the mean-field approximation. We start by writing the most general mean-field Hamiltonian, and introducing every relevant two-point correlators. We use first principles to derive the most general evolution equations for those two-point correlators. Then, we derive the different components involved in the effective Hamiltonian for a typical astrophysical environment. Finally, we write down explicitly the equations derived above in the case of ultra-relativistic neutrinos evolving in a homogeneous environment. We consider both Dirac and Majorana neutrinos and highlight the differences between the two cases. Note that the results derived in this section are based on the published work [25].

2.2.1 MOST GENERAL EQUATIONS IN THE MEAN-FIELD APPROXIMATION

IN THE MEAN-FIELD APPROXIMATION, neutrinos and antineutrinos are considered as free streaming, propagating in an averaged background field.

In this section, we derive the most general equations for neutrino propagation in the mean-field approximation, following the procedure of Ref. [25]. Alternative derivations can be found in the literature (for a review, see e.g. Ref. [26]). The density matrix formalism used here has been first introduced in Ref. [27], and used in several other works (see e.g. Ref. [28, 29, 30, 31, 32]). In Ref. [33], a coherent-state path formalism is used, and it is shown that mean-field equations correspond to the stationary phase of the path integral for the many-body system. The authors of Ref. [34] applied the Born-Bogoliubov-Green-Kirkwood-Yvon (BBGKY) hierarchy to derive an unclosed set of equations, which can be truncated to its first equation to obtain the mean-field evolution equations.

Starting with the most general mean-field Hamiltonian and every possible two-point correlators, we use the Ehrenfest theorem and anti-commutation relations to derive the most general equations for those two-point correlators. The differences between the Dirac and Majorana cases are discussed.

DIRAC NEUTRINOS

We start by writing the effective mean-field Hamiltonian of the propagating particle as a bilinear form

$$H_{\text{eff}}(t) = \int d^3\vec{x} \bar{\psi}_{\nu_i}(x) \Gamma_{ij}(x) \psi_{\nu_j}(x), \quad (2.35)$$

where $\Gamma_{ij}(x)$ is a Kernel that will be specified later on, depending on the interactions with the medium. Let us notice that this expression of the Hamiltonian is very general: Eq. (2.9) is directly expressed as such, while Eq. (2.8) can be rewritten in this form using a Wick-like transformation and Fierz identity (see Ref. [20]). The fields ψ_{ν_k} are massive neutrino fields, though the equations derived below are valid in any basis. In the interaction pictures, their expression is given by Eq. (2.2), with the non-zero anti-commutation relations at equal time given by Eq. (2.3).

The most general equations in the mean-field approximation should involve the equal-time two-point correlators

$$\rho_{ij}(t, \vec{q}, \sigma, \vec{q}', \sigma') = \langle a_j^\dagger(\vec{q}', \sigma') a_i(\vec{q}, \sigma) \rangle, \quad (2.36)$$

$$\bar{\rho}_{ij}(t, \vec{q}, \sigma, \vec{q}', \sigma') = \langle b_i^\dagger(\vec{q}, \sigma) b_j(\vec{q}', \sigma') \rangle, \quad (2.37)$$

$$\kappa_{ij}(t, \vec{q}, \sigma, \vec{q}', \sigma') = \langle b_j(\vec{q}', \sigma') a_i(\vec{q}, \sigma) \rangle, \quad (2.38)$$

$$\kappa_{ij}^\dagger(t, \vec{q}, \sigma, \vec{q}', \sigma') = \langle a_j^\dagger(\vec{q}', \sigma') b_i^\dagger(\vec{q}, \sigma) \rangle, \quad (2.39)$$

where the brackets denote the expectation value of the operator, taking into account the quantum and statistical average over the background in which the neutrinos are propagating. Usually, only the neutrino (2.36) and antineutrino (2.37) density matrices are considered when studying neutrino evolution in media. Reference [34] first pointed out that the pairing correlators (2.38, 2.39) also contribute to the mean-field evolution equations. The authors also discussed the possible contribution of terms due to non-zero neutrino mass, which are comprised here as the neutrino and antineutrino density matrices include all possible helicity states.

To derive the evolution equations of the two-point correlator, we use the Ehrenfest theorem $i \frac{\partial \langle A \rangle}{\partial t} = \langle [A, H_{\text{eff}}(t)] \rangle$. To this aim, we rewrite the effective Hamiltonian (2.35) as a function of the creation and annihilation operators of the neutrinos and antineutrinos. Introducing the notations

$$\int_{\vec{p}} \equiv \int d^3\vec{p}, \quad (2.40)$$

$$\int_{\vec{p}, \sigma} \equiv \int_{\vec{p}} \sum_{\sigma=\pm 1/2}, \quad (2.41)$$

and the matrix product $(A \cdot B)(t, \vec{q}, \sigma, \vec{q}', \sigma') = \int_{\vec{p}_1, \sigma_1} A(\vec{q}, \sigma, \vec{p}_1, \sigma_1) B(\vec{p}_1, \sigma_1, \vec{q}', \sigma')$, we get

$$\begin{aligned}
H_{\text{eff}}(t) = & \frac{1}{(2\pi)^3} \int_{\vec{p}_1, \sigma_1} \int_{\vec{p}_2, \sigma_2} \int d^3 \vec{x} \left[\bar{u}_i(\vec{p}_1, \sigma_1) \Gamma_{ij}(x) u_j(\vec{p}_2, \sigma_2) e^{-i(p_1 - p_2)x} a_i^\dagger(\vec{p}_1, \sigma_1) a_j(\vec{p}_2, \sigma_2) \right. \\
& + \bar{u}_i(\vec{p}_1, \sigma_1) \Gamma_{ij}(x) v_j(\vec{p}_2, \sigma_2) e^{-i(p_1 + p_2)x} a_i^\dagger(\vec{p}_1, \sigma_1) b_j^\dagger(\vec{p}_2, \sigma_2) \\
& + \bar{v}_i(\vec{p}_1, \sigma_1) \Gamma_{ij}(x) u_j(\vec{p}_2, \sigma_2) e^{-i(-p_1 - p_2)x} b_i(\vec{p}_1, \sigma_1) a_j(\vec{p}_2, \sigma_2) \\
& \left. + \bar{v}_i(\vec{p}_1, \sigma_1) \Gamma_{ij}(x) v_j(\vec{p}_2, \sigma_2) e^{-i(p_2 - p_1)x} b_i(\vec{p}_1, \sigma_1) b_j^\dagger(\vec{p}_2, \sigma_2) \right].
\end{aligned}$$

Defining the Fourier transform on the spatial part of Γ

$$\tilde{\Gamma}_{ij}(t, \vec{k}) \equiv \frac{1}{(2\pi)^3} \int d^3 \vec{x} e^{-i\vec{k} \cdot \vec{x}} \Gamma_{ij}(t, \vec{x}), \quad (2.42)$$

and the following matrix elements

$$\Gamma_{ij}^{\nu\nu}(t, \vec{p}_1, \sigma_1, \vec{p}_2, \sigma_2) = \bar{u}_i(\vec{p}_1, \sigma_1) \tilde{\Gamma}_{ij}(t, \vec{p}_1 - \vec{p}_2) u_j(\vec{p}_2, \sigma_2) e^{-i(p_2^0 - p_1^0)t}, \quad (2.43)$$

$$\Gamma_{ij}^{\nu\bar{\nu}}(t, \vec{p}_1, \sigma_1, \vec{p}_2, \sigma_2) = \bar{u}_i(\vec{p}_1, \sigma_1) \tilde{\Gamma}_{ij}(t, \vec{p}_1 + \vec{p}_2) v_j(\vec{p}_2, \sigma_2) e^{-i(-p_2^0 - p_1^0)t}, \quad (2.44)$$

$$\Gamma_{ij}^{\bar{\nu}\nu}(t, \vec{p}_1, \sigma_1, \vec{p}_2, \sigma_2) = \bar{v}_i(\vec{p}_1, \sigma_1) \tilde{\Gamma}_{ij}(t, -\vec{p}_1 - \vec{p}_2) u_j(\vec{p}_2, \sigma_2) e^{-i(p_1^0 + p_2^0)t}, \quad (2.45)$$

$$\Gamma_{ij}^{\bar{\nu}\bar{\nu}}(t, \vec{p}_1, \sigma_1, \vec{p}_2, \sigma_2) = \bar{v}_i(\vec{p}_1, \sigma_1) \tilde{\Gamma}_{ij}(t, \vec{p}_2 - \vec{p}_1) v_j(\vec{p}_2, \sigma_2) e^{-i(p_1^0 - p_2^0)t}, \quad (2.46)$$

we get the compact form for the effective Hamiltonian

$$H_{\text{eff}}(t) = [a^\dagger(t) \cdot \Gamma^{\nu\nu}(t) \cdot a(t) + a^\dagger(t) \cdot \Gamma^{\nu\bar{\nu}}(t) \cdot b^\dagger(t) + b(t) \cdot \Gamma^{\bar{\nu}\nu}(t) \cdot a(t) + b(t) \cdot \Gamma^{\bar{\nu}\bar{\nu}}(t) \cdot b^\dagger(t)]. \quad (2.47)$$

H_{eff} , $\Gamma^{\nu\nu}$ and $\Gamma^{\bar{\nu}\bar{\nu}}$ are Hermitian while $\Gamma^{\nu\bar{\nu}\dagger} = \Gamma^{\bar{\nu}\nu}$. Having expressed the effective Hamiltonian in terms of the creation and annihilation operators, we use the Ehrenfest theorem. For this purpose, we have computed commutation relations of the type $\langle [aa^\dagger, aa^\dagger] \rangle$ as functions of the different two-point correlators. In the end, we get the following evolution equations for the neutrino and antineutrino density matrices, as well as for the pair correlators

$$i\dot{\rho}(t) = ([\Gamma^{\nu\nu}, \rho] + \Gamma^{\nu\bar{\nu}} \cdot \kappa^\dagger - \kappa \cdot \Gamma^{\bar{\nu}\nu}), \quad (2.48)$$

$$i\dot{\bar{\rho}}(t) = ([\Gamma^{\bar{\nu}\bar{\nu}}, \bar{\rho}] + \kappa^\dagger \cdot \Gamma^{\nu\bar{\nu}} - \Gamma^{\bar{\nu}\nu} \cdot \kappa), \quad (2.49)$$

$$i\dot{\kappa}(t) = (\Gamma^{\nu\nu} \cdot \kappa - \kappa \cdot \Gamma^{\bar{\nu}\bar{\nu}} - \Gamma^{\nu\bar{\nu}} \cdot \bar{\rho} - \rho \cdot \Gamma^{\bar{\nu}\nu} + \Gamma^{\nu\bar{\nu}}). \quad (2.50)$$

These are the most general mean-field evolution equations. They correspond to the first equation truncation of the BBGKY hierarchy. They include corrections to the relativistic limit and neutrino-antineutrino

correlations which have been first pointed out in Ref. [34]. Note that all the matrices in the equations above are $2n_f \times 2n_f$, where n_f is the number of flavors, as they include both a flavor and helicity structure.

The effects of the neutrino-antineutrino correlations associated with the κ terms have been recently discussed. Currently, no numerical study of these effects has been performed. However, it has been argued in Ref. [35] that the contributions of these correlators are extremely small. Furthermore, the authors have shown that the MSW-like resonance condition associated with these correlators is unlikely to be met in a typical astrophysical environment.

The effects of the corrections to the relativistic limits, also called *helicity coherence*, are discussed in Chapter 4 as this study is the goal of the first project of this thesis. Such corrections, proportional to the neutrino masses, can create transitions between neutrinos and anti-neutrinos. We will explore their impact on neutrino flavor evolution in astrophysical environments.

We now discuss the differences between the Dirac and the Majorana cases.

MAJORANA NEUTRINOS

In the case of Majorana neutrinos, we write the effective Hamiltonian as the bilinear form

$$H_{\text{eff}}^M(t) = \int d^3\vec{x} \bar{\psi}_{\nu_i}^M(x) \Gamma_{ij}(x) \psi_{\nu_j}^M(x), \quad (2.51)$$

where ψ^M are Majorana fields given in Eq. (2.14). Although the Hamiltonian has the same form as the Dirac effective Hamiltonian (2.35), the kernel does not: the vacuum part of the Kernel has to be divided by 1/2, as discussed in section 2.1.2. We define the two-point correlators as follow

$$\rho_{ij}^M(t, \vec{q}, \sigma, \vec{q}', \sigma') = \langle a_j^\dagger(\vec{q}', \sigma') a_i(\vec{q}, \sigma) \rangle, \quad (2.52)$$

$$\bar{\rho}^M = (\rho^M)^\top, \quad (2.53)$$

$$\kappa_{ij}^M(t, \vec{q}, \sigma, \vec{q}', \sigma') = \langle a_j(\vec{q}', \sigma') a_i(\vec{q}, \sigma) \rangle, \quad (2.54)$$

$$\kappa_{ij}^{M\dagger}(t, \vec{q}, \sigma, \vec{q}', \sigma') = \langle a_j^\dagger(\vec{q}', \sigma') a_i^\dagger(\vec{q}, \sigma) \rangle. \quad (2.55)$$

As before, we develop the effective Hamiltonian (2.51) in terms of a and a^\dagger and we get

$$H_{\text{eff}}(t) = a^\dagger(t) \cdot \Gamma^{\nu\nu}(t) \cdot a(t) + a^\dagger(t) \cdot \Gamma^{\nu\bar{\nu}}(t) \cdot a^\dagger(t) + a(t) \cdot \Gamma^{\bar{\nu}\nu}(t) \cdot a(t) + a(t) \cdot \Gamma^{\bar{\nu}\bar{\nu}}(t) \cdot a^\dagger(t). \quad (2.56)$$

Alternatively, it is possible to obtain a formulation closer to the one obtained in the Dirac case by defining

$$\begin{aligned}\Gamma_M^{\nu\nu} &= \Gamma^{\nu\nu} - (\Gamma^{\bar{\nu}\bar{\nu}})^\dagger, & \Gamma_M^{\nu\bar{\nu}} &= \Gamma^{\nu\bar{\nu}} - (\Gamma^{\nu\bar{\nu}})^\dagger, \\ \Gamma_M^{\bar{\nu}\bar{\nu}} &= \Gamma^{\bar{\nu}\bar{\nu}} - (\Gamma^{\nu\nu})^\dagger, & \Gamma_M^{\bar{\nu}\nu} &= \Gamma^{\bar{\nu}\nu} - (\Gamma^{\bar{\nu}\nu})^\dagger.\end{aligned}\quad (2.57)$$

From these definitions, we get the relations $(\Gamma_M^{\nu\nu})^\dagger = -\Gamma_M^{\bar{\nu}\bar{\nu}}$ and $(\Gamma_M^{\bar{\nu}\bar{\nu}})^\dagger = -\Gamma_M^{\nu\nu}$, and rewrite the effective Hamiltonian (2.51) as

$$H_{\text{eff}}(t) = \frac{1}{2} [a^\dagger(t) \cdot \Gamma_M^{\nu\nu}(t) \cdot a(t) + a^\dagger(t) \cdot \Gamma_M^{\nu\bar{\nu}}(t) \cdot a^\dagger(t) + a(t) \cdot \Gamma_M^{\bar{\nu}\nu}(t) \cdot a(t) + a(t) \cdot \Gamma_M^{\bar{\nu}\bar{\nu}}(t) \cdot a^\dagger(t)]. \quad (2.58)$$

Using the Ehrenfest theorem and expressing the different commutation relations of the type $\langle [aa^\dagger, aa^\dagger] \rangle$ as a function of the two-point correlators (2.52-2.55), we find that the evolution equations in the Majorana case take the same form as in the Dirac case (2.48-2.50), with the Γ_M matrices (2.57) replacing the Γ matrices (2.43-2.46), namely

$$i\dot{\rho}^M(t) = ([\Gamma_M^{\nu\nu}, \rho^M] + \Gamma_M^{\nu\bar{\nu}} \cdot \kappa^{M\dagger} - \kappa^M \cdot \Gamma_M^{\bar{\nu}\nu}), \quad (2.59)$$

$$i\dot{\kappa}^M(t) = (\Gamma_M^{\nu\nu} \cdot \kappa^M - \kappa^M \cdot \Gamma_M^{\bar{\nu}\bar{\nu}} - \Gamma_M^{\nu\bar{\nu}} \cdot \bar{\rho}^M - \rho^M \cdot \Gamma_M^{\bar{\nu}\nu} + \Gamma_M^{\nu\bar{\nu}}). \quad (2.60)$$

Note again that although the structure of the equations are the same as for Dirac neutrinos, the content of the Γ_M matrices is different.

2.2.2 DERIVING THE EFFECTIVE HAMILTONIAN IN THE MEAN-FIELD APPROXIMATION

Having derived the evolution equations for the two-point correlators (2.36 - 2.39) —respectively (2.52 - 2.55) for Majorana neutrinos—, we derive the different elements of the $\Gamma^{\nu(\bar{\nu})}$ in a typical astrophysical environment, with a large number of self-interacting (anti)neutrinos in a background of electrons and nucleons. Therefore, three contributions have to be considered: *i*) the vacuum part of the effective Hamiltonian, *ii*) the CC and NC interactions of neutrinos with electrons, protons and neutrons in the medium, *iii*) the neutrino (NC) self-interactions.

VACUUM CONTRIBUTION

The kernel of the vacuum (or free) Hamiltonian is

$$\Gamma_{ij}^{\text{vac}}(t, \vec{x}) = \delta_{ij} (\not{\partial} + m_i), \quad (2.61)$$

for Dirac neutrinos. Note that for Majorana neutrinos, this kernel has to be divided by 2 to account for the fact that the number of degrees of freedom is divided by 2. Using Dirac equation and $q_{i,\mu} q_i^\mu = -m_i^2$, as well as the different definitions (2.43 - 2.46), we get for Dirac neutrinos

$$\Gamma_{ij}^{\nu\nu,\text{vac}}(t, \vec{q}, h, \vec{q}', h') = \delta_{ij} \delta^{(3)}(\vec{q} - \vec{q}') \delta_{h,h'} q^0, \quad (2.62)$$

$$\Gamma_{ij}^{\bar{\nu}\bar{\nu},\text{vac}}(t, \vec{q}, h, \vec{q}', h') = -\delta_{ij} \delta^{(3)}(\vec{q} - \vec{q}') \delta_{h,h'} q^0, \quad (2.63)$$

$$\Gamma_{ij}^{\bar{\nu}\nu,\text{vac}}(t, \vec{q}, h, \vec{q}', h') = 0, \quad (2.64)$$

$$\Gamma_{ij}^{\nu\bar{\nu},\text{vac}}(t, \vec{q}, h, \vec{q}', h') = 0, \quad (2.65)$$

and for Majorana neutrinos

$$\Gamma_{M,ij}^{\nu\nu,\text{vac}}(t, \vec{q}, h, \vec{q}', h') = \delta_{ij} \delta^{(3)}(\vec{q} - \vec{q}') \delta_{h,h'} q^0, \quad (2.66)$$

$$\Gamma_{M,ij}^{\nu\bar{\nu},\text{vac}}(t, \vec{q}, h, \vec{q}', h') = 0. \quad (2.67)$$

This vacuum contribution is, by definition, diagonal in the mass basis. We now discuss how to derive the contributions to the kernel from CC and NC interactions.

GENERAL PROCEDURE FOR DERIVING THE INTERACTIONS KERNELS

To compute the $\Gamma_{\nu}^{(\bar{\nu})}$ matrices, we first need to compute the kernel Γ^{int} of the different interactions undergone by neutrinos. According to the low-energy interaction Lagrangians (2.8, 2.9), we consider here that the effective Hamiltonian of the interaction reads

$$\mathcal{H}_{\text{int}} = c [\bar{\psi}_{\nu_\alpha} \gamma^\mu (1 - \gamma_5) \psi_{\nu_\beta}] [\bar{\chi} \gamma_\mu (k_1 - k_2 \gamma_5) \phi], \quad (2.68)$$

with c a coupling, ψ_{ν_α} the fermionic field of a neutrino ν_α , $(k_1, k_2) \in \mathbb{R}^2$, and χ and ϕ the fermionic fields of the other two particles involved in the interaction. We introduce a_χ and b_χ (respectively a_ϕ and b_ϕ) the annihilator operators of the particle described by χ (respectively ϕ) and its antiparticle. From Eq. (2.35), we wish to compute the kernel

$$\Gamma_{\alpha\beta} = c \gamma_\mu (1 - \gamma_5) T^\mu, \quad (2.69)$$

where we introduced the expectation value over the background

$$T^\mu \equiv \langle \bar{\chi} \gamma^\mu (k_1 - k_2 \gamma_5) \psi \rangle. \quad (2.70)$$

The procedure is then the following.

1. We expand χ and ϕ in T^μ (2.70) using their Fourier decomposition

$$T^\mu(x) = \left\langle \frac{1}{(2\pi)^3} \int_{\vec{p}_1, \sigma_1} \int_{\vec{p}_2, \sigma_2} (\bar{u}_\chi(\vec{p}_1, \sigma_1) e^{-ip_1 \cdot x} a_\chi^\dagger(\vec{p}_1, \sigma_1) + \bar{v}_\chi(\vec{p}_1, \sigma_1) e^{ip_1 \cdot x} b_\chi(\vec{p}_1, \sigma_1)) \right. \\ \left. \times \gamma^\mu (k_1 - k_2 \gamma_5) (u_\phi(\vec{p}_2, \sigma_2) e^{ip_2 \cdot x} a_\phi(\vec{p}_2, \sigma_2) + v_\chi(\vec{p}_2, \sigma_2) e^{-ip_2 \cdot x} b_\phi^\dagger(\vec{p}_2, \sigma_2)) \right\rangle. \quad (2.71)$$

2. We develop the product and use normal ordering, making the different two-points correlators appear

$$T^\mu(x) = \frac{1}{(2\pi)^3} \int_{\vec{p}_1, \sigma_1} \int_{\vec{p}_2, \sigma_2} \left[\bar{u}_\chi(\vec{p}_1, \sigma_1) \gamma^\mu (k_1 - k_2 \gamma_5) u_\phi(\vec{p}_2, \sigma_2) e^{-i(p_1 - p_2) \cdot x} \langle a_\chi^\dagger(\vec{p}_1, \sigma_1) a_\phi(\vec{p}_2, \sigma_2) \rangle \right. \\ \left. + \bar{u}_\chi(\vec{p}_1, \sigma_1) \gamma^\mu (k_1 - k_2 \gamma_5) v_\phi(\vec{p}_2, \sigma_2) e^{-i(p_1 + p_2) \cdot x} \langle a_\chi^\dagger(\vec{p}_1, \sigma_1) b_\phi^\dagger(\vec{p}_2, \sigma_2) \rangle \right. \\ \left. + \bar{v}_\chi(\vec{p}_1, \sigma_1) \gamma^\mu (k_1 - k_2 \gamma_5) u_\phi(\vec{p}_2, \sigma_2) e^{-i(-p_1 - p_2) \cdot x} \langle b_\chi(\vec{p}_1, \sigma_1) a_\phi(\vec{p}_2, \sigma_2) \rangle \right. \\ \left. - \bar{v}_\chi(\vec{p}_1, \sigma_1) \gamma^\mu (k_1 - k_2 \gamma_5) v_\phi(\vec{p}_2, \sigma_2) e^{-i(p_2 - p_1) \cdot x} \langle b_\phi^\dagger(\vec{p}_2, \sigma_2) b_\chi(\vec{p}_1, \sigma_1) \rangle \right]. \quad (2.72)$$

3. We use assumptions on the medium (e.g. homogeneity, neutrality, etc) to simplify the different correlators and compute $\Gamma_{\alpha\beta}$.

We now use this procedure to compute the matter contribution, induced by neutrino interactions with electrons, protons and neutrons in the medium, as well as the neutrino self-interaction contribution.

MATTER CONTRIBUTION

We consider CC and NC interactions of neutrinos with an unpolarized, electrically-neutral background of electrons, protons, and neutrons (see figure 2.4). While electron neutrinos can interact through both processes, muon and tau neutrinos are affected only by NC interactions.

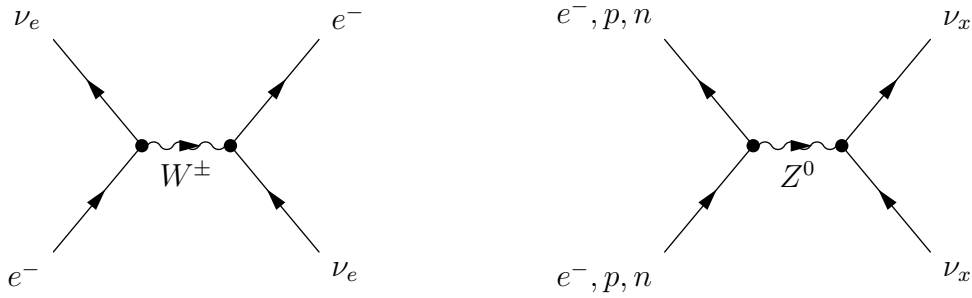


Figure 2.4: Feynman diagrams of the CC and NC interactions involved in the propagation of neutrino in a typical astrophysical environment. The CC interactions (left) involves only electron neutrinos, while the NC interactions are flavor blind: they can involve any neutrino flavor.

We derive the $\Gamma_{\nu\nu}^{(-)(-)}$ matter contributions in the flavor basis, as, by definition, the matter interaction kernel is diagonal in this basis. We follow the procedure of section 2.2.2 in order to compute the CC contribution due to neutrino electron scattering

$$T_{CC}^\mu(x) = \langle \bar{\psi}_e(x) \gamma^\mu (1 - \gamma_5) \psi_e(x) \rangle, \quad (2.73)$$

where ψ_e is the electron fermionic field, and the NC contribution

$$T_{\text{NC}}^\mu(x) = \sum_{f=e^-,p,n} \langle \bar{\psi}_f(x) \gamma^\mu (c_v^f - v_a^f \gamma_5) \psi_f(x) \rangle, \quad (2.74)$$

where the ψ_f are the fermionic field for particle $f = e^-, p, n$. We assume that the background is homogeneous, and suppose that there are only forward and elastic scattering so that

$$\rho_f(t, \vec{p}_1, \sigma_1, \vec{p}_2, \sigma_2) \equiv \langle a_f^\dagger(\vec{p}_2, \sigma_2) a_f(\vec{p}_1, \sigma_1) \rangle = \delta_{\sigma_1, \sigma_2} \delta^{(3)}(\vec{p}_1 - \vec{p}_2) \rho_f(t, \vec{p}_1), \quad (2.75)$$

with $f = e^-, p, n$. Using the procedure of section 2.2.2 and trace techniques, we get for the CC interaction

$$T_{\text{CC}}^\mu(x) = \frac{1}{(2\pi)^3} \int_{\vec{p}_1, \sigma_1} \bar{u}_e(\vec{p}_1, \sigma_1) \gamma^\mu (1 - \gamma_5) u_e(\vec{p}_1, \sigma_1) \rho_e(\vec{p}_1, \sigma_1), \quad (2.76)$$

$$= - \int \frac{d^3 \vec{p}_e}{(2\pi)^3} \frac{2i p_e^\mu}{p_e^0} \rho_e(t, \vec{p}_e), \quad (2.77)$$

$$\equiv -i J^{e,\mu}, \quad (2.78)$$

which gives the CC kernel, in the flavor basis

$$\Gamma_{\alpha\beta}^{\text{CC}} = \frac{-iG_F}{\sqrt{2}} \gamma_\mu (1 - \gamma_5) J^{e,\mu} \delta_{\alpha\beta} \delta_{\alpha e}. \quad (2.79)$$

The same computation can be done for the NC contribution (2.74), and we get

$$\Gamma_{\alpha\beta}^{\text{NC}} = \frac{-iG_F}{\sqrt{2}} \gamma_\mu (1 - \gamma_5) \sum_{f=e^-,p,n} c_v^f J^{f,\mu} \delta_{\alpha\beta}. \quad (2.80)$$

Assuming that the background is electrically neutral, we have $J^{e,\mu} = J^{p,\mu}$. We then use the value of the coefficients $c_v^f = I_3 - 2q_f \sin^2 \theta_W$ and obtain

$$\Gamma_{\alpha\beta}^{\text{NC}} = \frac{-iG_F}{\sqrt{2}} \gamma_\mu (1 - \gamma_5) \left(-\frac{1}{2} J^{n,\mu} \right) \delta_{\alpha\beta}, \quad (2.81)$$

which finally gives the entire matter contribution, adding Eqs. (2.79) and (2.81)

$$\Gamma_{\alpha\beta}^{\text{mat}} = \frac{-iG_F}{\sqrt{2}} \gamma_\mu (1 - \gamma_5) \delta_{\alpha\beta} \left(\delta_{\alpha e} J^{e,\mu} - \frac{1}{2} J^{n,\mu} \right). \quad (2.82)$$

Using the expression of the kernel and chiral spinor products A, introducing the notation $\hat{q} = \frac{\vec{q}}{q}$, where $q = |\vec{q}|$, as the unit vector in the direction of \vec{q} and the vectors $n_\mu(\hat{q})$ and $\epsilon_\mu(\hat{q})$ as defined in Appendix A,

we obtain, for Dirac neutrinos

$$\Gamma_{ij}^{\nu\nu,\text{mat}}(t, \vec{q}, h, \vec{q}', h') = \delta^{(3)}(\vec{q} - \vec{q}') \left[-\delta_{h,-}\delta_{h,h'} n^\mu(\hat{q}) \cdot \Sigma_{\mu,ij}^{\text{mat}} + \delta_{h,-h'} \left(\frac{m_j}{2q} \delta_{h,-} e^{i\phi} \epsilon^{\mu*}(\hat{q}) + \frac{m_i}{2q} \delta_{h,+} e^{-i\phi} \epsilon^\mu(\hat{q}) \right) \cdot \Sigma_{\mu,ij}^{\text{mat}} \right], \quad (2.83)$$

$$\Gamma_{ij}^{\bar{\nu}\bar{\nu},\text{mat}}(t, \vec{q}, h, \vec{q}', h') = \delta^{(3)}(\vec{q} - \vec{q}') \left[-\delta_{h,+}\delta_{h,h'} n^\mu(\hat{q}) \cdot \Sigma_{\mu,ij}^{\text{mat}} - \delta_{h,-h'} \left(\frac{m_j}{2q} \delta_{h,+} e^{i\phi} \epsilon^{\mu*}(\hat{q}) + \frac{m_i}{2q} \delta_{h,-} e^{-i\phi} \epsilon^\mu(\hat{q}) \right) \cdot \Sigma_{\mu,ij}^{\text{mat}} \right], \quad (2.84)$$

$$\Gamma_{ij}^{\bar{\nu}\nu,\text{mat}}(t, \vec{q}, h, \vec{q}', h') = \delta^{(3)}(\vec{q} + \vec{q}') \left[-\delta_{h,-}\delta_{h,-h'} \epsilon^{\mu*}(\hat{q}) \cdot \Sigma_{\mu,ij}^{\text{mat}} + \delta_{h,h'} \left(\frac{m_i}{2q} \delta_{h,+} e^{-i\phi} n^\mu(-\hat{q}) + \frac{m_j}{2q} \delta_{h,-} e^{i\phi} n^\mu(\hat{q}) \right) \Sigma_{\mu,ij}^{\text{mat}} \right], \quad (2.85)$$

where $\Sigma_{ij}^{\text{mat},\mu}$ is the matrix

$$\Sigma_{\alpha\beta}^{\text{mat},\mu} = \sqrt{2} G_F \delta_{\alpha\beta} \left(\delta_{\alpha e} J^{e,\mu} - \frac{1}{2} J^{n,\mu} \right), \quad (2.86)$$

expressed in the mass basis. For Majorana neutrinos, we get

$$\Gamma_M^{\nu\nu,\text{mat}}(t, \vec{q}, h, \vec{q}', h') = \delta^{(3)}(\vec{q} - \vec{q}') \left[\delta_{h,h'} n^\mu(\hat{q}) \left(-\delta_{h,-} \Sigma_\mu^{\text{mat}} + \delta_{h,+} \Sigma_\mu^{\text{mat},\tau} \right) + \delta_{h,-h'} \delta_{h,+} e^{-i\phi} \epsilon^\mu(\hat{q}) \left(\frac{m}{2q} \cdot \Sigma_\mu^{\text{mat}} + \Sigma_\mu^{\text{mat},\tau} \cdot \frac{m}{2q} \right) + \delta_{h,-h'} \delta_{h,-} e^{i\phi} \epsilon^{\mu*}(\hat{q}) \left(\Sigma_\mu^{\text{mat}} \cdot \frac{m}{2q} + \frac{m}{2q} \cdot \Sigma_\mu^{\text{mat},\tau} \right) \right], \quad (2.87)$$

$$\Gamma_M^{\bar{\nu}\bar{\nu},\text{mat}}(t, \vec{q}, h, \vec{q}', h') = \delta^{(3)}(\vec{q} + \vec{q}') \left[\delta_{h,-h'} \epsilon^{\mu*}(\hat{q}) \left(-\delta_{h,-} \Sigma_\mu^{\text{mat}} + \delta_{h,+} \Sigma_\mu^{\text{mat},\tau} \right) \right] \quad (2.88)$$

$$+ \delta_{h,h'} \delta_{h,+} e^{-i\phi} \left(n^\mu(-\hat{q}) \frac{m}{2q} \cdot \Sigma_\mu^{\text{mat}} - n^\mu(\hat{q}) \Sigma_\mu^{\text{mat},\tau} \cdot \frac{m}{2q} \right) \quad (2.89)$$

$$+ \delta_{h,h'} \delta_{h,-} e^{i\phi} \left(n^\mu(\hat{q}) \Sigma_\mu^{\text{mat}} \cdot \frac{m}{2q} - n^\mu(-\hat{q}) \frac{m}{2q} \cdot \Sigma_\mu^{\text{mat},\tau} \right) \Big], \quad (2.90)$$

where m is the mass matrix, $m = \text{diag}(m_i)$ in the mass basis.

These terms can be reduced to the well-known matter potential, as discussed in section 2.2.3, and produce the Mikheev-Smirnov-Wolfenstein (MSW) effect which will be discussed below (see section 2.3). Note that the expressions above all include first order corrections to the relativistic limit, proportional to $\frac{m}{q}$. The role of these corrections is discussed in Chapter 4.

SELF-INTERACTION CONTRIBUTION

In dense astrophysical environments, neutrino self-interactions become relevant as neutrino densities can be very large. It has been shown in 1993 [36] that these contributions can lead to new phenomena different from the MSW effect, as they introduce nonlinearity in the evolution equations. Since the first numerical investigation of this term in the context of Supernova neutrino [11], these interactions have triggered an intense theoretical activity, which will be discussed in Chapter 3.

The NC neutrino self-interaction term Hamiltonian is, in the contact-interaction approximation (2.9)

$$\mathcal{H}^{\text{self}}(x) = \frac{G_F}{4\sqrt{2}} \sum_{\alpha,\beta} (\bar{\psi}_{\nu_\alpha}(x) \gamma_\mu (1 - \gamma_5) \psi_{\nu_\alpha}(x)) (\bar{\psi}_{\nu_\beta}(x) \gamma^\mu (1 - \gamma_5) \psi_{\nu_\beta}(x)). \quad (2.91)$$

It was first pointed out by Pantaleone in 1992 [10] that this term is quite different from the matter term derived above, as it also includes non-diagonal contributions. Furthermore, this interaction is intrinsically nonlinear.

As this term involves a sum on neutrino flavors, it has the same form in the mass basis. Therefore, we will compute the interaction kernel in this basis. We estimate the background potential created by these interactions by using a Wick-like transformation and Fierz identity [36]

$$\begin{aligned} (\bar{\psi}_{\nu_\alpha} \gamma^\mu (1 - \gamma_5) \psi_{\nu_\alpha}) (\bar{\psi}_{\nu_\beta} \gamma_\mu (1 - \gamma_5) \psi_{\nu_\beta}) &\rightarrow \langle \bar{\psi}_{\nu_\alpha} \gamma^\mu (1 - \gamma_5) \psi_{\nu_\alpha} \rangle (\bar{\psi}_{\nu_\beta} \gamma_\mu (1 - \gamma_5) \psi_{\nu_\beta}) \\ &\quad + (\bar{\psi}_{\nu_\alpha} \gamma^\mu (1 - \gamma_5) \psi_{\nu_\alpha}) \langle \bar{\psi}_{\nu_\beta} \gamma_\mu (1 - \gamma_5) \psi_{\nu_\beta} \rangle \\ &\quad + \langle \bar{\psi}_{\nu_\alpha} \gamma^\mu (1 - \gamma_5) \psi_{\nu_\beta} \rangle (\bar{\psi}_{\nu_\beta} \gamma_\mu (1 - \gamma_5) \psi_{\nu_\alpha}) + (\bar{\psi}_{\nu_\alpha} \gamma^\mu (1 - \gamma_5) \psi_{\nu_\beta}) \langle \bar{\psi}_{\nu_\beta} \gamma_\mu (1 - \gamma_5) \psi_{\nu_\alpha} \rangle \\ &\quad - \langle \bar{\psi}_{\nu_\alpha} \gamma^\mu (1 - \gamma_5) \psi_{\nu_\alpha} \rangle \langle \bar{\psi}_{\nu_\beta} \gamma_\mu (1 - \gamma_5) \psi_{\nu_\beta} \rangle - \langle \bar{\psi}_{\nu_\alpha} \gamma^\mu (1 - \gamma_5) \psi_{\nu_\beta} \rangle \langle \bar{\psi}_{\nu_\beta} \gamma_\mu (1 - \gamma_5) \psi_{\nu_\alpha} \rangle, \end{aligned} \quad (2.92)$$

where we omitted the dependence on (x) for readability. Let us analyze and illustrate the different terms involved in Eq. (2.92).

- The first two terms are diagonal contributions, meaning that the propagating neutrino doesn't change its flavor (see an example in the left panel figure 2.5).



Figure 2.5: Illustration of the interaction terms in Eq. (2.92) corresponding to the mean-field approximation for the neutrino self-interaction terms. Background neutrinos are illustrated as dashed arcs, while the test neutrino is a solid straight line. The left panel corresponds to the diagonal contributions, and doesn't involve a flavor change. The right panel corresponds to the off-diagonal contributions and makes the test neutrino change its flavor. Antineutrinos also contribute to these terms.

- The third and fourth terms are off-diagonal contributions. They involve the propagating neutrino changing its flavor (see an example in the right panel figure 2.5).
- The two last terms are not interaction terms and only contribute to the vacuum energy. We eliminate them for the rest of the calculation.

Using the transformation (2.92), we get the following expression for the neutrino self-interaction kernel

$$\Gamma_{ij}^{\text{self}} = \frac{G_F}{2\sqrt{2}} \gamma_\mu (1 - \gamma_5) \left(\sum_k T_{kk}^{\text{self},\mu} + T_{ij}^{\text{self},\mu} \right) \equiv \frac{-i}{2} \gamma_\mu (1 - \gamma_5) \Sigma_{ij}^{\text{self},\mu}, \quad (2.93)$$

where we introduced

$$T_{ij}^{\text{self},\mu} \equiv \langle \bar{\psi}_{\nu_j} \gamma^\mu (1 - \gamma_5) \psi_{\nu_i} \rangle. \quad (2.94)$$

Developing the neutrino fields in $T_{ij}^{\text{self},\mu}$, we get the expression

$$\begin{aligned} T_{ij}^{\text{self},\mu}(x) = & \frac{1}{(2\pi)^3} \int_{\vec{p}_1, \sigma_1} \int_{\vec{p}_2, \sigma_2} \left[\bar{u}_j(\vec{p}_1, \sigma_1) \gamma^\mu (1 - \gamma_5) u_i(\vec{p}_2, \sigma_2) e^{-i(p_1 - p_2)x} \rho_{ij}(t, \vec{p}_2, \sigma_2, \vec{p}_1, \sigma_1) \right. \\ & + \bar{u}_j(\vec{p}_1, \sigma_1) \gamma^\mu (1 - \gamma_5) v_i(\vec{p}_2, \sigma_2) e^{-i(p_1 + p_2)x} \kappa_{ij}^\dagger(t, \vec{p}_2, \sigma_2, \vec{p}_1, \sigma_1) \\ & + \bar{v}_j(\vec{p}_1, \sigma_1) \gamma^\mu (1 - \gamma_5) u_i(\vec{p}_2, \sigma_2) e^{-i(-p_1 - p_2)x} \kappa_{ij}(t, \vec{p}_2, \sigma_2, \vec{p}_1, \sigma_1) \\ & \left. - \bar{v}_j(\vec{p}_1, \sigma_1) \gamma^\mu (1 - \gamma_5) v_i(\vec{p}_2, \sigma_2) e^{-i(p_2 - p_1)x} \bar{\rho}_{ij}(t, \vec{p}_2, \sigma_2, \vec{p}_1, \sigma_1) \right]. \quad (2.95) \end{aligned}$$

Note that usually, the mean-field term associated to neutrino self-interactions do not include the κ contributions. Using the expression of the kernel and chiral spinor products (Appendix A), we obtain, for Dirac neutrinos

$$\Gamma_{ij}^{\nu\nu,\text{self}}(t, \vec{q}, h, \vec{q}', h') = \delta^{(3)}(\vec{q} - \vec{q}') \left[-\delta_{h,-} \delta_{h,h'} n^\mu(\hat{q}) \cdot \Sigma_{\mu,ij}^{\text{self}} + \delta_{h,-h'} \left(\frac{m_j}{2q} \delta_{h,-} e^{i\phi} \epsilon^{\mu*}(\hat{q}) + \frac{m_i}{2q} \delta_{h,+} e^{-i\phi} \epsilon^\mu(\hat{q}) \right) \cdot \Sigma_{\mu,ij}^{\text{self}} \right], \quad (2.96)$$

$$\Gamma_{ij}^{\bar{\nu}\bar{\nu},\text{self}}(t, \vec{q}, h, \vec{q}', h') = \delta^{(3)}(\vec{q} - \vec{q}') \left[-\delta_{h,+} \delta_{h,h'} n^\mu(\hat{q}) \cdot \Sigma_{\mu,ij}^{\text{self}} - \delta_{h,-h'} \left(\frac{m_j}{2q} \delta_{h,+} e^{i\phi} \epsilon^{\mu*}(\hat{q}) + \frac{m_i}{2q} \delta_{h,-} e^{-i\phi} \epsilon^\mu(\hat{q}) \right) \cdot \Sigma_{\mu,ij}^{\text{self}} \right], \quad (2.97)$$

$$\Gamma_{ij}^{\nu\bar{\nu},\text{self}}(t, \vec{q}, h, \vec{q}', h') = \delta^{(3)}(\vec{q} + \vec{q}') \left[-\delta_{h,-} \delta_{h,-h'} \epsilon^{\mu*}(\hat{q}) \cdot \Sigma_{\mu,ij}^{\text{self}} + \delta_{h,h'} \left(\frac{m_i}{2q} \delta_{h,+} e^{-i\phi} n^\mu(-\hat{q}) + \frac{m_j}{2q} \delta_{h,-} e^{i\phi} n^\mu(\hat{q}) \right) \Sigma_{\mu,ij}^{\text{self}} \right]. \quad (2.98)$$

For Majorana neutrinos, a similar expression to Eq. (2.95) is obtained by replacing the Dirac two-point correlators by Majorana ones (2.52- 2.55). For the kernels, we get

$$\Gamma_M^{\nu\nu,\text{self}}(t, \vec{q}, h, \vec{q}', h') = \delta^{(3)}(\vec{q} - \vec{q}') \left[\delta_{h,h'} n^\mu(\hat{q}) \left(-\delta_{h,-} \Sigma_\mu^{\text{self}} + \delta_{h,+} \Sigma_\mu^{\text{self},\tau} \right) + \delta_{h,-h'} \delta_{h,+} e^{-i\phi} \epsilon^\mu(\hat{q}) \left(\frac{m}{2q} \cdot \Sigma_\mu^{\text{self}} + \Sigma_\mu^{\text{self},\tau} \cdot \frac{m}{2q} \right) + \delta_{h,-h'} \delta_{h,-} e^{i\phi} \epsilon^{\mu*}(\hat{q}) \left(\Sigma_\mu^{\text{self}} \cdot \frac{m}{2q} + \frac{m}{2q} \cdot \Sigma_\mu^{\text{self},\tau} \right) \right], \quad (2.99)$$

$$\Gamma_M^{\nu\bar{\nu},\text{self}}(t, \vec{q}, h, \vec{q}', h') = \delta^{(3)}(\vec{q} + \vec{q}') \left[\delta_{h,-h'} \epsilon^{*,\mu} \left(-\delta_{h,-} \Sigma_\mu^{\text{self}} + \delta_{h,+} \Sigma_\mu^{\text{self},\tau} \right) + \delta_{h,h'} \delta_{h,+} e^{-i\phi} \left(n^\mu(-\hat{q}) \frac{m}{2q} \cdot \Sigma_\mu^{\text{self}} - n^\mu(\hat{q}) \Sigma_\mu^{\text{self},\tau} \cdot \frac{m}{2q} \right) + \delta_{h,h'} \delta_{h,-} e^{i\phi} \left(n^\mu(\hat{q}) \Sigma_\mu^{\text{self}} \cdot \frac{m}{2q} - n^\mu(-\hat{q}) \frac{m}{2q} \cdot \Sigma_\mu^{\text{self},\tau} \right) \right]. \quad (2.100)$$

As mentioned before, the equations derived in this section include all first-order corrections to the relativistic limit. The corresponding contributions require an anisotropy of the medium to be non-zero. They create a coupling between the active and sterile component ("wrong helicity" component) of (anti)neutrinos in the Dirac case or between neutrinos and antineutrinos in the Majorana case. We explore their role in detail

in Chapter 4 in a detailed astrophysical environment.

The equations above can be simplified in the case of ultra-relativistic neutrinos propagating in a homogeneous system (see below) and will be used hereafter when studying neutrino propagation.

2.2.3 HOMOGENEOUS SYSTEM IN THE ULTRA-RELATIVISTIC LIMIT

In this section, we compute the expressions for the $\Gamma_{\nu\nu}^{(-)(-)}$ matrices in the special case of a spatially homogeneous system and assuming that neutrinos are ultra-relativistic. Therefore, only positive-helicity neutrinos and negative-helicity antineutrinos are involved. We also neglect the pair-correlators κ , which role will not be explored in this thesis; consequently, we do not need to calculate the matrices $\Gamma^{\nu\bar{\nu}}$ (or $\Gamma^{\bar{\nu}\nu}$).

The equations derived below are the equations generally used when studying neutrino flavor evolution in astrophysical environments. In the first project (Chapter 4), we study the effects of the helicity coherence terms and highlight how they modify the structure of the equations derived below. The same equations are used in Chapter 5 to study the effect on nonstandard interactions.

For Dirac neutrinos, we can restrict ourselves to the following two-point correlators

$$\rho(t, \vec{q}, -, \vec{q}', -) = \delta^{(3)}(\vec{q} - \vec{q}') \rho(t, \vec{q}), \quad (2.101)$$

$$\bar{\rho}(t, \vec{q}, +, \vec{q}', +) = \delta^{(3)}(\vec{q} - \vec{q}') \bar{\rho}(t, -\vec{q}), \quad (2.102)$$

and as the spatial homogeneity implies $\tilde{\Gamma}_{ij}(t, \vec{q}) = \delta^{(3)}(\vec{q}) \tilde{\Gamma}_{ij}(t)$, the only non-zero contributions to the $\Gamma_{\nu\nu}^{(-)(-)}$ matrices are

$$\Gamma^{\nu\nu}(t, \vec{q}, -, \vec{q}', -) = \delta^{(3)}(\vec{q} - \vec{q}') \Gamma^{\nu\nu}(t, \vec{q}), \quad (2.103)$$

$$\Gamma^{\bar{\nu}\bar{\nu}}(t, \vec{q}, +, \vec{q}', +) = \delta^{(3)}(\vec{q} - \vec{q}') \Gamma^{\bar{\nu}\bar{\nu}}(t, -\vec{q}). \quad (2.104)$$

The choice of sign in the argument is such that all particles appear with the same momentum \vec{q} in the evolution equations derived below.

For Majorana neutrinos, we introduce

$$\rho_M(t, \vec{q}, -, \vec{q}', -) = \delta^{(3)}(\vec{q} - \vec{q}') \rho_M(t, \vec{q}), \quad (2.105)$$

$$\rho_M(t, \vec{q}, +, \vec{q}', +) = \delta^{(3)}(\vec{q} - \vec{q}') \bar{\rho}_M^\top(t, \vec{q}), \quad (2.106)$$

and the only non-zero contributions to the $\Gamma_M^{\nu(-)\nu(-)}$ matrices are

$$\Gamma_M^{\nu\nu}(t, \vec{q}, -, \vec{q}', -) = \delta^{(3)}(\vec{q} - \vec{q}') \Gamma_M^{\nu\nu}(t, \vec{q}), \quad (2.107)$$

$$\Gamma_M^{\nu\nu}(t, \vec{q}, +, \vec{q}', +) = -\delta^{(3)}(\vec{q} - \vec{q}') \Gamma_M^{\bar{\nu}\bar{\nu}\dagger}(t, \vec{q}). \quad (2.108)$$

We derive below the expressions for these new matrices. The evolution equations are, for Dirac neutrinos

$$i\rho(t, \vec{q}) = [\Gamma^{\nu\nu}(t, \vec{q}), \rho(t, \vec{q})], \quad (2.109)$$

$$i\bar{\rho}(t, \vec{q}) = [\Gamma^{\bar{\nu}\bar{\nu}}(t, \vec{q}), \bar{\rho}(t, \vec{q})], \quad (2.110)$$

These are the equations generally used to study neutrino flavor evolution. Although their structure is similar to the one of equations (2.48 - 2.50), taking $\kappa = 0$, note that the matrices involved in (2.109, 2.110) are now $n_f \times n_f$ matrices as they only involve a flavor structure. For Majorana neutrinos, we get the set of equations

$$i\rho_M(t, \vec{q}) = [\Gamma_M^{\nu\nu}(t, \vec{q}), \rho_M(t, \vec{q})], \quad (2.111)$$

$$i\bar{\rho}_M(t, \vec{q}) = [\Gamma_M^{\bar{\nu}\bar{\nu}}(t, \vec{q}), \bar{\rho}_M(t, \vec{q})], \quad (2.112)$$

which have a similar structure as equations (2.59 - 2.60), taking $\kappa^M = 0$, but now involve $n_f \times n_f$ matrices.

Based on the equations derived in section 2.2.2, we now give the vacuum, matter and self-interaction contributions to the kernels (2.103, 2.104) —(2.107, 2.108) for Majorana neutrinos—, for a homogeneous system in the ultra-relativistic limit.

VACUUM CONTRIBUTION

Using the notation introduced previously, we use equations (2.62-2.65) and get for Dirac neutrinos

$$\Gamma^{\nu\nu, vac}(t, \vec{q}) = -\Gamma^{\bar{\nu}\bar{\nu}, vac}(t, \vec{q}) = h^0(\vec{q}), \quad (2.113)$$

with $h^0 = \text{diag}(q_i^0)$ in the mass basis. For Majorana neutrinos, we get from equations (2.66, 2.67)

$$\Gamma_M^{\nu\nu, vac}(t, \vec{q}) = -\Gamma_M^{\bar{\nu}\bar{\nu}, vac}(t, \vec{q}) = h^0(\vec{q}). \quad (2.114)$$

MATTER CONTRIBUTION

We introduce the particle number densities for the fermion $f = e^-, p, n$

$$n_f \equiv J^{f,0}, \quad (2.115)$$

and the scalar and vector contributions, diagonal in the flavor basis

$$h_{\alpha\beta}^{\text{mat}} = \sqrt{2}G_F\delta_{\alpha\beta} \left(n_e(t) \delta_{\alpha e} - \frac{1}{2}n_n(t) \right), \quad (2.116)$$

$$\vec{V}_{\alpha\beta}^{\text{mat}} = \sqrt{2}G_F\delta_{\alpha\beta} \left(\vec{J}^e(t) \delta_{\alpha e} - \frac{1}{2}\vec{J}^n(t) \right). \quad (2.117)$$

With these definitions, we use equations (2.83-2.85) and get for Dirac neutrinos

$$\Gamma^{\nu\nu,\text{mat}}(t, \vec{q}) = h^{\text{mat}} - \hat{q} \cdot \vec{V}^{\text{mat}}, \quad (2.118)$$

$$\Gamma^{\bar{\nu}\bar{\nu},\text{mat}}(t, \vec{q}) = h^{\text{mat}} + \hat{q} \cdot \vec{V}^{\text{mat}}. \quad (2.119)$$

In the Majorana case, equations (2.87, 2.90) become

$$\Gamma_M^{\nu\nu,\text{mat}}(t, \vec{q}) = \Gamma_M^{\bar{\nu}\bar{\nu},\text{mat}}(t, \vec{q}) = h^{\text{mat}} - \hat{q} \cdot \vec{V}^{\text{mat}}. \quad (2.120)$$

The matter potentials (2.118, 2.119) — 2.120) for Majorana neutrinos— are generally used when describing neutrino propagation in matter. In section 2.3, we use these expressions to unravel the MSW effect.

SELF-INTERACTION CONTRIBUTION

Using the definitions (2.103, 2.104) and setting $\kappa = 0$, Eq. (2.95) becomes for Dirac neutrinos

$$T_{ij}^{\text{self},\mu}(x) = -2i \frac{1}{(2\pi)^3} \int_{\vec{q}} [n^\mu(\hat{q}) (\rho_{ij}(t, \vec{q}) - \bar{\rho}_{ij}(t, -\vec{q}))], \quad (2.121)$$

and similarly for Majorana neutrinos, using (2.107, 2.108), with ρ and $\bar{\rho}$ replaced by ρ_M and $\bar{\rho}_M$. We introduce

$$h^{\text{self}} = \sqrt{2}G_F \left\{ \int_{\vec{q}} (\rho(t, \vec{q}) - \bar{\rho}(t, -\vec{q})) + \mathbb{1} \int_{\vec{q}} (\text{Tr} \rho(t, \vec{q}) - \text{Tr} \bar{\rho}(t, -\vec{q})) \right\}, \quad (2.122)$$

where $\mathbb{1}$ is the $n_f \times n_f$ identity matrix, and

$$\vec{V}^{\text{self}} = \sqrt{2}G_F \left\{ \int_{\vec{q}} \hat{q} (\rho(t, \vec{q}) - \bar{\rho}(t, -\vec{q})) + \mathbb{1} \int_{\vec{q}} \hat{q} (\text{Tr} \rho(t, \vec{q}) - \text{Tr} \bar{\rho}(t, -\vec{q})) \right\}. \quad (2.123)$$

Note that the terms proportional to the identity cannot be discarded, as usually done, in the presence of helicity coherence. With these definitions, we use equations (2.96-2.98) and get for Dirac neutrinos

$$\Gamma^{\nu\nu,\text{self}}(t, \vec{q}) = h^{\text{self}} - \hat{q} \cdot \vec{V}^{\text{self}}, \quad (2.124)$$

$$\Gamma^{\bar{\nu}\bar{\nu},\text{self}}(t, \vec{q}) = h^{\text{self}} + \hat{q} \cdot \vec{V}^{\text{self}}. \quad (2.125)$$

In the Majorana case, equations (2.99, 2.100) become

$$\Gamma_M^{\nu\nu,\text{self}}(t, \vec{q}) = \Gamma_M^{\bar{\nu}\bar{\nu},\text{self}}(t, \vec{q}) = h^{\text{self}} - \hat{q} \cdot \vec{V}^{\text{self}}. \quad (2.126)$$

These contributions to the kernels are the one generally used when describing neutrino propagation in dense astrophysical environments. In Chapter 4, we use a modified version of these equations to study the impact of helicity coherence terms on neutrino flavor evolution. In Chapter 5, they will be used to assess the effects of matter-neutrino nonstandard interactions.

In the following we discuss the impact of the matter terms derived above that produce the MSW effect. This effect, nowadays well established experimentally, is a reference for the investigation of matter effects in general in astrophysical environments such as core-collapse supernovae and accretion disks around compact objects.

2.3 NEUTRINO PROPAGATION IN MATTER: THE MSW EFFECT

When neutrinos propagate in matter, they can undergo significant flavor conversions, due to the so-called MSW effect [8, 37]. This effect arises from the interactions of neutrinos with particles —neutrons, protons, electrons— composing the medium through which neutrinos propagate. The solar neutrino deficit problem, first observed by the Homestake experiment and discussed in Section 2.4.1, led to the discovery of this conversion phenomenon.

In this section, we study neutrino propagation in a homogeneous environment where neutrino self-interaction is negligible —typically, the Sun—, and in the ultra-relativistic approximation. We also consider the matter as isotropic. We study here Dirac neutrinos, but the results in the Majorana case are unchanged. We consider a two-neutrino scheme with one electron neutrino ν_e and another flavor ν_x with $x = \mu$ or τ —as muon and tau neutrinos have the same potential in matter—, and two massive states ν_1 and ν_2 .

With these assumptions, the equations (2.109, 2.110) become

$$i\rho(t, \vec{q}) = [h(t, \vec{q}), \rho(t, \vec{q})], \quad (2.127)$$

$$i\bar{\rho}(t, \vec{q}) = [\bar{h}(t, \vec{q}), \bar{\rho}(t, \vec{q})], \quad (2.128)$$

where $h(t, \vec{q}) = h^0(\vec{q}) + h^{\text{mat}}(t)$ and $\bar{h}(t, \vec{q}) = -h^0(\vec{q}) + h^{\text{mat}}(t)$, as well as ρ and $\bar{\rho}$, are 2×2 matrices. Using the expression of the mixing matrix (2.32), as well as $q^0 = q \left(1 + \frac{m_s^2}{2q^2}\right)$ where $q = |\vec{q}|$ we express h and \bar{h} in the flavor basis

$$h(t, \vec{q}) = \frac{\Delta m^2}{4q} \begin{pmatrix} -c_{2\theta} & s_{2\theta} \\ s_{2\theta} & c_{2\theta} \end{pmatrix} + \sqrt{2}G_F n_e(t) \begin{pmatrix} 1 & 0 \\ 0 & 0 \end{pmatrix}, \quad (2.129)$$

$$\bar{h}(t, \vec{q}) = -\frac{\Delta m^2}{4q} \begin{pmatrix} -c_{2\theta} & s_{2\theta} \\ s_{2\theta} & c_{2\theta} \end{pmatrix} + \sqrt{2}G_F n_e(t) \begin{pmatrix} 1 & 0 \\ 0 & 0 \end{pmatrix}, \quad (2.130)$$

where we introduced $c_{2\theta} \equiv \cos 2\theta$ and $s_{2\theta} \equiv \sin 2\theta$, removed the component proportional to identity in the expression of h^{mat} (2.116) and set $\vec{V}^{\text{mat}} = \vec{0}$ (2.117), as the matter is isotropic.

For the discussion below, let us focus on the neutrino sector. A similar procedure can be used for antineutrinos, replacing h by \bar{h} . The Hamiltonian h is a real matrix, and can be diagonalized instantaneously by the orthogonal transformation

$$\tilde{U}^\top(t, \vec{q}) h(t, \vec{q}) \tilde{U}(t, \vec{q}) = \tilde{K}(t, \vec{q}), \quad (2.131)$$

where $\tilde{K}(t, \vec{q}) = \text{diag}(\tilde{k}_1(t, \vec{q}), \tilde{k}_2(t, \vec{q}))$ with $\tilde{k}_1(t, \vec{q}), \tilde{k}_2(t, \vec{q})$ the instantaneous eigenvalues of h in matter, and $\tilde{U}(t, \vec{q})$ is the instantaneous mixing matrix in matter,

$$\tilde{U}(t, \vec{q}) = \begin{pmatrix} \cos \tilde{\theta}(t, \vec{q}) & \sin \tilde{\theta}(t, \vec{q}) \\ -\sin \tilde{\theta}(t, \vec{q}) & \cos \tilde{\theta}(t, \vec{q}) \end{pmatrix}, \quad (2.132)$$

and $\tilde{\theta}(t, \vec{q})$ is the effective mixing angle in matter, related to the vacuum mixing angle θ through the transformation (from Eq. (2.129))

$$\tan 2\tilde{\theta}(t, \vec{q}) = \frac{2h_{ex}(t, \vec{q})}{h_{xx}(t, \vec{q}) - h_{ee}(t, \vec{q})} = \frac{\tan 2\theta}{1 - \frac{2\sqrt{2}G_F n_e(t)}{\Delta m^2 c_{2\theta}}}. \quad (2.133)$$

This transformation defines the so-called matter basis $|\tilde{\nu}_k\rangle$, in which the Hamiltonian is diagonal. The eigenvalues $\tilde{k}_1(t, \vec{q}), \tilde{k}_2(t, \vec{q})$ can be easily found from the (instantaneous) diagonalization of $h(t, \vec{q})$ (2.129), and

we get

$$\tilde{k}_2(t, \vec{q}) - \tilde{k}_1(t, \vec{q}) = \sqrt{\left(\frac{\Delta m^2}{2q} c_{2\theta} - \sqrt{2} G_F n_e(t)\right)^2 + \left(\frac{\Delta m^2}{2q}\right)^2 s_{2\theta}^2}. \quad (2.134)$$

Introducing the density matrix in matter, $\tilde{\rho}(t, \vec{q}) = \tilde{U}^\dagger(t, \vec{q}) \rho(t, \vec{q}) \tilde{U}(t, \vec{q})$, its evolution equation becomes

$$i\dot{\tilde{\rho}}(t, \vec{q}) = [\tilde{h}(t, \vec{q}), \tilde{\rho}(t, \vec{q})], \quad (2.135)$$

where

$$\tilde{h}(t, \vec{q}) = \tilde{K}(t, \vec{q}) + i\dot{\tilde{U}}^\dagger(t, \vec{q}) \tilde{U}(t, \vec{q}) = \begin{pmatrix} \tilde{k}_1(t, \vec{q}) & -i\dot{\tilde{\theta}}(t, \vec{q}) \\ i\dot{\tilde{\theta}}(t, \vec{q}) & \tilde{k}_2(t, \vec{q}) \end{pmatrix}. \quad (2.136)$$

From Eq. (2.133), it appears that the effective mixing angle in matter becomes maximal $\tilde{\theta} = \frac{\pi}{4}$ when the so-called MSW resonance condition

$$h_{xx}(t, \vec{q}) - h_{ee}(t, \vec{q}) = 0 \Leftrightarrow n_e(t_r, \vec{q}) \equiv n_e^r(q) = \frac{\Delta m^2 c_{2\theta}}{2\sqrt{2} G_F q}, \quad (2.137)$$

is met at time $t = t_r$. At very large density ($n_e \gg n_e^r$), $\tilde{\theta} \approx \frac{\pi}{2}$ and the flavor and mass bases almost coincide. Near the resonance, the value of $\tilde{\theta}$ varies quickly as a function of the electron density. At very small density ($n_e \ll n_e^r$), $\tilde{\theta}$ is close to the vacuum mixing angle θ . Note that for antineutrinos, the same approach gives us the resonance condition

$$\bar{h}_{xx}(t, \vec{q}) - \bar{h}_{ee}(t, \vec{q}) = 0 \Leftrightarrow n_e^r(q) = -\frac{\Delta m^2 c_{2\theta}}{2\sqrt{2} G_F q}. \quad (2.138)$$

As the maximum value of the matter mixing angle $\tilde{\theta}$ does not depend on the value of the vacuum mixing angle θ , it is possible to have complete transitions between two neutrino flavors even with a small vacuum mixing angle. From equations (2.137, 2.138), it appears that the resonance condition can be fulfilled either by neutrinos or by antineutrinos. Contrarily to neutrino oscillations in vacuum, the MSW resonance condition depends on the sign of the Δm^2 .

Because the matter mixing matrix \tilde{U} is not constant in time, the effective matter Hamiltonian \tilde{h} is not diagonal, which means that transitions between matter eigenstates can occur in time. Hence, we introduce the notion of adiabaticity: the resonance is said adiabatic if there are no transitions between matter eigenstates, and non-adiabatic if there are jumps between them. This notion can be quantified introducing the so-called adiabaticity parameter at the MSW resonance

$$\gamma(t, \vec{q}) = \frac{|\tilde{k}_2(t, \vec{q}) - \tilde{k}_1(t, \vec{q})|}{\left| \frac{d\tilde{\theta}}{dt}(t, \vec{q}) \right|}. \quad (2.139)$$

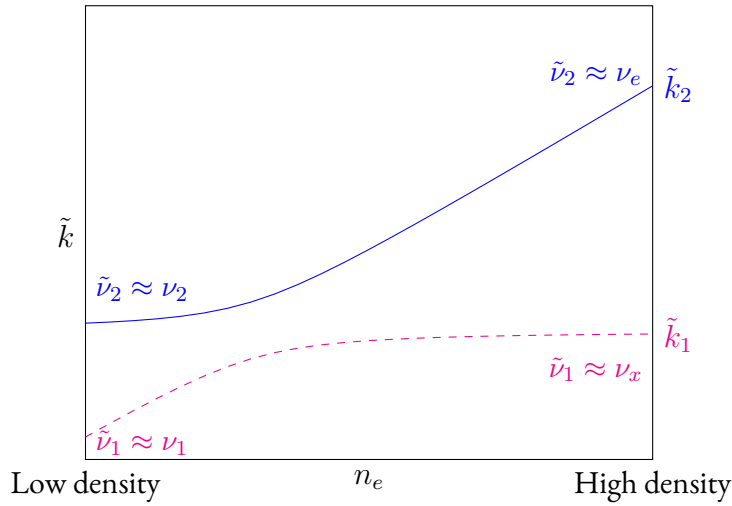


Figure 2.6: Instantaneous eigenvalues \tilde{k}_2 (blue, solid line) and \tilde{k}_1 (magenta, dashed line) of the Hamiltonian $h(t, \vec{q})$, as a function of the electron density n_e . As high density ($n_e \gg n_e^r$), the flavor and matter bases almost coincide. At low density ($n_e \ll n_e^r$), the mass and matter bases almost coincide. The difference between the eigenvalues \tilde{k}_1, \tilde{k}_2 is minimal at the MSW resonance.

If $\gamma \gg 1$ along the neutrino trajectory, then transitions between the matter eigenstates are negligible. From the equation above, it appears that the evolution is adiabatic if the electron density varies smoothly enough.

Figure 2.6 can be used in order to understand how the presence of such an adiabatic MSW resonance can lead to almost complete transitions from ν_e to ν_x . Consider here neutrinos produced near the core of a star. If the electron density n_e is very large, then electron neutrinos ν_e are produced almost as pure matter eigenstates $\tilde{\nu}_2$ as the effective mixing angle in matter is suppressed. Propagating outwards, the neutrinos will cross the MSW resonance at $n_e = n_e^r$, where the energy gap $|\tilde{k}_2 - \tilde{k}_1|$ is minimal.

If the evolution is adiabatic, then there are no transitions from $\tilde{\nu}_2$ to $\tilde{\nu}_1$. The neutrinos will continue to propagate as matter eigenstates $\tilde{\nu}_2$. As they exit the star and the electron density becomes null, the matter and mass bases coincide and the emitted neutrinos become $\nu_2 = \sin \theta \nu_e + \cos \theta \nu_x \approx \nu_x$ for a small mixing angle θ . Therefore, despite a small vacuum mixing angle, severe flavor conversions are achieved. This phenomenon has attracted a lot of interest since, even with a small vacuum mixing angle, adiabatic evolution through the resonance could produce significant flavor conversions. It turns out however that in the case of the Sun, the vacuum mixing angle θ is large enough to begin with ($\theta_{12} \approx 33^\circ$, see section 2.4.2). On the other hand, if the evolution is not adiabatic, it is possible to have $\tilde{\nu}_2$ to $\tilde{\nu}_1$ transitions, and those $\tilde{\nu}_1$ neutrinos become ν_1 in vacuum, outside of the star, which is mostly ν_e . Therefore, in the non-adiabatic case, the MSW resonance leads to little flavor conversions.

In the following section, we discuss the role of neutrino flavor conversions induced by matter in the case of solar neutrinos, and how the MSW effect has been discovered. We discuss the values of neutrino oscillation parameters and highlight key open questions which will be addressed by experiments in the future.

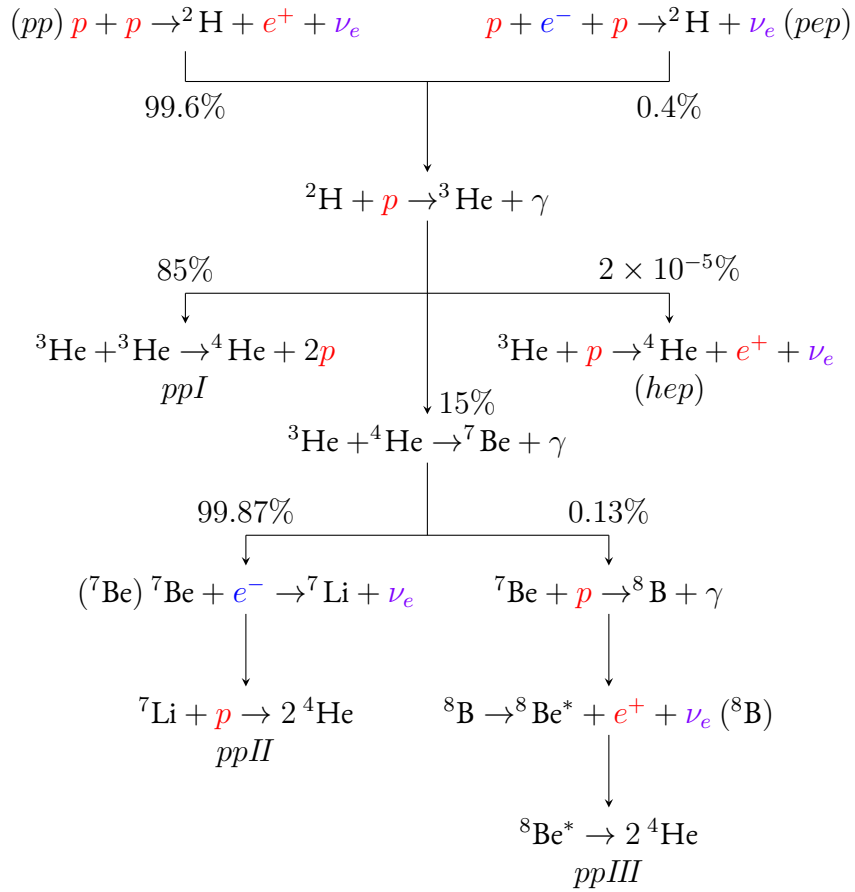


Figure 2.7: The pp chain of stellar thermonuclear reactions. Protons (p) are converted into Helium, producing neutrinos (ν_e) along the way. The traditional names of the neutrino-producing reactions are given, and percentages indicate branching ratios. Figure adapted from Ref. [19].

2.4 NEUTRINO OSCILLATIONS: EXPERIMENTAL STATUS

2.4.1 SOLAR NEUTRINOS

Thermonuclear reactions in main sequence stars are responsible for their energy and neutrino production. The so-called pp chain (figure 2.7) produces 99% of the energy of low-mass stars such as the Sun, while the CNO cycle (figure 2.8) dominates for high-mass stars [38]. Both processes transform protons into helium, creating electron neutrinos through nuclear reactions. The fluxes received on earth can be predicted using the standard solar model [39].

The first solar neutrino experiment was lead by R. Davis, Jr. and collaborators in the late 1960s, in the Homestake mine, based on the ν_e absorption on ${}^{37}\text{Cl}$ [1]



which threshold is 814 keV. From the standard solar model calculations, the dominant source in the chlorine experiment is ${}^8\text{B}$ neutrinos, with ${}^7\text{Be}$ neutrinos the second dominant source, and pep , ${}^{13}\text{N}$ and ${}^{15}\text{O}$ neutrinos

giving subdominant contributions (see Fig. 2.9). In this experiment, only a third of the expected fluxes was measured. The measurements of such a reduced neutrino flux, compared to the standard solar model predictions, defined the so-called "solar deficit neutrino problem", and questioned the standard solar model. Gallium experiments (SAGE from 1989 at Baksan in Russia [41], GALLEX from 1998 to 2003 [42, 43] and GNO from 1998 to 2003 [44] at Gran Sasso in Italy) based on the reaction



which threshold is 233 keV, were mostly sensitive to pp neutrinos and measured only about half on the expected flux.

In 1987, the Kamiokande experiment in Kamioka, Japan observed in real-time neutrinos using a Cherenkov detector [45], through the scattering



giving information on the time, energy and direction of the propagating neutrinos. Its successor, Super-Kamiokande [3, 46, 47, 48] observed in 1996 pure ${}^8\text{B}$ solar neutrinos and measured about half the expected electron neutrino flux. In 1999, the new real-time experiment SNO in Sudbury, Canada brought an important contribution to the solar neutrino problem [24]. This experiment used ultra-heavy pure heavy water (D_2O) to observe ${}^8\text{B}$ solar neutrinos via the NC and CC processes



and



as well as elastic scattering on electrons (2.142). The observed total neutrino flux was consistent with the standard solar model predictions, showing that solar electron neutrinos convert into the other active flavor (see e.g. figure 2.10). These results were consistent with the absence of a day-light asymmetry for solar neutrinos in Super-Kamiokande.

The observed fluxes can be explained by neutrino oscillations in vacuum and the MSW effect. Indeed, in the center of the Sun, the electron number density is about $100N_A\text{cm}^{-3}$ and decreases monotonically when propagating towards the surface. Using standard neutrino oscillation parameters (see section 2.4.2), figure 2.11 shows the resonant electron number density (2.137) as a function of the neutrino energy, and compares it to the electron number density in the center of the Sun. MSW resonant conversions are possible only

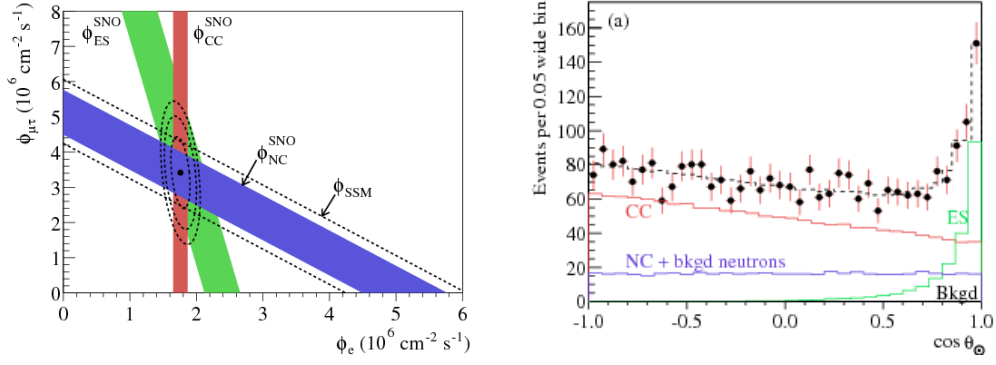


Figure 2.10: Left panel: Flux of 8B solar neutrinos which are μ or τ flavor vs flux of electron neutrinos deduced from the three neutrino reactions in SNO. The diagonal bands show the total 8B flux as predicted by the SSM (dashed lines) and that measured with the NC reaction in SNO (solid band). The intercepts of these bands with the axes represent the $\pm 1\sigma$ errors. The bands intersect at the fit values for ϕ_e and $\phi_{\mu\tau}$, indicating that the combined flux results are consistent with neutrino flavor transformation assuming no distortion in the 8B neutrino energy spectrum. Right panel: Distribution of events as a function of the cosine of the azimuthal angle θ_{\odot} . Also shown are the Monte Carlo predictions for CC, ES and NC + bkgd neutron events scaled to the fit results, and the calculated spectrum of Cherenkov background (Bkgd) events. The dashed lines represent the summed components, and the bands show $\pm 1\sigma$ uncertainties. Figures and captions adopted from [24].

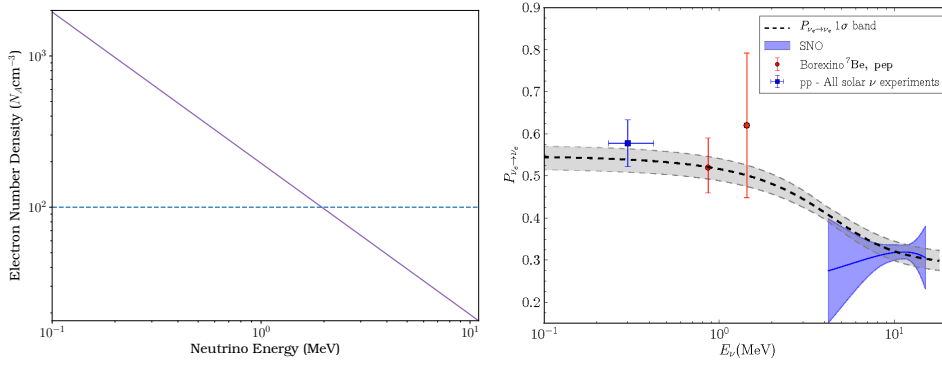


Figure 2.11: Left panel: Resonant electron number density (2.137) (solid, purple line) in units of $N_A \text{cm}^{-3}$ as a function of the neutrino energy in MeV. The electron number density in the center of the Sun is shown as a dashed, blue line. Right panel: Survival probabilities for pp, pep, ${}^7\text{Be}$, and 8B neutrinos deduced from global solar neutrinos analyses, Borexino, and the SNO combined analyses, compared to the MSW prediction, taking into account present uncertainties on mixing angles, from Ref. [49], with pep result from Ref. [50] added. Figure adopted from Ref. [51].

if the MSW resonant electron density is smaller than the electron density at the neutrino emission point. Therefore, for energies smaller than ~ 2 MeV, no resonant conversions are possible: the low energy neutrino deficit can be explained using the average transition probability in vacuum. However, for energies larger than ~ 2 MeV, neutrinos undergo MSW resonant conversions.

Recently, the Borexino experiment in Gran Sasso, Italy measured the low-energy part of the solar neutrino flux, namely pep , pp and ${}^7\text{Be}$ neutrinos [52, 50, 53], and the experiment KamLAND [54], an ultra-pure liquid scintillator detector, measured the ${}^7\text{Be}$ neutrino flux. The ensemble of these results is consistent with vacuum averaged-oscillations at low energy and MSW resonant conversions at high energy. Note that neutrinos from CNO cycle are yet to be detected.

2.4.2 NEUTRINO OSCILLATION PARAMETERS

STATUS

In the three-flavor neutrino framework, it appears from Eq. (2.31) that there are six oscillation parameters: the mass-squared differences Δm_{12}^2 , Δm_{13}^2 and Δm_{23}^2 , and the vacuum mixing angles θ_{12} , θ_{13} and θ_{23} introduced as

$$\cos^2 \theta_{12} = \frac{|U_{e1}|^2}{1 - |U_{e3}|^2}, \quad \sin^2 \theta_{12} = \frac{|U_{e2}|^2}{1 - |U_{e3}|^2}, \quad (2.145)$$

$$\sin^2 \theta_{13} = |U_{e3}|^2, \quad (2.146)$$

$$\cos^2 \theta_{23} = \frac{|U_{\tau 3}|^2}{1 - |U_{e3}|^2}, \quad \sin^2 \theta_{23} = \frac{|U_{\mu 3}|^2}{1 - |U_{e3}|^2}, \quad (2.147)$$

as well as the Dirac CP-violating phase δ . If neutrinos are Majorana particles, two additional phases α_{21} , α_{31} are included in the mixing matrix². From the definition of the mass-squared differences Δm_{ij}^2 , it appears that

$$\Delta m_{21}^2 + \Delta m_{32}^2 = \Delta m_{31}^2. \quad (2.148)$$

Therefore, only two of the three mass-squared differences are independent.

We choose to order the massive neutrinos such that $m_1 < m_2$ such that $\Delta m_{21}^2 > 0$: then, we have either $m_1 < m_2 < m_3$ (normal mass ordering) or $m_3 < m_1 < m_2$ (inverted mass ordering). As the mass square differences are such that $|\Delta m_{31}^2| \approx |\Delta m_{32}^2| \gg \Delta m_{21}^2$, the larger difference Δm_{31}^2 (or Δm_{32}^2) is associated with the observation of oscillations of atmospheric and accelerator ν_μ and $\bar{\nu}_\mu$, and of reactor $\bar{\nu}_e$ at a distance $L \sim 1$ km, while the smaller difference Δm_{21}^2 is associated with the observation of solar ν_e oscillations [55].

From the observation of the MSW effect for ν_e in the Sun, it appears that $\Delta m_{21}^2 \cos 2\theta_{21} > 0$, which implies $\cos 2\theta_{21} > 0$. In 2003, Chooz [56] provided an upper bound on the value of θ_{13} . The T2K, DoubleChooz, Daya Bay (with a 5.2σ discovery) and RENO experiments later measured the small value of this angle. The angle θ_{12} is identified as the solar mixing angle, while θ_{23} is identified as the atmospheric mixing angle. A global analysis of neutrino oscillation data was done in 2014 [57, 58, 59], and updated in 2016 [60] including the results of the NO ν A [61, 62] and T2K [63, 64] experiments, giving precise measurements of Δm_{12}^2 , Δm_{13}^2 , Δm_{23}^2 , as well as θ_{12} , θ_{13} and θ_{23} . The best fit values and the 3σ allowed ranges are presented in table 2.1 [55]. We will use these parameters for our numerical investigations.

For the Dirac CP-violating phase, the combined analysis [57] shows that the best fit value is $\delta \cong \frac{3\pi}{2}$, while the values $\delta = \frac{\pi}{2}$ and $\delta = 0$ (2π) are disfavored by 3σ and 2σ respectively, and $\delta = \pi$ is allowed at approximately 1.6σ CL (respectively 1.2σ CL) with normal ordering (respectively inverted ordering).

²Note that the Majorana phases do not play a role in vacuum oscillations.

Parameter	Best fit	3σ allowed range
Δm_{12}^2	$7.37 \times 10^{-5} \text{eV}^2$	$6.93 - 7.97 \times 10^{-5} \text{eV}^2$
$ \Delta m^2 , \text{NO}$	$2.50 \times 10^{-3} \text{eV}^2$	$2.37 - 2.63 \times 10^{-3} \text{eV}^2$
$ \Delta m^2 , \text{IO}$	$2.46 \times 10^{-3} \text{eV}^2$	$2.33 - 2.60 \times 10^{-3} \text{eV}^2$
$\sin^2 \theta_{12}$	0.297	0.250 - 0.354
$\sin^2 \theta_{23}, \text{NO}$	0.437	0.379 - 0.616
$\sin^2 \theta_{23}, \text{IO}$	0.569	0.383 - 0.637
$\sin^2 \theta_{13}, \text{NO}$	0.0214	0.0185 - 0.0246
$\sin^2 \theta_{13}, \text{IO}$	0.0218	0.0186 - 0.0248

Table 2.1: The best-fit values and 3σ allowed ranges of the 3-neutrino oscillations parameters (from Ref. [60]). The parameter Δm^2 is defined as $\Delta m^2 = m_3^2 - \frac{m_1^2 + m_2^2}{2}$, so that it is positive in case of normal mass ordering (NO), and negative in case of inverted mass ordering (IO).

ANOMALIES

The status above is based on the three-flavor neutrino framework, in which the three active neutrinos ν_e, ν_μ, ν_τ are combinations of the three massive neutrinos ν_1, ν_2, ν_3 with masses m_1, m_2, m_3 , respectively. However, three anomalies challenge this paradigm:

1. The reactor antineutrino anomaly [65], which is a deficit of about 6% of detected $\bar{\nu}_e$ compared to the expected flux in several short-baseline reactor neutrino experiments, due to a re-evaluation of the $\bar{\nu}_e$ spectra.
2. The GALLEX [66] and SAGE [41] experiments have reported anomalous results when calibrating their detectors. Both measured an observed to calculated rate lower than one [67].
3. The LNSD experiment [68, 69], which reported an excess of electron (anti)neutrino events, in contradiction with the results of the KARMEN experiment using similar beam and detection techniques. Note that this anomaly was not resolved by the MiniBooNE experiment.

These anomalies could be due to the existence of a fourth light massive neutrino ν_4 , which corresponds to a sterile neutrino, which doesn't couple to the gauge bosons. It is possible to use a global fit analysis of these experimental results to get best-fit values of the corresponding additional oscillation parameters (see e.g. Ref. [70]).

The experiments STEREO, DANSS, NEOS, PROSPECT, which have already started collecting data, as well as SoLiD, are planned to check for the existence of eV sterile neutrinos. So far, they seem to have excluded the best-fit values of the reactor antineutrino anomaly.

2.4.3 FUTURE PROGRESS

The following points are some of the main goals of the research program in neutrino physics.

NEUTRINO NATURE —DIRAC OR MAJORANA

Determining the nature of massive neutrinos —whether they are Dirac or Majorana particle— is a question of a fundamental importance, in particular, to understand the origin of neutrino masses as well as the symmetries governing the lepton sector of the standard model.

Experiments studying neutrino flavor oscillations cannot provide information on the nature of massive neutrinos. If neutrinos are of Majorana nature, the total lepton charge is not conserved. In order to potentially establish that massive neutrinos are Majorana particles, experiments are searching for neutrino-less double-beta decay $(A, Z) \rightarrow (A, Z + 2) + e^- + e^-$ (see e.g. Ref. [71, 72]). The observation of such a decay and the measurement of the corresponding half-life might also provide with information on the type of neutrino mass hierarchy, the absolute neutrino mass scale and the Majorana phases in the PMNS mixing matrix.

NEUTRINO MASS ORDERING

As mentioned previously, the sign of the mass squared difference Δm_{31}^2 (or Δm_{32}^2) is still unknown, that is, we need to determine the neutrino mass ordering. The neutrino mass spectrum also needs to be established, as, depending on the values of the lightest neutrino mass, it could be

- normal hierarchical (NH) if $m_1 \ll m_2 < m_3$,
- inverted hierarchical (IH) if $m_3 \ll m_1 < m_2$,
- quasi-degenerate (QD) if $m_1 \cong m_2 \cong m_3$.

The combined analysis of all available experimental results shows a preference for normal ordering. The sign of Δm_{32}^2 is searched for in long baseline experiments (e.g. NO ν A), as well as in experiments studying the oscillations of atmospheric neutrinos (PINGU, ORCA) and in experiments with reactor antineutrinos (JUNO [73]).

NEUTRINO ABSOLUTE MASS SCALE

The absolute scale of the neutrino mass is, currently, still unknown. Existing constraints on m_j come from experiments measuring the spectrum of electrons near the endpoint in ^3H β -decay experiments and from cosmological and astrophysical data.

The Troitsk experiment [74] obtained the most stringent upper bound on the $\bar{\nu}_e$ mass

$$m_{\bar{\nu}_e} < 2.05 \text{ eV}, \tag{2.149}$$

with the Mainz experiment [75] giving similar results ($m_{\bar{\nu}_e} < 2.3$ eV). The KATRIN experiment is expected to reach a sub-eV precision [76].

Cosmological constraints on the neutrino mass are model-dependent. Data from the Cosmic Microwave Background (CMB) observed in the WMAP experiments, along with supernovae data and data on galaxy clustering can be used to obtain an upper bound on the sum of the neutrino masses. Depending on the model used, this bound reads $\sum_j m_j \lesssim 0.3 - 1.3$ eV [77]. Constraints from the Planck collaboration were published in 2013 and updated in 2015 [78, 79], reporting $\sum_j m_j \lesssim 0.57$ eV with a 95% CL. Adding supernovae data and data on the baryon acoustic oscillations lowers the limit to $\sum_j m_j \lesssim 0.23$ eV. Note that these bounds imply that neutrino masses are much smaller than the masses of charged leptons and quarks. Such a smallness may be induced by physics beyond the standard model.

NEUTRINO PARAMETERS

High-precision measurements of the neutrino mixing parameters θ_{13} , Δm_{21}^2 , θ_{12} , $|\Delta m_{31}^2|$ and θ_{23} are part of the research goal. The status of CP symmetry also needs to be clarified. In particular, searches for CP violation effects are conducted in neutrino oscillation experiments with high-intensity accelerator neutrino beams, such as T2K or NO ν A, and will be pursued by experiments like DUNE.

3

Neutrino propagation in dense astrophysical environments

Contents

3.1	Introduction	48
3.2	Neutrinos in core-collapse supernovae	50
3.2.1	General description of core-collapse Supernovae	50
3.2.2	Neutrino flavor evolution in supernovae	56
3.2.3	Recent developments	59
3.3	Neutrinos in binary neutron star merger remnants	60
3.3.1	General description of binary neutron star merger remnants	60
3.3.2	Neutrino flavor evolution in binary neutron star merger remnants	65
3.3.3	Recent developments	68

3.1 INTRODUCTION

IN DENSE ASTROPHYSICAL ENVIRONMENTS, such as supernovae (SNe) or binary neutron star (BNS) merger remnants, a huge amount of neutrinos of all types is produced. Because of this, flavor evolution in dense

astrophysical environments has turned out to be complex. The presence of sizable neutrino self-interactions makes the study of neutrino evolution intrinsically nonlinear and of many-body nature, as first pointed out by Pantaleone [10]. The inclusion of such terms [11] has triggered a decade of theoretical investigations. Models of increasing complexity have revealed a variety of flavor instabilities, some of which have been interpreted in terms of collective conversion phenomena (see, e.g., the reviews [80, 81]).

Flavor instabilities due to the neutrino self-interaction occur in core-collapse SNe, and in accretion disks around black holes [82] and compact binary systems, including black hole–neutron star [83, 84] and neutron star–neutron star binaries [83, 85, 86]. Such studies are necessary to assess the actual impact on the supernova dynamics and on the nucleosynthetic r process abundances in neutrino-driven winds in these astrophysical sites. Observations of future core-collapse SN explosions or of the diffuse supernova neutrino background require a solid understanding of flavor evolution in media as well.

The origin of heavy elements remains one of the key open questions in nuclear astrophysics. Nucleosynthetic abundances produced in the rapid neutron capture process (r process) are formed in dense neutron-rich environments [87] including core-collapse supernovae, accretion disks around black holes or binary compact system remnants. It was first shown in Ref. [88] that r process nuclei could be formed in neutron star matter. The occurrence of a weak or of a strong r process depends mainly upon the astrophysical conditions and the properties of exotic nuclei. In particular, conditions for a strong r process are met in neutron star mergers, whereas elements with $A > 130$ are not produced in core-collapse supernovae, long-considered a favorite r process site (see e.g. [89, 90]).

The recent observation of gravitational waves from a BNS merger event in coincidence with a short gamma-ray burst and a kilonova constitute the first experimental evidence for r process nucleosynthesis in such sites [91, 92]. Weak interactions and neutrinos bring the ejecta to being hot. The role of neutrino flavor evolution in these environments still needs to be fully assessed.

Calculations of nucleosynthetic abundances of heavy elements show that dynamical ejecta can produce a strong r process while a weak r process can take place in neutrino-driven winds [93]. In fact, the presence of a significant amount of neutrinos in neutrino-driven winds influences the buildup of heavy elements through the electron neutrino and antineutrino interactions with neutrons and protons respectively. Such interactions tend to be detrimental to the r process since they reduce the number of available neutrons. The occurrence of flavor conversion phenomena can produce swappings of the neutrino spectra and modify the interaction rates that determine the electron fraction, that is, the proton-to-baryon ratio, as shown in numerous studies (see e.g. Refs. [94, 82, 84]).

In this chapter, we focus on describing neutrino evolution in core-collapse SNe and BNS merger remnants, starting in Section 3.2 with SNe. The astrophysical scenario, as well as neutrino emissions, are characterized in Section 3.2.1. We then present how neutrino evolution is modified in SNe compared to neutrinos prop-

agating in the Sun due to the presence of neutrino self-interactions in Section 3.2.2, and discuss the current progress in the domain in Section 3.2.3. In Section 3.3, we follow the same outline to describe neutrino propagation in BNS merger remnants. In particular, we focus in Section 3.3.1 on the astrophysical aspects of such an event. In Section 3.3.2, we model neutrino emissions and discuss a new MSW-like resonance phenomenon appearing in BNS merger remnants: the matter-neutrino resonance (MNR) as an example. Such aspects set the bases for Chapters 4 and 5. We conclude in Section 3.3.3 by discussing some open questions remaining in the field.

3.2 NEUTRINOS IN CORE-COLLAPSE SUPERNOVAE

3.2.1 GENERAL DESCRIPTION OF CORE-COLLAPSE SUPERNOVAE

ASTROPHYSICAL SCENARIO

The term supernova explosion was first introduced by Baade and Zwicky in 1934, describing the powerful explosion at the end of the life of a star of mass $M \gtrsim 8M_{\odot}$, creating a neutron star (NS).

Historically, SNe are labeled depending on their spectroscopic characteristics near their max luminosity and the properties of their light curve. However, the most important physical characteristic is the mechanism that generates the supernova. Type Ia SNe are created by thermonuclear explosions, while type Ib, Ic, and II are core-collapse SNe. We are here interested in the latter mechanism, as they produce a large number of neutrinos of all types. Indeed, during this process, the huge binding energy is mostly radiated as a pulse of neutrinos and antineutrinos, making it a very interesting site in which to study neutrino flavor conversions. Note that type Ia SNe can also produce neutrinos, which can be used to discriminate among the thermonuclear explosion mechanisms [95]. Because neutrinos typically carry away about 100 times more energy than the kinetic energy of a typical core-collapse SN, they were proposed in 1966 as possible agents to drive the SN explosion.

As stars evolve, they start by burning hydrogen to helium to produce energy, with the helium settling in the core of the star. Because of gravity, the core density will then increase and heat up, so helium will start burning to carbon. Again, the carbon being heavier will settle in the core, which will contract and heat up and start burning to neon. Similarly, neon will burn to oxygen, and oxygen will burn to silicon. For stars of masses larger than $8 - 11M_{\odot}$, that silicon can actually be burnt into iron. The star has, therefore, an onion-shell structure, as shown in Fig. 3.1. At this stage, a typical core has a baryonic mass ranging between roughly $1.3M_{\odot}$ and $2M_{\odot}$, a central temperature of around 10^{10} K, a central density ranging between roughly 10^9 g.cm^{-3} and $10^{10} \text{ g.cm}^{-3}$ and a radius of about $2000 - 4000$ km.

As iron has the highest binding energy per nucleon of all the elements, energy cannot be produced at the core by fusion. Therefore, the core, under gravitational pressure, contracts and heats up. The instability of

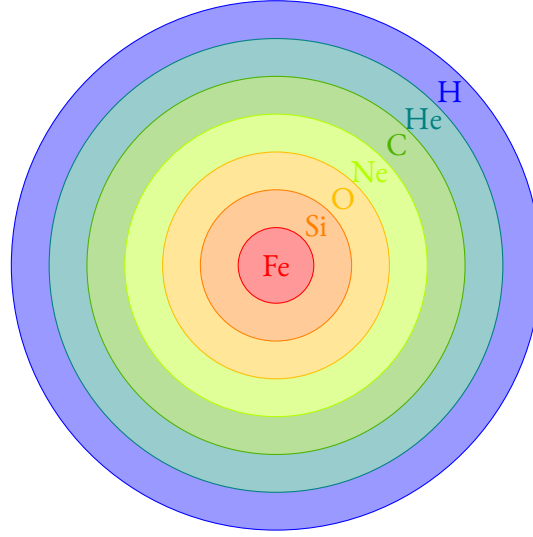
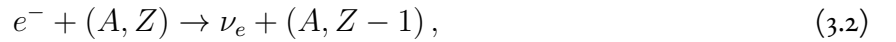


Figure 3.1: Onion-shell structure of a massive star towards the end of its stellar life, prior to the onset of its core collapse. The star is composed of shells of progressively heavier elements produced during nuclear burning stages, forming a core of oxygen, neon, magnesium or iron-group elements at the center. Layers are not drawn to scale.

the core is initiated by electron captures on nuclei and free protons,



as well as by photodesintegration of iron nuclei



yielding to a reduction of the electron pressure and hence a further contraction of the core. Neutrinos produced by electron capture, which can initially escape freely, are trapped when the core density reaches around $10^{12} \text{ g.cm}^{-3}$.

When the nuclear saturation density $\rho_{\text{nuc}} \approx 2.7 \times 10^{14} \text{ g.cm}^{-3}$ is reached at the center of the star, the implosion of the inner core is stopped. A new stable state is reached, with the internal pressure of the nucleon gas supporting the core against gravity. The collapse then bounces back, creating a supersonic shock wave at the transition between the infalling outer core. This shock wave then starts propagating outwards. Because the kinetic energy is dissipated in the infalling matter, the temperature increases in the shock wave. This produces high-energy photons which leads to the photodissociation (3.3) of iron nuclei into free nucleons, which dissipates more energy.

Within about a millisecond, the shock comes to a stop, still inside of the collapsing iron core. However, as the shock reaches the neutrinosphere, surface at which the density of the medium is sufficiently low -less than

about $10^{12} \text{ g.cm}^{-3}$ so that neutrinos can escape, electron neutrinos, produced in a large number by electron captures, start free streaming. This creates a luminous neutrino flash, called the neutronization burst, which is radiated and takes away additional energy—a few 10^{51} erg —, from the postshock layers.

In the delayed SN explosion model first proposed by Wilson and Bethe [96] and favored by SN1987A observations [97, 98], the shock expansion stalls and becomes an accretion shock. However, as neutrinos are produced in the proto-neutron star they deposit large amounts of energy behind the shock, causing the so-called neutrino heating. If it is strong enough, the shock can then be revived and pushed outwards, launching the SN explosion. ¹ During the revival of the shock, matter swept up by the shock is still accreted towards the proto-neutron star and interacts with the hot shocked matter. Neutrinos and anti-neutrinos of all flavors are produced during this accretion phase. As the shock wave propagates outwards through the progenitor star mantle towards the stellar surface, the compact remnant at the center cools and deleptonizes by radiating again neutrinos and antineutrinos of all flavors. Depending on the mass of the progenitor and on the mass loss history, the remnant can be a black hole.

The question of how core-collapse SNe explode is still under intensive study. So far, explosions have been successfully simulated for 2D models with relativistic effects, and 3D modeling has begun [101]. So far, only stars of a mass $M < 10M_{\odot}$ explode in 3D simulations. In the next section, we focus on neutrino emissions during such an event.

NEUTRINO FLUXES AND NEUTRINOSPHERES

During the formation of the proto-neutron star from the core collapse, the gravitational binding energy of the newly formed neutron star liberated is of the order of $3 \times 10^{53} \text{ erg}$. About 1% of this energy is released in a form of kinetic energy of the ejecta, 0.01% is released as electromagnetic radiations, while the rest is carried out by neutrinos produced at the different stages of the supernova explosion.

As stated before, electron neutrinos are produced in large amounts by electron capture (3.1, 3.2), while electron antineutrinos are produced in positron capture



Thermal neutrinos of all flavors are also produced in the core of the proto-neutron star through the processes of electron-positron pair annihilation



¹Note that the non-radial fluid instabilities such that the SASI instability also assists the neutrino-heating mechanism [99]. Other instabilities such as LESA have recently been found [100].

electron-nucleon bremsstrahlung

$$e^\pm + N \rightarrow e^\pm + N + \nu + \bar{\nu}, \quad (3.6)$$

nucleon-nucleon bremsstrahlung

$$N + N \rightarrow N + N + \nu + \bar{\nu}, \quad (3.7)$$

plasmon decay

$$\gamma \rightarrow \nu + \bar{\nu}, \quad (3.8)$$

and photoannihilation

$$\gamma + e^\pm \rightarrow e^\pm + \nu + \bar{\nu}. \quad (3.9)$$

Inside the core, the matter density is dense enough that the neutrinos are trapped, as their mean free path² is shorter than the size of the core. As the density decreases away from the core, the neutrinos are released and start free-streaming at densities of about $10^{11} \text{ g.cm}^{-3}$. As mentioned before, we define the neutrinosphere as the idealized surface after which neutrinos start free-streaming (see Fig 3.2).

As this definition depends on the mean free path of the neutrinos, the neutrinospheres are dependent on the flavor and on the energy of the neutrinos considered. The neutrinos produced interact with the medium, composed of electrons, neutrons, and protons, through charged- and neutral- current weak interactions. Only electron (anti)neutrinos undergo charged-current interactions, from the processes

$$\nu_e + n \rightarrow p + e^-, \quad (3.10)$$

$$\bar{\nu}_e + p \rightarrow n + e^+. \quad (3.11)$$

As the proto-neutron star is typically neutron-rich, electron neutrinos interact more frequently than electron antineutrinos at the same energy. Therefore, the electron neutrino neutrinosphere has a larger radius than the electron antineutrino one. Free-streaming electron antineutrinos are thus emitted from a denser, hotter region and have then typically a higher average energy than electron neutrinos. On the other hand, neutrinos and antineutrinos from the other flavors ($\nu_\mu, \bar{\nu}_\mu, \nu_\tau, \bar{\nu}_\tau$) interact only through neutral-current weak interaction processes, which are flavor blind: they share —for a given energy— the same neutrinosphere. As a consequence, this neutrinosphere has a smaller radius than the electron antineutrino one, and such neutrinos are produced with a larger average energy than electron antineutrinos.

²The mean free path $\lambda = \frac{1}{\sigma\rho}$ depends on the medium density ρ and the neutrino interaction cross section σ with the particles composing the environment.

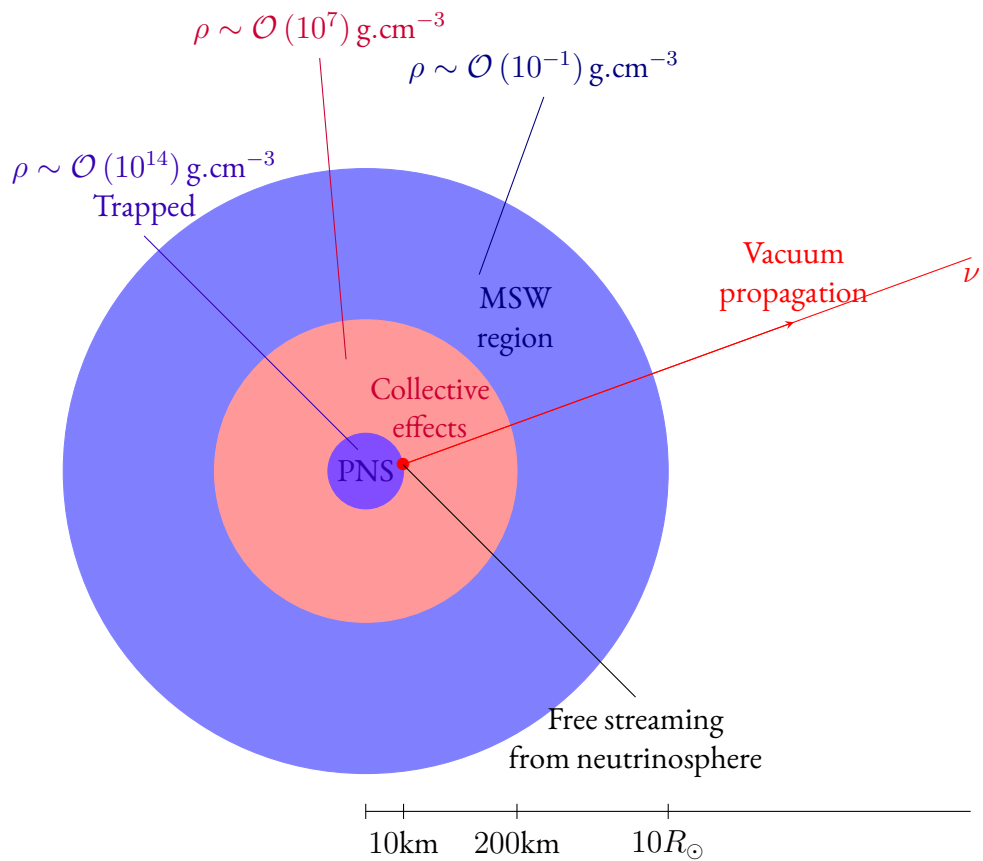


Figure 3.2: Schematic illustration of neutrino propagation in a core-collapse supernova, as well as different neutrino oscillation regimes with typical values for the hot bubble. Inside the proto-neutron star (PNS), neutrinos are trapped because of the large matter density. They are emitted at the so-called neutrinospheres, and undergo collective effects (see Section 3.2.2). The MSW resonances typically occur further away from the core.

According to the present supernova simulations, neutrino fluxes at the neutrinospheres can be well parametrized either by pinched Fermi-Dirac distributions [102] or by modified-power law distributions [103]. In this thesis, we will use Fermi-Dirac spectra f_ν of pinching parameter $\eta = 0$ to describe neutrino emissions, given by

$$f_\nu(p) = \frac{1}{F_2(0)} \frac{1}{T_\nu^3} \frac{p^2}{\exp\left(\frac{p}{T_\nu}\right) + 1}, \quad (3.12)$$

where T_ν is the neutrino temperature and p the energy of the emitted neutrino. In this expression, we have $F_2(0) = \frac{3}{2}\zeta(3) \approx 1.80$, and $F_k(0)$ corresponds to the Fermi-Dirac integral of order k with zero degeneracy parameter,

$$F_k(0) \equiv \int_0^\infty dx \frac{x^k}{\exp(x) + 1}. \quad (3.13)$$

The average energy is then given by

$$\langle E_\nu \rangle = T_\nu \frac{F_3(0)}{F_2(0)}. \quad (3.14)$$

Typically, the average energies of SN neutrinos range between 10 to 20 MeV. The primary fluxes released at the neutrinosphere can then be defined as

$$F_\nu(p) = \frac{L_\nu}{\langle E_\nu \rangle} f_\nu(p), \quad (3.15)$$

where L_ν is the neutrino luminosity. Typical values of the parameters $\langle E_\nu \rangle$ and L_ν depend on the progenitor and on the model used for the simulations. Figure 3.3 shows typical parameters for a 1D simulation of a $27M_\odot$ progenitor.

NEUTRINO OBSERVATIONS

On February 23, 1987, the progenitor star Sanduleak –69 202 exploded, producing a type II supernova called SN1987A. Located in the Large Magellanic Cloud, it occurred approximately 50 kpc away from the Earth. Observing the light-curve and using numerical simulations, the total mass of the progenitor was estimated at $18M_\odot$, with a core of $6M_\odot$, while the radius was estimated at 10^{10} m. It is a unique event as it was observed in all wavelengths, from gamma rays to radio. It was also the first time neutrinos known to be emitted from a supernova were observed directly, these neutrinos being detected first by Kamiokande II [105], IBM [105], and Baksan [106].

From those observations, an upper bound on the neutrino mass and charge, as well as the number of neutrino flavors, were obtained using the absence of nonstandard signatures, the intrinsic neutrino signal dispersion or the cooling time of the newborn star, for example. Since then, many of these results have been confirmed or tightened by other neutrino experiments conducted on Earth. The neutrino observations from

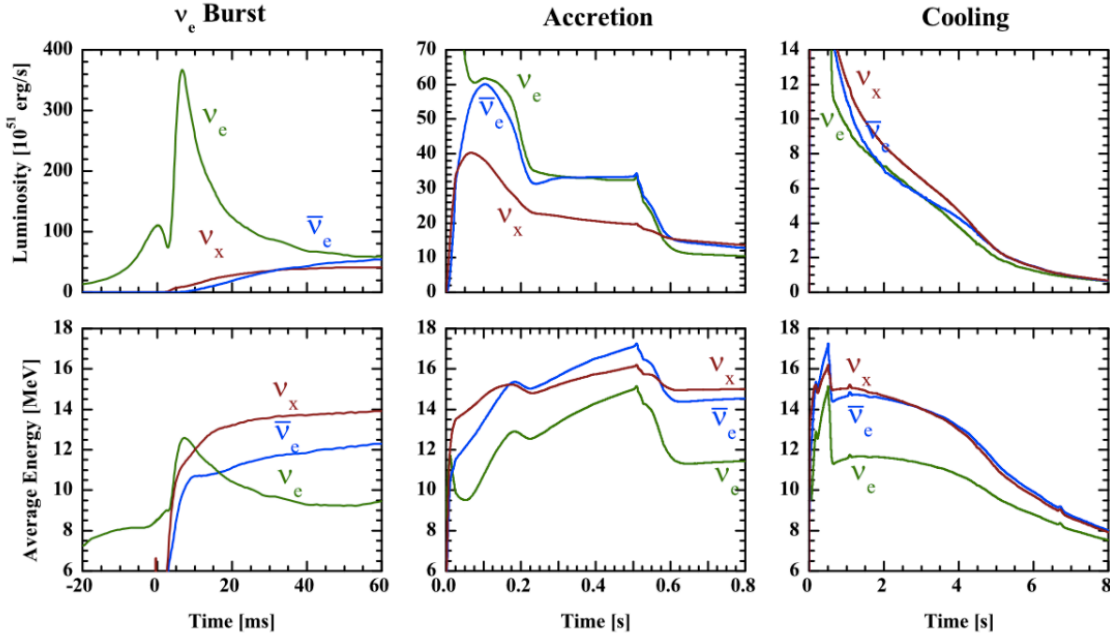


Figure 3.3: Neutrino luminosities (upper panel) and mean energies (lower panel) during the different phases of a supernova explosion (burst, accretion and cooling phase), for ν_e , $\bar{\nu}_e$ and the other neutrino flavors ν_x . These values come from a 1D simulation of a $27M_\odot$ star, obtained by Garching group. Figure adapted from Ref. [104].

SN1987A also confirmed some features of supernovae neutrino predictions, such as the total gravitational binding energy of 3×10^{53} erg (under the equipartition assumption) and the average energy or temperature of neutrinos [97, 107].

After reviewing how neutrinos are produced during a supernova explosion and what parameters are used to describe their emissions at the neutrinospheres, we now focus on their propagation outside the proto-neutron star. In particular, we study how the presence of a large self-interaction potential creates collective behaviors.

3.2.2 NEUTRINO FLAVOR EVOLUTION IN SUPERNOVAE

In the last years, important progress has been done in understanding how neutrinos change their flavors in supernovae. Beside the MSW effect (Section 2.3), it has been pointed out that the presence of sizable neutrino self-interactions, turbulence and shockwaves are responsible for new conversion phenomena.

As neutrinos of all types are produced during core-collapse supernovae, all three known neutrino flavors have to be considered. A three-flavor treatment shows the presence of two MSW resonances: the low (L-) resonance, governed by the mixing parameters $\Delta m_{21}^2, \theta_{21}$, and the high (H-) resonance, governed by the mixing parameters $\Delta m_{31}^2, \theta_{31}$ [102]. The L-resonance typically occurs at densities of about $10^1 - 10^2 \text{ g.cm}^{-3}$, while the H-resonance occurs at densities of about $10^3 - 10^4 \text{ g.cm}^{-3}$, for a neutrino energy of about 10 MeV. These effects occur therefore in the outer layers of the SN. In this section, we focus on the region closer to the production of neutrinos, assuming the mean-field description to be still valid, and discuss the impact of

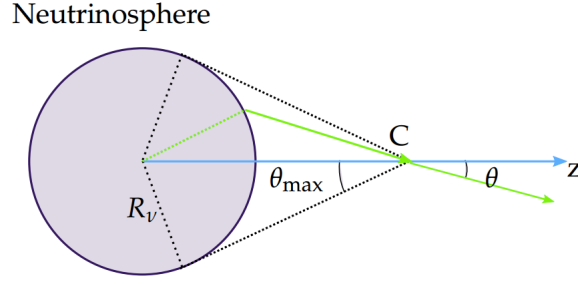


Figure 3.4: Sketch of the neutrino bulb model. Neutrinos are emitted isotropically at the surface of the neutrino sphere, and, for a neutrino propagating along the z -axis, a cylindrical symmetry is assumed. The neutrino background is made of the neutrinos being emitted at the intersection of the neutrinosphere with the cone of opening angle θ_{\max} . Figure adapted from Ref. [11].

neutrino self-interactions on flavor conversions in this environment.

THE BULB MODEL

In order to evaluate the self-interaction term, we use here the widely popular bulb model, introduced in Ref. [11]. Neutrinos are assumed to be emitted isotropically and uniformly at the surface of a sphere of radius R_ν called the neutrinosphere, with an energy spectrum following a Fermi-Dirac distribution (3.12-3.14). We assume that outside the neutrinosphere, the environment is spherically symmetric and stationary, with the physical conditions of the medium depending only on the distance from the core center, r . Furthermore, the neutrino emission is assumed to have a cylindrical symmetry around the z -axis (see figure 3.4). We also adopt here the *single-angle* approximation, in which the flavor evolution of a neutrino is assumed to be only a function of its energy and its initial flavor, and not of its emission angle. This gives us, for the neutrino density matrix introduced in Chapter 2, assuming that neutrinos follow light-like trajectories

$$\rho(t, \vec{q}) = \rho(r, q), \quad (3.16)$$

and similarly for the antineutrino density matrix.

Following the derivation of [11] and the expressions obtained in Section 2.2.3, we get the following form for the self-interaction part of the Hamiltonian (2.124)

$$\Gamma^{\nu\nu, \text{self}}(r, \vec{q}) = \frac{\sqrt{2}G_F}{2\pi R_\nu^2} D\left(\frac{r}{R_\nu}\right) \int dp \left(\rho(r, p) f_\nu(p) \frac{L_\nu}{\langle E_\nu \rangle} - \bar{\rho}(r, p) f_{\bar{\nu}}(p) \frac{L_{\bar{\nu}}}{\langle E_{\bar{\nu}} \rangle} \right), \quad (3.17)$$

where $D(x) \equiv \frac{1}{2} (1 - \sqrt{1 - x^{-2}})^2$, with $x = \frac{r}{R_\nu}$ is a geometric factor, f_ν is the distribution of (anti)neutrinos (3.12), L_ν is the (anti)neutrino luminosity, and $\langle E_\nu \rangle$ is the mean energy of the neutrinos (antineutrinos) associated with the distribution f_ν . Note that as r becomes much larger than R_ν , the geometric factor behaves as $D \sim \frac{R_\nu^4}{r^4}$. Therefore, while the self-interaction effects dominate the deep region nearby the neutrinosphere,

matter terms —which typically behave as $\frac{1}{r^3}$ — matter further away from the core, at lower densities, producing for example the MSW effect.

COLLECTIVE BEHAVIORS

As neutrinos are free streaming outwards in a supernova, they can experience different kinds of collective behaviors [80]. In the bulb model, near the core, as the typical neutrino number density exceeds the ordinary matter number density, neutrinos experience synchronized oscillations: neutrinos and antineutrinos of all energy modes are coupled and oscillate with the same frequency. Any flavor conversion is therefore frozen because of the neutrino self-interactions.

As the neutrinos propagate further away, the geometric factor decreases as $\frac{1}{r^4}$. Therefore, the strength of the self-interaction potential decreases. When it becomes comparable to the vacuum scale, neutrinos and antineutrinos of one flavor can simultaneously convert into the other flavor. These so-called bipolar oscillations are related to an instability in flavor space, due to the non-vanishing vacuum mixing. It has been shown that the onset of this instability was different when considering a full multiangle treatment, that is, not using the approximation (3.16) [108]. To estimate such an onset, linearizing the equation of motions has proven to be successful [109, 110, 111]. The authors of [112] also used the matter basis to describe such a phenomenon. It triggers conversions and oscillations which can be seen as the nutation and the precession of a gyroscopic pendulum [113].

Finally, neutrinos undergo a complete flavor conversion depending on their energy: this is called the spectral split. The authors of Ref. [114] showed that this corresponds to a MSW resonance in the co-rotating frame. Additionally, it has been shown in Ref. [115] that this split can be interpreted as a magnetic resonance phenomenon. In particular, the authors showed that the neutrino energies for which the resonant criteria are fulfilled are the same energies for which the spectral split phenomenon takes place, and that it occurs at the same location in the supernova. In two flavors, collective effects observed in the bulb model can be seen as $\nu_e \bar{\nu}_e \rightarrow \nu_x \bar{\nu}_x$ conversions, since the net electron number is a conserved quantity.

As an example of these collective behaviors, we show numerical results for the cooling phase of a supernova described by the bulb model developed above, using a single-angle treatment. These results were obtained using a FORTRAN90 code developed during the course of the thesis. We simulated the propagation of neutrinos emitted initially as pure electron neutrino at the neutrinosphere along with electron anti-neutrinos. We took the following parameters for the self-interaction, assuming that all neutrinos shared the same neutrinosphere of radius $R_\nu = 10$ km, and the same luminosities $L_\nu = L_{\bar{\nu}} = 1 \times 10^{51}$ erg \cdot s⁻¹, and we used the following average energies $\langle E_{\nu_e} \rangle = 12$ MeV, $\langle E_{\bar{\nu}_e} \rangle = 15$ MeV and $\langle E_{\nu_x} \rangle = \langle E_{\bar{\nu}_x} \rangle = 18$ MeV. As before, we considered only two flavors, and we adopted the atmospheric parameters in inverted hierarchy $\Delta m^2 = -2.4 \times 10^{-3}$ eV² and $\sin^2 2\theta = 0.087$. For the matter profile, we adopted as in Ref. [11]

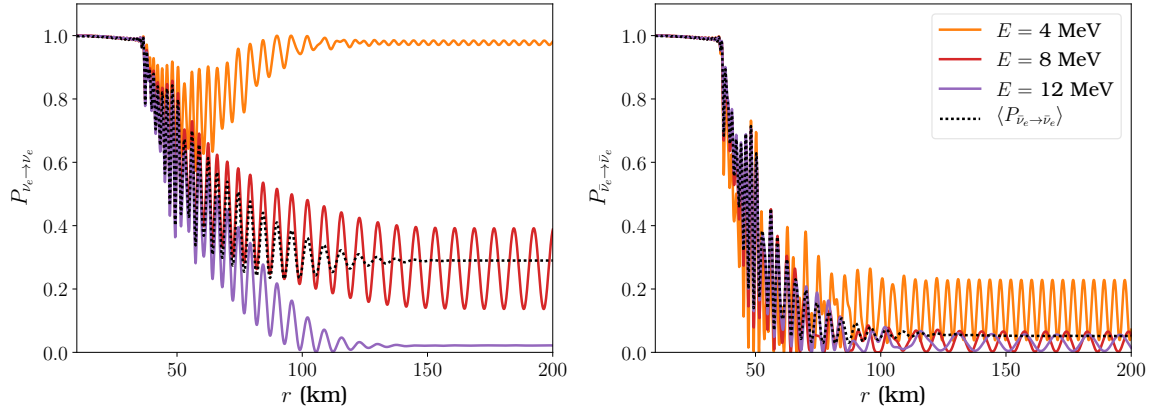


Figure 3.5: Electron neutrino (left) and antineutrino (right) survival probabilities as a function of the distance from the center of a cooling supernova. We show three different energy modes: 4 MeV (orange line), 8 MeV (red line) and 12 MeV, as well as the probabilities averaged over the energy flux (black dotted line). Up to 50 km, (anti)neutrinos undergo synchronized oscillations. Then, they enter bipolar modes up to 150 km, leading to a spectral split for neutrinos and full conversions for antineutrinos.

$$n_e(r) = n_e^0 \left(\frac{R_{\nu}}{r} \right)^3, \text{ where } n_e^0 = 1 \times 10^8 \text{ g} \cdot \text{cm}^{-3}.$$

Figure 3.5 shows the results in the case of two neutrino flavors. For clarity, we show the survival probabilities for only three different energy modes as well as the probabilities averaged over the neutrino spectra. In the calculation, 1000 neutrino energy bins were used from 1 to 100 MeV. The synchronization oscillations occur in the first 50 km, freezing neutrino flavor conversions. Then bipolar oscillations take place between 50 and 150 km, leading to the spectral split.

While being investigated intensely for the past decade, several aspects of neutrino collective behaviors still need to be better understood. For example, going beyond the single-angle approximation (3.16) has shown that a large matter potential could lead to decoherence, suppressing collective conversions [116]. In the next section, we discuss the state of the art as well as progress to be done in understanding neutrino conversions in SNe.

3.2.3 RECENT DEVELOPMENTS

The results shown above were derived under the assumption that we have a stationary, spherically symmetric supernova, where the neutrino fluxes evolve only as a function of the distance from the core. However, it has been pointed out recently that releasing certain of these approximations could lead to new flavor instabilities. For example, it has been shown, using simplified setups, that breaking the axial symmetry [117], the spatial and directional symmetry [118] or introducing temporal instabilities [119] could induce new flavor conversion phenomena. The models used go beyond the bulb model and are of increasing complexity.

Furthermore, it has been shown recently that the neutrino angular distributions from SNe could have a leading role in neutrino flavor conversions. In particular, close to the neutrino decoupling region, "fast" conversions could occur on a distance of $G_F |n_{\nu_e} - n_{\bar{\nu}_e}| = \mathcal{O}(10) \text{ cm}$ [32, 109, 120, 81, 121]. These fast

conversions could lead to a quick flavor equilibration close to neutrino emission, and are driven only by the angular distribution of the electron neutrino lepton number. In particular, they do not depend on neutrino mass differences.

Therefore, modeling carefully the SN environment is necessary in order to study in detail the oscillation phenomenology in this context. As the fast modes occur nearby the neutrinosphere, they could impact the SN dynamics through an enhanced neutrino heating, while so far collective behaviors have been shown to develop outside of the shock region. One of the aspects that have been questioned is the validity of the mean field approximation. At large distances from the SN core, while the neutrino flux is essentially reduced to a narrow beam, a non-zero flux of neutrino propagating inwards due to residual scattering may be significant [122]. Collisions could, therefore, be relevant. Corrections appearing to the most general mean field approximation equations have also been discussed, including pairing correlations [34] and helicity coherence. They have both been introduced in Section 2.2.1, with the corresponding neutrino evolution equations. In Chapter 4, we explore the role of such helicity coherence correlators and their impact on neutrino flavor evolution.

Despite the intense theoretical activity in this direction, our understanding is still incomplete, as neutrino self-interactions are nonlinear and it has been shown that releasing some traditionally-adopted assumptions could induce flavor instabilities. A good understanding of neutrino flavor conversion is also necessary for nucleosynthesis studies and for future observations of an extragalactic SN. For example, the electron fraction calculation [94] and the nucleosynthetic calculation in a schematic model [123] have clearly shown that flavor conversion effects could impact the abundances. Regarding observations, a network of observatories called SNEWS [124] is ready for the detection of the neutrino signal from a SN. The large size Hyper-K seems on its way to approval, while SK-Gd should detect the diffuse supernova background in the coming decade.

In the next section, we study neutrino propagation in binary neutron star mergers. Being computationally more demanding, this environment has been studied relatively recently with respect to the SN one.

3.3 NEUTRINOS IN BINARY NEUTRON STAR MERGER REMNANTS

3.3.1 GENERAL DESCRIPTION OF BINARY NEUTRON STAR MERGER REMNANTS

ASTROPHYSICAL SCENARIO

When two neutron stars orbit around each other closely, they spiral inwards because of gravitational radiation. When eventually they meet, they form, depending on the mass, either a hypermassive neutron star (HMNS) or a black hole, surrounded by a thick accretion disk. We focus here on the first scenario. These compact binary mergers have been among the very early suggestions for the production short gamma-ray bursts (sGRBs). They also produce kilonovae, which are radioactively powered transients from the decay of

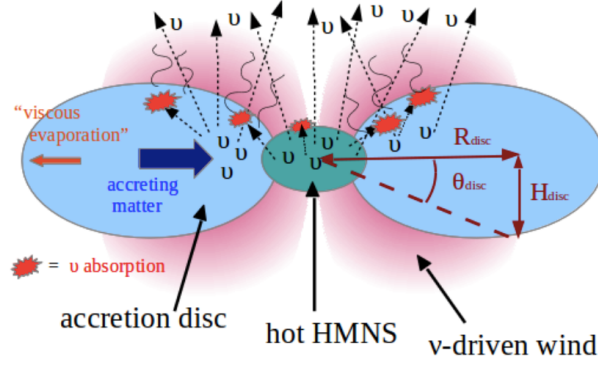


Figure 3.6: Schematic view of the neutrino-driven winds created from the remnants of a BNS merger. The HMNS and the accretion disk emit neutrinos. A fraction of these neutrinos are reabsorbed by the disk and unbind some matter out of its gravitational potential. Figure adopted from Ref. [126].

freshly produced r process elements [91, 125].

There are at least three different channels by which a BNS merger releases matter into space. First, during the merger process, a small fraction of the total mass is ejected via gravitational torques and hydrodynamics process, creating the so-called dynamic ejecta. The decompression of this cold and highly neutron-rich matter is favorable for the production of heavy elements through r process nucleosynthesis. While core-collapse SNe were long believed to be the main source of those heavy elements, hydrodynamical and nucleosynthetic numerical simulations consistently shows that the dynamic ejecta of a neutron star merger is an extremely promising site for the formation of the heaviest elements with $A > 130$, while core-collapse SN seem not to generate the conditions necessary for the production of elements with $A > 90$.

The second channel is the post-merger accretion disk. As the matter expands and cools, it is able to recombine into alpha particles, which together with viscous heating, can release enough energy to unbind an amount of material comparable to dynamic ejecta. Finally, the third channel is related to neutrino-driven winds. As neutrinos are emitted by the HMNS and the accretion disk, they can be reabsorbed by the disk and unbind some matter. Figure 3.6 illustrates the formation of such winds. Neutrinos could play a significant role in this environment by affecting the proton-to-neutron ratio—or equivalently, the electron fraction Y_e , which we define as

$$Y_e = \frac{n_p}{n_n + n_p}, \quad (3.18)$$

where n_p and n_n are respectively the proton and the neutron number densities. Figure 3.7 shows how the nucleosynthesis abundances produced in such neutrino-driven winds complement the production of the heavier elements in dynamic ejecta.

Chapters 4 and 5 present flavor investigations based on detailed astrophysical simulations. In both cases, we use results from a long-term three-dimensional Newtonian hydrodynamics simulation of the neutrino-driven wind that emerges from the remnant of the merger of two non-spinning $1.4M_\odot$ neutron stars [126].

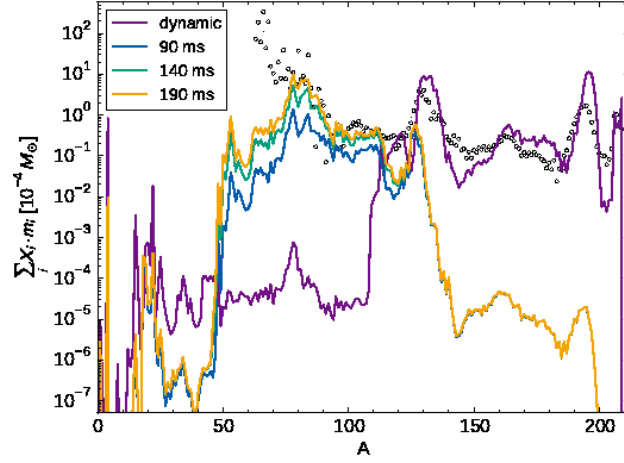


Figure 3.7: Comparison of the nucleosynthesis yields produced by dynamic ejecta (solid purple line) and neutrino-driven winds at different post-merger times (yellow, green, and blue lines). While the dynamic ejecta produces heavy elements of the second and third peaks, the neutrino-driven winds complement its abundance by producing elements of the first to the second peak. Figure adopted from Ref. [93].

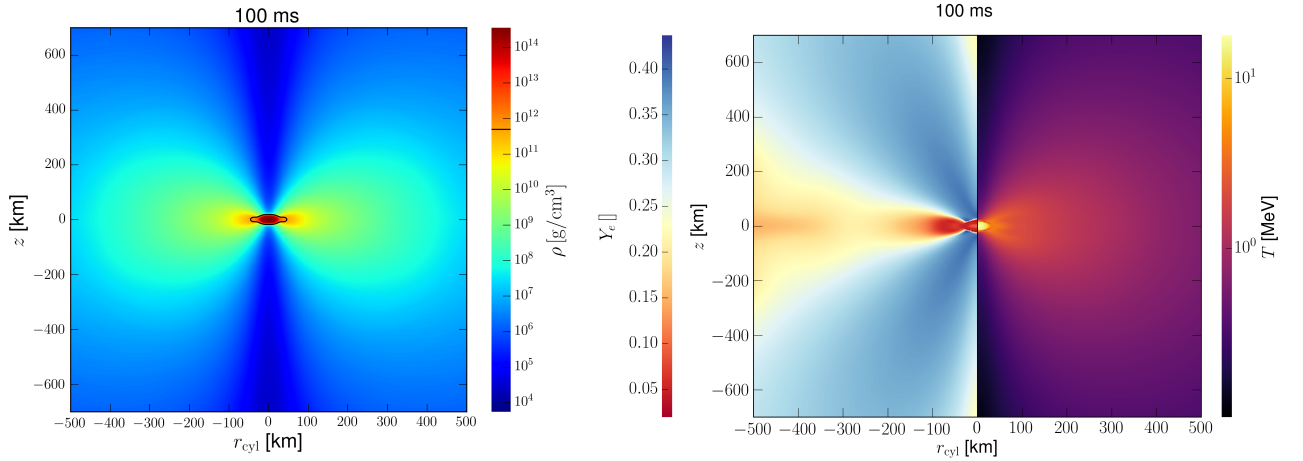


Figure 3.8: Matter density profile (left panel), electron fraction and matter temperature (right panel) as a function of the cylindrical coordinates z and r_{cyl} , at $t = 100$ ms after the merger (from Ref. [126]). On the left panel, the contour corresponds to $\rho \approx 5 \times 10^{11} \text{ g.cm}^{-3}$, and delimits the part of the disk which density is higher than the typical surface density of a proto-neutron star. Figures adopted from Ref. [86].

The HMNS is assumed to stay stable during the simulation time, that is of the order of 100 ms and is treated as a stationary rotating object. We also assume rotational symmetry around the HMNS rotational axis and use the axisymmetric averages of hydrodynamical quantities (matter density, temperature and electron fraction), which are shown in Figure 3.8 at time $t = 100$ ms after the merger. In the next section, we focus on neutrino production during such an event.

NEUTRINO FLUXES AND NEUTRINOSPHERES

During BNS merger events, neutrinos are produced through the same processes as the one mentioned in Section 3.2.1. The amount of gravitational energy released during a BNS merger, and the time-scale over which it is released is also comparable to the SN case, resulting in neutrinos with a luminosity of $L_\nu \approx 10^{53} \text{ erg.s}^{-1}$,

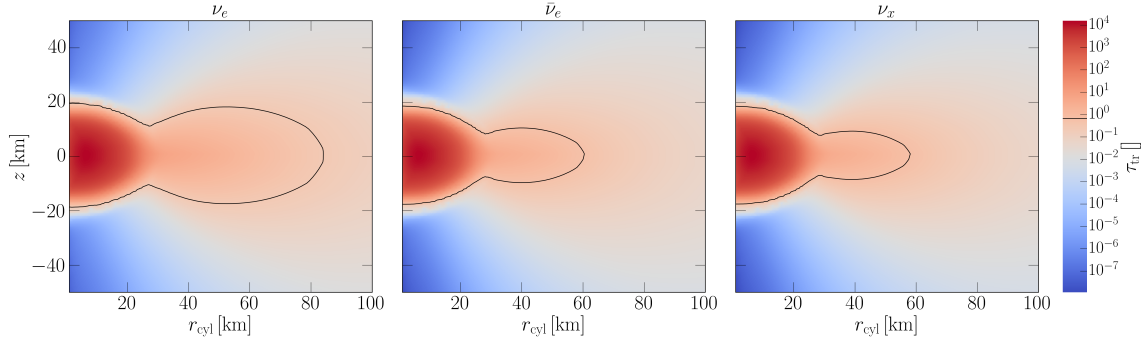


Figure 3.9: Transport optical depths (color coded) for ν_e (left panel), $\bar{\nu}_e$ (middle panel) and ν_x (right panel) as a function of the cylindrical coordinates r_{cyl} and z at time $t = 100$ ms after the merger. The contours correspond to $\tau \approx 2/3$, and define the neutrino transport surfaces. Figure adopted from Ref. [86].

and energies $\langle E_\nu \rangle \approx 10 - 15$ MeV. However, in contrast with proto-neutron stars, the starting point is extremely neutron-rich matter, which makes electron antineutrinos dominate over electron neutrinos. Moreover, as the geometry of a BNS merger remnant is very different from the geometry of a supernova, the neutrinospheres are also modified. Ref. [86] constructed the neutrino emission surfaces from the simulation results of Ref. [126], by calculating the neutrino opacities in the remnants. The results are shown in Figure 3.9.

In Section 3.3.2, we approximate these surfaces as infinitely thin disks to model neutrino emission and compute the self-interaction potentials generated by such a neutrino emission. Figure 3.10 shows the range of values obtained by different BNS merger simulations. Variations up to a factor 5 on the relative luminosities (left panel) and up to a factor 7 (right panel) on the luminosity-over-energy ratio can be observed. By contrast, Figure 3.11 shows a comparison of neutrino luminosities for different 1D supernova simulations, displaying much smaller variations.

r PROCESS NUCLEOSYNTHESIS AND OBSERVATIONS

On August, 17, 2017, the LIGO/Virgo collaboration detected a pulse of gravitational waves named GW170817 [91, 125]. This corresponds to the merger of two neutron stars located in NGC 4993 (at ~ 40 Mpc), of masses between 0.86 and $2.26 M_\odot$. Along with the gravitational wave signal, a short gamma-ray burst, GRB 170817A, of approximately 2s was detected. The association of these two signals in both space and time is strong evidence that neutron star mergers do create short gamma-ray bursts.

The astronomical transient AT 2017gfo was detected in the area in which GW170817 and GRB 170817A were known to have occurred, 11 hours after the gravitational wave event, and observed by numerous telescopes from radio to X-ray wavelengths. It was shown to be a fast-moving, rapidly-cooling cloud of neutron-rich material, as expected of debris ejected from a neutron-star merger, which are the expected characteristics for a kilonova. This is strong evidence that BNS mergers do produce kilonovae. The presence of such a

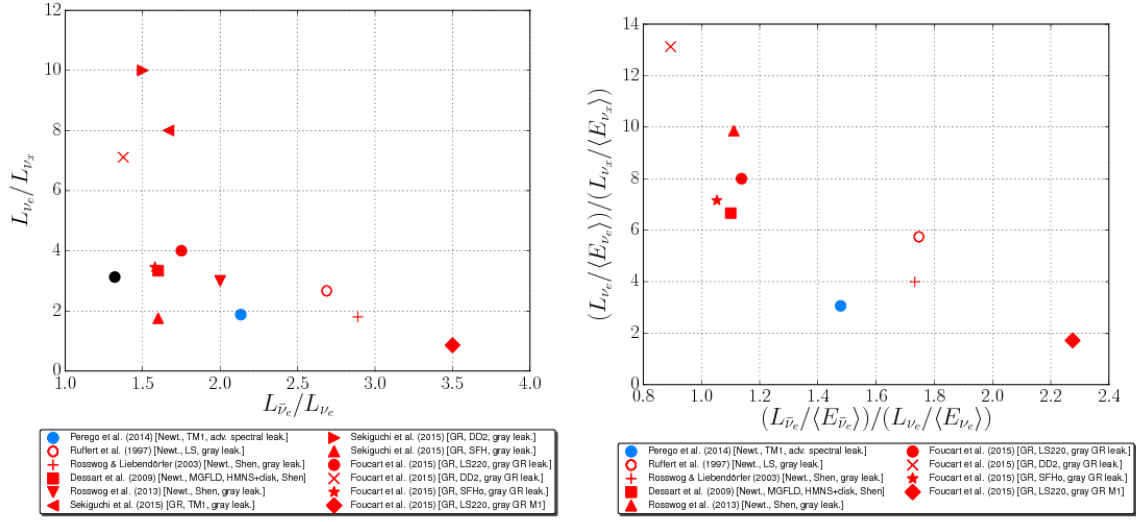


Figure 3.10: Ratio of luminosities (left panel) $\frac{L_{\nu_e}}{L_{\nu_x}}$ vs. $\frac{L_{\bar{\nu}_e}}{L_{\nu_e}}$ and ratio of emission rates (right panel) $\frac{L_{\nu_e}/\langle E_{\nu_e} \rangle}{L_{\nu_x}/\langle E_{\nu_x} \rangle}$ vs. $\frac{L_{\bar{\nu}_e}/\langle E_{\bar{\nu}_e} \rangle}{L_{\nu_e}/\langle E_{\nu_e} \rangle}$. The black point refers to the cooling luminosities of Ref. [126]. Figure adopted from Ref. [86].

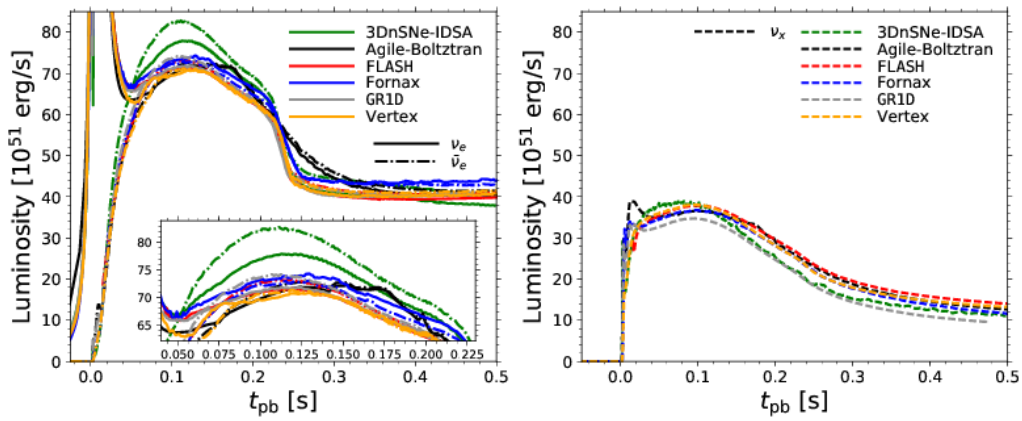


Figure 3.11: Neutrino luminosities for electron-type neutrinos (left panel) and heavy-lepton neutrinos (right panel) as a function of post-bounce time for different 1D supernova simulations. Figure adopted from Ref. [127].

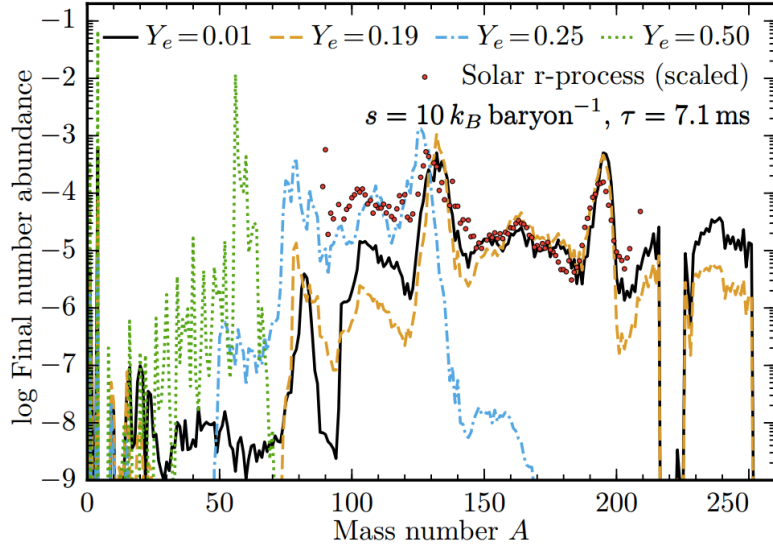


Figure 3.12: Final abundances of a selected nucleosynthesis calculation in binary neutron star mergers, with different values of Y_e . The full r process is made for $Y_e = 0.01$ and $Y_e = 0.19$. The $Y_e = 0.25$ trajectory is neutron-rich enough to make the second r process peak, but not the third and not a significant amount of lanthanides. In the symmetric case ($Y_e = 0.5$), mostly 4He and iron-peak elements are produced. Figure and caption adopted from [128].

kilonova implied the synthesis of about $0.05M_{\odot}$ of r process nuclei, proving that r process nucleosynthesis indeed occurred in BNS merger. The observed signal is compatible with lanthanide free ejecta (cold, blue component) and ejecta with lanthanides (hot, red component). As lanthanides are not produced for an electron fraction $Y_e > 0.25$ (as shown in Fig. 3.12) and neutrinos typically push the electron fraction higher than this value. This observation, compared with BNS mergers, indicate that the red component is most likely produced by dynamical ejecta from the early merging phase. On the other hand, the blue component would be produced by neutrino-driven winds and viscous ejecta in the post-merger phase.

3.3.2 NEUTRINO FLAVOR EVOLUTION IN BINARY NEUTRON STAR MERGER REMNANTS

The BNS merger remnant site brings many similarities with SNe, in particular as far as neutrino emission is concerned, and flavor evolution studies have developed side by side. One of the main difference comes from the fact that BNS studies involve a breaking of the spherical symmetry, in contrast with the simple bulb model described in 3.2.2, making them more demanding. Indeed, they require to perform 2D interpolations of the meaningful physical quantities (electron fraction and baryon number density), as well as solving the evolution equations for many neutrino energy modes. Numerical investigations performed during this thesis showed that the convergence of the solutions was achieved for a much higher number of energy bins than in the SN case. In addition, the excess of electron antineutrinos over electron neutrino introduces novel flavor conversion phenomena that we will discuss. Since, as in SNe, the neutrino emission is significant, in order to describe the neutrino flavor evolution in BNS mergers, the self-interaction contribution to the

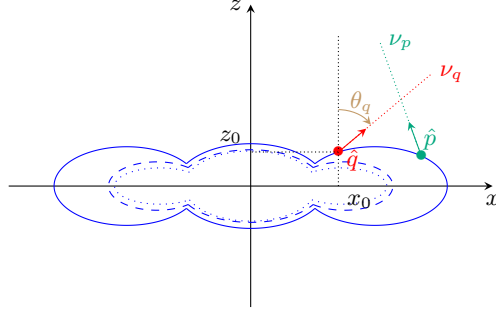


Figure 3.13: Schematic view of our model. Neutrinos start free streaming at the neutrinospheres, shown as a solid blue (respectively dashed and dotted) line for ν_e (respectively $\bar{\nu}_e$ and ν_x). The trajectory of a test neutrino ν_q is labeled by the coordinates of its emission point (x_0, z_0) , and the angle θ_q between the direction of its momentum \hat{q} and the z axis. The test neutrino propagates in a background of matter and (anti)neutrinos ν_p of momentum \hat{p} .

Hamiltonian (2.124) needs to be computed. It reads

$$h_{\nu\nu} = \sqrt{2}G_F \sum_{\alpha} \int (1 - \hat{q} \cdot \hat{p}) [dn_{\underline{\nu}_{\alpha}} \rho_{\underline{\nu}_{\alpha}}(\vec{p}) - dn_{\bar{\underline{\nu}}_{\alpha}} \bar{\rho}_{\bar{\underline{\nu}}_{\alpha}}(\vec{p})], \quad (3.19)$$

where the quantity $dn_{\underline{\nu}_{\alpha}}$ ($dn_{\bar{\underline{\nu}}_{\alpha}}$) denotes the differential number density of neutrinos (antineutrinos), the underline refers to the neutrinos initially born with α flavor at the neutrinosphere. In the next section, we focus on how to model the neutrino emission to compute this term.

MODELING THE NEUTRINO EMISSION: GEOMETRICAL COEFFICIENTS

In two-dimensional models, neutrino propagate with an azimuthal symmetry axis from point (x_0, z_0) , at the neutrinosphere following a straight line trajectory³ characterized by a radial r and an angular θ_q variables (Fig. 3.13). Note that we approximate the neutrinospheres as infinitely thin disks of radii R_{ν} that are flavor dependent, as done in Refs. [82, 84, 85, 86, 17].

For the neutrino self-interaction Hamiltonian Eq.(5.7) the simplest assumption is [82, 84, 85, 86, 17],

$$\rho_{\nu}(r, \vec{p}) = \rho_{\nu}(r, p), \quad (3.20)$$

namely the angular dependence of the neutrino density matrix is not retained. As a consequence, the neutrinos that are coupled by the self-interaction term have the same flavor history as the test neutrino. Assuming spherical and azimuthal symmetry of the neutrino emission at the neutrinosphere, this *ansatz* reduces to the single-angle approximation of the bulb model [80]. One can assume, as in the supernova case, that neutrinos are emitted as Fermi-Dirac distributions $f_{\nu_{\alpha}}$ with luminosities $L_{\nu_{\alpha}}$ and average energies $\langle E_{\nu_{\alpha}} \rangle$ at the neutrinosphere with neutrinosphere radii $R_{\nu_{\alpha}}$ (Table 3.1). Figure 3.10 shows the current spread on L_{ν} and

³In this description, we neglect the bending of the trajectory due to strong gravitational fields, shown to induce sizable effects in Ref. [129].

	$\langle E_\nu \rangle$ (MeV)	L_ν (10^{51} erg/s)	R_ν (km)
ν_e	10.6	15	84
$\bar{\nu}_e$	15.3	30	60
ν_x	17.3	8	58

Table 3.1: Electron and nonelectron neutrino flavors: Average neutrino energies from Ref. [86], luminosities from Ref. [126]. The last column gives the outermost radii (km) from Ref. [86]. Such values correspond to the neutrinospheres of a neutron star merger at 100 ms after the merging process. Please keep in mind that these luminosities have to be divided by two in Eq.(3.21) because we consider there only neutrino emission in the half plane above the emission disk.

the neutrino fluxes according to available simulations of neutrino emission in binary neutron star mergers.

By using Eqs.(3.19) and (3.20), the neutrino self-interaction term becomes⁴

$$h_{\nu\nu}(r, q, \ell_q) = \sqrt{2}G_F \sum_{\alpha=e,x} \int_0^\infty dp \left[G_{\nu_\alpha}(r, \ell_q) \rho_{\nu_\alpha}(r, p) \frac{L_{\nu_\alpha} f_{\nu_\alpha}(p)}{\pi^2 R_{\nu_\alpha}^2 \langle E_{\nu_\alpha} \rangle} - \bar{\rho}_{\bar{\nu}_\alpha}(r, p) G_{\bar{\nu}_\alpha}(r, \ell_q) \frac{L_{\bar{\nu}_\alpha} f_{\bar{\nu}_\alpha}(p)}{\pi^2 R_{\bar{\nu}_\alpha}^2 \langle E_{\bar{\nu}_\alpha} \rangle} \right], \quad (3.21)$$

where the geometrical factor G_{ν_α} reads

$$G_{\nu_\alpha}(r, \ell_q) = \int_{\Omega_{\nu_\alpha}} d\Omega (1 - \hat{q} \cdot \hat{p}), \quad (3.22)$$

with Ω_{ν_α} the angular variables and similarly for $G_{\bar{\nu}_\alpha}$ for the antineutrinos, and $\ell_q = (\theta_q, x_0, z_0)$. The detailed procedure of how to derive geometrical factors is given in Appendix C.

NEUTRINO CONVERSION MECHANISMS: THE EXAMPLE OF THE MATTER-NEUTRINO RESONANCE

Because the electron antineutrinos in BNS are typically emitted in a larger number than electron neutrinos, unique flavor conversions mechanisms appear compared to the SN case. For example, there can be a cancellation of the matter and self-interaction potentials, since the large flavor-diagonal neutrino-neutrino potential and the matter potential have an opposite sign close to the neutrino emission point. Such a cancellation is easily seen by comparing the matter potential to the unoscillated neutrino potential

$$\mu(r, \ell_q) \equiv h_{\nu\nu,ee}^{\text{unosc}}(r, \ell_q) - h_{\nu\nu,xx}^{\text{unosc}}(r, \ell_q) = \frac{\sqrt{2}G_F}{\pi^2} \left[G_{\nu_e}(r, \ell_q) \frac{L_{\nu_e}}{R_{\nu_e}^2 \langle E_{\nu_e} \rangle} - G_{\bar{\nu}_e}(r, \ell_q) \frac{L_{\bar{\nu}_e}}{R_{\bar{\nu}_e}^2 \langle E_{\bar{\nu}_e} \rangle} \right], \quad (3.23)$$

and leads to large-scale MSW-like conversions. The bottom panel of Fig. 3.14 shows such a cancellation. This phenomenon is known as the Matter-Neutrino Resonance (MNR) [83, 130, 131, 86]. Previous work has shown that the presence of this resonance could trigger intense conversions for neutrinos, as shown in the top panel of Fig. 3.14.

So far, two cases have been distinguished: the "standard" MNR [83], in which only neutrinos convert

⁴Note that here we show the full dependence on the variables for clarity.

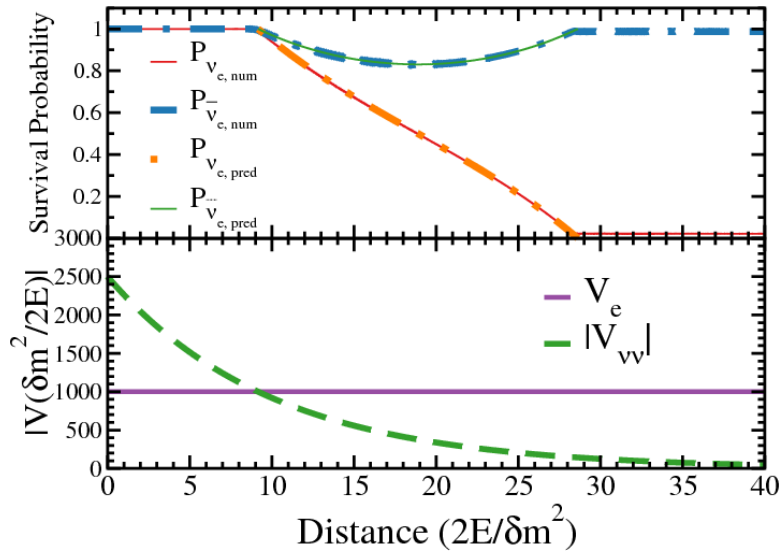


Figure 3.14: Top panel: Survival probabilities for electron neutrinos (solid red line) and antineutrinos (dashed blue line) compared with their predictions. Bottom panel: matter (solid purple line) and unoscillated self-interaction (dashed green) (3.23) potentials. Conversion occur when the two potentials cancel each other. Figure adopted from Ref. [83].

their flavor while antineutrinos do not, and the "symmetric" MNR [84], in which both neutrinos and antineutrinos get converted into the other flavors. Such conversions could have a significant effect on nucleosynthesis. Figure 3.15 shows an example of the impact of the MNR on Y_e (3.18) and on the nucleosynthetic abundances. Note however that this is calculated along a single trajectory.

In the first two projects of this thesis (Chapters 4 and 5), part of the investigation has been devoted to the study of the MNR, discussing in depth the details of the resonance conditions and the corresponding mechanism.

3.3.3 RECENT DEVELOPMENTS

Most flavor studies in the context of BNS merger remnants, in particular involving the MNR are based on the single trajectory approximation (3.20) [82, 84, 16, 17, 85, 86]. Reference [132] has made the first investigation of the MNR in a multiangle treatment, based on a schematic calculation with infinite plan emission and constant matter profile. The author finds that the MNR does not survive under such conditions. Note, however, that only the oscillated potential of an average angle is shown, while survival probabilities would be needed to fully assess the adiabaticity of the MNR.

Clearly, simulations implementing the full angular dependence of the density matrix (3.19) are needed in the future to determine for example the role of decoherence in the flavor evolution. The linearized analysis of Ref. [133] has included the angular dependence. Ref. [134] made the first full multi-angle calculation, using the bulb model though, and found that MNRs still occurred for a subset of angular bins, but were less efficient than in the single-trajectory treatment. This is a promising result since multi-angle simulations are

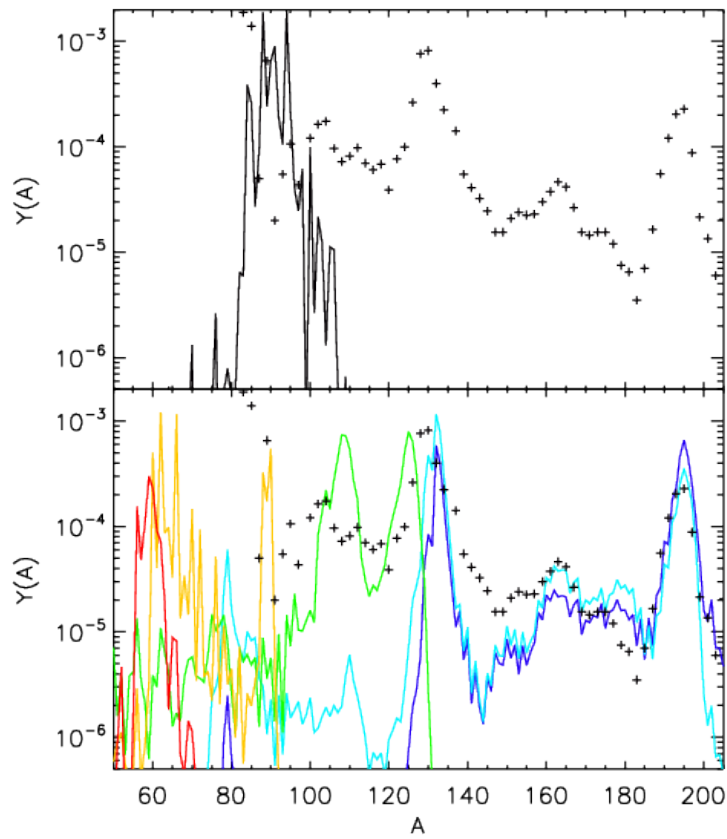


Figure 3.15: Comparison of the nucleosynthesis abundances produced in merging compact objects remnants using a multiple disks model. In both figures, the black pluses show the scaled solar r process residuals. On the top panel, the black line shows the elements produced without the inclusion of neutrino oscillations. On the bottom panel, the colored lines show the elements produced including neutrino flavor conversions, with different ν_e over ν_x fluxes ratios. Figure adopted from Ref. [84].

necessary to definitely assess if the presence of MNRs can influence nucleosynthesis. They also found new flavor conversion phenomena.

It is also worth noting that the presence of fast modes close to the neutrino decoupling region could lead to flavor equilibration on a very short scale. Ref. [133] pointed out that, contrary to the SN case, fast flavor conversions seemed to be unavoidable in compact mergers because of the typical angular distributions found in those environments. Based on the flavor equilibration ansatz, Ref. [135] showed that neutrino conversions due to fast modes would speed up lanthanides production. However, it needs to be emphasized that there is currently no calculation performed in the full nonlinear regime showing that fast modes can induce flavor equilibration.

In conclusion, further developments are necessary to quantify the impact of flavor evolution in neutrino-driven winds where flavor conversion is treated in full multi-angle and nonstationary models. Such investigations are important in relation to the recent and the future kilonovae observations.

4

Helicity coherence in binary neutron star mergers and nonlinear feedback

Contents

4.1	Introduction	72
4.2	Theoretical framework	73
4.2.1	Mean-field evolution equations with mass contributions	73
4.2.2	The Majorana case with $N_f = 2$	77
4.2.3	The Dirac case with $N_f = 2$	79
4.2.4	Our schematic model based on neutron star mergers simulations	79
4.3	Results	84
4.3.1	Resonance conditions for helicity coherence	84
4.3.2	Numerical results on flavor evolution	87
4.4	Nonlinear feedback mechanisms	94
4.4.1	Nonlinear feedback in the MNR	94
4.4.2	Nonlinear feedback in a one-flavor model	96
4.4.3	Nonlinear feedback and helicity coherence	97
4.5	Conclusions	99

The goal of the first project is to investigate the possible role of helicity coherence within a two-flavor framework, based on detailed astrophysical simulations. The aim is to identify under which conditions the helicity coherence resonance can be fulfilled and nonlinear feedback can operate. The results presented constitute the first exploration of these mean-field corrections in a realistic setting. They bring definite conclusions about the impact of helicity coherence in flavor evolution in dense environments.

4.1 INTRODUCTION

Theoretical investigations of neutrino flavor evolution in dense media are usually based on the Liouville–von Neumann equations for one-body neutrino density matrices (Section 2.2) [30, 33]. Three corrections have been discussed recently, coming from collisions [122], pairing correlations [34, 25], and helicity coherence [34, 136, 136, 25]. In fact, at the neutrinospheres, a small fraction of the neutrino flux can still propagate along non-forward directions due to final collisions. A small contribution of a backward flux can produce significant flavor change, as shown in Ref. [122] in the context of a core-collapse supernova schematic model. Demanding simulations that self-consistently implement collisions, neutrino mixings, and mean-field terms in a full Boltzmann treatment are still missing.

Contributions from neutrino-antineutrino pairing correlators and non-zero neutrino mass appear in the most general mean-field equations (Chapters 2 and 3). The authors of Ref. [34] obtained a rigorous derivation of the neutrino evolution equations based on the Born-Bogoliubov-Green-Kirkwood-Yvon hierarchy approach. Moreover, neutrino-antineutrino pairing correlations were implemented explicitly for the first time. Quantum kinetic equations for Majorana neutrinos including corrections due to the neutrino mass first appeared in Ref. [136], where they were referred to as *spin coherence*. This terminology was then corrected in [25] to *helicity coherence*. The concise quantum field theory derivation of Ref. [25] provided the mass and the pairing mean-field contributions in both the Dirac and Majorana cases. As discussed in Chapter 2, these works have shown that both corrections introduce a coupling between neutrinos and antineutrinos. The anisotropy of the medium is necessary for the mass and the pairing contributions to the neutrino Hamiltonian to be nonzero.

Spin coherence can produce a MSW-like phenomenon between neutrinos and antineutrinos, as shown by the first one-flavor numerical study [13]. Under specific conditions, a cancellation between the matter and neutrino self-interactions can fulfill the resonance condition. Moreover, the nonlinearity of the equations can introduce a nonlinear feedback. This has a twofold effect: the region where the cancellation (and the resonance) occur can be extended, and the adiabaticity of the evolution at the resonance can be increased. The results of Ref. [13] show that significant swapping of the neutrino and antineutrino fluxes is produced for some choices of the parameters. This nonlinear mechanism is particularly intriguing since the mass con-

tributions turn out to be suppressed by the ratio of the neutrino mass over energy, as one would naively expect [136, 25]. Note that a rough estimate of the size of mass and pairing mean-field terms was given in [35], where it was also pointed out that a MSW-like phenomenon might be produced by the mass terms, while the MSW-like resonance condition cannot be fulfilled for pairing contributions. In order to assess if helicity coherence can influence flavor evolution, an in-depth analysis was needed.

In the first project, we explore the possible role of helicity coherence in a realistic astrophysical setting and choose to set ourselves in a binary neutron star merger environment. We employ the results for the matter density profiles, the electron fraction, and the neutrino luminosities from the binary neutron star (BNS) merger simulation [126]. We perform numerical calculations to determine neutrino flavor evolution, oscillation probabilities, and the associated adiabaticity parameters through the helicity coherence resonances. We consider three model cases that are representative of the ensemble of astrophysical conditions that we explore. In order to interpret our numerical findings, we provide with a simple first-order perturbative analysis of the conditions to have multiple resonances induced by a nonlinear feedback, producing efficient flavor conversions. We take the cases of the matter neutrino resonance (MNR)—found in accretion disks around black holes or binary neutron star mergers—and the model of Ref. [13] as examples of situations where this mechanism operates and comparatively discuss the situation with helicity coherence in our setting.

The chapter is structured as follows. Section 4.2 introduces the helicity structure of the Hamiltonian and of the mean-field evolution equations, with mass contributions, both for Majorana and Dirac neutrinos. Then our schematic model is described and the geometrical factors are given. Section 4.3 presents the two-flavor results on the neutrino flavor evolution. The resonance and the adiabaticity conditions are discussed for three model cases. Section 4.4 provides a lowest-order linear analysis of multiple crossings induced by nonlinear feedback. Section 4.5 contains our conclusions.

4.2 THEORETICAL FRAMEWORK

4.2.1 MEAN-FIELD EVOLUTION EQUATIONS WITH MASS CONTRIBUTIONS

We remind that neutrino evolution in an homogeneous astrophysical background of matter, neutrinos, and antineutrinos is usually described through two-point correlation functions Eqs. (2.36-2.39) for Dirac and Eqs. (2.52-2.55) for Majorana neutrinos. The mass contributions are due to corrections to the relativistic limit, which are proportional to the mass and are associated with two-point correlators coupling particles of helicity $h \neq h'$, which account for helicity changes [136, 25]. Obviously, neutrino evolution studies also include the usual mixing terms that depend on the mass-squared differences. We will not refer to these when discussing effects from mass contributions, although they are included in our simulations.

Neglecting collisions, the most general mean-field Hamiltonian has the form (2.35). We quote here results

that are relevant for the investigation of the effects from mass contributions; while the explicit expression of Γ and the detailed derivation of neutrino evolution equations are given in Chapter 2 [25]. We will present results for Majorana neutrinos, while those for Dirac are reported in Appendix B. The full set of equations for Dirac and Majorana neutrinos with such contributions is given in Section 2.2.1 [25]. We start with the evolution equation

$$i\dot{\rho}_{\mathcal{G}}(t, \vec{q}) = [h_{\mathcal{G}}(t, \vec{q}), \rho_{\mathcal{G}}(t, \vec{q})], \quad (4.1)$$

where the generalized density matrix is¹

$$\rho_{\mathcal{G}}(t, \vec{q}) \equiv \rho(t, \vec{q}, h, \vec{q}, h') = \begin{pmatrix} \rho(t, \vec{q}) & \zeta(t, \vec{q}) \\ \zeta^\dagger(t, \vec{q}) & \bar{\rho}^T(t, \vec{q}) \end{pmatrix}, \quad (4.2)$$

with ρ and $\bar{\rho}$ $N_f \times N_f$ submatrices, corresponding to the usual neutrino and antineutrino density matrices (2.105, 2.106). N_f is the number of neutrino families and the superscript T indicates transposition. The generalized Hamiltonian is

$$h_{\mathcal{G}}(t, \vec{q}) \equiv \Gamma_M^{\nu\nu}(t, \vec{q}, h, \vec{q}, h') = \begin{pmatrix} H(t, \vec{q}) & \Phi(t, \vec{q}) \\ \Phi^\dagger(t, \vec{q}) & -\bar{H}^T(t, \vec{q}) \end{pmatrix}. \quad (4.3)$$

Both matrices have a $2N_f \times 2N_f$ flavor (or mass) and helicity structure. The quantities H and \bar{H} are the neutrino and antineutrino Hamiltonians respectively, while the off-diagonal term Φ is the *helicity coherence* matrix, coupling the neutrino and antineutrino sectors.

In the mass basis, the mean-field Hamiltonian contributions are given by

$$H(t, \vec{q}) = S(t, q) - \hat{q} \cdot \vec{V}(t) - \hat{q} \cdot \vec{V}_m(t), \quad (4.4)$$

for the neutrino sector and

$$\bar{H}(t, \vec{q}) = \bar{S}(t, q) - \hat{q} \cdot \vec{V}(t) - \hat{q} \cdot \vec{V}_m(t), \quad (4.5)$$

for the antineutrino sector. The quantity $\hat{q} = \vec{q}/q$ denotes the unit vector pointing in the neutrino momentum direction (q is the modulus of \vec{q}).

The $N_f \times N_f$ scalar $S(t, q)$ and vector $\vec{V}(t)$ matrices receive contributions from the neutrino mixings, the neutrino-matter charged- and neutral-current interactions, as well as the neutral-current neutrino self-

¹Note that here we denote with \vec{q} instead of $-\vec{q}$ the momentum for antineutrinos. This former convention introduces sign differences in the expressions where antineutrino momenta are present, compared to Ref. [25], where the latter convention was employed.

interactions. Their explicit expressions in the flavor basis read

$$S(t, q) = h_0(q) + h_{\text{mat}}(t) + h_{\text{self}}(t), \quad (4.6)$$

$$\bar{S}(t, q) = -h_0(q) + h_{\text{mat}}(t) + h_{\text{self}}(t), \quad (4.7)$$

for neutrinos and antineutrinos, respectively. The first terms correspond to the vacuum contributions, which are

$$h_0 = U h_{\text{vac}} U^\dagger, \quad (4.8)$$

with $h_{\text{vac}} = \text{diag}(E_i)$, $E_{i,i=1,N_f}$ being the eigenenergies of the propagation eigenstates. The quantity U is the Maki-Nakagawa-Sakata-Pontecorvo (MNSP) $N_f \times N_f$ unitary matrix relating the mass to the flavor basis [5]. The second terms in Eqs. (4.6)-(4.7) are the scalar neutrino-matter contribution to the mean-field

$$h_{\text{mat},\alpha\beta}(t) = \sqrt{2}G_F \delta_{\alpha\beta} \left[n_e(t) \delta_{\alpha e} - \frac{1}{2} n_n(t) \right], \quad (4.9)$$

with the particle number density

$$n_f(t) = 2 \int \frac{d^3 p}{(2\pi)^3} \rho_f(t, \vec{p}), \quad (4.10)$$

$f = e$ and n standing for electrons and neutrons respectively. Note that, both the charged-current neutrino-electron and the neutral-current neutrino-neutron contributions in (4.9) need to be included. In fact, in our investigation, the neutral current term cannot be discarded from the Hamiltonian h_G Eq. (4.3), as usually done, since its contribution is not proportional to the identity matrix.

The third terms in Eqs. (4.6)-(4.7) come from neutral-current neutrino-neutrino interactions

$$h_{\text{self}}(t) = \sqrt{2}G_F \int \frac{d^3 p}{(2\pi)^3} [\rho(t, \vec{p}) - \bar{\rho}(t, \vec{p})] + L, \quad (4.11)$$

with L the conserved lepton number in two flavors

$$L = \sqrt{2}G_F \text{tr} \left[\int \frac{d^3 p}{(2\pi)^3} [\rho(t, \vec{p}) - \bar{\rho}(t, \vec{p})] \right], \quad (4.12)$$

with tr indicating the trace. Note that, again, the trace terms have to be retained. The mean-field matrices Eqs. (4.4)-(4.5) involve the vector term

$$\vec{V}(t) = \vec{V}_{\text{mat}}(t) + \vec{V}_{\text{self}}(t), \quad (4.13)$$

that receives contributions from the matter-neutrino current

$$\vec{V}_{\text{mat},\alpha\beta}(t) = \sqrt{2}G_F\delta_{\alpha\beta} \left[\vec{J}_e(t)\delta_{\alpha e} - \frac{1}{2}\vec{J}_n(t) \right] \quad (4.14)$$

and the neutrino-neutrino one

$$\vec{V}_{\text{self}}(t) = \sqrt{2}G_F \int \frac{d^3p}{(2\pi)^3} \left\{ \hat{p} [\rho(t, \vec{p}) - \bar{\rho}(t, \vec{p})] \right\} + \vec{k}. \quad (4.15)$$

The particle velocity densities are

$$\vec{J}_f(t) = 2 \int \frac{d^3p}{(2\pi)^3} \vec{v}_f \rho_f(t, \vec{p}), \quad (4.16)$$

with $\vec{v}_f = \vec{p}/E_p^f$, $E_p^f = \sqrt{p^2 + m_f^2}$, and the quantity \vec{k} is

$$\vec{k} = \sqrt{2}G_F \text{tr} \int \frac{d^3p}{(2\pi)^3} \left\{ \hat{p} [\rho(t, \vec{p}) - \bar{\rho}(t, \vec{p})] \right\}, \quad (4.17)$$

where $\hat{p} = \vec{p}/p$. In Eqs. (4.4)-(4.5) the inclusion of mass contributions gives a supplementary diagonal term

$$\begin{aligned} \vec{V}_m(t) = & -\sqrt{2}G_F \int \frac{d^3p}{(2\pi)^3} \left\{ e^{-i\phi_p} \hat{\epsilon}_p \Omega(t, \vec{p}) \frac{m}{2p} + \text{h.c.} \right\} \\ & - \sqrt{2}G_F \text{tr} \int \frac{d^3p}{(2\pi)^3} \left\{ e^{-i\phi_p} \hat{\epsilon}_p \Omega(t, \vec{p}) \frac{m}{2p} + \text{h.c.} \right\}, \end{aligned} \quad (4.18)$$

with

$$\Omega(t, \vec{p}) = \zeta(t, \vec{p}) + \bar{\zeta}(t, \vec{p}). \quad (4.19)$$

Finally the off-diagonal *helicity coherence* matrix reads [136, 25]

$$\Phi(t, \vec{q}) = e^{i\phi_q} \hat{\epsilon}_q^* \cdot \left[\vec{V}(t) \frac{m}{2q} + \frac{m}{2q} \vec{V}^T(t) \right], \quad (4.20)$$

where m denotes the mass matrix, and ϕ_q is the polar angle of the vector \vec{q} in spherical coordinates. This off-diagonal term mixes neutrino and antineutrino evolution. The contributions in Eqs. (4.18)-(4.20) come from the matter and neutrino currents perpendicular to the neutrino direction of motion, since the complex vectors

$$\epsilon^\mu(\hat{p}) = \begin{pmatrix} 0 \\ \hat{\epsilon}_p \end{pmatrix}, \quad (4.21)$$

and $\hat{\epsilon}_p^*$ span the plane orthogonal to \vec{p} .² As expected the mass terms are suppressed by m/q . Note that, in the ultrarelativistic limit, the different helicity sectors are decoupled and one recovers the commonly used theoretical description of neutrino propagation in media.

4.2.2 THE MAJORANA CASE WITH $N_f = 2$

Here we present our model to explore effects from the mass contributions on the neutrino propagation in an astrophysical environment. We consider Majorana neutrinos within a two-flavor theoretical framework. As we will discuss, such results are also representative of the Dirac case. The neutrino evolution can be determined using (4.1). Unless otherwise specified, from now on all the expressions will be in the flavor basis. The 4×4 generalized density matrix Eq. (4.2) is given by

$$\rho_G(t, \vec{q}) = \left(\begin{array}{c|c} \rho & \zeta \\ \hline \zeta^\dagger & \bar{\rho}^T \end{array} \right) = \left(\begin{array}{cc|cc} \rho_{ee} & \rho_{ex} & \rho_{ee}^{-+} & \rho_{ex}^{-+} \\ \rho_{ex}^* & \rho_{xx} & \rho_{xe}^{-+} & \rho_{xx}^{-+} \\ \hline \rho_{ee}^{+-} & \rho_{xe}^{+-} & \bar{\rho}_{ee} & \bar{\rho}_{ex}^* \\ \rho_{ex}^{+-} & \rho_{xx}^{+-} & \bar{\rho}_{ex} & \bar{\rho}_{xx} \end{array} \right). \quad (4.22)$$

Note that, to simplify notations, the explicit dependence on the variables (t, \vec{q}) is not shown on the rhs of the equation.

For Majorana neutrinos in two flavors, the MNSP matrix reduces to

$$U = VD = \begin{pmatrix} \cos \theta & e^{i\alpha/2} \sin \theta \\ -\sin \theta & e^{i\alpha/2} \cos \theta \end{pmatrix}, \quad (4.23)$$

where V is a rotation matrix, while $D = \text{diag}(1, e^{i\alpha}/2)$ with α the (unknown) Majorana phase. The vacuum Hamiltonian in the flavor basis (4.8) reduces to the usual form

$$h_0 = \omega \begin{pmatrix} -c_{2\theta} & s_{2\theta} \\ s_{2\theta} & c_{2\theta} \end{pmatrix}, \quad (4.24)$$

with $\omega = \frac{\Delta m^2}{4E}$, $\Delta m^2 = m_2^2 - m_1^2$, $E = q$ is the neutrino energy, $s_{2\theta} = \sin 2\theta$ and $c_{2\theta} = \cos 2\theta$. The matter term (4.9) is

$$h_{\text{mat}, \alpha\beta}(t) = \frac{\sqrt{2}}{2} G_F \delta_{\alpha\beta} [2\delta_{\alpha e} Y_e(t) - (1 - Y_e(t))] n_B(t), \quad (4.25)$$

²In terms of an oriented triad of real orthogonal unit vectors $(\hat{p}, \hat{p}_\theta, \hat{p}_\phi)$, for instance the standard unit vectors associated to \vec{p} in spherical coordinates, one has $\hat{\epsilon}_p = \hat{p}_\theta - i\hat{p}_\phi$. Note that, $\hat{\epsilon}_p \cdot \hat{\epsilon}_p = 0$, $\hat{\epsilon}_p \cdot \hat{\epsilon}_p^* = 2$, $\epsilon^\mu(\hat{p})\epsilon_\mu(\hat{p}) = 0$, $\epsilon^\mu(\hat{p})\epsilon_\mu^*(\hat{p}) = -2$ and that $\epsilon_\mu(-\hat{p}) = \epsilon_\mu^*(\hat{p})$.

with n_B the baryon number density, Y_e the electron fraction. Note that we did not include the contributions to the diagonal matrix elements from the matter currents, since they are much smaller than the scalar term. The neutrino self-interaction Hamiltonian (4.11)-(4.13) reads

$$h_{\nu\nu}(t, \vec{q}) = \sqrt{2}G_F \sum_{\alpha=e,x} \left[\int (1 - \hat{q} \cdot \hat{p}) \times (dn_{\nu_\alpha} \rho_{\nu_\alpha}(t, \vec{p}) - dn_{\bar{\nu}_\alpha} \bar{\rho}_{\bar{\nu}_\alpha}(t, \vec{p})) \right] + L - \hat{q} \cdot \vec{k}, \quad (4.26)$$

with L and \vec{k} given by (4.12) and (4.17) respectively. The quantity dn_{ν_α} denotes the differential number density of neutrinos and the underline refers to the neutrinos initially born with α flavor. Besides such contributions that are usually included in flavor evolution studies, the Hamiltonian presents the diagonal mass term and the off-diagonal one that depends on the matter and the neutrino currents. As we will discuss, since the diagonal contribution from the neutrino mass (4.18) is very small, it will not be implemented in our calculations.

The generalized Hamiltonian matrix (4.3) reads³

$$h_G(t, \vec{q}) = \left(\begin{array}{cc|cc} -\omega c_{2\theta} + \lambda Y_e + h_{\nu\nu}^{ee} & \omega s_{2\theta} + h_{\nu\nu}^{ex} & \Phi_{ee} & \Phi_{ex} \\ \omega s_{2\theta} + h_{\nu\nu}^{xe} & \omega c_{2\theta} + h_{\nu\nu}^{xx} & \Phi_{xe} & \Phi_{xx} \\ \hline \Phi_{ee}^\dagger & \Phi_{ex}^\dagger & -\omega c_{2\theta} + \lambda(1 - 2Y_e) - h_{\nu\nu}^{ee} & \omega s_{2\theta} - h_{\nu\nu}^{xe} \\ \Phi_{xe}^\dagger & \Phi_{xx}^\dagger & \omega s_{2\theta} - h_{\nu\nu}^{ex} & \omega c_{2\theta} + \lambda(1 - Y_e) - h_{\nu\nu}^{xx} \end{array} \right), \quad (4.27)$$

where $\lambda = \sqrt{2}G_F n_B$. Note that the quantity $\frac{\lambda}{2}(Y_e - 1)\mathbb{1}_{4 \times 4}$, with $\mathbb{1}_{4 \times 4}$ the identity matrix, has been subtracted from the diagonal.

The helicity coherence terms (4.20) in the flavor basis are given by

$$\Phi(t, \vec{q}) = \left[e^{i\phi_q} \hat{\epsilon}_q^* \cdot \vec{V}(t) \right] U \frac{m}{2q} U^T + U \frac{m}{2q} U^T \left[e^{i\phi_q} \hat{\epsilon}_q^* \cdot \vec{V}^T(t) \right]. \quad (4.28)$$

By using $c_\theta = \cos \theta$ and $s_\theta = \sin \theta$, one can rewrite the factor associated with the mass matrix as

$$U \frac{m}{2q} U^T = m_0 \begin{pmatrix} c_\theta^2 + e^{i\alpha} s_\theta^2 & s_\theta c_\theta (e^{i\alpha} - 1) \\ s_\theta c_\theta (e^{i\alpha} - 1) & s_\theta^2 + e^{i\alpha} c_\theta^2 \end{pmatrix} + \frac{\Delta m^2}{4m_0} \begin{pmatrix} -c_\theta^2 + e^{i\alpha} s_\theta^2 & s_\theta c_\theta (e^{i\alpha} + 1) \\ s_\theta c_\theta (e^{i\alpha} + 1) & -s_\theta^2 + e^{i\alpha} c_\theta^2 \end{pmatrix}, \quad (4.29)$$

where we have introduced the quantity $m_0 = (m_1 + m_2)/2$.

³Here we have omitted again the explicit dependence on the variables not to overburden notations.

4.2.3 THE DIRAC CASE WITH $N_f = 2$

We present here the explicit expression for the Hamiltonian in the Dirac case. The equations of motion are given in Appendix B. The main difference from the Majorana case is that the subsectors with the “wrong” helicities, ρ_{++} and $\bar{\rho}_{--}$, involve sterile components. Moreover, in the Dirac case, there are two 4×4 generalized Hamiltonians that need to be evolved: one for neutrinos, and one for antineutrinos. For neutrino, the generalized density matrix (B.4) reads

$$\rho_{D,G}(t, \vec{q}) = \left(\begin{array}{c|c} \rho & \zeta \\ \hline \zeta^\dagger & \tilde{\rho} \end{array} \right) = \left(\begin{array}{cc|cc} \rho_{ee} & \rho_{ex} & \rho_{ee}^{-+} & \rho_{ex}^{-+} \\ \rho_{ex}^* & \rho_{xx} & \rho_{xe}^{-+} & \rho_{xx}^{-+} \\ \hline \rho_{ee}^{+-} & \rho_{ex}^{+-} & \tilde{\rho}_{ee} & \tilde{\rho}_{ex} \\ \rho_{xe}^{+-} & \rho_{xx}^{+-} & \tilde{\rho}_{ex}^* & \tilde{\rho}_{xx} \end{array} \right). \quad (4.30)$$

The $(--)$ sub-sector in the generalized Hamiltonian (B.3) is very similar to the one in the Majorana case; however, due to the fact that the sterile component does not interact with matter or neutrinos, the $(++)$ sub-sector includes only the 2×2 vacuum Hamiltonian. The generalized Hamiltonian for neutrinos is therefore

$$h_{D,G}(t, \vec{q}) = \left(\begin{array}{cc|cc} -\omega c_{2\theta} + \lambda'(3Y_e - 1) + h_{\nu\nu}^{ee} & \omega s_{2\theta} + h_{\nu\nu}^{ex} & \tilde{\Phi}_{ee} & \tilde{\Phi}_{ex} \\ \omega s_{2\theta} + h_{\nu\nu}^{xe} & \omega c_{2\theta} + \lambda'(Y_e - 1) + h_{\nu\nu}^{xx} & \tilde{\Phi}_{xe} & \tilde{\Phi}_{xx} \\ \hline & & & \\ \tilde{\Phi}_{ee}^\dagger & \tilde{\Phi}_{ex}^\dagger & -\omega c_{2\theta} & \omega s_{2\theta} \\ \tilde{\Phi}_{xe}^\dagger & \tilde{\Phi}_{xx}^\dagger & \omega s_{2\theta} & \omega c_{2\theta} \end{array} \right), \quad (4.31)$$

with $2\lambda' = \lambda$. A similar expression can be written for the generalized Hamiltonian for anti-neutrinos, $\bar{h}_{D,G}$ (B.6), with, of course, the $(--)$ and $(++)$ sectors reversed.

4.2.4 OUR SCHEMATIC MODEL BASED ON NEUTRON STAR MERGERS SIMULATIONS

Neutron star mergers produce lots of low-energy neutrinos in the accretion disk during the post-merger phase. At such sites, flavor evolution studies show the presence of MNR conversion phenomena that require a cancellation between the matter and the neutrino self-interaction contributions. As we will show, the corresponding resonant condition is very close to one of the resonant conditions due to the helicity coherence term. Moreover, MNR also shows a nonlinear feedback mechanism that presents a similarity (in the sense that it is capable of maintaining the resonance over long distances) with the one found in the first (one-

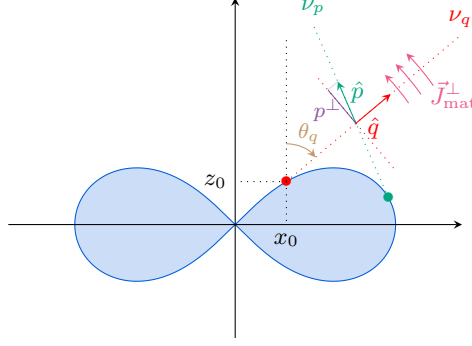


Figure 4.1: Geometry of our model. The blue surface shows the neutrinospheres, that we will approximate later on as infinitely thin disks. We chose the emission point (x_0, z_0) of our test neutrino ν_q on this surface, while the angle θ_q fixes the direction of its momentum \hat{q} (ϕ_q is set to zero). The quantity $\vec{J}_{\text{mat}}^\perp$ indicates the perpendicular matter current. The momentum \hat{p} of the background neutrino ν_p also has a component p^\perp perpendicular to the test neutrino, creating a neutrino current perpendicular to the test neutrino trajectory.

flavor) study of mass effects in core-collapse supernovae [13]. In order to explore mass effects in more realistic settings, we have built a two-flavor schematic model in an extended mean-field approximation, based on simulations of BNS mergers. Our goal is to identify if and under which conditions the mass contributions can produce efficient flavor conversion. Such effects could impact the r-process nucleosynthesis of heavy elements. Indeed, this process can occur in neutrino-driven winds in BNS mergers, as investigated in [93].

According to the detailed simulations of Ref. [126] a central object is formed by the merging process, with a radius of about 30 km. In our scenario neutrinos produced in such an event evolve in a static background of matter, neutrinos, and antineutrinos. Therefore, we will replace the t dependence of our variables with a r dependence, i.e., the distance r traveled by the neutrino from its point of emission. To simplify the problem while keeping the essential features, we approximate the neutrinospheres as infinitely thin disks with maximal sizes R_ν , as previously done in the literature [82, 83, 85, 86]. Three different disk sizes are considered for ν_e , $\bar{\nu}_e$ and ν_x (or $\bar{\nu}_x$) (Table 3.1). In particular, the ν_x and $\bar{\nu}_e$ neutrinosphere radii are very close and smaller than the ν_e outermost radius. Note that this difference in R_ν and in the luminosities can induce a change of sign in the neutrino self-interaction potential, producing the so-called symmetric matter neutrino resonance (sMNR) phenomenon where both electron neutrinos and antineutrinos modify their flavor content. This phenomenon is first pointed out in an accretion-disk black hole scenario [82] and further investigated in [83, 85, 86].

Our model is two-dimensional and has an azimuthal symmetry axis (see Figure 4.1). Neutrinos evolve along a straight line trajectory (we neglect the bending due to the presence of strong gravitational fields). In order to follow neutrino evolution along a given trajectory, we use a spherical coordinate system given by (r, θ, ϕ) (Fig. 4.1), while for the neutrino background it is useful to express (θ, ϕ) back to the emission point $(r_d, \varphi, 0)$ on the disk, as first introduced in Ref.[137] (see Appendix C and Figure C.2). For the matter Hamiltonian (4.9) we have used cylindrical averages of the the electron fraction and the baryon number

density results of Ref.[126]. Therefore, in our calculations, both $n_B = n_B(r)$ and $Y_e = Y_e(r)$.

As for the self-interaction Hamiltonian, one needs to implement the differential number density dn_{ν_α}

$$dn_{\nu_\alpha} = j_{\nu_\alpha}(p) dp d\phi_p d\cos\theta_p, \quad (4.32)$$

for neutrinos emitted isotropically from any point on the surface of the disk. A similar expression holds for antineutrinos. The quantity

$$j_{\nu_\alpha}(p) = \frac{L_{\nu_\alpha} f_{\nu_\alpha}(p)}{\pi^2 R_{\nu_\alpha}^2 \langle E_{\nu_\alpha} \rangle}, \quad (4.33)$$

is the neutrino number density per unit angle per unit energy, and (θ_p, ϕ_p) the spherical coordinates of \hat{p} (Figure C.1). The angular integration is performed over the boundaries Ω_{ν_α} ($\Omega_{\bar{\nu}_\alpha}$) of the corresponding ν ($\bar{\nu}$) neutrinosphere. Introducing Eq. (4.32)-(4.33) into (4.26) the explicit expression for the neutrino-neutrino term reads

$$h_{\nu\nu}(r, q, \ell_q) = \sqrt{2}G_F \sum_{\alpha=e,\mu} \int_0^\infty dp d\Omega (1 - \hat{q} \cdot \hat{p}) \left[\rho_{\nu_\alpha}(r, p, \ell_p) \frac{L_{\nu_\alpha} f_{\nu_\alpha}(p)}{\pi^2 R_{\nu_\alpha}^2 \langle E_{\nu_\alpha} \rangle} - \bar{\rho}_{\bar{\nu}_\alpha}(r, p, \ell_p) \frac{L_{\bar{\nu}_\alpha} f_{\bar{\nu}_\alpha}(p)}{\pi^2 R_{\bar{\nu}_\alpha}^2 \langle E_{\bar{\nu}_\alpha} \rangle} \right], \quad (4.34)$$

where the underline in ν_α and $\bar{\nu}_\alpha$ indicates the initial neutrino flavor. The variables, on which the neutrino evolution depends, include $\ell_i \equiv (\theta_i, \phi_i, \mathbf{Q}_0)$ with the angles (θ_i, ϕ_i) ($i = p$ or q) defining the neutrino trajectory and the coordinates $\mathbf{Q}_0 \equiv (x_0, z_0)$ giving the neutrino point of emission in the π_{xz} plane. The functions L_{ν_α} ($L_{\bar{\nu}_\alpha}$) are the total neutrino luminosities, that have to be divided by two in (4.34) since we consider the neutrino emitted in only one hemisphere, whereas f_{ν_α} ($f_{\bar{\nu}_\alpha}$) are the neutrino (antineutrino) spectra, at the neutrinospheres.

In this first exploratory work based on a two-dimensional model for two-neutrino flavors, we have used an approximate treatment of the self-interaction Hamiltonian that consists in assuming that neutrino trajectories are all coupled and follow the same flavor history as the test neutrino along a given trajectory, i.e.

$$\rho_\nu(r, \vec{p}) = \rho_\nu(r, p), \quad (4.35)$$

and similarly for $\bar{\rho}_\nu$. This procedure is analogous to the so-called "single-angle" approximation in the core-collapse supernova context, first introduced in the *bulb* model [11]. We emphasize that our treatment of the self-interaction reduces to the "single-angle" approximation, if one imposes spherical and azimuthal symmetry, as in the bulb model. According to multi-angle studies of flavor evolution in core-collapse supernovae, the inclusion of the full angular dependence of the density matrices can introduce decoherence of collective

flavor conversion effects (see e.g. [138]). In the event of positive findings in future studies, one would need to go beyond and implement the full angular dependence in Eq. (4.35).

By imposing Eq. (4.35) the integral over the angular variables can be performed giving the geometrical factor

$$G_{\nu_\alpha}(r, \ell_q) = \int_{\Omega_{\nu_\alpha}} d\Omega (1 - \hat{q} \cdot \hat{p}), \quad (4.36)$$

and similarly for $G_{\bar{\nu}_\alpha}$. As a consequence, Eq. (4.34) becomes

$$h_{\nu\nu}(r, q, \ell_q) = \sqrt{2}G_F \sum_{\alpha=e,x} \int_0^\infty dp \left[G_{\nu_\alpha}(r, \ell_q) \rho_{\nu_\alpha}(r, p) \frac{L_{\nu_\alpha} f_{\nu_\alpha}(p)}{\pi^2 R_{\nu_\alpha}^2 \langle E_{\nu_\alpha} \rangle} - \bar{\rho}_{\bar{\nu}_\alpha}(r, p) G_{\bar{\nu}_\alpha}(r, \ell_q) \frac{L_{\bar{\nu}_\alpha} f_{\bar{\nu}_\alpha}(p)}{\pi^2 R_{\bar{\nu}_\alpha}^2 \langle E_{\bar{\nu}_\alpha} \rangle} \right]. \quad (4.37)$$

The angular variables in (4.36) can be expressed as a function of the (r_d, φ) variables defining the point in the emission plane π_{xz} (see Appendix C). The integral over φ is easily performed and the geometric factor becomes

$$G_{\nu_\alpha}(r, \ell_q) = z \int_0^{R_{\nu_\alpha}} dr_d r_d \Gamma(r_d, \ell_q, r), \quad (4.38)$$

where the explicit expression for Γ is given by Eqs.(C.13-C.14) (Appendix C).

For the mass effects, one needs to specify the matter and self-interaction $\bar{\rho}$ contributions to the helicity coherence term (4.20) as well as the supplementary diagonal contribution (4.18). By taking constant matter velocities, the matter currents contribution in Eq. (4.20) becomes

$$\hat{\epsilon}_q^* \cdot \vec{V}_{\text{mat}, \alpha\beta}(r) = \frac{\sqrt{2}}{2} G_F \beta \delta_{\alpha\beta} [2\delta_{\alpha e} Y_e(r) - (1 - Y_e(r))] n_B(r). \quad (4.39)$$

For the self-interaction contribution to the helicity coherence term, one needs to calculate $\hat{\epsilon}_q^* \cdot \vec{V}_{\text{self}}(r)$, that is

$$h_{\nu\nu}^\perp(r, q, \ell_q) = \sqrt{2}G_F \sum_\alpha \int_0^\infty dp \left\{ \int_{\Omega_{\nu_\alpha}} (\hat{\epsilon}_q^* (\hat{q}) \cdot \hat{p}) \rho_{\nu_\alpha}(r, p, \ell_p) dn_{\nu_\alpha} - \int_{\Omega_{\bar{\nu}_\alpha}} (\hat{\epsilon}_q^* (\hat{q}) \cdot \hat{p}) \bar{\rho}_{\bar{\nu}_\alpha}(r, p, \ell_p) dn_{\bar{\nu}_\alpha} \right\}. \quad (4.40)$$

Using the hypothesis (4.35), a perpendicular geometrical factor can be defined as

$$\begin{aligned} G_{\nu_\alpha}^\perp(r, \ell_q) &= \int_{\Omega_{\nu_\alpha}^*} d\Omega (\hat{\epsilon}_q^* (\hat{q}) \cdot \hat{p}) \\ &= \int_0^{R_{\nu_\alpha}} dr_d (r_d z) \Gamma^\perp(r_d, \ell_q, r), \end{aligned} \quad (4.41)$$

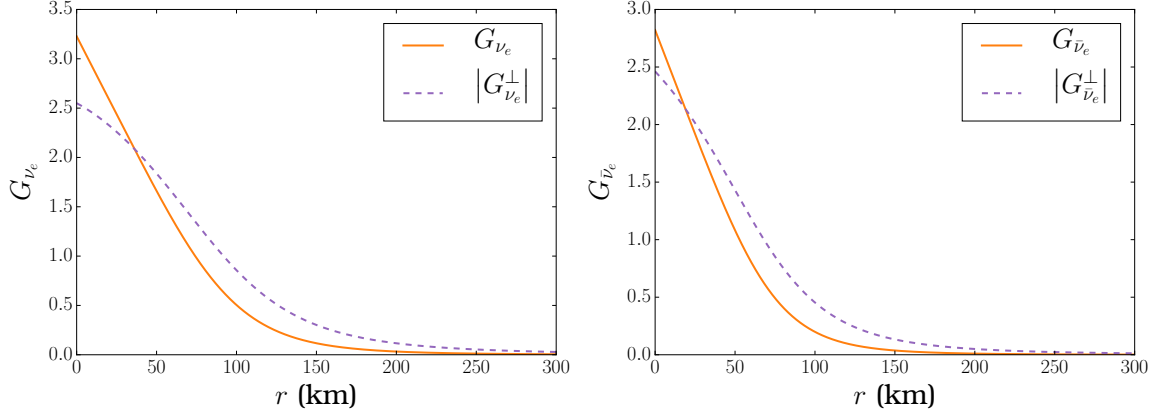


Figure 4.2: Geometrical factors for neutrinos (left) and antineutrinos (right figure), as a function of distance, in our schematic model based on binary star mergers. The two curves correspond to G_ν (4.38) (solid line) and G_ν^\perp (4.41) (dashed line) in the self-interaction Hamiltonian Eq. (4.37) and Eq. (4.40) respectively. Results correspond to Model C (Table 4.3).

Symbol	Name	Expression
h_0	Vacuum contribution to the Hamiltonian	$h_0 = \omega \begin{pmatrix} -c_{2\theta} & s_{2\theta} \\ s_{2\theta} & c_{2\theta} \end{pmatrix}$
h_{mat}	Diagonal matter Hamiltonian	$h_{\text{mat},\alpha\beta} = \frac{\sqrt{2}}{2} G_F n_B \delta_{\alpha\beta} [2\delta_{\alpha e} Y_e - (1 - Y_e)]$
$\hat{\epsilon}_q^* \cdot \vec{V}_{\text{mat}}$	Off-diagonal matter Hamiltonian	$\hat{\epsilon}_q^* \cdot \vec{V}_{\text{mat},\alpha\beta} = \frac{\sqrt{2}}{2} G_F n_B \beta \delta_{\alpha\beta} [2\delta_{\alpha e} Y_e - (1 - Y_e)]$
$G_{\nu\alpha}$	Geometrical factor	$G_{\nu\alpha} = \int_{\Omega_{\nu\alpha}} d\Omega (1 - \hat{q} \cdot \hat{p})$
$G_{\nu\alpha}^\perp$	Perpendicular geometrical factor	$G_{\nu\alpha}^\perp = \int_{\Omega_{\nu\alpha}} d\Omega (\hat{\epsilon}^*(\hat{q}) \cdot \hat{p})$
$h_{\nu\nu}$	Diagonal self-interaction Hamiltonian	$h_{\nu\nu} = \sqrt{2} G_F \sum_\alpha \int dp \left[G_{\nu\alpha} \rho_{\nu\alpha} \frac{L_{\nu\alpha} f_{\nu\alpha}}{\pi^2 R_{\nu\alpha}^2 \langle E_{\nu\alpha} \rangle} - \bar{\rho}_{\bar{\nu}\alpha} G_{\bar{\nu}\alpha} \frac{L_{\bar{\nu}\alpha} f_{\bar{\nu}\alpha}}{\pi^2 R_{\bar{\nu}\alpha}^2 \langle E_{\bar{\nu}\alpha} \rangle} \right]$
$h_{\nu\nu}^\perp$	Off-diagonal self-interaction Hamiltonian	$h_{\nu\nu}^\perp = \sqrt{2} G_F \sum_\alpha \int dp \left[G_{\nu\alpha}^\perp \rho_{\nu\alpha} \frac{L_{\nu\alpha} f_{\nu\alpha}}{\pi^2 R_{\nu\alpha}^2 \langle E_{\nu\alpha} \rangle} - \bar{\rho}_{\bar{\nu}\alpha} G_{\bar{\nu}\alpha}^\perp \frac{L_{\bar{\nu}\alpha} f_{\bar{\nu}\alpha}}{\pi^2 R_{\bar{\nu}\alpha}^2 \langle E_{\bar{\nu}\alpha} \rangle} \right]$

Table 4.1: Symbols, names and expressions of the relevant quantities involved in the neutrino evolution equations (see text).

where the dependence on the emission variables is shown. The explicit expression for Γ^\perp is given by Eqs. (C.9)-(C.10) C. Figures 4.2 and 4.3 show the geometrical factor (4.41) as a function of the distance travelled by the neutrinos from the neutrinospheres. The results correspond to the cases A and C (Table 4.3) which can be considered as representative of the typical behaviors of G_ν^\perp , as we have been observing in our runs. One can see that G_ν^\perp have a similar r dependence as G_ν (4.38), as expected. Their absolute values turn out to be suppressed by a few percents up to several factors, with respect to the G_ν value. As we will discuss, the r dependence of G_ν plays a crucial role on the possibility to have multiple crossings and a nonlinear feedback mechanism in presence of helicity coherence (see Section 4.4). By including Eq.(4.41) into (4.40) one gets the same expression Eq. (4.37) for $h_{\nu\nu}^\perp$ with $G_{\nu\alpha}^\perp$ Eq.(4.41) replacing $G_{\nu\alpha}$ Eq.(4.36). Table 4.1 sums up the relevant quantities involved in the generalized Hamiltonian.

The neutrino total luminosities and spectra at the neutrinospheres are an essential ingredient of the self-

interaction Hamiltonians $h_{\nu\nu}$ and $h_{\nu\nu}^\perp$. As in Ref. [86], we take the neutrino spectra $f_{\bar{\nu}}$ and f_ν at the neutrinospheres as Fermi-Dirac distributions,

$$f_\nu(p) = \frac{1}{F_2(0)} \frac{1}{T^3} \frac{p^2}{\exp(p/T) + 1}, \quad (4.42)$$

where T is the neutrino temperature. In this expression, we have $F_2(0) = \frac{3}{2}\zeta(3) \approx 1.80$, and $F_k(0)$ corresponds to the Fermi-Dirac integral of order k with zero degeneracy parameter,

$$F_k(0) \equiv \int_0^\infty dx \frac{x^k}{\exp(x) + 1}. \quad (4.43)$$

Table 3.1 gives the values of the luminosities and average energies for the different neutrino species used in our investigation.

Unoscillated ν self-interaction potentials constitute a useful quantity to search for the location of helicity coherence resonances. They have been exploited in previous studies of the MNR and sMNR Ref. [82, 83, 85, 86]. Such potentials are defined as

$$h_{\nu\nu}^{\text{unosc}}(r) = \sqrt{2}G_F \sum_{\alpha=e,x} \int_0^\infty dp \left[G_{\nu_\alpha}(r, \ell_q) \frac{L_{\nu_\alpha} f_{\nu_\alpha}(p)}{\pi^2 R_{\nu_\alpha}^2 \langle E_{\nu_\alpha} \rangle} - G_{\bar{\nu}_\alpha}(r, \ell_q) \frac{L_{\bar{\nu}_\alpha} f_{\bar{\nu}_\alpha}(p)}{\pi^2 R_{\bar{\nu}_\alpha}^2 \langle E_{\bar{\nu}_\alpha} \rangle} \right]. \quad (4.44)$$

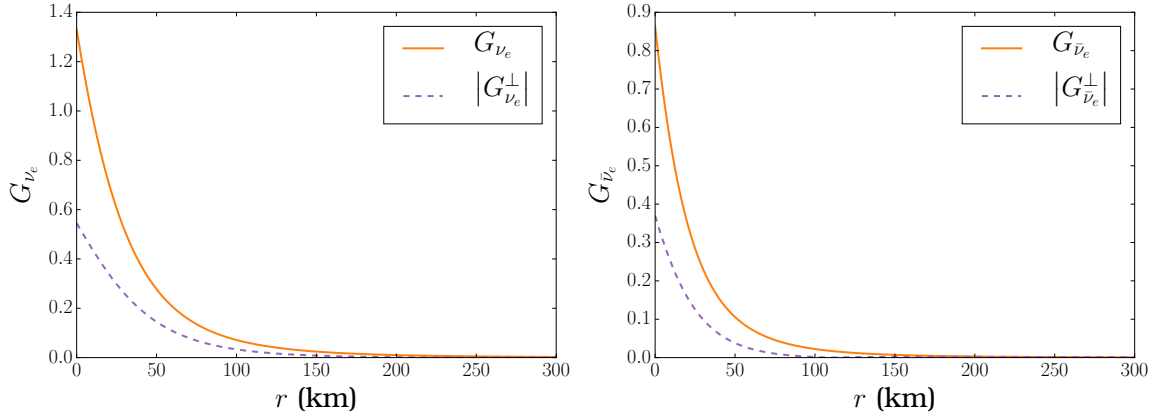


Figure 4.3: Same as Figure 4.2 for Model A (see Table 4.3).

4.3 RESULTS

4.3.1 RESONANCE CONDITIONS FOR HELICITY COHERENCE

We present here our analysis on the resonance conditions in presence of mass contributions. Such situations can be identified by looking at the unoscillated potentials, which will use to characterize our model cases (A,

B, C) that will be presented in Section 4.3.2. As shown previously, the extended equations with mass terms include both the diagonal Eq. (4.18)-(4.19) and the off-diagonal Eq. (4.20) contributions. In the following discussion, we will neglect the diagonal one since they are suppressed by several orders of magnitude compared to the other terms, as we have been verifying numerically. This is due to the fact that \vec{V}_m Eq. (4.18) involves correlators with helicity change Eq. (4.2), in addition to being proportional to the neutrino mass.

MAJORANA CASE

Conditions for the occurrence of MSW-like resonances⁴ are met when differences of diagonal elements of the generalized Hamiltonian Eq. (4.3) become small, i.e. $h_{G,ii} - h_{G,jj} \simeq 0$ for $i, j = 1$ to 4 ($i \neq j$).

In treatments where neutrino evolution does not include mass terms, neutrino and antineutrino equations of motions are only coupled through the usual self-interaction Hamiltonian Eq. (4.37). In this case, the resonance condition in the neutrino sector reads

$$h_{G,11} - h_{G,22} = -2\omega c_{2\theta} + \sqrt{2}G_F n_B Y_e + h_{\nu\nu}^{ee} - h_{\nu\nu}^{xx} \simeq 0. \quad (4.45)$$

In accretion disks around neutron star merger remnants or black holes, the matter and neutrino self-interaction terms have opposite signs, because the $\bar{\nu}_e$ luminosity is larger than the ν_e one (see Table 3.1). This can produce a cancellation of the two contributions. The fulfillment of condition (4.45) and the presence of sizeable H_{ex} triggers the MNR resonance phenomenon where ν_e change their flavors while $\bar{\nu}_e$ do not. The location at which this instability starts can be identified by looking at the matter and unoscillated neutrino profiles, as pointed out in Ref. [83]. The same cancellation as (4.45) can take place in the antineutrino sector, since the resonance condition is given by

$$h_{G,33} - h_{G,44} = -2\omega c_{2\theta} - \sqrt{2}G_F n_B Y_e - h_{\nu\nu}^{ee} + h_{\nu\nu}^{xx} \simeq 0. \quad (4.46)$$

Note that depending on the neutrino luminosities and the geometrical factors, the self-interaction term can change sign twice, triggering flavor conversion also in the antineutrino sector. This is a necessary condition for the symmetric matter-neutrino resonance (sMNR) where neutrinos and antineutrinos can modify their flavors [82].

Since we are looking for a situation in which the neutrino-antineutrino coupling produced by the Φ term in Eq. (4.3) is effective, there are four resonant conditions between the neutrino and the antineutrino sectors. The first one is

$$h_{G,11} - h_{G,33} = \sqrt{2}G_F n_B (3Y_e - 1) + 2h_{\nu\nu}^{ee} \simeq 0, \quad (4.47)$$

⁴Note that other resonance phenomena might take place that do not necessarily require such conditions.

Name	Type	Condition
MNR (neutrino sector)	$\nu_e \leftrightarrow \nu_x$	$h_{\mathcal{G},11} - h_{\mathcal{G},22} \simeq 0$
MNR (antineutrino sector)	$\bar{\nu}_e \leftrightarrow \bar{\nu}_x$	$h_{\mathcal{G},33} - h_{\mathcal{G},44} \simeq 0$
Helicity coherence (electron flavor)	$\nu_e \leftrightarrow \bar{\nu}_e$	$h_{\mathcal{G},11} - h_{\mathcal{G},33} \simeq 0$
Helicity coherence (nonelectron flavor)	$\nu_x \leftrightarrow \bar{\nu}_x$	$h_{\mathcal{G},22} - h_{\mathcal{G},44} \simeq 0$

Table 4.2: Relevant resonance conditions to the study of the role of helicity coherence on neutrino propagation in BNS merger remnants. Note that the resonance conditions Eqs. (4.48) and (4.50) are not met in such environments (see text).

where we have made use of the explicit expressions for $h_{\mathcal{G}}$ (4.27). Note that this relation does not involve vacuum terms, and therefore will not depend on the neutrino hierarchy nor on the neutrino energy. Its fulfillment involves a cancellation between the matter term and the self-interaction term that is very similar to the MNR condition (4.45), and it can be identified by using the matter and the unoscillated neutrino self-interaction potential (4.44). Relation (4.47) can be met if $Y_e > 1/3$ for $h_{\nu\nu}^{ee} < 0$ or if $Y_e < 1/3$ for $h_{\nu\nu}^{ee} > 0$. We recall that here $h_{\nu\nu}$ terms also include trace terms Eqs. (4.12) and (4.17).

The second relation

$$h_{\mathcal{G},11} - h_{\mathcal{G},44} = -2\omega c_{2\theta} + \sqrt{2}G_F n_B (2Y_e - 1) + h_{\nu\nu}^{ee} + h_{\nu\nu}^{xx} \simeq 0, \quad (4.48)$$

cannot be satisfied in the standard MNR set-up: a neutron-rich environment which is also $\bar{\nu}_e$ dominated nearby the neutrinosphere with $h_{\nu\nu}^{ee} + h_{\nu\nu}^{xx} < 0$. When a change of sign of $h_{\nu\nu}^{ee} + h_{\nu\nu}^{xx}$ occurs, which is the case in the sMNR, this resonance may appear. The third relation

$$h_{\mathcal{G},22} - h_{\mathcal{G},44} = -\sqrt{2}G_F n_B (1 - Y_e) + 2h_{\nu\nu}^{xx} \simeq 0. \quad (4.49)$$

is difficult to meet. Indeed, unless there is a sMNR, $h_{\nu\nu}^{xx}$ is negative, hence (4.49) cannot be fulfilled since Y_e is always smaller than 1. Finally the last condition is given by

$$h_{\mathcal{G},22} - h_{\mathcal{G},33} = 2\omega c_{2\theta} + \sqrt{2}G_F n_B (2Y_e - 1) + h_{\nu\nu}^{ee} + h_{\nu\nu}^{xx} \simeq 0, \quad (4.50)$$

which [like (4.48)] cannot be met in the case of a standard MNR. Note that the location of resonances from the neutrino mass terms are affected by the presence of the MNR, since the MNR obviously modifies the self-interaction contributions that appear in the helicity resonance conditions. Note that (4.47)-(4.50) agree with those of Ref. [139]. Table 4.2 summarizes the resonance conditions which are relevant to our numerical studies.

From (4.45)-(4.47), a general relation for the resonance conditions associated with the neutrino mass can

be obtained

$$\sqrt{2}G_F n_B Y_e > \sqrt{2}G_F n_B (3Y_e - 1) \simeq 2|h_{\nu\nu}^{ee}| > |h_{\nu\nu}^{ee} - h_{\nu\nu}^{xx}| > |h_{\nu\nu}^{ee}|. \quad (4.51)$$

The first inequality holds if $Y_e < 1/2$, while the second is valid in the case of a standard MNR, where $|h_{\nu\nu}^{ee}| > |h_{\nu\nu}^{xx}|$. The central approximate equality corresponds to relation (4.47), while the two quantities on the left and on the right correspond to the MNR resonance condition (4.45). Relation (4.51) shows that the standard MNR and the helicity coherence condition (4.47) cannot be satisfied simultaneously, while this is possible in the case of a symmetric MNR.

DIRAC CASE

If neutrinos are Dirac particles, the generalized Hamiltonian that governs the evolution is given by Eq. (4.31).

In this case the resonance conditions read

$$h_{D,\mathcal{G},11} - h_{D,\mathcal{G},33} = \frac{1}{2} [h_{\mathcal{G},11} - h_{\mathcal{G},33}] \simeq 0, \quad (4.52)$$

$$h_{D,\mathcal{G},22} - h_{D,\mathcal{G},44} = \frac{1}{2} [h_{\mathcal{G},22} - h_{\mathcal{G},44}] \simeq 0, \quad (4.53)$$

$$h_{D,\mathcal{G},11} - h_{D,\mathcal{G},44} = \frac{1}{2} [h_{\mathcal{G},11} - h_{\mathcal{G},33}] - 2\omega c_\theta \simeq 0, \quad (4.54)$$

$$h_{D,\mathcal{G},22} - h_{D,\mathcal{G},33} = \frac{1}{2} [h_{\mathcal{G},22} - h_{\mathcal{G},44}] + 2\omega c_\theta \simeq 0. \quad (4.55)$$

In the Dirac case the two conditions Eqs. (4.52) and (4.54) can be satisfied in the same conditions than (4.47); while Eqs. (4.53) and (4.55) requires a change of sign of $h_{\nu\nu}^{ee} + h_{\nu\nu}^{xx}$.

4.3.2 NUMERICAL RESULTS ON FLAVOR EVOLUTION

We now present our numerical results on flavor evolution. We show neutrino survival probabilities and quantify the adiabaticity of neutrino evolution through the resonances. We have studied a large ensemble of conditions, both for the potential profiles and parameters. We emphasize that computations are particularly demanding; indeed, we solve the coupled evolution equations of the full 4×4 generalized density matrices with four different initial conditions, in a two-dimensional model, using 10^3 energy bins. We present results on the neutrino evolution up to 300 km from the neutrinosphere, distance at which the numerical convergence is achieved. Note that the inputs from BNS merger simulations Ref. [126] have been obtained

Model	Type	x_0	z_0	θ_0
A	MNR	15	32	15°
B	helicity coherence	12	27	40°
C	MNR and helicity coherence	-30	20	55°

Table 4.3: Characteristics of the three scenarios considered in our schematic model. The second and third columns give the location of the neutrino emission point x_0 (km), z_0 (km) while θ_q defines the neutrino trajectory in the π_{xz} plane (Figure 4.1).

following the same procedure as in Ref. [86].

In the present study, we have searched mostly for the helicity coherence resonance conditions (4.47), which is the most interesting one in our astrophysical setting, as well as more generally when $Y_e < 1/2$. We choose to present three model cases A, B, and C, that correspond to different astrophysical conditions during neutrino evolution. In Model A the MNR condition (4.45) is met, while mass contributions are included without fulfillment of the helicity coherence resonance (4.47). In Model B, the helicity coherence resonance condition (4.47) is met, while the MNR condition, which is also met, leads to no flavor conversions. Model C has both the MNR (4.45) and helicity (4.47) conditions fulfilled and the MNR effectively leads to flavor conversions. Table 4.3 shows the initial location and the angles defining the neutrino trajectory followed in the three models. Note that we set $\phi_q = 0$ since neutrinos follow straight-line trajectories.

In order to fully unravel the effects of the mass terms, we have explored a range of values for each parameter. For the total neutrino luminosity, we have used values from Ref. [126] and rescaled ones, to investigate luminosity variations within the range compatible with available BNS merger simulations (see Ref.[86] for a detailed discussion). For the anisotropic matter term, we have considered matter velocities in the range $\beta \in [0.05, 0.1]$, the value of $\beta = 0.1$ being an upper bound for this type of scenarios. In particular, we make the *ansatz* that the perpendicular quantity is of the same order as the radial ones (see Figures 15, 16, 19 of Ref. [126]). Our numerical results show that anisotropies from the matter currents are always suppressed compared to the neutrino current anisotropies. Therefore our optimistic *ansatz* for the perpendicular velocities will have little impact on our conclusions. The results shown below are all obtained with the value $\beta = 0.1$.

The additional contributions due to the neutrino mass depend on the mass matrix Eq.(4.29). The neutrino mixing parameters used in our simulations are $\Delta m^2 = 2.43 \times 10^{-3} \text{ eV}^2$ and $\sin^2 \theta = 0.087$, which are consistent with measured values [55]. As for the hierarchy, which is still unknown, the mass effects do not appear to depend on the sign of Δm^2 , Eq. (4.47). A slight dependence is present when the MNR occurs. We have performed calculations both by taking/neglecting the Δm^2 term in Eq.(4.29) and the Majorana phase. Our results turned out to be insensitive to them.

Adiabaticity of the evolution at a resonance location is crucial for flavor or helicity conversions to occur. Different approaches can be used to quantify it (see e.g. [80, 112]), including the SU(2) neutrino isospin

formalism which is applicable to the two-flavor framework (Appendix D). Since in our model two neutrino and antineutrino flavors are coupled to each other, the density matrix is a 4×4 matrix. However, it turns out that in most cases either there are flavor conversions because of the MNR while neutrinos and antineutrinos propagations are decoupled, or the helicity coherence resonance is met while MNR is ineffective. Therefore, we can effectively apply the $SU(2)$ neutrino isospin formalism to our system. In the numerical results presented below, the angle between the effective isospin and magnetic field will be shown to quantify adiabaticity.

MODEL A

In this first model, our goal is to establish whether some effects due to neutrino mass would appear in the absence of a helicity coherence resonance. For this reference case, the luminosities used are rescaled as $L_{\nu_e, \text{res}} = 0.65L_{\nu_e}$, $L_{\nu_x, \text{res}} = 1.16L_{\nu_x}$, while the $\bar{\nu}_e$ luminosity is unchanged. Figure ?? shows the matter and unoscillated ν - ν potential (4.44) for Model A. While neutrino self-interaction is larger than the matter potential close to the neutrinosphere, they cross at 40 km, the location for a MNR resonance. In Model A, though there is a helicity coherence resonance which would occur around 150 km due to flavor conversions, we will focus on the region before to show a reference calculation where the resonance helicity condition is not fulfilled. We expect that, in the absence of resonance condition for the mass terms, no new effects appear in the MNR region, since the coupling $\frac{m}{q}$ is small. Indeed, we find the same flavor conversion due to the MNR, as in absence of mass contributions.

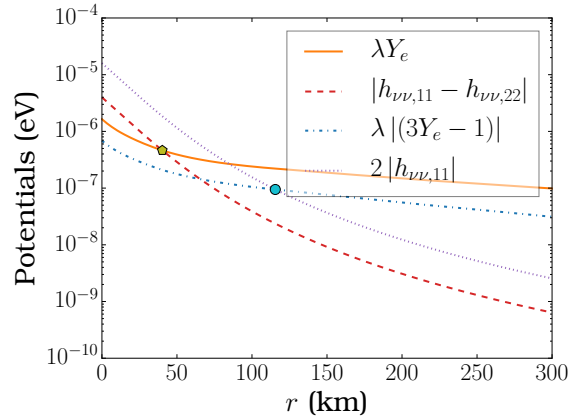


Figure 4.4: Matrix elements appearing in the MNR Eq. (4.45) and helicity resonance conditions (4.47) for Model A (Table 4.3). The values correspond to the matter and to the unoscillated self-interaction potentials Eqs. (4.25) and (4.44) respectively. The green pentagon shows the location of the beginning of the MNR, while the blue dot shows the location of the helicity coherence resonance.

The numerical results here are given for $\alpha = \frac{5\pi}{6}$ and $m_0 = 0.1$ eV. The survival probabilities for neutrinos and antineutrinos are given in Figure 4.5 for the MNR resonance region only and for several neutrino energies. One can see that electron neutrinos efficiently convert into ν_x whereas the antineutrinos do not

modify their flavor content, which is characteristic of MNR.

For neutrinos, there is an energy range between 4 MeV and 13 MeV for which flavor conversions are efficient. Above 13 MeV, though the resonance condition is fulfilled, Figure 4.5 shows that the isospins do not follow the evolution of the effective magnetic field, making the resonance non-adiabatic. A detailed discussion on adiabaticity in presence of the MNR is made within schematic models in Refs. [131, 130]. In order to establish the importance of each term in (4.45) to maintain the resonance over such a long distance, we have performed a run where artificially the oscillating part of the term $h_{\nu\nu}^{xx}$ is set to zero (keeping only the trace part). The results are intriguing since we find that even with this term set to zero, the resonance still maintains over tens of kilometers, the value of $h_{\nu\nu}^{ee}$ being readjusted at each time by the nonlinearity.

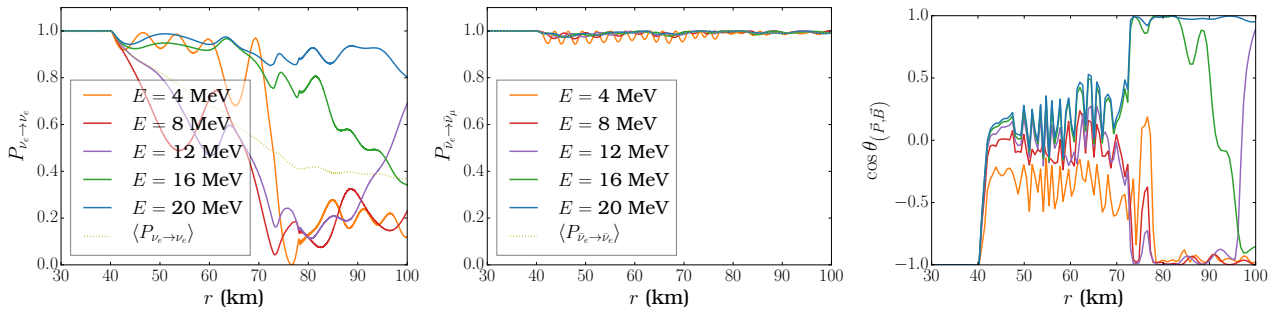


Figure 4.5: Model A: Electron neutrino (left) and antineutrino (middle figure) survival probabilities for different energies, in presence of a MNR starting at 40 km (see Figure 4.4). The averaged probability is also presented. The right figure shows the locally-averaged cosine of the angle between the effective isospin and magnetic field.

MODEL B

Having shown that in the absence of helicity coherence resonance, no effects arise from the mass terms, we now explore the case in which there are resonances. Results for the matter and unoscillated ν - ν potential Eq. (4.44) for Model B are shown in Figure 4.6. Nearby the neutrinosphere, the neutrino potential dominates over the matter one, while after a few tens of km the situation gets reversed: the MNR condition is met at the crossing point, around 12 km. However, the adiabaticity of the evolution is not sufficient to trigger flavor conversions. On the other hand, the helicity coherence resonance Eq. (4.47) is met at 34 km.

As explained before, the computations in this scenario are very demanding. Since we established that in the absence of a helicity coherence resonance, the results were the same for the full 4×4 problem as for two decoupled 2×2 neutrino and antineutrino matrices, we solve the full problem around the helicity coherence resonances using as initial conditions the results obtained in the absence of the mass couplings³. Note that the results correspond to the first helicity coherence resonance in Figure 4.6. Similar results were obtained for the second resonance.

³This is done to keep the computational times manageable.

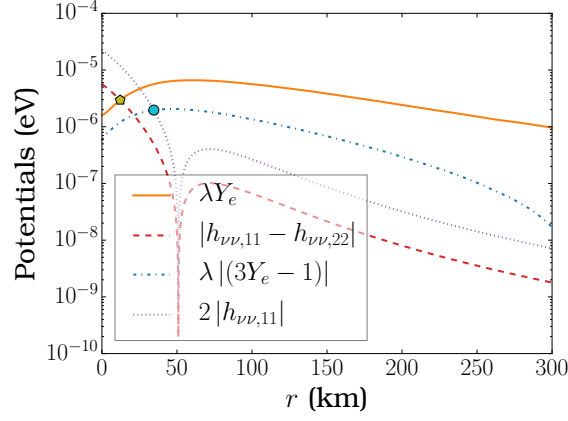


Figure 4.6: Same as Figure 4.4 but for Model B (Table 4.3).

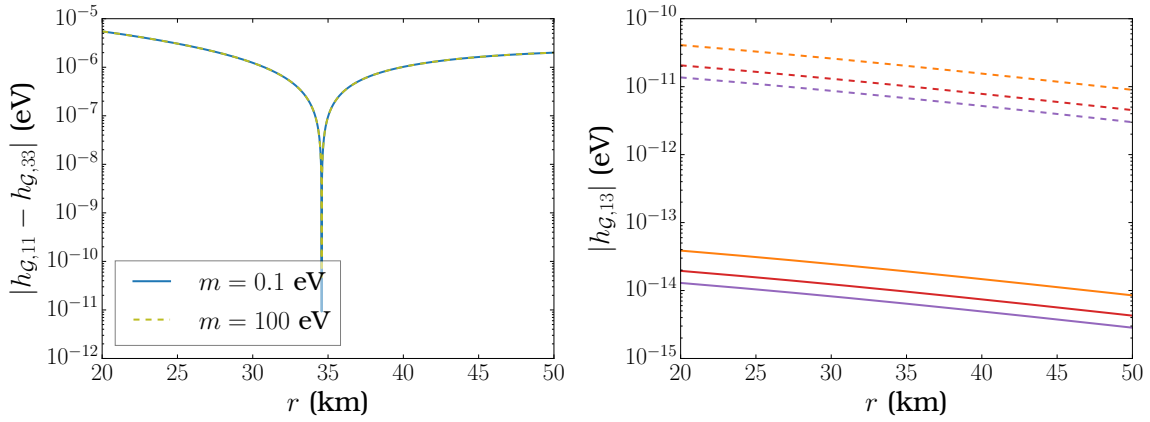


Figure 4.7: Model B: Resonance condition (4.47) (left) as well as the off-diagonal matrix element $h_{G,13}$ (right) that is non-zero in presence of the neutrino mass. The helicity coherence resonance can be seen at 34 km. The different colors correspond to different neutrino energies. The solid lines are the results for $m_0 = 0.1$ eV, while the dotted lines are for the unrealistic value of $m_0 = 100$ eV.

Figure 4.7 shows the resonance condition (4.47) as well as the off-diagonal matrix element $h_{G,13}$ that is non-zero in presence of the neutrino mass, for an absolute mass of $m_0 = 0.1$ eV, and for the unrealistic value $m_0 = 100$ eV. In both cases, the Majorana phase is taken to be $\alpha = \frac{\pi}{3}$. This case is taken as an example to point out that, even when the off-diagonal terms are multiplied by a factor of 10^3 artificially, it is not sufficient to trigger a nonlinear feedback mechanism and the resonance width stays very narrow. We will elaborate on this aspect in Section 4.4.

Figure 4.8 shows the electron neutrino survival probability and the angle quantifying the adiabaticity through the helicity coherence resonance for three different energies as typical examples. As one can see the evolution is completely non-adiabatic at the resonance, explaining why there are no helicity conversions. Note that the evolution stays non-adiabatic even when the absolute neutrino mass is larger by a factor of 10^3 .

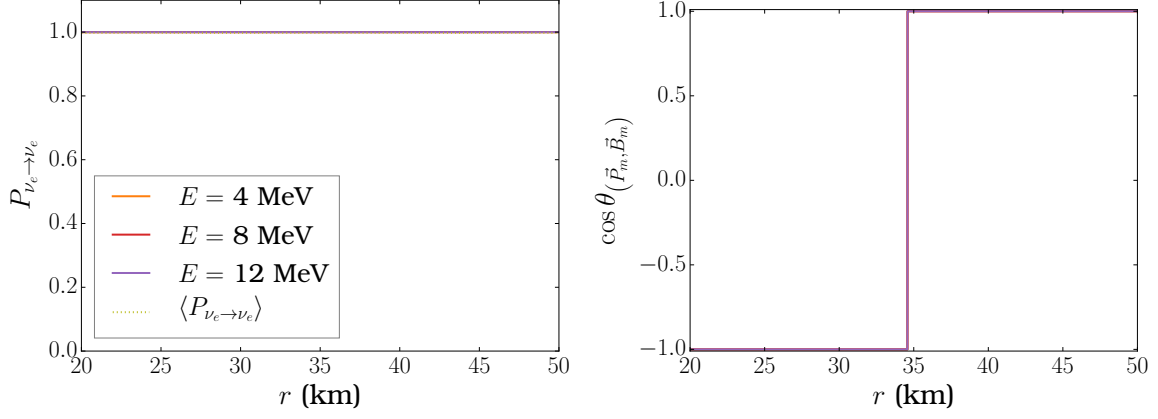


Figure 4.8: Model B: Electron neutrino survival probability (left) and adiabaticity (right). The results for different energies are indistinguishable.

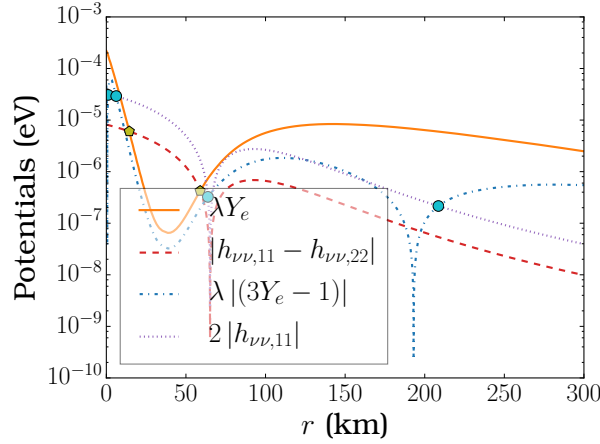


Figure 4.9: Same as Figure 4.4 but for Model C (Table 4.3).

MODEL C

In model C, we look into the scenario where both an effective MNR and the helicity coherence resonance are met. The luminosities used here are rescaled ν_e and $\bar{\nu}_e$ luminosities $L_{\nu_e, \text{res}} = 1.67L_{\nu_e}$, $L_{\bar{\nu}_e, \text{res}} = 1.1L_{\bar{\nu}_e}$, while the ν_x luminosities are unchanged. Figure 4.9 shows the matter potentials and the unoscillated neutrino potentials. In the first kilometers, the matter dominates over the neutrino potential, with two helicity coherence resonances around 2 km and 7 km, up to 15 km where a first MNR crossing occurs. Then, the neutrino potential dominates until the second MNR crossing at 59 km, which is a symmetric MNR. There is another helicity coherence resonance at 64 km. In this model, there is a change of sign for $h_{\nu\nu}^{ee}$, and a little bit later, Y_e goes from $Y_e > \frac{1}{3}$ to $Y_e < \frac{1}{3}$: because of these two changes, there is a fourth helicity coherence resonance at 208 km.

The first two helicity coherence resonances are very similar to the one observed in model B because they occur prior to any flavor conversions. Indeed, numerical computations give the same results as before: a very narrow resonance, without any helicity conversion. The first MNR crossing does not lead to any flavor

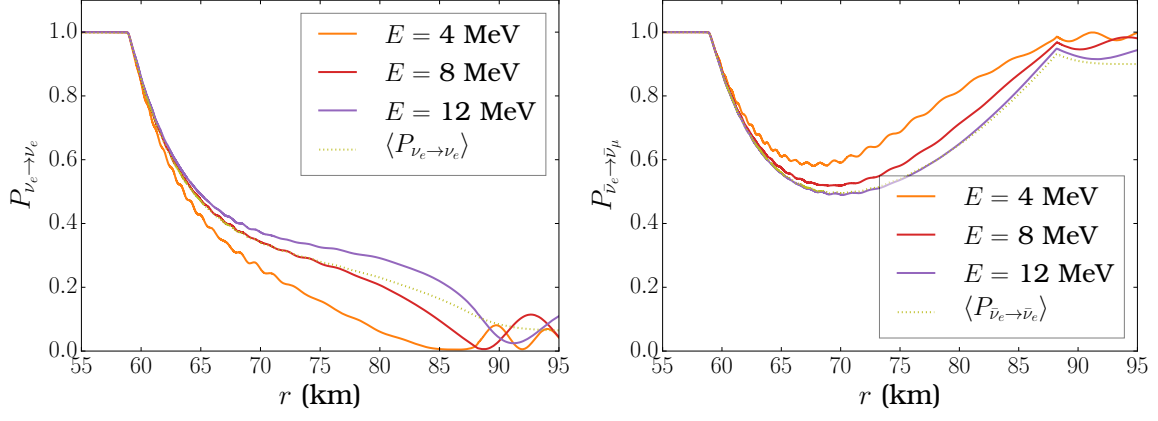


Figure 4.10: Model C: Electron neutrino (left) and antineutrino (right) survival probabilities for different energies, in presence of a symmetric MNR at 59 km (see Figure 4.9) and of a helicity coherence resonance around 103 km. The averaged probabilities are also shown.

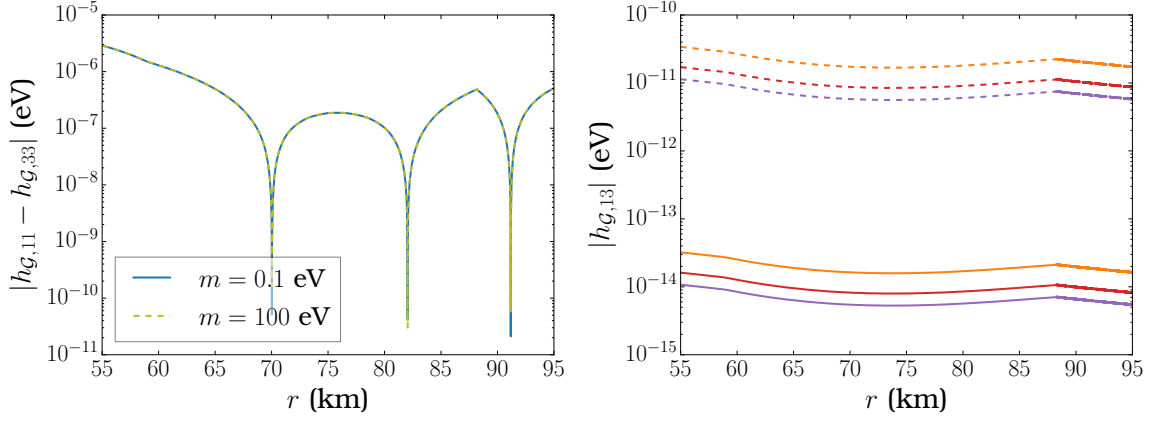


Figure 4.11: Model C: Resonance condition (4.47) (left) and the off-diagonal matrix element $h_{G,13}$ (right) for two different values of the absolute mass m_0 .

conversions, the adiabaticity of the evolution being not sufficient, while the second MNR crossing is efficient. Because of these conversions, the potential $h_{\nu\nu}^{ee}$ is modified and no longer changes of sign. The oscillated neutrino potentials obtained with our 2×2 code shows that because of flavor conversions, the last two helicity coherence resonances are turned into three resonances at 70, 82 and 91 km.

We numerically investigated these resonances, which are superimposed with the symmetric MNR, and obtained the same results as for the symmetric MNR without mass terms. Neutrinos and anti-neutrinos survival probabilities are shown in Figure 4.10 for different neutrino energies, in the region where both the MNR and the helicity resonance condition are fulfilled. At the MNR, neutrinos undergo a strong (adiabatic) conversion while antineutrinos evolve semi-adiabatically through the resonance. At the helicity coherence resonance, both neutrinos and antineutrinos have a non-adiabatic evolution.

Figure 4.11 shows $|h_{G,11} - h_{G,33}|$ and its associated off-diagonal element with two different values of the neutrino absolute mass $m_0 = 0.1$ eV and $m_0 = 100$ eV, around the helicity coherence resonance. As in the case of model B, we take $\alpha = \frac{\pi}{3}$. Their behaviors are similar to those of model B. In particular, despite

having $|h_{G,13}|$ close to $|h_{G,11} - h_{G,33}|$ for the lower energies and for $m_0 = 100$ eV, the resonance is too narrow to render helicity conversions possible.

Note that, in this model, the MNR is symmetric, and $h_{\nu\nu}^{ee} + h_{\nu\nu}^{xx}$ changes of sign. Because of this, we also meet the three other resonances Eqs. (4.48), (4.50) and (4.49). Numerical investigations show that they are very similar to the helicity coherence resonance (4.47): the evolution through these extremely narrow resonances is completely non-adiabatic, hence, no conversion occurs.

4.4 NONLINEAR FEEDBACK MECHANISMS

We discuss here general aspects of the conditions to have multiple MSW resonances and a nonlinear feedback mechanism. By using first-order perturbative developments of the matrix elements, we first analyze two cases where such mechanisms operate, using heuristic arguments. Then, we study why the necessary matching conditions are difficult to meet in more realistic helicity coherence models. Obviously, the arguments we give are valid if the average variations on short timescales catch the behavior on larger timescales.

4.4.1 NONLINEAR FEEDBACK IN THE MNR

The MNR phenomenon can extend over long distances (several hundreds of kilometers) due to a nonlinear feedback mechanism that appears because of the self-interaction term. It involves multiple MSW-like resonances, as discussed in Refs. [131, 86]. Therefore to maintain the resonant phenomenon, condition (4.45)

$$\lambda Y_e \simeq - (h_{\nu\nu}^{ee} - h_{\nu\nu}^{xx}) + 2\omega c_{2\theta}, \quad (4.56)$$

has to be encountered several times. On the left-hand side, the matter profile depends on the distance r and is determined by the model used. On the right-hand side, the self-interaction term depends on the geometrical factors (C.11)-(C.14) (Appendix C), the conversion probabilities and the neutrino fluxes. Note that for antineutrinos, the vacuum term has an opposite sign, making the value of the electron density at the resonance location slightly smaller than the one for neutrinos. In Eq. (4.56) the difference between the diagonal elements of the self-interaction Hamiltonian can be rewritten as⁶

$$h_{\nu\nu}^{ee} - h_{\nu\nu}^{xx} = \sqrt{2}G_F \int_0^\infty dp \{ (2\mathcal{P}_{\nu_e \rightarrow \nu_e} - 1) (G_{\nu_e} j_{\nu_e} - G_{\nu_x} j_{\nu_x}) \\ - (2\mathcal{P}_{\bar{\nu}_e \rightarrow \bar{\nu}_e} - 1) (G_{\bar{\nu}_e} j_{\bar{\nu}_e} - G_{\nu_x} j_{\nu_x}) \}. \quad (4.57)$$

where trace conservation has been used. Figure 4.12 presents an enlarged region of the matter potential as well as the oscillated self-interaction term $h_{\nu\nu}^{ee} - h_{\nu\nu}^{xx}$ for neutrinos and antineutrinos. This is a typical example

⁶Note that, in this section, the dependence on time and energy of the various quantities is not explicitly shown for readability.

of the situations encountered in simulations. One can see that the resonance condition is multiply crossed, which is a characteristics of a nonlinear feedback.

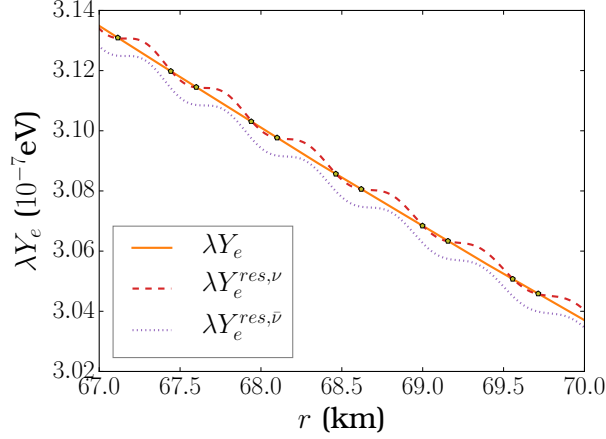


Figure 4.12: Matter profile λY_e for model A (solid line), and the right-hand side of Eq. (4.56) for neutrinos (dashed line) and antineutrinos (dotted line). The pentagons show the multiple crossing where NMR resonance condition Eq. (4.56) is fulfilled.

Let us assume that the resonance condition (4.56) is reached for neutrinos at time t , and estimate if it would be possible to encounter it at time $t + \Delta t$. By assuming that the resonance triggers a small conversion of neutrinos, during the time lapse $t \rightarrow t + \Delta t$, the electron neutrino survival probability becomes

$$\mathcal{P}_{\nu_e \rightarrow \nu_e} \rightarrow \mathcal{P}_{\nu_e \rightarrow \nu_e} - \Delta \mathcal{P}, \quad (4.58)$$

with $\Delta \mathcal{P} > 0^7$, while the matter term in (4.56) gets

$$\lambda Y_e \rightarrow \lambda Y_e + \frac{d(\lambda Y_e)}{dt} \Delta t. \quad (4.59)$$

On the other hand, the corresponding variation of the self-interaction term in Eq.(4.56) includes two contributions

$$\begin{aligned} \frac{1}{\sqrt{2}G_F} (h_{\nu\nu}^{ee} - h_{\nu\nu}^{xx}) &\rightarrow \frac{1}{\sqrt{2}G_F} (h_{\nu\nu}^{ee} - h_{\nu\nu}^{xx}) \\ &\quad - 2 \int_0^\infty dp \Delta \mathcal{P} (G_{\nu_e} j_{\nu_e} - G_{\nu_x} j_{\nu_x}) \\ &\quad + \Delta t \int_0^\infty dp \left[(2\mathcal{P}_{\nu_e \rightarrow \nu_e} - 1) (\dot{G}_{\nu_e} j_{\nu_e} - \dot{G}_{\nu_x} j_{\nu_x}) - (2\mathcal{P}_{\bar{\nu}_e \rightarrow \bar{\nu}_e} - 1) (\dot{G}_{\bar{\nu}_e} j_{\bar{\nu}_e} - \dot{G}_{\nu_x} j_{\nu_x}) \right]. \end{aligned} \quad (4.60)$$

The second term, arising from $\Delta \mathcal{P}$, is negative because $G_{\nu_e} j_{\nu_e} > G_{\nu_x} j_{\nu_x}$. As for the third term, in the case of the MNR, $(2\mathcal{P}_{\nu_e \rightarrow \nu_e} - 1) \leq (2\mathcal{P}_{\bar{\nu}_e \rightarrow \bar{\nu}_e} - 1)$ and as it can be observed from Figures 4.2-4.3, $|\dot{G}_{\bar{\nu}_e} j_{\bar{\nu}_e} -$

⁷We assume that the amplitude of the oscillations of the probabilities are small compared to the conversions triggered by the resonance, hence the sign of $\Delta \mathcal{P}$. Note that antineutrinos are not converted since we consider the MNR and not the sMNR.

$\dot{G}_{\nu_x} j_{\nu_x} \geq |\dot{G}_{\nu_e} j_{\nu_e} - \dot{G}_{\nu_x} j_{\nu_x}|$. Hence, the third term has a positive sign since it is dominated by antineutrinos and the derivatives of the geometric coefficients are always negative.

To fulfill condition (4.56) again at time $t + \Delta t$, we need to have a matching between the variation of the self-interaction contribution and the slope of the matter potential. This matching requires the flavor conversions and the decrease of the geometric factors to compensate. For example, for an increasing matter profile, we find that the flavor conversion must have a bigger weight than the decrease of the geometric factor in order to have multiple crossings due to nonlinear feedback. Let us emphasize that the oscillations of the self-interaction term, on the right-hand side of Eq. (4.56), around the matter potential, are possible because these two contributions have opposite signs; hence, they create a yo-yo effect (see Fig. 4.12)⁸.

Interestingly we have observed that imposing the nontrace part of $h_{\nu\nu}^{xx}$ to be zero does not prevent the nonlinear feedback to happen. Indeed, the same analysis can be repeated and shows that nonlinear feedback is still possible.

4.4.2 NONLINEAR FEEDBACK IN A ONE-FLAVOR MODEL

Having discussed under which conditions the nonlinearity of the equations enables multiple resonances for the MNR, we perform a similar analysis for helicity coherence effects within the model of Ref. [13]. In fact, it is found that a cancellation between the matter and the self-interaction terms occurs over long distances, and a nonlinear feedback mechanism produces significant flavor change (depending on the parameters of the model). Such a model considers only one neutrino flavor and the associated antineutrino, propagating in a matter background of electrons, (anti)neutrinos, and neutrons. Neutrinos traveling along the symmetry axis of a cone interact with those emitted with a fixed angle $\theta = 45^\circ$.

With these assumptions, the generalized Hamiltonian is

$$h_{\mathcal{G}}(t) = \left(\begin{array}{c|c} \sqrt{2}G_F n_B Y_e + h_{\nu\nu}^{ee} & \frac{m}{p} h_{\nu\nu}^{\perp, ee} \\ \hline \frac{m}{p} (h_{\nu\nu}^{\perp, ee})^\dagger & \sqrt{2}G_F n_B (1 - 2Y_e) - h_{\nu\nu}^{ee} \end{array} \right), \quad (4.61)$$

where $h_{\nu\nu}^{ee} = 2\sqrt{2}G_F (1 - u) (n_\nu - n_{\bar{\nu}})$, $u = \cos(\theta)$, with the (anti)neutrino number density n_ν ($n_{\bar{\nu}}$) and

$$n_\nu - n_{\bar{\nu}} = \int dp \phi(p) \rho_{ee}(r, p) = \int dp \phi(p) \mathcal{P}_{\nu_e \rightarrow \nu_e}(r, p), \quad (4.62)$$

ϕ being a function that includes the Fermi-Dirac distributions and other numerical factors (which are not

⁸Had they had the same sign, more peculiar conditions would have been needed to get several crossings.

relevant here). The off-diagonal term in Eq. (4.61) is

$$h_{\nu\nu}^{\perp,ee} = 2\sqrt{2}G_F\sqrt{1-u^2}(n_\nu - n_{\bar{\nu}}). \quad (4.63)$$

With this generalized Hamiltonian, the helicity coherence resonance condition becomes

$$\sqrt{2}G_F n_B (3Y_e - 1) + 2h_{\nu\nu}^{ee} \simeq 0, \quad (4.64)$$

and is satisfied if a cancellation between the matter and the self-interaction terms takes place. The Y_e value at resonance can be written as

$$Y_e^{\text{res}} \simeq \frac{1}{3} - \frac{4}{3}(1-u)\frac{n_\nu - n_{\bar{\nu}}}{n_B}. \quad (4.65)$$

In [13], it is argued that the neutrino contribution being relatively small, this resonance is located around $Y_e^0 = \frac{1}{3}$. In the model, n_B is taken to be a constant while Y_e is increasing according to the profile $Y_e = Y_e^0 + \frac{r}{\lambda} \left(1 + \frac{r^2}{\kappa^2}\right)$, where λ and κ are two parameters that are allowed to vary.

Let us perform the same analysis as for the MNR, and suppose that the resonance condition (4.65) has been fulfilled at time t , and has triggered a small neutrino conversion $\mathcal{P}_{\nu_e \rightarrow \nu_e} \rightarrow \mathcal{P}_{\nu_e \rightarrow \nu_e} - \Delta\mathcal{P}$. Note that, here, $\Delta\mathcal{P}$ is due to a conversion of neutrinos into antineutrinos and vice versa. Then, the lepton number density (4.62) decreases

$$n_\nu - n_{\bar{\nu}} \rightarrow n_\nu - n_{\bar{\nu}} - \Delta n_{\nu-\bar{\nu}}, \quad (4.66)$$

where $\Delta n_{\nu-\bar{\nu}} = \int dp \phi(p) \Delta\mathcal{P}$.

Therefore the Y_e value at resonance increases according to

$$Y_e^{\text{res}} \rightarrow Y_e^{\text{res}} + \frac{4}{3}(1-u)\frac{\Delta n_{\nu-\bar{\nu}}}{n_B}. \quad (4.67)$$

Since the chosen Y_e profile increases, it is possible to encounter the resonance more than once. However, as in the case of the MNR, one needs the matching between the slope of Y_e and the conversion $\Delta\mathcal{P}$ of neutrinos into antineutrinos on a short timescale, which is expected to be small. Therefore, this analysis indicates that, provided that Y_e increases very slowly, the resonance condition can be fulfilled several times⁹.

4.4.3 NONLINEAR FEEDBACK AND HELICITY COHERENCE

Let us now explore the possibility of having a nonlinear feedback for the helicity coherence resonance. We study here the resonance condition (4.47), though the discussion can be easily extended to the three other

⁹Note that, since here there are no variations due to geometry, the small oscillations of the survival probabilities are sensible, and lead oscillations of Y_e^{res} (see Figure 3 of Ref. [136]).

resonance conditions (4.48), (4.50) and (4.49). The resonance condition (4.47) is fulfilled for

$$n_B (3Y_e - 1) \simeq -\frac{2}{\sqrt{2}G_F} h_{\nu\nu}^{ee}. \quad (4.68)$$

In most cases we have studied, the electron-antineutrino contribution dominates along the trajectories, hence $h_{\nu\nu}^{ee} \leq 0$, making resonance condition fulfilled for $Y_e \geq \frac{1}{3}$. The self-interaction term (4.37) can be written as

$$\begin{aligned} \frac{1}{\sqrt{2}G_F} h_{\nu\nu}^{ee} = & \int_0^\infty dp [(\mathcal{P}_{\nu_e \rightarrow \nu_e} + 1) G_{\nu_e} j_{\nu_e} \\ & - (\mathcal{P}_{\bar{\nu}_e \rightarrow \bar{\nu}_e} + 1) G_{\bar{\nu}_e} j_{\bar{\nu}_e} \\ & + (\mathcal{P}_{\nu_x \rightarrow \nu_e} - \mathcal{P}_{\bar{\nu}_x \rightarrow \bar{\nu}_e}) G_{\nu_x} j_{\nu_x}]. \end{aligned} \quad (4.69)$$

We consider the case of Model B where the MNR resonance condition is not met while the helicity coherence one is. In this case, $\mathcal{P}_{\nu_x \rightarrow \nu_e}$ and $\mathcal{P}_{\bar{\nu}_x \rightarrow \bar{\nu}_e}$ are frozen and equal to zero, while the variations of $\mathcal{P}_{\nu_e \rightarrow \nu_e}$ and $\mathcal{P}_{\bar{\nu}_e \rightarrow \bar{\nu}_e}$ are both equal to $\Delta\mathcal{P}$.

Let us suppose that the resonant condition (4.68) is fulfilled at time t and has triggered conversion of neutrinos into antineutrinos. By using Eq. (4.58) and a similar relation for antineutrinos, the self-interaction term varies as¹⁰

$$\begin{aligned} \frac{1}{\sqrt{2}G_F} h_{\nu\nu}^{ee} \rightarrow & \frac{1}{\sqrt{2}G_F} h_{\nu\nu}^{ee} - \int_0^\infty dp \Delta\mathcal{P} (G_{\nu_e} j_{\nu_e} - G_{\bar{\nu}_e} j_{\bar{\nu}_e}) \\ & + \Delta t \int_0^\infty dp [(\mathcal{P}_{\nu_e \rightarrow \nu_e} + 1) \dot{G}_{\nu_e} j_{\nu_e} \\ & - (\mathcal{P}_{\bar{\nu}_e \rightarrow \bar{\nu}_e} + 1) \dot{G}_{\bar{\nu}_e} j_{\bar{\nu}_e}]. \end{aligned} \quad (4.70)$$

The contribution due to $\Delta\mathcal{P}$ is positive when antineutrinos dominate the emissions at the neutrinosphere, while the one from the gradient of the geometrical factors is also positive in BNS merger environments. This gives an overall positive sign. If the matter potential gradient is positive, the matching condition becomes impossible. On the other hand, if the matter gradient is negative, peculiar conditions would be necessary to produce oscillations (which is characteristic of a nonlinear feedback mechanism) of $h_{\nu\nu}^{ee}$ around the matter term $\sqrt{2}G_F n_B (3Y_e - 1)$ (similarly to Fig. 4.12 for the MNR).

It can be noticed that even if we had an electron-neutrino-dominated environment such as core-collapse supernovae, in which the fulfillment of the resonance condition (4.68) would require $Y_e < \frac{1}{3}$, the two con-

¹⁰As for the MNR, we suppose that the small oscillations in the survival probabilities are negligible in comparison with the variations of the geometric coefficients.

tributions to the variation of $h_{\nu\nu}^{ee}$ would still have the same sign^u, making it difficult to establish a nonlinear feedback mechanism. A different geometry with softer geometric factors might make the matching of the two terms in the helicity resonance condition easier to meet.

Let us conclude that for such a resonance, a nonlinear feedback would enable to increase greatly the adiabaticity. Indeed, using the expression of the adiabaticity parameter γ_m introduced in (D.5), we find that without a matching of the derivatives of $h_{\mathcal{G},11}$ and $h_{\mathcal{G},33}$, γ_m is proportional to $(\frac{m}{q})^2$. For a typical value of $\frac{m}{q} \approx 10^{-7} - 10^{-8}$, we see that this adiabaticity parameter is extremely small. A nonlinear feedback would enable the matching of the derivative, and increase γ_m up to $\gamma_m = \mathcal{O}(\frac{m}{q})$.

4.5 CONCLUSIONS

We have explored the impact of mass contributions on neutrino flavor evolution in astrophysical environments. These nonrelativistic corrections appear in extended mean-field descriptions of neutrino propagation. We have discussed conditions for the resonances associated with such mass terms and pointed out that, in particular, they require the matter potential to be larger than the neutrino self-interaction potentials.

We have presented the first study of mass effects in a binary neutron star merger environment. In particular, we have built a two-flavor model based on two-dimensional BNS merger simulations. We have presented numerical results on the neutrino probabilities and adiabaticity during flavor evolution for the following three model cases where resonance conditions are fulfilled: A) MNR, B) helicity coherence, and C) MNR and helicity coherence. These are representative of the ensemble of results we have obtained. An important result is that resonance conditions can be met in simulations of astrophysical environments such as BNS mergers. However, adiabaticity is not sufficient to produce efficient flavor conversion due to helicity coherence.

It has to be noted that our model is based on the ansatz that, in the self-interaction Hamiltonian, the flavor evolution of the neutrino modes behaves the same as the test neutrino. This approximation gives more weight to the geometrical factor present in the helicity coherence term. Therefore, one cannot exclude the possibility that the implementation of the full geometrical dependence of the density matrix might introduce some differences with respect to our findings. It is likely, however, that the induced decoherence among the neutrino modes might also not be in favor of adiabaticity.

Some general conclusions can be drawn from the present investigation regarding mass effects. First of all, resonance conditions for helicity coherence can be met in realistic astrophysical scenarios. On the other hand, the factor m/q suppresses the mass terms values by $10^{-7} - 10^{-8}$, if one considers a typical neutrino energy and 0.1 eV as an upper limit on the absolute neutrino mass. However, their role could be magnified

^uUnless there are very specific flavor conversions beforehand.

by a nonlinear feedback mechanism. We have investigated why multiple crossings (which are characteristic of such a feedback) are absent in our study. To this aim, two cases have been considered where nonlinear feedback is operative: the neutrino-matter resonances and the model of Ref. [13]. In fact, in the case of the MNR, there is a matching between the derivative of the matter potential and the variations of the self-interaction contribution. Such a matching is possible if the variation arising from the flavor contribution and the one arising from the decrease of the geometric factors have the proper weights in order to enable the difference of the self-interaction terms to follow the matter term.

In the model of Ref. [13] the signs of the variations on short time scales still allow for multiple resonances. Because the adiabaticity is governed by the derivative of the matter term, this matching produces sufficiently adiabatic evolution and a nonlinear feedback. This is in agreement with the results of Ref. [13], where it was shown that, for a given value of the mass m , λ has to be chosen large enough so that the nonlinear mechanism can take place. Note that there the nonlinear adjustment does not involve geometrical factors.

Our analysis reveals that the MNR and helicity coherence resonances are essentially of the same nature. Indeed, they both come from the cancellation of a matter term and a self-interaction term. Moreover, the conditions required to trigger a nonlinear feedback phenomenon are very similar, though the weighting of the different terms differs.

For the case of helicity coherence we have argued that the peculiar conditions for multiple crossings of the resonance condition are difficult to meet because of the strong r dependence of the geometrical factors, the $\bar{\nu}_e$ over ν_e dominance in BNS mergers, and the derivative of the matter potentials. However, our findings also show that —even in a core-collapse environment where $Y_e < 1/3$ —it would still be difficult to have multiple resonances under normal conditions. Softer geometric coefficients (found in different environments) could make it easier to achieve this matching. Therefore, based on our results, we can state that the findings of Refs. [13] and [140] are due to peculiar chosen matter profiles which are unlikely to be found in general conditions.

In conclusion, the results obtained in the presented work confirm that the mean-field equations usually employed are on a safe ground as far as flavor evolution is concerned and that helicity coherence is unlikely to produce significant flavor changes in realistic astrophysical environments.

5

Neutrino propagation in binary neutron star mergers in presence of nonstandard interactions

Contents

5.1	Introduction	102
5.2	The model	103
5.2.1	Neutrino evolution equations in presence of nonstandard interactions	103
5.2.2	Two-neutrino flavor evolution in binary neutron star mergers	104
5.3	Impact of nonstandard interactions on neutrino flavor evolution	106
5.3.1	New conditions for the I resonance	107
5.3.2	NSI, the MNR and the I resonance	114
5.4	Discussion and conclusions	117

The main goal of the second project of the thesis is to explore the role of nonstandard neutrino-matter interactions on the neutrino evolution in accretion disks around binary neutron star merger remnants. The study is based on the detailed simulation of [126] for the astrophysical setting. We employ the usual mean-field equations for density matrices for this investigation.

5.1 INTRODUCTION

The presence of nonstandard interactions can alter flavor conversion. Limits on nonstandard neutrino self-interactions are rather loose [141], whereas scattering and oscillation experiments give tight bounds on nonstandard neutrino-matter interactions (NSI) [142, 143, 144]. The first measurement of neutrino-nucleus coherent scattering provides interesting NSI constraints [145]. The existence of NSI would modify the interpretation of oscillation experiments in particular for the inferred values of the squared-masses and the mixings, and could provide with an explanation of observed anomalies.

Within a supernova core, flavor changing neutral current interactions would impact the scattering rates and the electron fraction, altering the infall [146]. Nonstandard four-fermion neutrino self-interactions might produce flavor equilibration both in normal and inverted mass ordering [147] or could modify the neutronization burst signal of a supernova explosion [148]. Novel interactions can also produce resonant conversion near the neutrinosphere and influence the r process in supernovae [149]. In particular, the Inner (I) resonance —a Mikheev Smirnov Wolfenstein (MSW)-like resonance [8, 37]— can take place due to the cancellation between the matter and the NSI contributions to the neutrino Hamiltonian [14]. Refs. [15, 16] have pointed out that the I location appears to be little affected by neutrino self-interactions. Moreover, Ref. [16] has shown that NSI contributions can provide with the necessary cancellation for the occurrence of MNR in supernovae.

In the second project, we investigate nonstandard interactions in BNS remnants and focus on the NSI impact on flavor evolution. We shed a new light on the I resonance mechanism and show that the neutrino self-interactions can produce I resonances as synchronized MSW effects. Moreover, we present how NSI can modify both location and adiabaticity of the MNRs. Our calculations are based on the matter density profiles and electron fractions taken from detailed astrophysical simulations of BNS remnants [126]. We discuss the effects of nonstandard interactions on the electron fraction Y_e , a key parameter for r process nucleosynthesis in neutrino-driven winds, in the light of the study of Ref. [93].

The chapter is structured as follows. Section 5.2 presents the model with NSI. Numerical results on the flavor evolution for different sets of NSI parameters are given in Section 5.3. The NSI effects on the I and MNR resonances are discussed. Section 5.4 is a conclusion.

5.2 THE MODEL

5.2.1 NEUTRINO EVOLUTION EQUATIONS IN PRESENCE OF NONSTANDARD INTERACTIONS

We remind that the evolution of a system of neutrinos and antineutrinos in an astrophysical environment is governed by the Liouville-Von Neumann equations

$$i\dot{\rho}(t, \vec{q}) = [h(t, \vec{q}), \rho(t, \vec{q})], \quad i\dot{\bar{\rho}}(t, \vec{q}) = [\bar{h}(t, \vec{q}), \bar{\rho}(t, \vec{q})], \quad (5.1)$$

where $\rho(t, \vec{q})$ (2.101) and $\bar{\rho}(t, \vec{q})$ (2.102) are single-particle density matrices, and $h(t, \vec{q}) \equiv \Gamma^{\nu\nu}(t, \vec{q})$ (2.103) and $\bar{h}(t, \vec{q}) \equiv \Gamma^{\bar{\nu}\bar{\nu}}(t, \vec{q})$ (2.104) mean-field Hamiltonians for neutrinos and antineutrinos respectively. Since neutrinos propagate through an astrophysical background, the mean-field Hamiltonians include the neutrino charged- and neutral-current interactions with the particles composing the medium, usually electrons, protons, and neutrons, as we will be considering in the present work. Therefore h is given by

$$h = h_0 + h_{\text{mat}} + h_{\nu\nu}, \quad (5.2)$$

where the first term corresponds to the vacuum Hamiltonian, the second to the neutrino standard and non-standard interactions with matter and the last one to neutrino self-interactions. The same expression holds for \bar{h} with a minus sign for the h_0 contribution. In the flavor basis, the vacuum term reads

$$h_0 = U h_{\text{vac}} U^\dagger, \quad (5.3)$$

with $h_{\text{vac}} = \text{diag}(E_i)$, $E_{i=1, N_f}$ being the eigenenergies of the propagation eigenstates with N_f the number of neutrino flavors. The quantity U is the Pontecorvo-Maki-Nakagawa-Sakata (PMNS) $N_f \times N_f$ unitary matrix relating the mass to the flavor basis [5].

As for the matter term, it comprises the standard contribution from neutrino-electron charged currents¹ and a nonstandard term related to neutrino-matter interactions

$$h_{\text{mat}} = h_{\text{CC}} + h_{\text{NSI}}, \quad (5.4)$$

where $h_{\text{CC}} = \text{diag}(V_{\text{CC}}, 0)$ and $V_{\text{CC}} = \sqrt{2}G_F\rho_e$, with G_F the Fermi coupling constant and ρ_e the net electron number density. Note that here anisotropic contributions to the matter Hamiltonian are not included².

¹We note that the standard neutrino-matter neutral current contributions are not included since they are proportional to the identity matrix and therefore do not produce flavor modifications.

²Such contributions are e.g. implemented in Ref. [17]. Also, trace terms can be subtracted from the Hamiltonian whereas this is not possible in presence of helicity coherence [17].

The nonstandard interaction Hamiltonian is

$$h_{\text{NSI}} = \sqrt{2}G_F \sum_f n_f \epsilon^f, \quad (5.5)$$

where a sum over the electron, down and up quark³ number densities is performed ($f = e, d, u$). The ϵ matrices correspond to the nonstandard interactions couplings, constrained by several observations [142, 143, 144, 145]. In the case of three neutrino flavors, these are [143]

$$\left(\begin{array}{ccc} |\epsilon_{ee}| < 2.5 & |\epsilon_{e\mu}| < 0.21 & |\epsilon_{e\tau}| < 1.7 \\ & |\epsilon_{\mu\mu}| < 0.046 & |\epsilon_{\mu\tau}| < 0.21 \\ & & |\epsilon_{\tau\tau}| < 9.0 \end{array} \right), \quad (5.6)$$

if matter is composed only of protons and electrons (solarlike). One can see that the bounds on the NSI parameters are rather loose, with the exception of $\epsilon_{\mu\mu}$.

The third contribution in Eq.(5.2) corresponds to the neutrino self-interaction Hamiltonian

$$h_{\nu\nu} = \sqrt{2}G_F \sum_{\alpha} \int (1 - \hat{q} \cdot \hat{p}) [dn_{\nu_{\alpha}} \rho_{\nu_{\alpha}}(\vec{p}) - dn_{\bar{\nu}_{\alpha}} \bar{\rho}_{\bar{\nu}_{\alpha}}(\vec{p})], \quad (5.7)$$

where the quantity $dn_{\nu_{\alpha}}$ ($dn_{\bar{\nu}_{\alpha}}$) denotes the differential number density of neutrinos (antineutrinos), the underline refers to the neutrinos initially born with α flavor at the neutrinosphere.

5.2.2 TWO-NEUTRINO FLAVOR EVOLUTION IN BINARY NEUTRON STAR MERGERS

We employ the theoretical framework of two-neutrino flavors and stationary evolution⁴. In the flavor basis the neutrino density matrix reads

$$\rho = \begin{pmatrix} \rho_{ee} & \rho_{ex} \\ \rho_{ex}^* & \rho_{xx} \end{pmatrix}, \quad (5.8)$$

and similarly for $\bar{\rho}$. The vacuum Hamiltonian Eq. (5.3) involves the PMNS matrix that for three flavors depends on three measured mixing angles and three unknown CP -violating phases (one Dirac- and two Majorana-type) [5]. In two flavors, these fundamental parameters reduce to one mixing angle θ (one phase as well in the case of Majorana neutrinos). Therefore the vacuum contribution becomes

$$h_0 = \omega \begin{pmatrix} -c_{2\theta} & s_{2\theta} \\ s_{2\theta} & c_{2\theta} \end{pmatrix}, \quad (5.9)$$

³The heavy quark content of the nucleon is neglected.

⁴From now on, only the radial dependence of all quantities is retained and not explicitly shown to simplify notations.

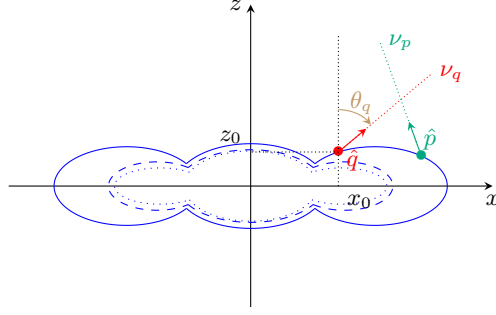


Figure 5.1: Schematic view of our model. Neutrinos start free streaming at the neutrinospheres, shown as a solid blue (respectively dashed and dotted) line for ν_e (respectively $\bar{\nu}_e$ and ν_x). The trajectory of a test neutrino ν_q is labeled by the coordinates of its emission point (x_0, z_0) , and the angle θ_q between the direction of its momentum \hat{q} and the z axis. The test neutrino propagates in a background of matter and (anti)neutrinos ν_p of momentum \hat{p} .

with $\omega = \frac{\Delta m^2}{4E}$, $\Delta m^2 = m_2^2 - m_1^2$ with m_1, m_2 the mass values of the mass eigenstates and $E = q$ the neutrino energy, $s_{2\theta} = \sin 2\theta$ and $c_{2\theta} = \cos 2\theta$.

For the standard matter Hamiltonian in Eq.(5.4) we write

$$V_{CC} = \lambda Y_e, \quad (5.10)$$

where $\lambda = \sqrt{2}G_F n_B$, with n_B the baryon number density and $Y_e = \rho_e/(n + p)$ the electron fraction, with n and p the neutron and proton number densities, respectively. As in Refs.[85, 86, 17] our investigation is anchored to the detailed simulations in which the BNS merger remnant is a central object, lasts up to 200 ms and has about a 30 km radius. We take information on the baryon number densities and electron fraction from cylindrical averages of detailed three-dimensional Newtonian simulations [126]. In our two-dimensional model neutrino propagate with an azimuthal symmetry axis from point (x_0, z_0) , at the neutrinosphere following a straight line trajectory characterized by a radial r and an angular θ_q variables (Fig. 5.1). Note that we approximate the neutrinospheres as infinitely thin disks of radii R_ν that are flavor dependent, as done in Refs.[82, 84, 85, 86, 17].

In two flavors, by retaining only the nonstandard contribution Eqs. (5.5-5.6) with loosest constraints, we get for the ϵ matrix

$$\left(\begin{array}{cc} |\epsilon_{ee}| < 2.5 & |\epsilon_{e\tau}| < 1.7 \\ & |\epsilon_{\tau\tau}| < 9.0 \end{array} \right). \quad (5.11)$$

We rewrite the NSI potential Eq. (5.5) in terms of the fermion fraction Y_f . In fact, using the charge neutrality of the medium, we get the relation

$$Y_f \equiv \frac{n_f}{n_B}, \quad (5.12)$$

which for up and down quarks can be rewritten as $Y_d = 2 - Y_e$ and $Y_u = 1 + Y_e$. The NSI contribution is

then

$$h_{\text{NSI}} = \sqrt{2}G_F n_B [Y_e \epsilon^e + (1 + Y_e)\epsilon^u + (2 - Y_e)\epsilon^d]. \quad (5.13)$$

Finally we follow Ref. [16] and impose the requirement that, at the MSW resonance in the Sun, with an electron fraction $Y_\odot \approx 0.7$, the NSI contribution should vanish as no effect has been observed (see also [150]), namely

$$Y_\odot \delta\epsilon^e + (1 + Y_\odot)\delta\epsilon^u + (2 - Y_\odot)\delta\epsilon^d = 0, \quad (5.14)$$

with $\delta\epsilon^f = \epsilon_{ee}^f - \epsilon_{xx}^f$. This equation gives a relation between $\delta\epsilon^e$ as a function of $\delta\epsilon^u, \delta\epsilon^d$. The off-diagonal couplings $\epsilon_{ex}^e, \epsilon_{ex}^u, \epsilon_{ex}^d$ are fixed at the same value ϵ_0 . As a result, the NSI Hamiltonian only depends on two NSI parameters, the diagonal one $\delta\epsilon^n$ and the off-diagonal ϵ_0

$$h_{\text{NSI}} = \lambda \begin{pmatrix} (\frac{Y_\odot - Y_e}{Y_\odot})\delta\epsilon^n & (3 + Y_e)\epsilon_0 \\ (3 + Y_e)\epsilon_0^* & 0 \end{pmatrix}, \quad (5.15)$$

with the constraints $|\delta\epsilon^n| \lesssim \mathcal{O}(10)$ and $|\epsilon_0| \lesssim \mathcal{O}(1)$. For the neutrino self-interaction Hamiltonian Eq.(5.7) we assume, as done in previous works [82, 84, 85, 86, 17], that

$$\rho_\nu(r, \vec{p}) = \rho_\nu(r, p), \quad (5.16)$$

namely that the angular dependence of the neutrino density matrix is not retained. As a consequence, the neutrinos that are coupled by the self-interaction term have the same flavor history as the test neutrino. We assume in our calculations that neutrinos are emitted as Fermi-Dirac distributions f_{ν_α} with luminosities L_{ν_α} and average energies $\langle E_{\nu_\alpha} \rangle$ at the neutrinosphere with neutrinosphere radii R_{ν_α} (Table 3.1). Concerning the neutrino luminosities and average energies, these are stable for long times (see Ref. [126]). By using Eqs.(5.7) and (5.16), the neutrino self-interaction term is given by Eq. (3.21). The unoscillated neutrino potential is given by Eq. 3.23.

5.3 IMPACT OF NONSTANDARD INTERACTIONS ON NEUTRINO FLAVOR EVOLUTION

In order to investigate the role of NSI on the flavor evolution we have performed simulations by varying ϵ_0 and $\delta\epsilon^n$ within the range given by relations (5.11). We have explored a large set of trajectories with different emission points (x_0, z_0) and angles θ_q (Fig. 5.1)⁵. By analyzing the neutrino flavor evolution behaviors along numerous trajectories we have identified different regimes depending on the NSI parameters. Here we take some trajectories as typical examples to illustrate the flavor mechanisms and their interplay we have observed

⁵Here also ϕ_q is set to zero.

over the full set. As for the oscillation parameters we fix $\Delta m^2 = 2.43 \times 10^{-3} \text{ eV}^2$ and $\sin^2 2\theta = 0.087$ [55] for the normal mass ordering, and $\Delta m^2 = -2.38 \times 10^{-3} \text{ eV}^2$ and $\sin^2 2\theta = 0.092$ for the inverted mass ordering. We discuss the dependence of the results both on the normal and on the inverted mass ordering since the neutrino mass ordering has not been determined yet.

In this section, we show examples with NSI parameters $\delta\epsilon^n \in [-0.9, -0.7]$. These are the parameters for which we observed the presence of the I resonance in most of the trajectories explored that were relevant for nucleosynthesis [93]. Negative values of $\delta\epsilon^n$ with a greater absolute value lead to the disappearance of the I resonances, as the matter potential V_M (5.17) would always be negative on the region of space studied, and would also make the MNR further away. Negative values of $\delta\epsilon^n$ with a smaller absolute value would still present I resonances, but in a different region of space, and would also shift the MNRs. It is worth noting that positive values of $\delta\epsilon^n$ have also been considered as they can shift the MNR closer to the neutrinosphere.

As for the value of ϵ_0 , we have restricted ourselves to values smaller than 10^{-3} . Indeed, values larger than that create oscillation patterns analogous to vacuum oscillations but driven by the large matter off-diagonal element. These oscillations have a very short wavelength —shorter than a kilometer— and can start as soon as the neutrino propagation begins. Given that, in our calculations, we assume that neutrinos are free streaming, our results are reliable only if flavor conversions happen well outside the neutrinospheres, and therefore using larger values of ϵ_0 would give unphysical results. These oscillations appearing because of a larger ϵ_0 also have a large amplitude, making the behavior difficult to analyze. For all these reasons, we chose to work with a value of ϵ_0 well below the current experimental constraints.

5.3.1 NEW CONDITIONS FOR THE I RESONANCE

The presence of NSI produces a new MSW-like resonance, called the I resonance [14]. Refs. [14, 15, 16] have shown that its occurrence is due to the matter terms only. In the present work we will be discussing two situations in which the I resonance occurs: *i*) the self-interaction is subdominant, in accord with [14, 15, 16]; *ii*) the neutrino self-interaction dominates and leads to a I resonance as a synchronized MSW mechanism. We explore this scenario using the SU (2) spin formalism.

We would like to emphasize that the results presented in this section are independent of the approximation (3.20) that is employed here. Indeed, the occurrence of the I resonance, synchronized or not, only depends on the matter profile and on the unoscillated neutrino potentials, which are both independent of multiangle effects. Therefore, the results we present here will remain unaffected in a full multiangle calculation.

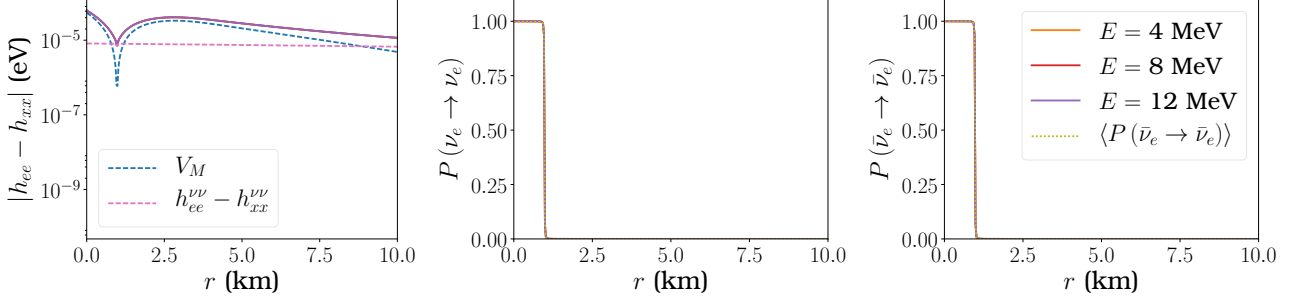


Figure 5.2: Left panel: Difference of the diagonal elements of the total neutrino Hamiltonian (solid line), matter potential V_M (dashed line) Eq.(5.17) in presence of NSI contributions with $\delta\epsilon^n = -0.7$ and $\epsilon_0 = 1 \times 10^{-4}$ and self-interaction oscillated potential (dotted line), as a function of distance from the emission point. The initial parameters are $x_0 = -30$ km, $z_0 = 20$ km, and $\theta_q = 55^\circ$. Middle and right panels: Survival probabilities for neutrinos (middle) and antineutrinos (right). Different energies corresponding to different colors as well as the averaged probability (dotted line) are indistinguishable. The results are obtained by using baryon densities and electron fraction from the detailed simulations [126].

I RESONANCE WITH NEGLIGIBLE SELF-INTERACTION

The I resonance occurs when the difference between the diagonal elements of the total Hamiltonian goes to zero, requiring for the total matter potential to meet the condition

$$V_M \equiv \lambda \left[Y_e + \frac{Y_\odot - Y_e}{Y_\odot} \delta\epsilon^n \right] \approx 2\omega c_{2\theta} - (h_{ee}^{\nu\nu} - h_{xx}^{\nu\nu}). \quad (5.17)$$

References [14, 15, 16] have pointed out that the presence of $\nu\nu$ self-interactions have negligible effects on the location and adiabaticity of the I resonance, thus making it occur when the matter potential Eq.(5.17) is very small.

First, we consider here a case in which the self-interaction potential is subdominant compared to the matter one. In such cases, the location of the I resonance coincides with the point where the matter potential V_{mat} becomes very small, which is possible in the presence of NSI because of a cancellation between the standard matter term and the nonstandard contribution. Figure 5.2 (left panel) presents the difference of the diagonal elements, the total matter potential with $\delta\epsilon^n = -0.88$ and $\epsilon_0 = 1 \times 10^{-4}$ and the oscillated self-interaction potential. Condition (5.17) can be satisfied for both neutrinos and antineutrinos simultaneously and is very little dependent on the neutrino energy. Depending on the value of the diagonal NSI parameter $\delta\epsilon^n$, the I resonance can arise extremely close to the neutrinosphere, as already pointed out in the literature. In this example, it occurs at 1 km from it.

The survival probabilities for neutrinos and antineutrinos as well as the average one are shown in Fig. 5.2 for different neutrino energies (middle and right panels). Given a specific matter profile, the resonance location only depends on the value of the diagonal NSI parameter, $\delta\epsilon^n$, whereas the value of ϵ_0 impacts the adiabaticity. For the case shown, the I resonance is adiabatic and induces significant conversion for both neutrinos and antineutrinos. It is worth noting that even in the presence of a small ϵ_0 parameter, the flavor con-

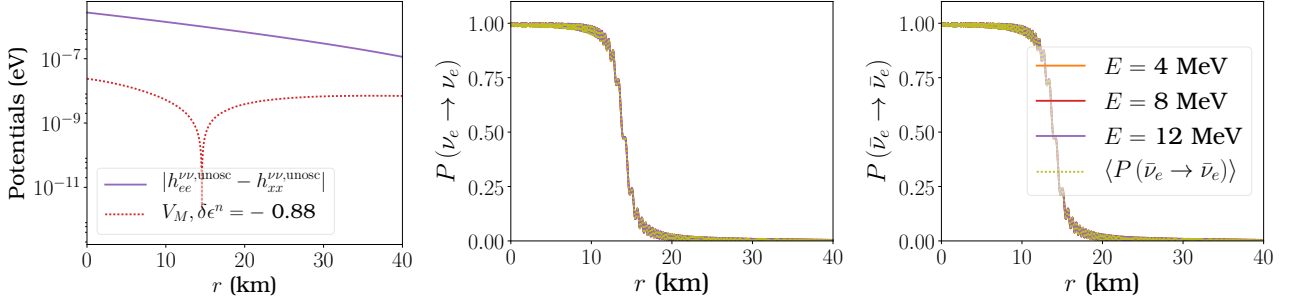


Figure 5.3: Left panel: Matter potential V_M (solid line) Eq.(5.17) in presence of NSI contributions $\delta\epsilon^n = -0.88$ and $\epsilon_0 = 1 \times 10^{-4}$ and self-interaction unoscillated potential Eq.(3.23) (dotted line), as a function of distance from the emission point. The initial parameters are $x_0 = 15$ km, $z_0 = 32$ km, and $\theta_q = 15^\circ$. Middle and right panels: Survival probabilities for neutrinos (middle) and antineutrinos (right). Different energies corresponding to different colors as well as the averaged probability (dotted line) are indistinguishable.

version behaviors stay independent of the energy. This is due to the fact that the off-diagonal self-interaction contribution to the Hamiltonian is, at the considered location, much larger than the vacuum one, therefore suppressing the energy dependence.

I RESONANCE AS A SYNCHRONIZED MSW

While exploring the parameter space and different trajectories for the neutrino propagation, we have encountered situations where, although the self-interaction unoscillated potential is several orders of magnitude larger than the matter potential, an I resonance takes place and leads to significant flavor conversions. Figure 5.3 shows a typical example of this situation with the NSI parameters $\delta\epsilon^n = -0.88$ and $\epsilon_0 = 1 \times 10^{-4}$. One can see that although the unoscillated self-interaction potential μ (3.23) dominates the matter one λ (5.10), flavor conversions occur at the same location where the I resonance condition is fulfilled. Note that the difference between the self-interaction oscillated diagonal elements do cancel at the same point. We will be unraveling this effect in the light of synchronized flavor conversions.

SPIN DESCRIPTION In order to describe this phenomenon, we use the SU (2) isospin formalism in flavor space. The effective isospin vector $\vec{P}_{\nu_\alpha}(r, q)$ denoting a neutrino of initial flavor α is related to the neutrino density matrix according to

$$\rho_{\nu_\alpha}(r, q) = \frac{1}{2} \left(\mathbb{1} + \vec{\sigma} \cdot \vec{P}_{\nu_\alpha}(r, q) \right), \quad (5.18)$$

and similarly for antineutrinos, where $\mathbb{1}$ is the 2×2 identity matrix and $\vec{\sigma} = (\sigma_x, \sigma_y, \sigma_z)$ is a vector in flavor space whose components are the Pauli σ matrices. In this theoretical framework, the Liouville-Von Neumann equations are replaced by precession equations for $\vec{P}_{\nu_\alpha}(r, q)$ with an effective magnetic field defined as

$$h(r, q) = \frac{1}{2} \left(\mathbb{1} + \vec{\sigma} \cdot \vec{B}(r, q) \right). \quad (5.19)$$

and receiving three contributions

$$\vec{B}(r, q) = \vec{B}_{\text{vac}}(q) + \vec{B}_{\text{mat}}(r) + \vec{B}_{\nu\nu}(r), \quad (5.20)$$

Note that the expressions for $\vec{P}_{\bar{\nu}_\alpha}$ and \vec{B} are analogous to Eqs.(5.18) and (5.20) respectively. In the antineutrino case, the vacuum contribution in Eq.(5.20) has a minus sign. The vacuum term is given by

$$\vec{B}_{\text{vac}} = 2\omega\vec{B}_0 = 2\omega \begin{pmatrix} s_{2\theta} \\ 0 \\ -c_{2\theta} \end{pmatrix} \quad (5.21)$$

while the matter term includes the standard and nonstandard contributions

$$\vec{B}_{\text{mat}} = \lambda \left[Y_e \begin{pmatrix} 0 \\ 0 \\ 1 \end{pmatrix} + \begin{pmatrix} 2(3 + Y_e) \text{Re}\epsilon_0 \\ -2(3 + Y_e) \text{Im}\epsilon_0 \\ \delta\epsilon^n \left(\frac{Y_\odot - Y_e}{Y_\odot} \right) \end{pmatrix} \right] \quad (5.22)$$

The third term in Eq.(5.20) comes from the self-interaction term of the neutrino Hamiltonian

$$\vec{B}_{\nu\nu} = \sqrt{2}G_F \sum_{\alpha=e,x} \int_0^\infty dp \left(G_{\nu_\alpha} j_{\nu_\alpha}(p) \vec{P}_{\nu_\alpha}(p) - G_{\bar{\nu}_\alpha} j_{\bar{\nu}_\alpha}(p) \vec{P}_{\bar{\nu}_\alpha}(p) \right), \quad (5.23)$$

where $j_{\nu_\alpha}(p) = \frac{L_{\nu_\alpha} f_{\nu_\alpha}(p)}{\pi^2 R_{\nu_\alpha}^2(E_{\nu_\alpha})}$ and similarly for antineutrinos. Note that the explicit r dependences are not shown for readability.

In order to describe the collective neutrino mode associated to the I resonance, we introduce the \vec{J} vector

$$\vec{J} = \sum_{\alpha=e,x} \int_0^\infty dp \left(G_{\nu_\alpha} j_{\nu_\alpha}(p) \vec{P}_{\nu_\alpha}(p) - G_{\bar{\nu}_\alpha} j_{\bar{\nu}_\alpha}(p) \vec{P}_{\bar{\nu}_\alpha}(p) \right). \quad (5.24)$$

We emphasize that, in a BNS merger scenario, one needs to include the geometrical factors in the definition of the collective vector, contrary to what is usually done in the bulb model for supernovae (single-angle approximation), as e.g. in [151]. The reason is that here the geometrical factors differ for different flavors even when one employs the *ansatz* given by Eq.(5.16). With definition (5.24) one can write the neutrino self-interaction term proportional to a unique vector \vec{J} , namely

$$\vec{B}_{\text{self}} = \sqrt{2}G_F \vec{J}. \quad (5.25)$$

The evolution equation for \vec{J} can be derived from the ones of \vec{P}_{ν_α} (and $\vec{P}_{\bar{\nu}_\alpha}$) and using the explicit expres-

sions of \vec{B} (\vec{B}). One finds

$$\begin{aligned} \partial_r \vec{J} = \vec{B}_{\text{mat}} \times \vec{J} + \vec{B}_0 \times \sum_{\alpha=e,x} \int_0^\infty dp \frac{\Delta m^2}{2p} \left(G_{\nu_\alpha} j_{\nu_\alpha}(p) \vec{P}_{\nu_\alpha}(p) + G_{\bar{\nu}_\alpha} j_{\bar{\nu}_\alpha}(p) \vec{P}_{\bar{\nu}_\alpha}(p) \right) \\ + \sum_{\alpha=e,x} \int_0^\infty dp \left(\partial_r G_{\nu_\alpha} j_{\nu_\alpha}(p) \vec{P}_{\nu_\alpha}(p) - \partial_r G_{\bar{\nu}_\alpha} j_{\bar{\nu}_\alpha}(p) \vec{P}_{\bar{\nu}_\alpha}(p) \right). \end{aligned} \quad (5.26)$$

Let us assume now that, during the evolution, the modes all start along the z axis, i.e. $\vec{P}_{\nu_\alpha}(r, p) \approx P_{\nu_\alpha, z}(0, p) \hat{J}$, and stay aligned with the collective mode \vec{J} (similarly for antineutrinos). If neutrinos and antineutrinos of any momentum stay synchronized in flavor space during the propagation, the evolution equation for \vec{J} becomes

$$\partial_r \vec{J} \approx \vec{B}_{\text{mat}} \times \vec{J} + \vec{B}_0 \times \hat{J} \int_0^\infty dp \frac{\Delta m^2}{2p} [G_{\nu_e} j_{\nu_e}(p) + G_{\bar{\nu}_e} j_{\bar{\nu}_e}(p) - 2G_{\nu_x} j_{\nu_x}(p)] + \hat{J} \frac{\partial_r \mu}{\sqrt{2}G_F}, \quad (5.27)$$

where μ is the unoscillated neutrino self-interaction potential (3.23). While the first two terms are ordinary oscillation terms, the last one is a damping term, taking into account that the norm of this collective mode decreases with time. This is due to the fact that the geometry of the problem is included in the definition of \vec{J} . Note that such a decrease should not be interpreted as lepton number conservation violation, but as a neutrino density decrease along a given trajectory, due to the geometry. Let us characterize this decrease by multiplying the evolution equation (5.27) by \vec{J}

$$\vec{J} \cdot \partial_r \vec{J} = \frac{1}{2} \partial_r \vec{J}^2 \approx |\vec{J}| \frac{\partial_r \mu}{\sqrt{2}G_F}, \quad (5.28)$$

which gives $|\vec{J}(r)| \approx \frac{\mu(r)}{\sqrt{2}G_F}$. Plugging this expression into Eq. (5.27), one finds

$$\partial_r \vec{J} \approx \vec{B}_J \times \vec{J} + \hat{J} \frac{\partial_r \mu}{\sqrt{2}G_F}. \quad (5.29)$$

The effective magnetic field associated with the collective mode \vec{J} is $\vec{B}_J = \omega_{\text{sync}} \vec{B}_0 + \vec{B}_{\text{mat}}$ which components are

$$\vec{B}_J = \begin{pmatrix} 2\lambda(3 + Y_e) \text{Re}\epsilon_0 + \omega_{\text{sync}} s_{2\theta} \\ -2\lambda(3 + Y_e) \text{Im}\epsilon_0 \\ -\omega_{\text{sync}} c_{2\theta} + V_M \end{pmatrix}. \quad (5.30)$$

The synchronized frequency ω_{sync} is \vec{J} precession frequency

$$\omega_{\text{sync}} = \frac{\sqrt{2}G_F}{\mu} \int_0^\infty dp \frac{\Delta m^2}{2p} [G_{\nu_e} j_{\nu_e}(p) + G_{\bar{\nu}_e} j_{\bar{\nu}_e}(p) - 2G_{\nu_x} j_{\nu_x}(p)]. \quad (5.31)$$

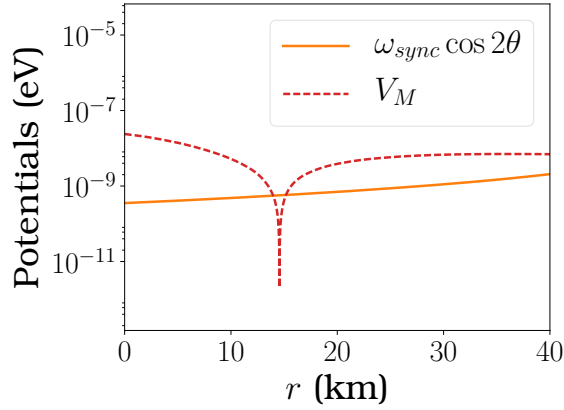


Figure 5.4: Contributions to the z component of the effective magnetic field \vec{B}_J . The solid line represents $\omega_{\text{sync}} c_{2\theta}$, while the dashed line shows the matter potential V_M . It can be seen that when V_M cancels, due to the presence of NSI, the synchronized resonance condition (5.33) is met. The NSI and trajectory parameters used here are the same as the ones used in Fig. 5.3.

Assuming the fluxes follow Fermi-Dirac distributions, the integral above can be computed, and ω_{sync} can be expressed as

$$\omega_{\text{sync}} = \frac{\sqrt{2}G_F\Delta m^2 F_1(0) F_3(0)}{2\mu F_2^2(0)} \left[\frac{L_{\nu_e} G_{\nu_e}}{R_{\nu_e}^2 \langle E_{\nu_e} \rangle^2} + \frac{L_{\bar{\nu}_e} G_{\bar{\nu}_e}}{R_{\bar{\nu}_e}^2 \langle E_{\bar{\nu}_e} \rangle^2} - 2 \frac{L_{\nu_x} G_{\nu_x}}{R_{\nu_x}^2 \langle E_{\nu_x} \rangle^2} \right]. \quad (5.32)$$

RESONANCE CONDITION In addition to a precession motion, the collective mode \vec{J} can also meet a MSW-like resonance condition $B_{J,z} \approx 0$, which requires

$$\omega_{\text{sync}}(r_I) c_{2\theta} = V_M(r_I), \quad (5.33)$$

where r_I is the resonance location. From (5.32), it can be seen that $\omega_{\text{sync}} \propto \frac{1}{\mu}$: in situations where the neutrino background dominates, the lhs of (5.33) is often several orders of magnitude smaller than the rhs. However, in cases where the total matter potential V_M goes to zero, this resonance condition can be met. The reversed situation, in which the resonance condition is met because μ goes to zero, has been already pointed out in [86].

Figure 5.4 shows the rhs and the lhs of (5.33) corresponding to the case of Figure 5.3. One can see that the synchronized MSW resonance condition given by Eq.(5.33) is met almost at the location where V_M goes to zero, i.e. at the location of the I resonance, as can be seen from the conversion probabilities. Another example of synchronized I resonance is shown in Fig. 5.5 with the neutrino self-interaction dominating over the matter potential. Significant conversion can be seen at 29 km, 40 km, 65 km and 78 km.

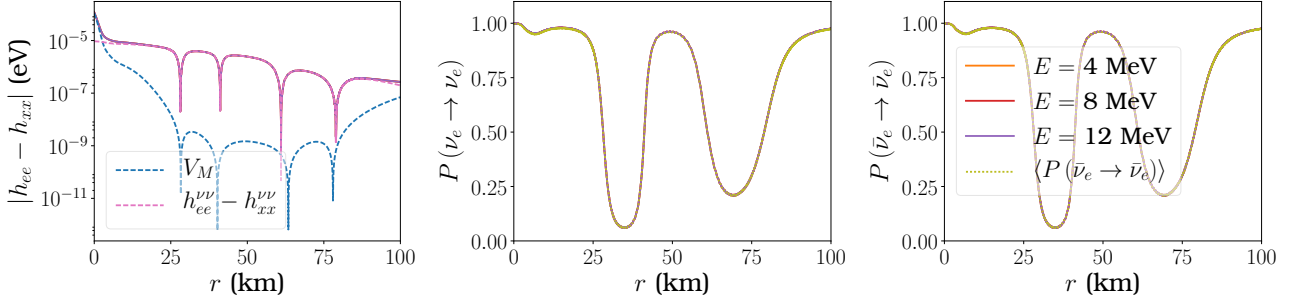


Figure 5.5: Left panel: Difference of the diagonal elements of the total neutrino Hamiltonian (solid line), matter potential V_M (dashed line) Eq.(5.17) in presence of NSI contributions with $\delta\epsilon^n = -0.90$ and $\epsilon_0 = 1 \times 10^{-3}$ and self-interaction oscillated potential (dotted line), as a function of distance from the emission point. The initial parameters are $x_0 = -35$ km, $z_0 = 25$ km, and $\theta_q = 50^\circ$. Middle and right panels: Survival probabilities for neutrinos (middle) and antineutrinos (right). Different energies corresponding to different colors as well as the averaged probability (dotted line) are indistinguishable. Several synchronized I resonances are present in this case, at 29 km, 40 km, 65 km and 78 km.

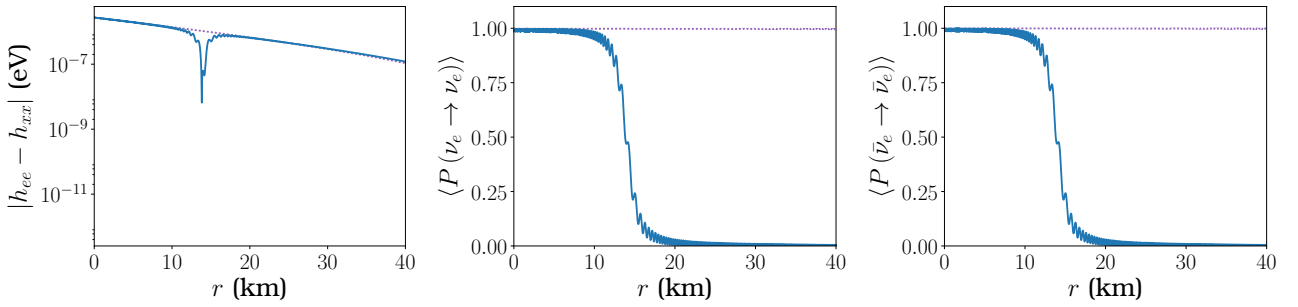


Figure 5.6: Left panel: Difference of the diagonal elements of the total neutrino Hamiltonian, as a function of distance from the emission point. The initial parameters are $x_0 = 15$ km, $z_0 = 32$ km and $\theta_q = 15^\circ$. Middle and right panels: Averaged survival probabilities for neutrinos (middle) and antineutrinos (right). The NSI parameters are set to $\delta\epsilon^n = -0.88$ and $\epsilon_0 = 1 \times 10^{-4}$ (solid lines) and $\epsilon_0 = 1 \times 10^{-5}$ (dotted lines).

ADIABATICITY AND INFLUENCE OF ϵ_0 In order to characterize further flavor conversion at the I resonance, we can define an adiabaticity parameter as

$$\gamma = \frac{|\vec{B}_J|^3}{\left| \frac{d\vec{B}_J}{dt} \times \vec{B}_J \right|_{r=r_I}}. \quad (5.34)$$

From (5.33), it can be seen that the value of ϵ_0 has no influence on the resonance location whereas it influences the adiabaticity of the transformation.

Figure 5.6 shows an example of the influence of ϵ_0 on the adiabaticity. Going from $\epsilon_0 = 10^{-4}$ to 10^{-5} , the oscillation probabilities for neutrinos and antineutrinos go from complete flavor conversion from ν_e to ν_x to no conversion. The adiabaticity parameter Eq.(5.34) corresponding to this case is presented in Fig. 5.7. It can be seen that, at the location of the resonance, the adiabaticity parameter in the case of $\epsilon_0 = 1 \times 10^{-5}$ is two orders of magnitude smaller than the one for $\epsilon_0 = 1 \times 10^{-4}$, consistent with the behaviors observed for the survival probabilities. Note that the cancellation of the adiabaticity parameter around the resonance in the case of $\epsilon_0 = 1 \times 10^{-5}$ comes from the fact that for this value of ϵ_0 , the matter contribution and the ω_{sync} contribution in $B_{J,x}$ (5.30) are of the same order of magnitude and of opposite signs, making $B_{J,x}$ very

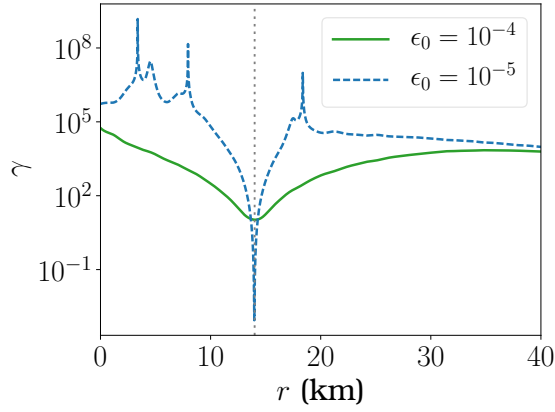


Figure 5.7: Adiabaticity parameter as the right-hand side of Eq.(5.34), corresponding to Fig. 5.6. The solid line corresponds to $\epsilon_0 = 1 \times 10^{-4}$, while the dashed line corresponds to $\epsilon_0 = 1 \times 10^{-5}$. The location of the I resonance is shown as a vertical dotted line.

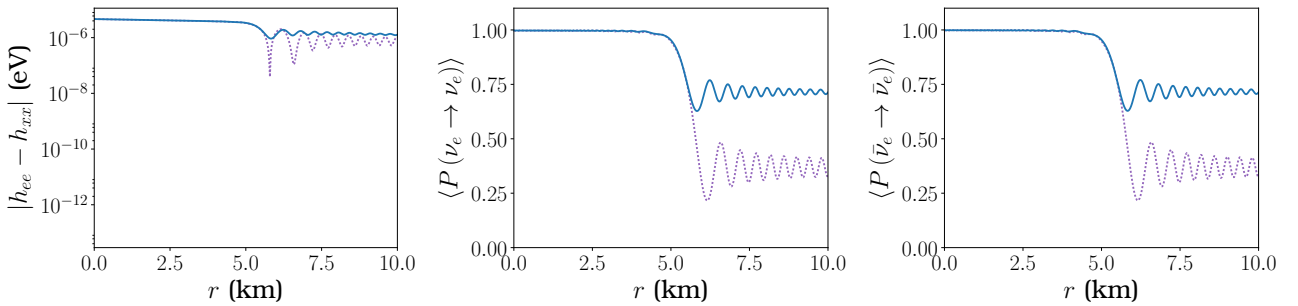


Figure 5.8: Left panel: Difference of the diagonal elements of the total neutrino Hamiltonian, as a function of distance from the emission point, for normal (solid lines) and inverted (dotted lines) mass ordering. The initial parameters are $x_0 = -10$ km, $z_0 = 30$ km and $\theta_q = 25^\circ$. Middle and right panels: Averaged survival probabilities for neutrinos (middle) and antineutrinos (right). The NSI parameters are set to $\delta\epsilon^n = -0.90$ and $\epsilon_0 = 1 \times 10^{-4}$.

small. Therefore, at the resonance, as $B_{J,z}$ tends to 0, $\gamma \rightarrow \frac{B_{J,x}^2}{\partial_r B_{J,z}}$ becomes much smaller at the same time.

EFFECT OF THE NEUTRINO MASS ORDERING The sign of ω_{sync} changes when going from normal to inverted mass ordering. However, due to the fact that the resonance location almost coincides with the location at which V_M changes its sign, the mass ordering will have little impact on it. In our calculations, we have found modifications of the resonance location smaller than 1 km between normal and inverted mass ordering. As for the adiabaticity parameter (5.34), it also depends on ω_{sync} and its derivative. Figure 5.8 shows the effect of neutrino mass ordering on the adiabaticity of flavor evolution for a case with $\delta\epsilon^n = -0.90$ and $\epsilon_0 = 1 \times 10^{-4}$ where the I resonance is located very close the neutrinosphere, at 5 km.

5.3.2 NSI, THE MNR AND THE I RESONANCE

The occurrence of the MNR in BNS might impact r process nucleosynthesis in neutrino-driven winds. As discussed previously, the MNR phenomenon is due to a cancellation between the standard matter term Eq.(5.10) and the neutrino self-interaction Eq.(3.21). This occurs because of the excess of the antineutrino

Name	Condition
MNR (neutrino sector)	$h_{ee} - h_{xx} \simeq 0$
MNR (antineutrino sector)	$\bar{h}_{ee} - \bar{h}_{xx} \simeq 0$
I resonance (negligible self-interaction)	$V_M \simeq 2\omega c_{2\theta}$
Synchronized I resonance	$V_M \simeq \omega_{\text{sync}} c_{2\theta}$

Table 5.1: Relevant resonance conditions to the study of the role of nonstandard interactions on neutrino propagation in BNS merger remnants and core-collapse supernovae.

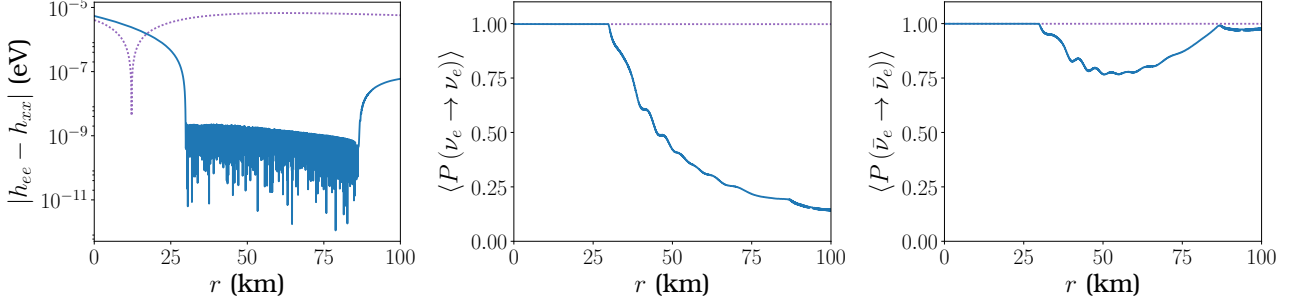


Figure 5.9: Left panel: Difference of the diagonal elements of the total neutrino Hamiltonian, as a function of distance from the emission point, without NSI (dotted line) and with NSI parameters $\delta\epsilon^n = -0.70$ and $\epsilon_0 = 1 \times 10^{-4}$ (dotted line). The initial parameters are $x_0 = 12$ km, $z_0 = 27$ km and $\theta_q = 40^\circ$. Middle and right panels: Averaged survival probabilities for neutrinos (middle) and antineutrinos (right).

over the neutrino near the disk in the BNS context, compared to the supernova case, that gives a negative sign to the neutrino self-interaction potential μ (3.23). However, Ref. [16] has shown the presence of NSI can trigger the MNR also in the supernova context. In our numerical investigations, we have observed various NSI effects on the flavor behaviors in presence of MNR. Table 5.1 summarizes the different resonance conditions encountered in our numerical simulations. First, the existence of NSI can modify the location of the MNR. Figure 5.9 shows that the cancellation between the matter and the neutrino self-interaction terms shifts from 10 km to 30 km when NSI are included. Moreover, neutrino evolution turns from completely nonadiabatic to adiabatic, as the survival probabilities show. By looking at the difference of the neutrino Hamiltonian diagonal elements, one can see that they keep being very small from 30 km to 80 km due to the non-linear feedback that matches the nonlinear neutrino self-interaction contribution to the matter potential as we have been discussing in Chapter 4 [17].

While exploring numerous trajectories and sets of NSI parameters, we have observed an intriguing interplay between the I resonance, synchronized or not, and the MNR. Figures 5.10, 5.11 and 5.12 furnish three examples of such behaviours. Figure 5.10 shows a combination of I resonance and MNR. There are two I resonances, the first at 5 km, which is partially adiabatic, and the second at 21 km, which triggers a MNR between 20 km and 100 km, followed by a second one between 160 km and 240 km where the $\bar{\nu}_e$ are converted while ν_e are not ⁶. Note that this is in opposition to what the MNR typically creates in the absence of NSI:

⁶Note that this corresponds to the same parameters as the ones of Fig. 5.8 with a larger range shown.

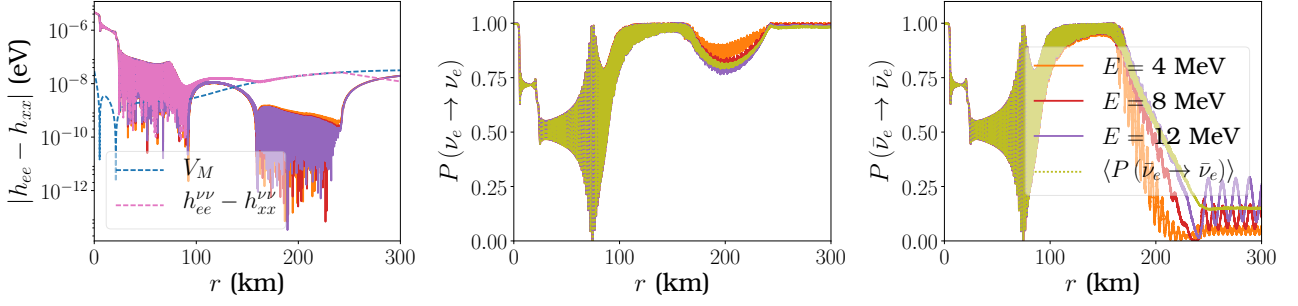


Figure 5.10: Left panel: Difference of the diagonal elements of the total neutrino Hamiltonian (solid line), matter potential V_M (dashed line) Eq.(5.17) in presence of NSI contributions with $\delta\epsilon^n = -0.90$ and $\epsilon_0 = 1 \times 10^{-4}$ and self-interaction oscillated potential (dotted line), as a function of distance from the emission point. The initial parameters are $x_0 = -10$ km, $z_0 = 30$ km and $\theta_q = 25^\circ$. Middle and right panels: Survival probabilities for neutrinos (middle) and antineutrinos (right). Different energies correspond to different colors, and the averaged probabilities (dotted line) are shown. The slight dependence on the energy is due to the fact that as the MNR occurs further away from the emission point, the difference between the diagonal elements becomes comparable to the vacuum term, which then plays a role.

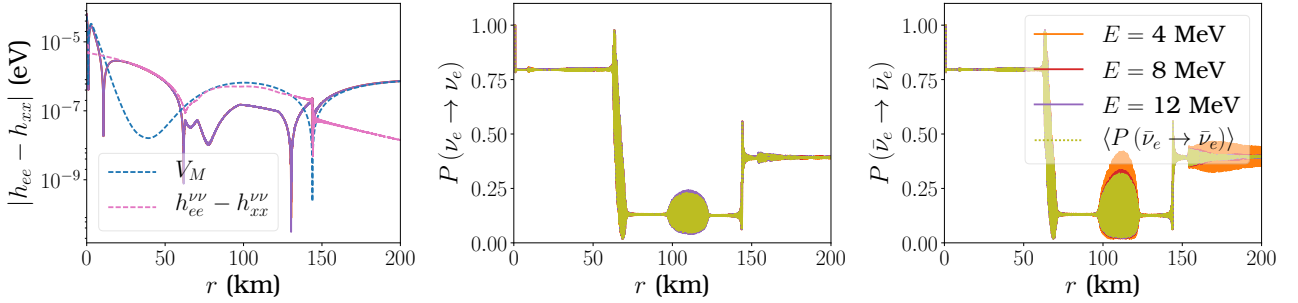


Figure 5.11: Left panel: Difference of the diagonal elements of the total neutrino Hamiltonian (solid line), matter potential V_M (dashed line) Eq.(5.17) in presence of NSI contributions with $\delta\epsilon^n = -0.70$ and $\epsilon_0 = 1 \times 10^{-5}$ and self-interaction oscillated potential (dotted line), as a function of distance from the emission point. The initial parameters are $x_0 = -30$ km, $z_0 = 20$ km and $\theta_q = 55^\circ$. Middle and right panels: Survival probabilities for neutrinos (middle) and antineutrinos (right). Different energies corresponding to different colors as well as the averaged probability (dotted line) are indistinguishable.

indeed, without NSI, the MNR tends to lead to flavor conversions for neutrinos while for antineutrinos the evolution is generally non- or partially adiabatic. In Figure 5.11, an I resonance is located at 2 km, followed by a nonadiabatic MNR at 12 km. Then, between 60 km and 70 km MNR conversions take place. Between 100 km and 125 km the difference of the diagonal elements stays very small, creating small conversions. Finally, at 144 km, an I resonance occurs. The third example of a combination of MNR and I resonances is given in Fig. 5.12. This case in point is interesting as it shows four I resonances: the first, located around 2 km, being a standard one, completely adiabatic, and the other three being synchronized resonances. At 12 km, the second resonance is also very adiabatic, then the third, at 26 km creates only partial conversions. A fourth resonance occurs at 58 km and produces a short MNR-like cancellation between 60 km and 66 km, followed by a MNR between 96 km and 126 km. Notice, again, the peculiar behavior of this MNR, which creates conversions for antineutrinos while the evolution for neutrino is nonadiabatic.

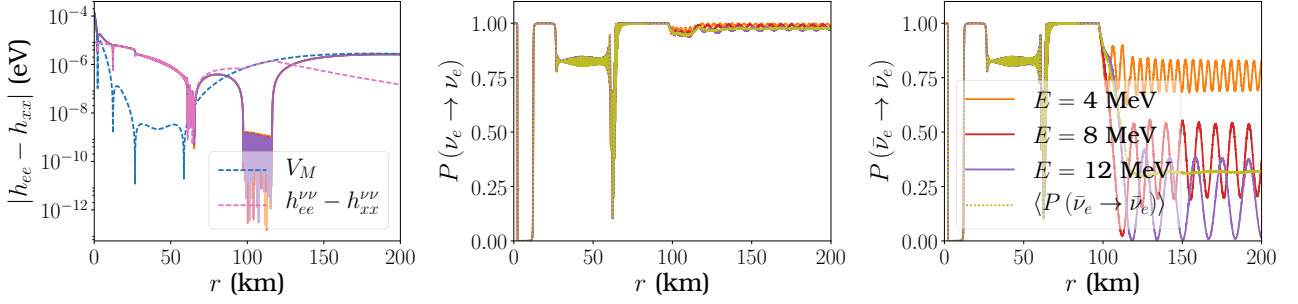


Figure 5.12: Left panel: Difference of the diagonal elements of the total neutrino Hamiltonian (solid line), matter potential V_M (dashed line) Eq.(5.17) in presence of NSI contributions with $\delta\epsilon^n = -0.90$ and $\epsilon_0 = 1 \times 10^{-4}$ and self-interaction oscillated potential (dotted line), as a function of distance from the emission point. The initial parameters are $x_0 = -30$ km, $z_0 = 20$ km and $\theta_q = 55^\circ$. Middle and right panels: Survival probabilities for neutrinos (middle) and antineutrinos (right). Different energies correspond to different colors, and the averaged probabilities (dotted line) are shown. The slight dependence on the energy is due to the fact that as the MNR occurs further away from the emission point, the difference between the diagonal elements becomes comparable to the vacuum term, which then plays a role.

5.4 DISCUSSION AND CONCLUSIONS

In order to assess the role of flavor evolution on nucleosynthesis in neutrino-driven winds a self-consistent calculation of the electron fraction modification coupled with the flavor evolution should be performed, as e.g. the one performed in Ref. [152] in core-collapse supernovae. First steps in this direction are presented in Refs.[82, 84]⁷. However, the trajectory dependence on the abundances and investigations without the *ansatz*(3.20) need to be performed. Such studies go beyond the scope of the present work. Figure 5.13 shows the I resonance location according to Eq.(5.17) in the dimensional space. One can see that such a resonance can occur close to the neutrinosphere and for a large set of NSI parameters. Obviously, for the cases where only the matter term matters, the resonance location would keep unchanged if the *ansatz* (3.20) is relaxed. Using the at-equilibrium Y_e as a reference, one would expect that the Y_e value should be increased by the presence of I resonances since the ν_e and $\bar{\nu}_e$ conversion to ν_x and $\bar{\nu}_x$, respectively, brings the former to have the average energies of the latter. However, the at-equilibrium Y_e is certainly not a good reference for the conditions encountered very close to the neutrinosphere. Only a consistent calculation of Y_e modification including the feedback on the probabilities and the full angular dependence of the neutrino emission would tell us how much flavor evolution impacts the electron fraction.

In our investigation of nonstandard matter-neutrino interactions within 2ν flavor framework. In particular, we have included the electron-tau couplings for which current bounds from scattering and oscillation experiments are still rather loose. By solving the mean-field Liouville-Von Neumann equations along a large ensemble of trajectories, we have uncovered aspects of NSI impact on flavor evolution and, in particular, on the I resonance and the MNR. First, we have shown the conditions for the I resonance are met in this kind of setting, based on detailed BNS simulations, when the matter term dominates over the self-interaction contri-

⁷Note that in these calculations are not fully consistent since the feedback effect of the modified electron fraction on the probabilities is not included

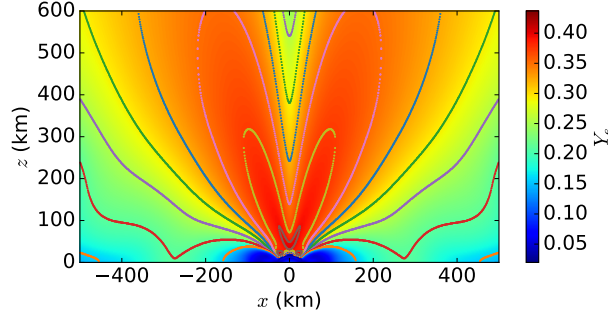


Figure 5.13: Locations where the I resonance condition Eq. (5.17) is fulfilled, depending on the NSI parameters $\delta\epsilon^n$. The curves from outside (orange) to inside (brown) correspond to values from $\delta\epsilon^n = -0.2$ to -0.9 in steps of -0.1 . The Y_e distribution is taken from the BNS simulations of Ref. [126].

bution to the neutrino Hamiltonian. Then, we have uncovered the role of the neutrino self-interaction term and shown that the I resonance can be a synchronized MSW effect if the self-interaction potential dominates over the matter one. The synchronized precession frequency, depending on by the self-interaction potential, matches the resonance condition when the total matter term becomes very small. This mechanism has been dismissed in previous investigations. Note that in Ref. [86] a synchronized MSW effect is observed when, on the contrary, the self-interactions become very small. Second, for the MNR we have shown that NSI little modify the resonance location while the adiabaticity can be significantly changed. Third, we have shown complex situations where MNR, I and synchronized I combine, producing intriguing flavor patterns.

To answer the longstanding puzzle of the origin of r process nuclei, one needs to assess the BNS rate as well as the amount of elements from each individual event. In this respect, it is necessary to determine if and under which conditions flavor evolution takes place as well as its influence on nucleosynthetic abundances. The work presented here provides insight to progress in this direction, in particular if new physics such as nonstandard interactions are discovered in the future.

6

Decoherence of neutrinos in curved space-time

Contents

6.1	Introduction	119
6.2	Neutrino wave packets	121
6.2.1	Describing neutrinos as wave packets	121
6.2.2	Neutrino wave packets in astrophysical environments	122
6.2.3	Coherence length: a heuristic approach	124
6.3	Evolution equation for the neutrino WP in flat space-time	127
6.3.1	Evolution of the neutrino state vector	127
6.3.2	Vacuum oscillations in flat space-time	129
6.4	Evolution equation for the neutrino WP in curved space-time	132
6.4.1	Evolution of the neutrino state vector and covariant phase	132
6.4.2	Vacuum oscillations in Schwarzschild metric	133
6.5	Discussions and conclusions	138

6.1 INTRODUCTION

When studying neutrino propagation in astrophysical environments such as core-collapse supernovae or binary neutron star mergers, most studies do not include general relativity effects. The strong gravitational

fields around these objects can affect neutrino oscillations through different effects: time dilation, energy redshift, or yet trajectory bending. So far, these effects have been studied in the case of vacuum oscillations (see e.g. [153, 154]), or including effects on the localization and adiabaticity of the MSW resonance in the case of propagation in matter (see e.g. [155]). The authors of Ref. [156] have included general relativity effects on supernova neutrino flavor transformations and showed that the self-interaction potential can be increased up to three times in this context. They showed that the presence of gravitational fields delays the appearance of bipolar oscillations in the cooling phase of a supernova. Gravitational effects on neutrino emissions from black hole accretion disks were considered in Ref. [129] and shown to have significant effects on the neutrino fluxes.

Neutrino oscillations in vacuum appear to be a well-known quantum mechanic interference phenomenon. However, a closer look shows that the standard derivation is full of paradoxical issues. In particular, the traditional derivation usually makes the assumption that neutrinos have the same momentum, which comes down to describing neutrinos as plane waves. Yet, plane waves are not localized in space which contradicts the idea of localized production and detection processes. In order to solve these paradoxes, quantum mechanic and experimental uncertainties associated with the production and detection processes have to be considered, hence neutrinos have to be described as wave packets (WPs). Ref. [157] proposed the first WP description for neutrinos, and introduced the notion of decoherence by WPs separation. The first complete analytical derivation of the oscillation probabilities using Gaussian WPs was performed in Ref. [158]. The authors of this work showed explicitly how neutrino oscillations are destroyed when coherence conditions are violated.

The question remains of how coherence is modified in the most general case including neutrino-matter and neutrino-neutrino interactions. Ref. [159] studied coherence in case of adiabatic transformations in a matter background, as well as in the case of propagation in a multi-layer medium with density jumps at the borders of the layers. Ref. [160] considered decoherence effects within the density matrix formalism and showed that it appears as a damping term in the equations of motion. They also considered neutrino oscillations in a background including matter and neutrino interactions, in the adiabatic regime, and in two specific models of adiabaticity violation. However, none of these studies include general relativity effects.

Formal equations for neutrino propagation in curved space-time have been discussed before. Ref. [28] first derived the quantum mechanical phase associated with the propagation of a particle in a given external gravitational field. The authors of Ref. [155] found, in agreement with the previous literature, that the contributions from gravitational fields were diagonal in the flavor basis.

So far, studies in curved space-time have been limited to the effects of gravity on the oscillation phases. In this chapter, we study for the first time decoherence by WP separation in curved space-time. This requires to extend a WP treatment to the case of neutrinos propagating in an external gravitational field. This question

is of particular interest as gravitational fields around compact objects (black holes or binary neutron stars) or supernovae could be large enough to have an impact on neutrino flavor conversions.

The goal of this chapter is to explore decoherence in curved space-time, using a density matrix formalism. In Section 6.2, we discuss the wave packet description and evaluate the size of the neutrino wave packets in astrophysical environments such as supernovae and binary neutron star merger remnants. We estimate the expected neutrino coherence length using heuristic arguments in flat space-time, and discuss the modifications in curved space-time. Then, in Section 6.3 we use the density matrix formalism to describe decoherence as a damping term in flat space-time. We then adapt this procedure in Section 6.4 to the case of decoherence in curved space-time, and in particular in the Schwarzschild metric. We discuss the modifications arising in the presence of gravitational fields and conclude in Section 6.5.

6.2 NEUTRINO WAVE PACKETS

6.2.1 DESCRIBING NEUTRINOS AS WAVE PACKETS

In most studies describing neutrino oscillations, neutrinos are considered as particles described by plane waves, with definite energy and momentum. However, as the processes of neutrino production and detection are localized, a plane wave description is not appropriate. Instead, real localized particles are described by WPs.

As the production and detection processes occupy a finite region in space-time, two massive neutrinos of different masses produced in the same region are not necessarily detected coherently. Figure 6.1 illustrates this phenomenon, showing the propagation of two neutrino wave packets: one massless, and the other ultrarelativistic.

Neutrinos are produced as flavor eigenstates and are therefore composed of a superposition of massive neutrino WPs propagating with different group velocities (see Fig. 6.1). The size of a massive neutrino WP σ_x can be estimated as the coherence time of the production process P through which it is produced. In this simplified illustration, the separation of the wave packets in the detection process is $\Delta x = \Delta v T$, where Δv is the difference between the two massive neutrinos group velocities, and T is the time between the production and detection processes. If the production-to-detection distance is large, this separation may be larger than the size of the WPs itself, so that the neutrino WPs would cease to overlap. Because of this, the notion of coherence length is introduced as the distance beyond which the interference of the massive neutrino is suppressed because of the separation of their wave packets: they can no longer be detected coherently.¹ Therefore, a wave-packet approach of the massive neutrinos is needed to understand decoherence in neu-

¹Note that, if the individual detection processes have large enough space uncertainties (ie small enough energy resolutions), separated neutrino WPs can still be detected coherently. However, we will not discuss this possibility as it is not relevant when talking about the detection of Supernova neutrinos on Earth.

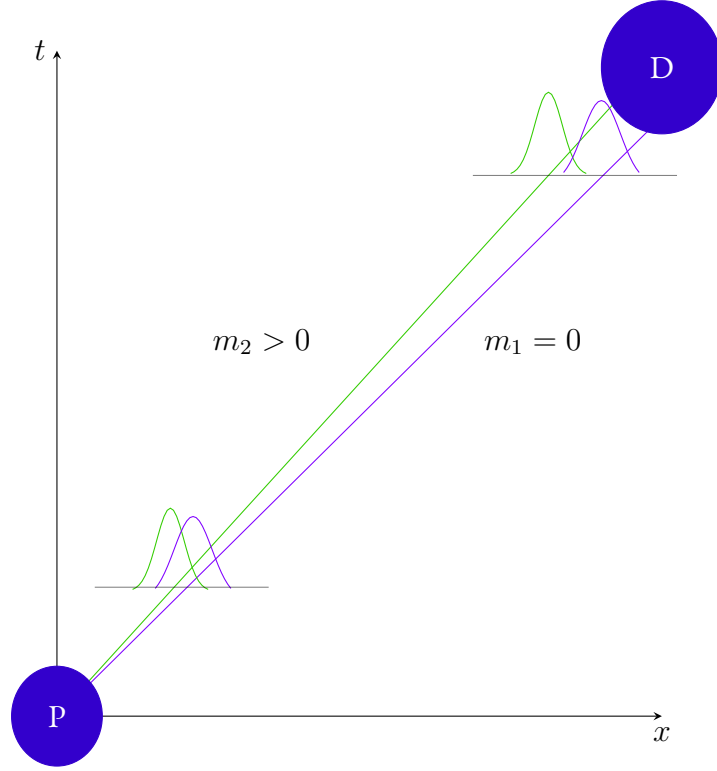


Figure 6.1: Space-time diagram representing schematically the propagation of two neutrino WPs of mass m_1 and m_2 , ν_1 being massless, and ν_2 being ultrarelativistic, from one production process (P) to one detection process (D). Figure adapted from [19].

trino oscillations.

In the next section, we estimate the coherent time of neutrino production processes in typical dense environments such as supernovae or binary neutron star merger remnants. This gives us an estimate of the size of neutrino WPs in those sites. We will then use heuristic arguments to get a rough estimate of the coherence length in flat and curved space-time.

6.2.2 NEUTRINO WAVE PACKETS IN ASTROPHYSICAL ENVIRONMENTS

We follow the reasoning of Ref. [160] to estimate the size of neutrino WPs in astrophysical environments such as supernovae or binary neutron star merger remnants. As the energy uncertainty is smaller than the momentum uncertainty, the spatial length of the neutrino WPs is determined mostly by the temporal localization of the production process [161, 162], which is given by the overlap time σ_t of all the particles involved in the process. We note 1 the particle in this process with the shortest WP, 2 the particle with the next-to-shortest WP, and \vec{v}_i, σ_{xi} ($i = 1, 2$) the respective velocities of the particles and spatial lengths of their WPs. Assuming that all the particles involved in the process have velocities of the same order of magnitude, the overlap time can be estimated as [161]

$$\sigma_t \sim \frac{\sigma_{x2}}{|\vec{v}_1 - \vec{v}_2|}. \quad (6.1)$$

This formula can be easily interpreted: as a process requires all the involved WPs to overlap, it is over as soon as at least one ceases to overlap, that is, when the shortest WP "slides over" the next-to-shortest WP. Note that, in the case of neutrino production processes involving relativistic electrons and non-relativistic nucleons, which are the main production processes in supernovae and binary neutron star merger remnants, the assumption made above on the velocities of the particles is not true. However, as we will see below, the estimate (6.1) remains correct.

We consider now the production of neutrinos through processes involving nucleons, such as beta-processes. In that case, the particles with shortest and next-to-shortest WPs are the nucleons, of lengths $\sigma_{x1} \sim \sigma_{x2} \sim r_0$, where r_0 is the average distance between the nucleons in the medium which can be estimated using

$$n_b = \frac{\rho_b}{m_n} \sim \left(\frac{4}{3} \pi r_0^3 \right)^{-1}, \quad (6.2)$$

where n_b is the baryon number density, ρ_b the baryon matter density and m_n the nucleon mass. The relative velocities of the nucleons can be estimated as their mean thermal velocities, \bar{v} which satisfies the relation

$$\frac{1}{2} m_n \bar{v}^2 = \frac{3}{2} T, \quad (6.3)$$

where T is the temperature at the neutrino production point. Using (6.2) and (6.3), we get for r_0

$$r_0 \approx 7.36 \times 10^{-13} \times \left(\frac{\rho_b}{10^{12} \text{ g.cm}^{-3}} \right)^{-\frac{1}{3}} \text{ cm}, \quad (6.4)$$

and for \bar{v}

$$\bar{v} \approx 0.179 \left(\frac{T}{10 \text{ MeV}} \right)^{\frac{1}{2}}. \quad (6.5)$$

We estimate the length of the neutrino WP σ_x as $\sigma_x \sim v_g \sigma_t$, where $v_g \lesssim 1$ is the mean group velocity of the neutrino propagation eigenstates, and σ_t is given by (6.1), and we get

$$\sigma_x \lesssim 4.1 \times 10^{-12} \left(\frac{\rho_b}{10^{12} \text{ g.cm}^{-3}} \right)^{-\frac{1}{3}} \left(\frac{T}{10 \text{ MeV}} \right)^{\frac{1}{2}} \text{ cm}. \quad (6.6)$$

Note that this length depends weakly on the matter density. For typical values at the neutrino production of $T \approx 10 \text{ MeV}$ and $\rho_b \approx 10^{12} \text{ g.cm}^{-3}$, this gives

$$\sigma_x \lesssim 4.1 \times 10^{-12} \text{ cm}. \quad (6.7)$$

This estimate is based on the formula (6.1) which was obtained under the assumptions that the velocities

of the different particles involved in the process are of the same order of magnitude. However, this is not true in the case of beta-processes, as relativistic electrons are involved. With the velocity of the electron being much larger than the velocities of the nucleons, one could assume that the overlap time between the electron and the nucleon WPs would be shorter than the overlap time between the two nucleons WPs, and would, therefore, determine the spatial length of the neutrino WP. This approach was indeed used in [163]. We will test this assumption by evaluating the electron-nucleon overlap time and comparing it with the nucleon-nucleon overlap time given by (6.1).

We start by estimating the spatial length of the electron WP as [159]

$$\sigma_{xe} \sim (4\pi\alpha^2 n_e)^{-\frac{1}{3}}, \quad (6.8)$$

where α is the fine structure constant and $n_e = Y_e n_b$ is the electron number density, Y_e being the electron fraction and n_b the baryon number density (6.2). Using typical values of $Y_e \approx \frac{1}{2}$ and $\rho_b \approx 10^{12} \text{ g.cm}^{-3}$, we get $\sigma_{xe} \approx 10^{-11} \text{ cm}$, which is much larger than the size of the nucleons WPs. We then calculate the ratio of the electron-nucleon overlap time over nucleon-nucleon overlap time, and obtain

$$\frac{\sigma_{xe}}{\frac{r_0}{|\vec{v}_1 - \vec{v}_2|}} \approx 4.2 \left(\frac{1}{2Y_e} \right)^{\frac{1}{3}} \left(\frac{T}{10 \text{ MeV}} \right)^{\frac{1}{2}}. \quad (6.9)$$

This estimate shows that for typical values of Y_e and T given before, the electron-nucleon overlap time is about four times larger than the nucleon-nucleon one. As a consequence, it will have a small effect on the size of the neutrino wave packets, and the estimate (6.6) is valid. Note that the size of the neutrino WPs is not increased by their propagation from their production site to the neutrinosphere, from which they start free-streaming.

Having estimated the size of neutrino WPs, we now use first principles to define and then evaluate the coherence length.

6.2.3 COHERENCE LENGTH: A HEURISTIC APPROACH

We consider here a flavor neutrino being produced at a given point of space-time as a combination of two propagation eigenstate WPs ν_i ($i = 1, 2$), of different group velocities. Because of the two propagation eigenstates propagate with different group velocities, they will progressively separate. We define L_{coh} the distance after which the separation between the two WPs is larger than the length of one individual WP, σ_x .

In this section, we give a first approach to determine the coherence length L_{coh} using heuristic arguments in flat space-time and discuss the modifications arising when working in curved space-time.

COHERENCE LENGTH IN FLAT SPACE-TIME

In flat space-time, the coherence length can be simply estimated as

$$L_{\text{coh}} \sim \frac{\sigma_x v_g}{\Delta v_g}, \quad (6.10)$$

where v_g is the average group velocity and Δv_g is the difference between the group velocities of the two WPs. For the propagation eigenstates, the group velocities are well defined as [160]

$$v_{gi} = \frac{\partial}{\partial p} E_i, \quad (6.11)$$

where E_i is the energy of the corresponding eigenvalues of the effective neutrino Hamiltonian. In the case of vacuum propagation, we find that

$$v_{gi} = 1 - \frac{m_i^2}{2E^2}, \quad (6.12)$$

where E is the average energy of the two WPs, and hence equation (6.10) becomes

$$L_{\text{coh}} = \frac{2E^2}{|\Delta m^2|} \sigma_x, \quad (6.13)$$

with $\Delta m^2 = m_2^2 - m_1^2$. For the neutrino WPs to be detected coherently, the physical distance l they travel should satisfy

$$l \lesssim L_{\text{coh}} \Leftrightarrow l \lesssim \frac{2E^2}{|\Delta m^2|} \sigma_x. \quad (6.14)$$

This defines the coherence condition: the separation between the two massive WPs has to be smaller than the size of the WPs. If the physical distance traveled l is much larger than the coherence length, then the interference between the two massive neutrinos is suppressed, and oscillations are absent. This phenomenon is illustrated in Fig. 6.2. In section 6.3, we use formal arguments to calculate the coherence length, and find the same dependence on the parameters E and Δm^2 .

In the next paragraph, we study the differences arising when neutrinos propagate in curved space-time rather than flat space-time.

COHERENCE LENGTH IN CURVED SPACE-TIME

The same reasoning as above can be made in general relativity to determine the coherence condition. This is performed in Ref. [155], although no justification of the relation is given. The width of the neutrino wave packets Δd has to be larger than the separation between the two massive WPs, which gives, at constant time

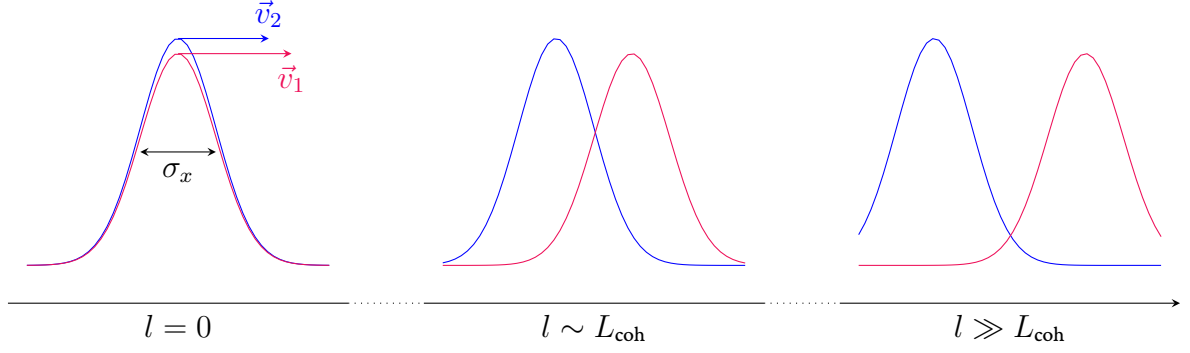


Figure 6.2: Illustration of the separation of two WPs ν_1 and ν_2 , of different group velocities \vec{v}_1 and \vec{v}_2 , and of size σ_x , as a function of the physical distance traveled l . The WPs are produced together at $l = 0$, then slowly separate. We define the coherence length L_{coh} as the distance after which the separation between the two WPs is larger than σ_x . When the distance traveled l is much larger than the coherence length, the WPs do not overlap anymore and are not detected coherently. Figure adapted from [19].

$$\Delta d \gtrsim \left| \int (g_{ij} P_2^i P_2^j)^{\frac{1}{2}} d\lambda - \int (g_{ij} P_1^i P_1^j)^{\frac{1}{2}} d\lambda \right|, \quad (6.15)$$

where λ is an affine parameter along the neutrino world line, $g_{\mu\nu}$ is the metric tensor, and P_i ($i = 1, 2$) is the four-momentum operator that generates spacetime translations of the propagation eigenstate ν_i , and which satisfies $P_i^\mu P_{i\mu} = -m_i^2$. Note again that no justification of this formula has been given in Ref. [155], and the dimensions of the left and right hand side of the equation seem not to be compatible.

We assume that neutrinos follow null geodesics of tangent vector p_{null}^μ such as $p_{\text{null}}^\mu p_{\text{null}\mu} = 0$, and assume $P_i^0 = p_{\text{null}}^0$ and $P_i^j = p_{\text{null}}^j (1 - \epsilon_i)$, with $\epsilon \ll 1$ due to the neutrino small masses. It follows from the neutrino mass-shell relation that

$$\epsilon_i = \frac{m_i^2}{2g_{jk} p_{\text{null}}^j p_{\text{null}}^k}. \quad (6.16)$$

Using this relation along with (6.15), and defining $dl^2 = g_{jk} p_{\text{null}}^j p_{\text{null}}^k = -g_{00} (p_{\text{null}}^0)^2$ the differential physical distance at constant time, we get the condition

$$\Delta d \gtrsim \frac{|\Delta m^2|}{2} \int \frac{dl}{-g_{00} (p_{\text{null}}^0)^2}. \quad (6.17)$$

This relation generalizes (6.14) in curved space-time. It depends on the metric describing the environment in which neutrino propagates, on Δm^2 and on p_{null}^0 which is linked to the neutrino energy.

We have derived the evolution equation for the neutrino density matrices in Chapter 2. We wish to generalize such equations for the neutrino WPs in curved space-time. To this aim, we first introduce the density matrix formalism to derive mathematically the expression of the coherence length in flat space-time. In section 6.4, we use the same formalism to make the first steps in the determination of the coherence length in curved space-time.

6.3 EVOLUTION EQUATION FOR THE NEUTRINO WP IN FLAT SPACE-TIME

In this section, we study decoherence in flat space-time through the density matrix formalism, following the procedure described in Ref. [160]. Note that different approaches can be used, in particular, Ref. [19] studies decoherence through the evolution of the neutrino state vector only. These methods both give the same results.

We start by studying the evolution of the neutrino state vector and derive from it the evolution of the density matrix. We then focus on the case of neutrino oscillations in vacuum. We will use the density matrix formalism in our derivations of the results in curved space-time.

6.3.1 EVOLUTION OF THE NEUTRINO STATE VECTOR

In this section, we consider the evolution of a neutrino state vector in an homogeneous system of ultra-relativistic neutrinos, propagating in a background of ordinary matter composed of electrons, protons, neutrons and neutrinos. The neutrino state vector in coordinate space $|\nu(t, \vec{x})\rangle$ can be Fourier-expanded as

$$|\nu(t, \vec{x})\rangle = \int \frac{d^3\vec{p}}{(2\pi)^3} e^{i\vec{p}\cdot\vec{x}} |\nu(t, \vec{p})\rangle, \quad (6.18)$$

where $|\nu(t, \vec{p})\rangle$ represents the neutrino state vector of a neutrino of a given momentum \vec{p} . We assume that $|\nu(t, \vec{p})\rangle$ is solution of the Schrödinger-like evolution equation

$$i \frac{d}{dt} |\nu(t, \vec{p})\rangle = \mathcal{H}(t, \vec{p}) |\nu(t, \vec{p})\rangle, \quad (6.19)$$

where $\mathcal{H}(t, \vec{p}) \equiv \Gamma^{\nu\nu}(t, \vec{p})$ (2.103) has been derived in Section 2.2.3. It is given by

$$\mathcal{H}(t, \vec{p}) = U h^0(\vec{p}) U^\dagger + h^{\text{mat}}(t) - \hat{p} \cdot \vec{V}^{\text{mat}}(t) + h^{\text{self}}(t) - \hat{p} \cdot \vec{V}^{\text{self}}(t), \quad (6.20)$$

where the different components h^0 , h^{mat} , \vec{V}^{mat} , h^{self} , and \vec{V}^{self} are explicitly given in Section 2.2.3. Note that this expression assumes that neutrinos are particles of definite momenta, which corresponds to plane waves. For WPs, it is still valid as long as the momentum spread σ_p of a WP is large enough compared to the inverse of the distance over which the matter h^{mat} , \vec{V}^{mat} (2.116, 2.117) and self-interaction h^{self} , \vec{V}^{self} (2.122, 2.123) contributions vary significantly, while being still small enough compared to the momentum p .

In order to study WP separation, it is convenient to introduce the propagation basis, first mentioned in Section 2.3, in which the Hamiltonian (6.20) is diagonal. The Hamiltonian $\mathcal{H}(t, \vec{p})$ can be instantaneously

diagonalized at any time t by the unitary transformation

$$\tilde{U}^\dagger(t, \vec{p}) \mathcal{H}(t, \vec{p}) \tilde{U}(t, \vec{p}) = \tilde{K}(t, \vec{p}), \quad (6.21)$$

where $\tilde{K}(t, \vec{p}) = \text{diag}(\tilde{k}_i(t, \vec{p}))$ is a diagonal matrix of eigenvalues \tilde{k}_i ($i = 1, \dots, n_f$), and $\tilde{U}(t, \vec{p})$ is the instantaneous mixing matrix. At any time t , the flavor neutrino state vector $|\nu_\alpha(\vec{p})\rangle$ can be represented as a linear combination of the propagation eigenstates $|\tilde{\nu}_j(t, \vec{p})\rangle$

$$|\nu_\alpha(\vec{p})\rangle = \sum_j \tilde{U}_{\alpha j}^*(t, \vec{p}) |\tilde{\nu}_j(t, \vec{p})\rangle. \quad (6.22)$$

If the evolution is adiabatic, there are no transitions between the propagation eigenstates $|\tilde{\nu}_j(t, \vec{p})\rangle$ and studying coherence can be done by studying the separation of the different propagation eigenstates WPs.

In the rest of this chapter, we consider the propagation of a neutrino WP, produced as a state of flavor α at the position $\vec{x}_0 = \vec{0}$ and at time $t_0 = 0$, which can be written according to equation (6.22) as

$$|\nu(0, \vec{p})\rangle = |\nu_\alpha(\vec{p})\rangle = \sum_j \tilde{U}_{\alpha j}^*(0, \vec{p}) |\tilde{\nu}_j(0, \vec{p})\rangle. \quad (6.23)$$

We assume that the propagation eigenstates initially describing our flavor state are described by WPs of momentum-space wave functions $f_{\vec{p}_j}(\vec{p})$, where \vec{p}_j is the centroid of the momentum distribution, such that

$$|\tilde{\nu}_j(0, \vec{p})\rangle = f_{\vec{p}_j}(\vec{p}) |\tilde{\nu}_j^{(0)}(0, \vec{p})\rangle. \quad (6.24)$$

Here, $|\tilde{\nu}_j^{(0)}(0, \vec{p})\rangle$ denotes the state vectors of the propagation eigenstates satisfying

$$\langle \tilde{\nu}_j^{(0)}(0, \vec{p}) | \tilde{\nu}_k^{(0)}(0, \vec{p}') \rangle = (2\pi)^3 \delta^3(\vec{p} - \vec{p}') \delta_{jk}, \quad (6.25)$$

and we normalize the amplitudes $f_{\vec{p}_j}(\vec{p})$ so that

$$\int \frac{d^3\vec{p}}{(2\pi)^3} |f_{\vec{p}_j}(\vec{p})|^2 = 1. \quad (6.26)$$

In the rest of this chapter, we describe neutrinos by Gaussian WPs of width σ_p , such that

$$f_{\vec{p}_j}(\vec{p}) = \left(\frac{2\pi}{\sigma_p^2}\right)^{\frac{3}{4}} \exp\left[-\frac{(\vec{p} - \vec{p}_j)^2}{4\sigma_p^2}\right]. \quad (6.27)$$

We introduce the (one-particle) density matrix in the propagation eigenstate basis as

$$\rho(t, \vec{x}) = |\tilde{\nu}(t, \vec{x})\rangle\langle\tilde{\nu}(t, \vec{x})|. \quad (6.28)$$

The formalism derived here will now be used to describe decoherence in vacuum. Note that the same procedure can easily be adapted in the case of the adiabatic evolution of neutrinos in a matter background (see Ref. [160]).

6.3.2 VACUUM OSCILLATIONS IN FLAT SPACE-TIME

In this section, we consider again the propagation in vacuum of a neutrino WP, produced as a flavor state ν_α at the position $\vec{x}_0 = \vec{0}$ and at time $t_0 = 0$. Since there is no matter background, the propagation and mass bases coincide. We start by describing the neutrino state vector and then use the density matrix formalism to study decoherence.

At (t, \vec{x}) , the neutrino state is described by

$$|\nu(t, \vec{x})\rangle = \sum_j U_{\alpha j}^* \psi_j(t, \vec{x}) |\nu_j\rangle. \quad (6.29)$$

In the equation above, $\psi_j(t, \vec{x})$ is the coordinate-space wave function of the j th neutrino mass eigenstate,

$$\psi_j(t, \vec{x}) = \int \frac{d^3\vec{p}}{(2\pi)^3} e^{i\vec{p}\cdot\vec{x}} \psi_j(t, \vec{p}), \quad (6.30)$$

where $\psi_j(t, \vec{p})$ is the time-dependent wave function for a neutrino of given momentum \vec{p} . It is solution of the Schrödinger-like equation (6.19) in vacuum

$$i \frac{d}{dt} \psi_j(t, \vec{p}) = E_j(\vec{p}) \psi_j(t, \vec{p}), \quad (6.31)$$

where $E_j(\vec{p})$ is the energy of the j th neutrino WP, of momentum \vec{p} . Solving this equation is straightforward, and leads to

$$\psi_j(t, \vec{p}) = \psi_j(0, \vec{p}) e^{-iE_j(\vec{p})t} = f_{\vec{p}_j}(\vec{p}) e^{-iE_j(\vec{p})t}, \quad (6.32)$$

where the second equality derives from (6.24). We now use the density matrix formalism to study decoherence. Using the definition (6.28), we introduce the one-neutrino density matrix in the mass basis whose elements are

$$\rho_{jk}(t, \vec{x}) = U_{\alpha j}^* U_{\alpha k} \psi_j(t, \vec{x}) \psi_k^*(t, \vec{x}). \quad (6.33)$$

Assuming that the mass eigenstates are described in momentum space by Gaussian WPs of width σ_p (6.27),

and using equations (6.30) and (6.32), we get for this matrix element

$$\rho_{jk}(t, \vec{x}) = U_{\alpha j}^* U_{\alpha k} \left(\frac{2\pi}{\sigma_p^2} \right)^{\frac{3}{2}} \int \int \frac{d^3 \vec{p}}{(2\pi)^3} \frac{d^3 \vec{q}}{(2\pi)^3} \exp \left[i (\vec{p} - \vec{q}) \cdot \vec{x} - i (E_j(\vec{p}) - E_k(\vec{q})) t - \frac{(\vec{p} - \vec{p}_j)^2}{4\sigma_p^2} - \frac{(\vec{q} - \vec{p}_k)^2}{4\sigma_p^2} \right]. \quad (6.34)$$

In order to calculate the integrals in (6.34), we expand the neutrino energies about the peak momenta \vec{p}_j , and retain only the first two terms of the expansion

$$E_j(\vec{p}) = E_j + (\vec{p} - \vec{p}_j) \cdot \vec{v}_j + \mathcal{O} [(\vec{p} - \vec{p}_j)^2]. \quad (6.35)$$

We introduced here $E_j \equiv E_j(\vec{p}_j)$, and $\vec{v}_j = \frac{\partial E_j}{\partial \vec{p}}|_{\vec{p}=\vec{p}_j}$ the group velocity of the j th WP. Note that neglecting the high order terms in the expansion of $E_j(\vec{p})$ amounts to neglecting the spread of the neutrino WP. Indeed, it has been shown in Ref. [163] that this spread has no effect on the coherence of supernova neutrinos, as the coherence is determined by the original size of the WP without spread.

Expanding E_j and E_k according to (6.35), we find that the integrals in (6.34) can be integrated as Gaussian integrals, and $\rho(t, \vec{x})$ takes the form

$$\rho_{jk}(t, \vec{x}) = U_{\alpha j}^* U_{\alpha k} \frac{1}{(2\pi\sigma_x^2)^{\frac{3}{2}}} \exp \left[-i (E_j - E_k) t + i (\vec{p}_j - \vec{p}_k) \cdot \vec{x} - \frac{(\vec{x} - \vec{v}_j t)^2}{4\sigma_x^2} - \frac{(\vec{x} - \vec{v}_k t)^2}{4\sigma_x^2} \right], \quad (6.36)$$

where we introduced $\sigma_x = \frac{1}{2\sigma_p}$ the size of the neutrino WPs in coordinate space.

In the situations we are interested in, we observe decoherence as a function of the known distance \vec{x} traveled by a neutrino. Therefore, the matrix element (6.36) must be integrated over the unknown time t .²

Since the WP amplitudes decrease very quickly as t grows different from the stationary point of the exponent $t_{\text{stat}} = \frac{\vec{v}_j + \vec{v}_k}{v_j^2 + v_k^2} \cdot \vec{x}$, the integral can be extended over the coordinate to infinity, and we consider the quantity

$$\rho_{jk}(\vec{x}) \equiv \int dt \rho_{jk}(t, \vec{x}). \quad (6.37)$$

²Note that the opposite approach can also be used: we could have considered that we observe neutrino oscillations at a known time, and integrate over the unknown region of space [160]. This leads to the same decoherence term.

Performing the Gaussian integration in (6.36), we get

$$\rho_{jk}(\vec{x}) = U_{\alpha j}^* U_{\alpha k} \frac{1}{2\pi\sigma_x^2} \sqrt{\frac{2}{v_j^2 + v_k^2}} \exp\left[-\frac{(\Delta E_{jk})^2 \sigma_x^2}{v_j^2 + v_k^2}\right] \exp\left[i\left\{(\vec{p}_j - \vec{p}_k) - \frac{2\Delta E_{jk}\vec{v}_g}{v_j^2 + v_k^2}\right\}\vec{x}\right] \exp\left[-\frac{(\vec{v}_j - \vec{v}_k)^2 x^2}{4\sigma_x^2 (v_j^2 + v_k^2)}\right], \quad (6.38)$$

where we introduced the difference of energy $\Delta E_{jk} \equiv E_j - E_k$ and the average group velocity $\vec{v}_g \equiv \frac{1}{2}(\vec{v}_j + \vec{v}_k)$. Note that, at first order, the dependence of \vec{v}_g on j or k can be omitted. The first exponential term in Eq. (6.38) does not depend on \vec{x} and has no influence on oscillations. The second exponential generates neutrino oscillations. Note that it resembles the standard oscillation formula, but with an additional term $\frac{2\Delta E_{jk}\vec{v}_g}{v_j^2 + v_k^2}$. This is because the density matrix in (6.38) is integrated over all its momentum modes. Finally, the last exponential term is a damping term, responsible for decoherence. It sets the conditions on which neutrino oscillations are observable.

Writing this damping term as

$$\exp\left[-\frac{x^2}{L_{\text{coh},jk}^2}\right], \quad (6.39)$$

where $L_{\text{coh},jk}^2$ is the coherence length, that is, the distance over which the j th and k th WPs will cease to overlap, we get the expression

$$L_{\text{coh},jk}^2 = \frac{4(v_j^2 + v_k^2)}{(\vec{v}_j - \vec{v}_k)^2} \sigma_x^2. \quad (6.40)$$

For ultra-relativistic neutrinos, we introduce E the average energy of ν_j and ν_k . Equation (6.40) then becomes

$$L_{\text{coh},jk} = \frac{4\sqrt{2}E^2}{|\Delta m_{jk}^2|} \sigma_x. \quad (6.41)$$

Interestingly, this formula is extremely close to (6.14) obtained through the heuristic derivation of Section 6.2.3. From equation (6.40), it is clear that neutrino decoherence appears from the different group velocities of the j th and k th WPs, making their overlap decrease when they propagate over long distances. Note also that the coherence length depends on the assumed shape of the neutrino WPs.

As pointed out before, the damping in ρ_{jk} for $j \neq k$ corresponds physically to the separation of the WPs of the j th and k th propagation eigenstates. Therefore, we expect this to be modified in the presence of gravity modifying the space-time geometry.

6.4 EVOLUTION EQUATION FOR THE NEUTRINO WP IN CURVED SPACE-TIME

In this section, we make the first steps towards the investigation of decoherence by WP separation in curved space-time through the density matrix formalism, generalizing the procedure described in Section 6.3.

We start by studying the evolution of the neutrino state vector and derive from it the evolution of the density matrix. We then focus on the case of neutrino oscillations in vacuum, considering the case of a strong static gravitational field with a spherical symmetry and without rotation. We have in mind the application to a Schwarzschild black hole, a binary neutron star merger remnants, or the proto-neutron star in a core-collapse supernova. The study is performed in two steps. First, we consider the case of a non-covariant Gaussian WP, then the one of a covariant relativistic Gaussian WP. For the latter, unfortunately, final results have not been obtained due to a lack of time. We conclude with a general discussion.

6.4.1 EVOLUTION OF THE NEUTRINO STATE VECTOR AND COVARIANT PHASE

We consider here a neutrino being produced at the space-time point $A (t_A, \vec{x}_A)$, as a flavor state ν_α ,

$$|\nu(A)\rangle = |\nu_\alpha\rangle = \sum_j U_{\alpha j}^*(A) |\nu_j\rangle, \quad (6.42)$$

and that the mass eigenstates are described at production by Gaussian WPs of width σ_p . We study here the propagation of the different massive WPs from A to an averaged space-time region $C (t_C, \vec{x}_C)$. This assumes that the WPs are not completely separated, so that this region C can be defined (see Fig. 6.3). When propagating between A and C , the mass eigenstate becomes

$$|\nu_j(A, C)\rangle = e^{-i\phi_j(A, C)} |\nu_j\rangle. \quad (6.43)$$

The quantum mechanical phase ϕ_j associated with the propagation of the j th eigenstate in a gravitational field is given by [28]

$$\phi_j(A, C) = \int_A^C p_\mu^{(j)} dx^\mu, \quad (6.44)$$

where $p_\mu^{(j)}$ is the canonical conjugate momentum to the coordinate x^μ for the j th eigenstates. It is given by

$$p_\mu^{(j)} = m_j g_{\mu\nu} \frac{dx^\nu}{ds}, \quad (6.45)$$

with ds the line element along the j th neutrino trajectory, and $g_{\mu\nu}$ is the metric tensor.

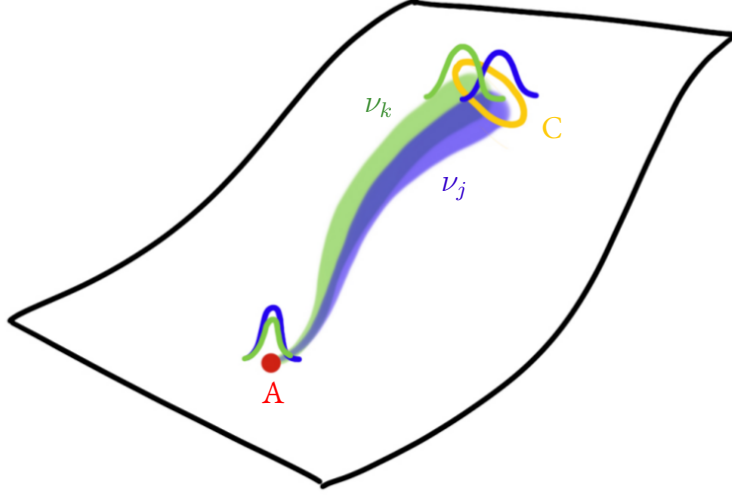


Figure 6.3: The j th (blue) and k th (green) neutrino WPs are produced together at the same point A . As they propagate through space-time, they spread and separate themselves. We study the separation of the WPs in the region C , which is an averaged point on the two trajectories.

6.4.2 VACUUM OSCILLATIONS IN SCHWARZSCHILD METRIC

From now on, we assume that the space-time is described by the Schwarzschild metric and use the specific coordinates $\{t, r, \theta, \varphi\}$ so that the line element ds becomes

$$ds^2 \equiv g_{\mu\nu} dx^\mu dx^\nu = -B(r) dt^2 + \frac{1}{B(r)} dr^2 + r^2 d\theta^2 + r^2 \sin^2 \theta d\varphi^2, \quad (6.46)$$

where $B(r) = 1 - \frac{r_s}{r}$, where $r_s = 2M$ is the Schwarzschild radius, with M the mass of the mass of the object. We follow the procedure of Ref. [153] to describe the neutrino trajectories. As the gravitational field described by Eq. (6.46) is isotropic, the neutrino trajectories can be confined to a plane. We choose to work in the plan $\theta = \frac{\pi}{2}$. The relevant components of $p_\mu^{(j)}$ are then

$$p_t^{(j)} = -m_j B(r) \frac{dt}{ds}, \quad (6.47)$$

$$p_r^{(j)} = \frac{m_j}{B(r)} \frac{dr}{ds}, \quad (6.48)$$

$$p_\varphi^{(j)} = m_j r^2 \frac{d\varphi}{ds}. \quad (6.49)$$

They are all related by the on-shell mass relation $p_\mu^{(j)} p^{(j)\mu} = -m_j^2$. As the metric tensor $g_{\mu\nu}$ does not depend on t and φ , the canonical momentum components $p_t^{(j)}$ and $p_\varphi^{(j)}$ are constant along the neutrino trajectory. We denote those constants as $E_j(\vec{p}) \equiv -p_t^{(j)}$ and $J_j(\vec{p}) = p_\varphi^{(j)}$. They represent respectively the energy and the angular momentum of the mass eigenstate ν_j observed at $r = +\infty$, and depend on the neutrino momentum at production \vec{p} . Note that $E_j(\vec{p})$ and $J_j(\vec{p})$ differ from those measured by an observer at a

position C or at the production point A . The local energy, that is, the energy measured by an observer at rest at a given space-time point, can be related to E_j through a transformation between the two frames. Having defined those constants, we develop $p_\mu^{(j)} dx^\mu$ in (6.44) as

$$p_\mu^{(j)} dx^\mu = -E_j(\vec{p}) dt + \frac{m_j}{B(r)} \left(\frac{dr}{ds} \right) dr + J_j(\vec{p}) d\varphi. \quad (6.50)$$

As done in Ref. [153], it would be interesting to consider the case of radial propagation so that $d\varphi = 0$ as well as of non-radial propagation. We present here the case of radial propagation for which the on-shell mass relation becomes

$$-B(r) \left(\frac{dt}{ds} \right)^2 + \frac{1}{B(r)} \left(\frac{dr}{ds} \right)^2 = -1. \quad (6.51)$$

Using the relation (6.47) along with $p_t^{(j)} = -E_j$, the equation above reads

$$\frac{1}{B(r)} \left(\frac{dr}{ds} \right)^2 = -1 + \frac{E_j^2(\vec{p})}{m_j^2} \frac{1}{B(r)}, \quad (6.52)$$

which, assuming that neutrinos are propagating outwards, gives

$$\frac{dr}{ds} = \sqrt{\frac{E_j^2(\vec{p})}{m_j^2} - B(r)}. \quad (6.53)$$

Combining the equations (6.50) and (6.53), under the assumption of radial propagation, we get

$$p_\mu^{(j)} dx^\mu = -E_j(\vec{p}) dt + \frac{1}{B(r)} \sqrt{E_j^2 - B(r) m_j^2} dr. \quad (6.54)$$

When studying the propagation of neutrinos in curved space-time, most of the literature (see e.g. Refs [155, 153, 156]) calculates the phase differences along light-like trajectories so that $ds^2 = 0$. This gives a relation between dt and dr . Since we want to study the separation of the mass eigenstates WPs, the trajectories need to be slightly different (see Fig. 6.3). As described above, we consider that the WPs in the region C (t_C, \vec{x}_C) are still overlapping a bit, so that we can measure the phases ϕ_j and ϕ_k at C .³ In our derivation, we also assume that neutrinos are relativistic at infinity, that is $\frac{m_j}{E_j} \ll 1$. As pointed out in Ref. [153], this assumption ensures that neutrinos are relativistic everywhere on their trajectory. This is not necessarily the case if neutrinos are assumed to be relativistic at the source. Under this assumption, Eq. (6.54) becomes

$$p_\mu^{(j)} dx^\mu = -E_j(\vec{p}) dt + \frac{1}{B(r)} \left(E_j(\vec{p}) - \frac{m_j^2}{2E_j(\vec{p})} B(r) \right) dr. \quad (6.55)$$

³As discussed in Ref. [153], the use of classical trajectories for the interference of the different massive neutrinos at the same space-time location should account from a difference in the production times. Since we consider neutrinos with very close masses, we follow close-to light-ray trajectories.

Plugging this in Eq. (6.44), we get

$$\phi_j(A, C; \vec{p}) = -E_j(\vec{p})(t_C - t_A) + \int_{r_A}^{r_C} \frac{E_j(\vec{p})}{B(r)} dr - \frac{m_j^2}{2E_j(\vec{p})}(r_C - r_A). \quad (6.56)$$

This expression is also valid for the k th mass eigenstate produced with the momentum \vec{q} . We now define the phase difference $\phi_{kj} = \phi_k - \phi_j$, which reads

$$\phi_{kj}(A, C; \vec{p}, \vec{q}) = (E_j(\vec{p}) - E_k(\vec{q})) \left(t_C - t_A - \int_{r_A}^{r_C} \frac{1}{B(r)} dr \right) + \left(\frac{m_j^2}{2E_j(\vec{p})} - \frac{m_k^2}{2E_k(\vec{q})} \right) (r_C - r_A). \quad (6.57)$$

Following the procedure of Section 6.3, we develop $E_j(\vec{p})$ (respectively $E_k(\vec{q})$) in the phase difference using the first-order expansion (6.35) as a function of \vec{p} (respectively \vec{q}). This gives

$$\begin{aligned} \phi_{kj}(A, C; \vec{p}, \vec{q}) &= (E_j - E_k) \left(t_C - t_A - \int_{r_A}^{r_C} \frac{1}{B(r)} dr \right) + \left(\frac{m_j^2}{2E_j} - \frac{m_k^2}{2E_k} \right) (r_C - r_A) \\ &\quad + \vec{v}_j(\vec{p} - \vec{p}_j) [t_C - t_A - \lambda_j(r_C, r_A)] - \vec{v}_k(\vec{q} - \vec{p}_k) [t_C - t_A - \lambda_k(r_C, r_A)], \end{aligned} \quad (6.58)$$

where we introduced the notation

$$\lambda_j(r_C, r_A) = \frac{m_j^2}{2E_j^2}(r_C - r_A) + \int_{r_A}^{r_C} \frac{1}{B(r)} dr. \quad (6.59)$$

FIRST STEP: A NON-COVRTANT GAUSSIAN WP FORMULATION In our investigation of decoherence in curved space-time, we start by making some considerations by taking a non-covariant Gaussian WP, as done in Refs. [164, 165]. Ref. [164] has shown that the use of a non-covariant Gaussian WP can give quite different results as far as the spread of the WP is concerned, compared to a covariant formulation. Clearly, one should consider the spread of the WP, both at production but also due to propagation. For simplicity, here we make first the assumption that the width of the WP is only due to its spread at production (as done in Refs. [163, 160] in flat space-time). We use the definition of the density matrix for the entire neutrino WPs (6.28), describing mass eigenstates as Gaussian WPs of width σ_p , which, similarly to Eqs. (6.33) and (6.34), gives us in the mass basis

$$\begin{aligned} \rho_{jk}(A, C) &= U_{\alpha j}^* U_{\alpha k} \left(\frac{2\pi}{\sigma_p^2} \right)^{\frac{3}{2}} \\ &\quad \iint \frac{d^3\vec{p}}{(2\pi)^3} \frac{d^3\vec{q}}{(2\pi)^3} \exp \left[-i\phi_{kj}(A, C; \vec{p}, \vec{q}) - \frac{(\vec{p} - \vec{p}_j)^2}{4\sigma_p^2} - \frac{(\vec{q} - \vec{p}_k)^2}{4\sigma_p^2} \right]. \end{aligned} \quad (6.60)$$

Using the first-order expansion in terms of \vec{p} and \vec{q} in ϕ_{kj} , we perform the Gaussian integrals in (6.60) and get for the density matrix the expression

$$\rho_{jk}(A, C) = U_{\alpha j}^* U_{\alpha k} \frac{1}{(2\pi\sigma_x^2)^{\frac{3}{2}}} \exp \left\{ -\sigma_p^2 \left[v_k^2 (t_C - t_A - \lambda_k(r_C, r_A))^2 + v_j^2 (t_C - t_A - \lambda_k(r_C, r_A))^2 \right] \right\} \\ \exp \left\{ -i \left[(E_j - E_k) \left(t_C - t_A - \int_{r_A}^{r_C} \frac{1}{B(r)} dr \right) - \left(\frac{m_j^2}{2E_j} - \frac{m_k^2}{2E_k} \right) (r_A - r_C) \right] \right\}. \quad (6.61)$$

As we did in the case of propagation in flat space-time in Section 6.3, in order to interpret the formula above, we perform the integration over t . Computing the Gaussian integral, we get

$$\rho_{jk}(r_C, r_A) \equiv \int dt_C \rho_{jk}(A, C) = U_{\alpha j}^* U_{\alpha k} \frac{1}{2\pi\sigma_x^2} \sqrt{\frac{2}{v_j^2 + v_k^2}} \exp \left[-\frac{(E_j - E_k)^2 \sigma_x^2}{v_j^2 + v_k^2} \right] \\ \exp \left\{ i (r_C - r_A) \left[\left(\frac{m_j^2}{2E_j} - \frac{m_k^2}{2E_k} \right) - \frac{E_j - E_k}{v_j^2 + v_k^2} \left(v_k^2 \frac{m_k^2}{2E_k^2} + v_j^2 \frac{m_j^2}{2E_j^2} \right) \right] \right\} \\ \exp \left\{ -\frac{v_j^2 v_k^2}{4\sigma_x^2 (v_k^2 + v_j^2)} (r_C - r_A)^2 \left[\frac{m_k^2}{2E_k^2} - \frac{m_j^2}{2E_j^2} \right]^2 \right\}. \quad (6.62)$$

Once again, the first exponential term in Eq. (6.62) does not depend on $(r_C - r_A)$ and has no influence on neutrino propagation. The second exponential term generates neutrino oscillations. Note that it has the same form as in flat space time ; however, in the Schwarzschild metric, $(r_C - r_A)$ does not represent a physical distance, so the oscillation length is actually modified by the presence of gravity.

The last exponential term is a damping term, responsible for decoherence. For relativistic neutrinos, introducing E the mean energy of ν_j and ν_k , this damping term becomes, at first order in $\frac{m_j}{E}$

$$\exp \left\{ -\frac{v_j^2 v_k^2}{4\sigma_x^2 (v_k^2 + v_j^2)} (r_C - r_A)^2 \left[\frac{m_k^2}{2E_k^2} - \frac{m_j^2}{2E_j^2} \right]^2 \right\} = \exp \left\{ -\frac{(r_C - r_A)^2}{8\sigma_x^2} \left[\frac{\Delta m_{jk}^2}{2E^2} \right]^2 \right\}. \quad (6.63)$$

Note that in the flat space-time limit, $(r_C - r_A)$ becomes the physical distance traveled by neutrinos and this term gives back the damping term of Eq. (6.38). However, if r_s is non-null, the coherence length does not immediately appear in the damping term above as $(r_C - r_A)$ does not represent a physical distance. Furthermore, E does not represent the local energy of the neutrinos but rather the energy at infinity.

We introduce the differential proper distance $d\ell \equiv \sqrt{g_{\mu\nu}} dx^\mu dx^\nu$, which becomes in the case of radial propagation in the Schwarzschild metric

$$d\ell = \frac{1}{\sqrt{B(r)}} dr. \quad (6.64)$$

We define r_{coh} the value of the coordinate r_C after which the damping term (6.63) is equal to $1/e$. It is

therefore given by

$$r_{\text{coh}} = r_A + 2\sqrt{2}\sigma_x \frac{2E^2}{|\Delta m_{kj}^2|}. \quad (6.65)$$

Using the definition of the proper distance (6.64), we then get for the coherence length

$$L_{\text{coh}} = \int_{r_A}^{r_{\text{coh}}} \frac{1}{\sqrt{B(r)}} dr = \int_{r_A}^{r_A + 2\sqrt{2}\sigma_x \frac{2E^2}{|\Delta m_{kj}^2|}} \frac{1}{\sqrt{B(r)}} dr. \quad (6.66)$$

Note that this result is quite different from the expression obtained using (unjustified) heuristic arguments in Eq. (6.17). It is also apparent, comparing Eqs. (6.41) and (6.66), that the proper coherent length is increased in the presence of a gravitational field.

In order to assess the effects of gravity on the coherence length, we show here some numerical estimates. We compare the coherence length in flat space-time (6.41) for the mass eigenstates ν_1 and ν_3

$$L_{\text{coh}}^{\text{flat}} = \frac{4\sqrt{2}E^2}{|\Delta m_{13}^2|} \sigma_x, \quad (6.67)$$

to the coherence length in curved space-time (6.66) for the mass eigenstates ν_1 and ν_3

$$L_{\text{coh}}^{\text{curved}} = \int_{r_A}^{r_A + \frac{4\sqrt{2}E^2}{|\Delta m_{13}^2|} \sigma_x} \frac{1}{\sqrt{B(r)}} dr, \quad (6.68)$$

where we use the estimate of $\sigma_x \approx 4 \times 10^{-12}$ cm of Section 6.2.2.

We make an estimate here for the cooling phase of a core-collapse supernova. We assume that neutrinos are emitted at a neutrinosphere of radius $R_\nu \approx 10$ km, with an energy of about $E = 11$ MeV. We consider values for the Schwarzschild mass between $0.8M_\odot$ and $2.5M_\odot$. The coherence length estimates as well as their relative difference are shown in Fig. 6.4 as a function of the Schwarzschild mass.

We notice first that, with the parameters used here, the coherence length for ν_1 and ν_3 is of the order of tens of kilometers. This corresponds to the scale on which effects such as bipolar oscillations in supernovae or matter-neutrino resonance in binary neutron star merger remnants. If the coherence length remains of the same order of magnitude in the presence of matter and self-interaction, the decoherence could take place before those oscillation phenomena and destroy the interference patterns. Note however that partial coherence would be maintained as the coherence length for ν_1 and ν_2 is approximately 100 times longer.

Second, we notice that, as pointed out before, the coherence length is increased by the presence of gravity. This is analogous to the results of e.g. Ref. [156], where they find that gravitational fields shift the occurrence of oscillations phenomena to further distances. Furthermore, the relative difference between the values of

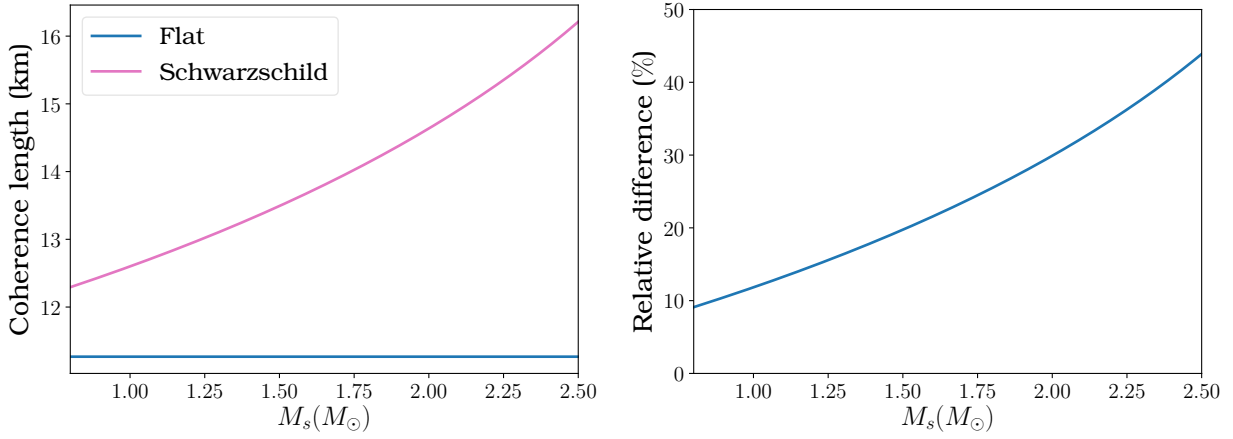


Figure 6.4: Numerical estimates of the coherence lengths in flat (6.67) (dashed, orange line) and curved (6.68) (solid, blue line) space-time (left panel), as well as the relative difference between the two (right panel), as a function of the Schwarzschild mass M_s .

the coherence length in flat or in curved space-time can go up to 40% for $M_s = 2.5M_\odot$, which is a significant effect.

SECOND STEP: A COVARIANT GAUSSIAN WP FORMULATION The second step in our procedure is to implement a covariant Gaussian WP, as the ones discussed in Refs. [164, 165]. It is also worth noting that, while Ref. [163] showed that the spread of the neutrino WPs during their propagation had no impact on the coherence condition in flat space-time, this has not been shown in curved space-time.

It would also have been interesting to consider the case of non-radial propagation. These aspects have not been completed unfortunately because of a lack of time.

6.5 DISCUSSIONS AND CONCLUSIONS

In this chapter, we have studied neutrino propagation and decoherence by WP separation in the presence of gravitational fields. In particular, we have introduced the density matrix of a neutrino as a whole (that is, including the integration over all its momentum modes) to describe decoherence as a damping term.

Decoherence occurs when the distance between the different propagation eigenstate WPs becomes larger than the size of the WPs. Therefore, we have estimated the length of neutrino WPs in environments such as supernovae or binary neutron star mergers and showed that it is of the order of 10^{-12} cm. Then, we used the density matrix approach of Ref. [160] to show that decoherence is characterized by a damping term in the off-diagonal elements of the neutrino density matrix in the propagation basis.

We adapted this procedure to the case of neutrino propagation in vacuum in the presence of gravitational fields and showed that this damping term is modified. We observed that the coherence length is increased in curved space-time. These are the first steps towards a WP description of neutrino propagation in curved space-time. We have first discussed the case of a non-covariant Gaussian WP and obtained a coherence length

formula for which numerical estimates have been given. We also discussed the use of a covariant Gaussian WP.

In order to fully assess decoherence effects in astrophysical environments, a calculation including neutrino-matter and neutrino self-interactions effects would be needed as well. The authors of Ref. [160] included these effects. They showed that if neutrino transformations were adiabatic, a damping term still appeared in the density matrix expressed in the propagation basis, showing that decoherence still occurs. They also considered two specific models of adiabaticity violation and showed that no such term appears in general. This is because, in the case of non-adiabatic conversions, the propagation eigenstates are not physically meaningful as they are strongly mixed. As of now, these results have not been extended to the propagation of neutrinos in the presence of strong gravitational fields. However, in the adiabatic case, the procedure should be fairly similar. The work presented here provides with a first step in the description of neutrino WPs in curved space-time.

7

Conclusions

The present thesis has focused on neutrino flavor conversions in dense astrophysical environments. In particular, novel aspects have been explored in the context of binary neutron star mergers, including helicity coherence and nonstandard interactions, and more generally neutrino decoherence in presence of strong gravitational fields.

A sharp boundary between the dense, collision-dominated and the dilute, mean-field-treated regions is often used both in core-collapse supernovae and accretion disk around compact mergers. The role of corrections to the mean-field equations usually employed when studying neutrino propagation in astrophysical environments has been debated in the last years. In the dilute region, such corrections could have an impact on neutrino flavor evolution.

In our first project, we have tested the validity of the mean-field equations and explored, in particular, the role of correlators, arising from the first order corrections to the relativistic approximation that couple left- to right-handed neutrinos in the Dirac case, and neutrinos to antineutrinos in the Majorana case. This coupling is referred to in the literature as helicity (or spin) coherence. We have chosen to explore their role in the context of binary neutron star merger remnants, but the results we have obtained allow to draw conclusions for the supernova case as well.

We have explored numerically a large range of trajectories and parameters, based on a detailed astrophysical simulation of a binary neutron star merger remnant. We have found that while a MSW-like resonance condition associated with helicity coherence is met in the context of binary neutron star merger remnants, its adiabaticity is never enough to create conversions. This is in contraction with previous claims in a one

flavor toy model. We have used a perturbative analysis to understand the conditions under which multiple MSW-like resonances can occur through the so-called nonlinear feedback. Such an analysis not only explains our results but also shows that they would remain valid in core-collapse supernovae. This study has shown that, in a realistic astrophysical scenario, helicity coherence is unlikely to produce flavor conversions, making the usually-employed mean-field equations reliable.

Our results have been derived under several approximations. First of all, the self-interaction term in the Hamiltonian is computed under the assumption that the flavor history of a neutrino at a given point in space does not depend on its emission point. This boils down to considering that the flavor content of the background neutrinos at a given location is the same as the flavor content of the test neutrino, and is usually referred to as the "single-trajectory" approximation. As the existence of nonlinear feedback relies on the geometry of neutrino emission, using a full multi-angle treatment might change our results. However, as such treatments usually lead to matter decoherence, it is unlikely that it would favor helicity-coherence-induced conversions. Moreover, we used a two-neutrino mixing framework. The inclusion of a third flavor should not change our conclusions since the matching condition between the self-interaction and the matter potentials, necessary to increase the adiabaticity, should not be affected. Finally, the stationary hypothesis has been employed. Its relaxation may have some effects on our results.

The presence of new physics beyond the standard model could influence neutrino flavor conversions and, in particular, explain some anomalies observed in oscillation experiments. So far, the experimental constraints on nonstandard matter-neutrino interactions are still rather loose, in particular for the $e - \tau$ coupling. While the recent observation of coherent elastic neutrino-nucleus scattering did not tighten these limits, it may bring more information in the future.

In the second project of this thesis, we have focused on the role of such nonstandard interactions in the context of binary neutron star merger remnants, performing numerical simulations. We have found that the inner resonance — a MSW resonance observed in the presence of nonstandard interactions in supernovae — can be met and have an interesting interplay with the matter-neutrino resonance. Interestingly, such effects occur even in the case of very small off-diagonal coupling ϵ_0 — up to four or five order of magnitudes lower than the experimental bounds —, as long as the diagonal coupling is not too small. Furthermore, we have shed a new light on the inner resonance by showing that its condition can still be met in the presence of sizable self-interaction potentials, and occur as a synchronized MSW resonance. Several examples have been presented and analyzed in details in terms of flavor conversion mechanisms. Our results have shown that, in the presence of nonstandard interactions, strong flavor conversions can occur very close to the central object. Therefore, they could have a substantial effect on r process nucleosynthesis in neutrino-driven winds.

As in the first project, the results derived in presence of nonstandard interactions are based on the "single-trajectory" approximation. However, the condition for having an inner resonance in the presence of non-

standard interactions depend only on the matter profile. Therefore, relaxing this approximation has no effect on its location. While in the case of a synchronized inner resonance the adiabaticity could be affected, it remains unchanged for a "standard" inner resonance. Similarly, using a three-neutrino framework should not impact this resonance. In fact, the two-neutrino framework is well-justified as the nonstandard parameters coupling $e - \mu$ and $\mu - \tau$ are much smaller than the $e - \tau$ ones. Adopting a full-nonstationary model could, however, have significant effects on flavor conversions.

As in supernovae or binary neutron star mergers, neutrinos are produced at large densities, they are described by very short wave packets in configuration space. As the wave packets of the different propagation eigenstates propagate with different group velocities, the very short neutrino wave packets are expected to quickly separate in space, leading to a suppression of neutrino oscillations by decoherence.

In the third project of this thesis, we have studied decoherence by wave-packet separation. We have estimated the size of neutrino wave packets produced in supernovae or binary neutrino star mergers. Then, we used the density matrix formalism to show that decoherence appears as a damping term in the equations of motion. This approach can be extended to the case of propagation in a matter and neutrino background. We have also discussed the effects of strong gravitational fields on wave-packet separation. However, a fully covariant derivation is needed in order to obtain an analytic formula for the coherence length.

Identifying the sites for heavy elements nucleosynthesis through the so-called r process is a longstanding open question in astrophysics. The recent kilonova observation in coincidence with gravitational waves has brought the first direct evidence for the production of heavy elements in binary neutron star mergers. Neutrinos may have an effect on such a production in the so-called neutrino-driven winds in these sites, as for core-collapse supernovae. Unraveling fully flavor conversions in this context could, therefore, bring a new understanding of this open issue.

The results of this thesis shed a new light on neutrino flavor conversions in dense astrophysical environments in three different aspects. First, our analysis of helicity coherence strengthens the mean-field equations generally used in these contexts. Furthermore, our investigations of nonstandard interactions show that the presence of new physics could impact on neutrino flavor evolution in binary neutron star merger remnants, as well as on nucleosynthesis. Finally, understanding decoherence by wave-packet separation in curved space-time is a crucial point, as, if it occurs over short distances, it could suppress extensively-investigated oscillation phenomena. Our work provides with the first steps towards such an understanding which could have significant theoretical and observational implications.



Spinor products

We compute here the spinor products necessary to the derivation of the most general equations for neutrinos (Section 2.2.1). The Dirac bispinors $u(\vec{q}, \sigma)$ and $v(\vec{q}, \sigma)$, which are solutions of the equations $(i\not{p} + m_i) u_i(\vec{q}, \sigma) = (-i\not{p} + m_i) v_i(\vec{q}, \sigma) = 0$, have expressions that depends on the representation chosen for the gamma matrices. We choose a specific representation in order to derive the spinor products which are useful for our calculations.

For any vector \vec{p} of norm p , $\hat{p} \equiv \frac{\vec{p}}{p}$ denotes the unitary vector associated to the direction of \vec{p} . We introduce the two following light-like vectors

$$n^\mu(\hat{p}) = \begin{pmatrix} 1 \\ \hat{p} \end{pmatrix}, \quad \epsilon^\mu(\hat{p}) = \begin{pmatrix} 0 \\ \vec{\epsilon}(\hat{p}) \end{pmatrix}, \quad (\text{A.1})$$

where $(\vec{\epsilon}(\hat{p}), \vec{\epsilon}^*(\hat{p}))$ spans the plane orthogonal to \vec{p} . Then, it is possible to show the following expressions

of the spinors associated with the massive neutrino fields

$$\bar{u}_j(\vec{q}, h) \gamma^\mu (1 - \gamma_5) u_i(\vec{q}, h) = \bar{v}_j(\vec{q}, -h) \gamma^\mu (1 - \gamma_5) v_i(\vec{q}, -h) \quad (\text{A.2})$$

$$= -2i\delta_{h,-} n^\mu(\hat{p}), \quad (\text{A.3})$$

$$\bar{u}_j(\vec{q}, -h) \gamma^\mu (1 - \gamma_5) u_i(\vec{q}, h) = -\bar{v}_j(\vec{q}, h) \gamma^\mu (1 - \gamma_5) v_i(\vec{q}, -h) \quad (\text{A.4})$$

$$= i\frac{m_i}{p}\delta_{h,+}e^{i\phi}\epsilon^\mu(\hat{p}) + i\frac{m_j}{p}\delta_{h,-}e^{-i\phi}\epsilon^\mu(\hat{p}), \quad (\text{A.5})$$

$$\bar{v}_j(-\vec{p}, h) \gamma^\mu (1 - \gamma_5) u_i(\vec{q}, h) = i\frac{m_i}{p}\delta_{h,+}e^{i\phi}n^\mu(-\hat{p}) + i\frac{m_j}{p}\delta_{h,-}e^{-i\phi}n^\mu(\hat{p}) \quad (\text{A.6})$$

$$\bar{v}_j(-\vec{p}, -h) \gamma^\mu (1 - \gamma_5) u_i(\vec{q}, h) = -2i\delta_{h,-}\epsilon^\mu(\hat{p}), \quad (\text{A.7})$$

$$\bar{v}_j(\vec{q}, h) \gamma^\mu (1 - \gamma_5) v_i(\vec{p}, h') = hh'\bar{u}_j(\vec{q}, -h) \gamma^\mu (1 - \gamma_5) u_i(\vec{p}, -h'), \quad (\text{A.8})$$

$$\bar{u}_j(\vec{q}, h) \gamma^\mu (1 - \gamma_5) v_i(-\vec{p}, h') = -(\bar{v}_i(-\vec{p}, h') \gamma^\mu (1 - \gamma_5) u_j(\vec{q}, h))^*. \quad (\text{A.9})$$

B

Extended evolution equations with mass contributions : Dirac case

In the investigation of helicity coherence, we have considered both the case of Majorana neutrino and of Dirac neutrinos. In the case neutrinos are Dirac particles, one has to evolve two extended equations including the mass contributions, namely

$$i\dot{\rho}_{D,\mathcal{G}}(t, \vec{q}) = [h_{D,\mathcal{G}}(t, \vec{q}), \rho_{D,\mathcal{G}}(t, \vec{q})], \quad (\text{B.1})$$

and

$$i\dot{\bar{\rho}}_{D,\mathcal{G}}(t, \vec{q}) = [\bar{h}_{D,\mathcal{G}}(t, \vec{q}), \bar{\rho}_{D,\mathcal{G}}(t, \vec{q})]. \quad (\text{B.2})$$

The explicit expressions of the generalised Hamiltonian in Eq.(4.1) is

$$h_{D,\mathcal{G}}(t, \vec{q}) \equiv \begin{pmatrix} H(t, \vec{q}) & \tilde{\Phi}(t, \vec{q}) \\ \tilde{\Phi}^\dagger(t, \vec{q}) & \tilde{H}(t, \vec{q}) \end{pmatrix}, \quad (\text{B.3})$$

while the generalized density is given by

$$\rho_{D,\mathcal{G}}(t, \vec{q}) \equiv \begin{pmatrix} \rho_{--}(t, \vec{q}) & \rho_{-+}(t, \vec{q}) \\ \rho_{+-}(t, \vec{q}) & \rho_{++}(t, \vec{q}) \end{pmatrix} \equiv \begin{pmatrix} \rho(t, \vec{q}) & \zeta(t, \vec{q}) \\ \zeta^\dagger(t, \vec{q}) & \tilde{\rho}(t, \vec{q}) \end{pmatrix}, \quad (\text{B.4})$$

where the subscripts in the density matrix $\rho_{--}, \rho_{-+}, \rho_{++}$ indicate the possible helicity states. In particular, the correlator ρ_{++} refers to a sterile state and the ρ_{-+} couples neutrinos to such sterile component.

For the antineutrino sector, the generalized density is given by

$$\bar{\rho}_{D,G}(t, \vec{q}) \equiv \begin{pmatrix} \bar{\rho}_{--}(t, \vec{q}) & \bar{\rho}_{-+}(t, \vec{q}) \\ \bar{\rho}_{+-}(t, \vec{q}) & \bar{\rho}_{++}(t, \vec{q}) \end{pmatrix} \equiv \begin{pmatrix} \tilde{\bar{\rho}}(t, \vec{q}) & \bar{\zeta}^\dagger(t, \vec{q}) \\ \bar{\zeta}(t, \vec{q}) & \bar{\rho}(t, \vec{q}) \end{pmatrix}, \quad (\text{B.5})$$

with $\bar{\rho}_{++}$ the usual density matrix for antineutrinos, $\bar{\rho}_{--}$ corresponding to a sterile state and $\bar{\rho}_{-+}$ that couples the sterile with active antineutrino states. The generalized Hamiltonian in the antineutrino sector reads

$$\bar{h}_{D,G}(t, \vec{q}) \equiv \begin{pmatrix} \tilde{\bar{H}}(t, \vec{q}) & \bar{\Phi}^\dagger(t, \vec{q}) \\ \bar{\Phi}(t, \vec{q}) & \bar{H}(t, \vec{q}) \end{pmatrix}, \quad (\text{B.6})$$

In the Hamiltonian expressions (B.3) and (B.6), the off-diagonal terms couple the neutrinos or antineutrinos with sterile components, as in presence of magnetic fields [166].

Therefore one gets for the component of $h_{D,G}(t)$ Eq.(B.3) the following expressions, by retaining contributions up to order $\mathcal{O}(m/q)$ from the neutrino mass in the interaction terms

$$H(t, \vec{q}) = S(t, q) - \hat{q} \cdot \vec{V}(t) - \hat{q} \cdot \vec{V}_m(t), \quad (\text{B.7})$$

$$\tilde{\Phi}(t, \vec{q}) = e^{i\phi_q} \hat{e}_q^* \cdot \vec{V}(t) \frac{m}{2q}, \quad (\text{B.8})$$

$$\tilde{H}(t, \vec{q}) = h_0(q), \quad (\text{B.9})$$

and for $\bar{\rho}_{D,G}(t)$ Eq.(B.6)

$$\bar{H}(t, \vec{q}) = \bar{S}(t, q) - \hat{q} \cdot \vec{V}(t) - \hat{q} \cdot \vec{V}_m(t), \quad (\text{B.10})$$

$$\bar{\Phi}(t, \vec{q}) = e^{i\phi_q} \hat{e}_q \cdot \vec{V}(t) \frac{m}{2q}, \quad (\text{B.11})$$

$$\tilde{\bar{H}}(t, \vec{q}) = -h_0(q), \quad (\text{B.12})$$

The quantities $S(t, q)$, $\bar{S}(t, q)$ and $\vec{V}(t)$ are defined in Eqs. (4.6), (4.7), and (4.13) respectively. The mass correction to the vector component of the self-interaction Hamiltonian reads

$$\begin{aligned} \vec{V}_m(t) = & -\sqrt{2}G_F \int \frac{d^3p}{(2\pi)^3} \left\{ e^{-i\phi_p} \hat{e}_p \Omega(t, \vec{p}) \frac{m}{2p} + \text{h.c.} \right\} \\ & - \sqrt{2}G_F \text{tr} \int \frac{d^3p}{(2\pi)^3} \left\{ e^{-i\phi_p} \hat{e}_p \Omega(t, \vec{p}) \frac{m}{2p} + \text{h.c.} \right\}, \end{aligned} \quad (\text{B.13})$$

which gives an extra contribution to the diagonal part of the generalized Hamiltonians.



Geometric factor in the context of binary neutron star merger remnants

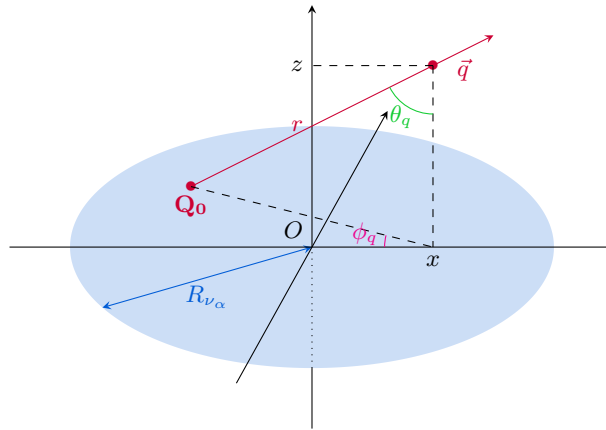


Figure C.1: Side view of the accretion disk, with the central object located at the center. The radius of the disk is flavor dependent and is denoted R_{ν_α} . A neutrino is emitted near the disk at the point \mathbf{Q}_0 , and then leaves it with a momentum \hat{q} located by its spherical coordinates (q, θ_q, ϕ_q) . The coordinate r is the distance between the location of the neutrino at time t and its emission point, with the corresponding cartesian coordinates $(x, 0, z)$.

We compute the geometric factor that is involved in [17, 18]

$$h_{\nu\nu}^\perp(r, q, \ell_q) = \sqrt{2}G_F \sum_\alpha \int_0^\infty dp \left\{ \int_{\Omega_{\nu_\alpha}} (\hat{\epsilon}^*(\hat{q}) \cdot \hat{p}) \rho_{\nu_\alpha}(r, p, \ell_p) dn_{\nu_\alpha} - \int_{\Omega_{\bar{\nu}_\alpha}} (\hat{\epsilon}^*(\hat{q}) \cdot \hat{p}) \bar{\rho}_{\bar{\nu}_\alpha}(r, p, \ell_p) dn_{\bar{\nu}_\alpha} \right\}, \quad (\text{C.1})$$

where \hat{q} is the vector of the propagating neutrino, with coordinates (θ_q, ϕ_q) , $\hat{\epsilon}(\hat{q})$ is the unitary vector in-

roduced in Eq.(4.21), dn_{ν_α} denotes the differential neutrino number density. In the spherical coordinates introduced before, $\hat{\epsilon}(\hat{q})$ reads

$$\epsilon(\hat{q}) = \hat{q}_\theta - i\hat{q}_\phi = \begin{pmatrix} \cos \phi_q \cos \theta_q + i \sin \theta_q \\ \sin \theta_q \cos \theta_q - i \cos \phi_q \\ -\sin \theta_q \end{pmatrix}, \quad (\text{C.2})$$

hence,

$$\begin{aligned} \epsilon^*(\hat{q}) \cdot \hat{p} &= (\cos \phi_q \cos \theta_q - i \sin \theta_q) \sin \theta_p \cos \phi_p \\ &\quad + (\sin \theta_q \cos \theta_q + i \cos \phi_q) \sin \theta_p \sin \phi_p - \sin \theta_q \cos \theta_p. \end{aligned} \quad (\text{C.3})$$

With the approximation given by Eq.(4.35) for the density matrix, the angular integral that needs to be performed is reduced and becomes

$$G_{\nu_\alpha}^\perp(r, \ell_q) = \int_{\Omega_{\nu_\alpha}} (\hat{\epsilon}^*(\hat{q}) \cdot \hat{p}) d\phi_p d\cos \theta_p. \quad (\text{C.4})$$

The procedure to perform the angular integral Eq.(C.4) is analogous to the case of the geometrical factor appearing in the usual self-interaction Hamiltonian Eq.(4.34) (see Refs.[82, 84, 86]).

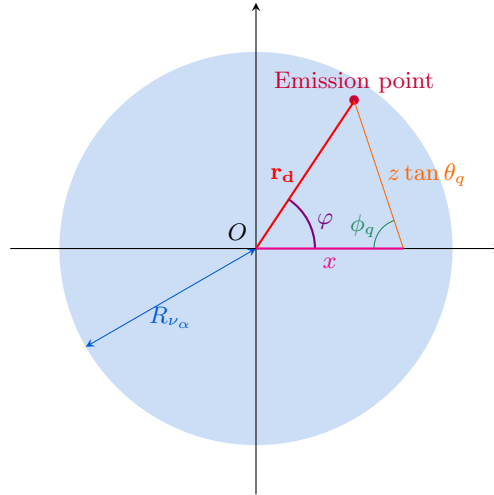


Figure C.2: Bird's eye view of the accretion disk. The emission point of the neutrino is located by its polar coordinates (r_d, φ) .

Following Ref.[137], we express the variables (θ_p, ϕ_p) as functions of the polar coordinates of the emission point on the disk, (r_d, φ) (Figure C.2). The following relations

$$\tan \theta_p = \frac{1}{z} \sqrt{x^2 + r_d^2 - 2xr_d \cos \varphi}, \quad (\text{C.5})$$

$$\cos \phi_p = \frac{x - r_d \cos \varphi}{\sqrt{x^2 + r_d^2 - 2xr_d \cos \varphi}}, \quad (\text{C.6})$$

with $x = x_0 + r \sin \theta_q$ and $z = z_0 + r \cos \theta_q$, enable to compute the Jacobian of the transformation, leading to

$$\int_{\Omega_{\nu_\alpha}} d\phi_p d \cos \theta_p = \int_0^{R_{\nu_\alpha}} dr_d \int_0^{2\pi} d\varphi \frac{r_d z}{(x^2 + z^2 + r_d^2 - 2xr_d \cos \varphi)^{3/2}}. \quad (\text{C.7})$$

Let us define $\Gamma^\perp(r_d, r, \ell_q)$ such that

$$G_{\nu_\alpha}^\perp(r, \ell_q) = \int_0^{R_{\nu_\alpha}} dr_d (r_d z) \Gamma^\perp(r_d, r, \ell_q). \quad (\text{C.8})$$

Then, using (C.3) and (C.7), the angular integration over φ can be performed and leads to :

$$\Gamma^\perp(r_d, r, \ell_q) = \frac{\pi}{(ml)^{3/2}} \left\{ (m+l) [x (\cos \phi_q \cos \theta_q - i \sin \phi_q) - z \sin \theta_q] - 4xr_d^2 (\cos \phi_q \cos \theta_q - i \sin \phi_q) \right\}, \quad (\text{C.9})$$

where $m = (x + r_d)^2 + z^2$ and $l = (x - r_d)^2 + z^2$. Note that the integrals performed here are the same as the ones in the case of the usual self-interaction term Eq.(4.37), but weighted differently. In the case of $\phi_q = 0$, Γ^\perp is reduced to

$$\Gamma^\perp(r_d, r, \ell_q) = \frac{\pi}{(ml)^{3/2}} [(m+l)(x \cos \theta_q - z \sin \theta_q) - 4xr_d^2 \cos \theta_q]. \quad (\text{C.10})$$

As for the geometrical factor along the neutrino direction of motion, one has

$$G_{\nu_\alpha}(r, \ell_q) = \int_0^{R_{\nu_\alpha}} dr_d (r_d z) \Gamma(r_d, r, \ell_q). \quad (\text{C.11})$$

where we define $\Gamma(r_d, r, \ell_q)$ similarly to Γ^\perp . It also involves angular integrals, with different weights as in the case of the perpendicular term

$$\Gamma(r_d, r, \ell_q) = \int_0^{2\pi} d\varphi [1 - \sin \theta_q \sin \theta_p (\cos \phi_q \cos \phi_p + \sin \phi_q \sin \phi_p) - \cos \theta_q \cos \theta_p] \times \frac{1}{(x^2 + z^2 + r_d^2 - 2xr_d \cos \varphi)^{3/2}}, \quad (\text{C.12})$$

where the angles θ_p and ϕ_p must be expressed as functions of (r_q, φ) . The explicit φ -integration in (C.12)

yields, for $\phi_q = 0$

$$\Gamma(r_d, r, \ell_q) = \frac{4}{l\sqrt{m}} E\left(\sqrt{\frac{m-l}{m}}\right) - \frac{\pi}{(ml)^{3/2}} [(m+l)(z \cos \theta_q + x \sin \theta_q) - 4xr_d^2 \sin \theta_q], \quad (\text{C.13})$$

where the relation $m - l = 4xr_d$ has been used, with m and l defined previously, and $E(k)$ denotes Legendre's complete elliptic integral of the second kind

$$E(k) \equiv \int_0^{\pi/2} d\theta \sqrt{1 - k^2 \sin^2 \theta}, \quad (\text{C.14})$$

where we have extended the usual definition domain from $k \in [0, 1]$ to $k \in [0, 1] \cap i\mathbb{R}$. Note that $-\Gamma/2$ with the replacement $\phi_q \mapsto \pi - \phi_q$ corresponds to the geometric factor C given in [82]. Note also the different convention used to denote the elliptic integral.

D

Adiabaticity

We remind that in the $SU(2)$ isospin formalism the equations of motion are replaced by precession equations where an effective magnetic field is built from the Hamiltonian. In the two flavor case it is given by

$$\vec{B} = \begin{pmatrix} 2 \operatorname{Re}(H_{ex}) \\ -2 \operatorname{Im}(H_{ex}) \\ H_{ee} - H_{xx} \end{pmatrix}, \quad (\text{D.1})$$

and the effective isospins are constructed from the density matrices

$$\vec{P} = \frac{1}{2} \begin{pmatrix} 2 \operatorname{Re}(\rho_{ex}) \\ -2 \operatorname{Im}(\rho_{ex}) \\ \rho_{ee} - \rho_{xx} \end{pmatrix}, \quad (\text{D.2})$$

The third component of the isospin vectors gives information on the flavor content, while the x - and y -components of the isospins contain the mixings.

In our analysis of mass effects, we consider that at the helicity coherence resonance, flavor conversions are frozen, which is well justified when MNR and the helicity coherence resonances are separated or the MNR is ineffective. Hence, the system is effectively reduced to 2×2 corresponding to electron neutrinos and electron antineutrinos. We can then define the effective magnetic field as a function of the elements of the

generalized Hamiltonian (4.3), such that

$$\vec{B}_m = \begin{pmatrix} 2 \operatorname{Re}(h_{\mathcal{G},13}) \\ -2 \operatorname{Im}(h_{\mathcal{G},13}) \\ h_{\mathcal{G},11} - h_{\mathcal{G},33} \end{pmatrix}, \quad (\text{D.3})$$

and the effective isospin

$$\vec{P}_m = \frac{1}{2} \begin{pmatrix} 2 \operatorname{Re}(\rho_{ee}^{-+}) \\ -2 \operatorname{Im}(\rho_{ee}^{-+}) \\ \rho_{ee}^{--} - \rho_{ee}^{++} \end{pmatrix}. \quad (\text{D.4})$$

Within this formalism, the MSW resonance condition corresponds to the third component of the magnetic field being zero while the evolution is adiabatic if the precession of the isospins is fast compared to the rate of change of the magnetic field. In this case, the isospins manage to approximately stay aligned with the effective magnetic fields, so that the cosine of the angle between the total isospin and the magnetic fields remains similar before and after the resonance. Another way of quantifying adiabaticity of the evolution is through the gamma factor

$$\gamma = \frac{|\vec{B}|^3}{\left| \frac{d\vec{B}}{dt} \times \vec{B} \right|}. \quad (\text{D.5})$$

where \vec{B} stands for \vec{B} (D.1) or \vec{B}_m (D.3) in our notations. If $\gamma \gg 1$ evolution is adiabatic.

References

- [1] C. L. Cowan, F. Reines, F. B. Harrison, H. W. Kruse, and A. D. McGuire, “Detection of the Free Neutrino: a Confirmation,” *Science*, vol. 124, no. 3212, p. 103, 1956.
- [2] R. Davis, D. S. Harmer, and K. C. Hoffman, “Search for Neutrinos from the Sun,” *Physical Review Letters*, vol. 20, no. 21, p. 1205, 1968.
- [3] Y. *et al.* Fukuda, “Evidence for oscillation of atmospheric neutrinos,” *Phys. Rev. Lett.*, vol. 81, p. 1562, 1998.
- [4] B. Pontecorvo, “Mesonium and anti-mesonium,” *Sov. Phys. JETP*, vol. 6, p. 429, 1957.
- [5] Z. Maki, M. Nakagawa, and S. Sakata, “Remarks on the unified model of elementary particles,” *Prog. Theor. Phys.*, vol. 28, p. 870, 1962.
- [6] V. Gribov and B. Pontecorvo, “Neutrino astronomy and lepton charge,” *Physics Letters B*, vol. 28, no. 7, p. 493, 1969.
- [7] Q. R. Ahmad, *et al.*, “Direct evidence for neutrino flavor transformation from neutral current interactions in the Sudbury Neutrino Observatory,” *Phys.Rev.Lett.*, vol. 89, p. 011301, 2002.
- [8] L. Wolfenstein, “Neutrino Oscillations in Matter,” *Phys. Rev.*, vol. D17, p. 2369, 1978.
- [9] S. Mikheev and A. Y. Smirnov, “Resonance Oscillations of Neutrinos in Matter,” *Sov.Phys.Usp.*, vol. 30, p. 759, 1987.
- [10] J. T. Pantaleone, “Neutrino oscillations at high densities,” *Phys.Lett.*, vol. B287, p. 128, 1992.
- [11] H. Duan, G. M. Fuller, J. Carlson, and Y.-Z. Qian, “Simulation of Coherent Non-Linear Neutrino Flavor Transformation in the Supernova Environment. I. Correlated Neutrino Trajectories,” *Phys. Rev.*, vol. D74, p. 105014, 2006.
- [12] LIGO Scientific Collaboration and Virgo Collaboration, *et al.*, “GW170817: Observation of Gravitational Waves from a Binary Neutron Star Inspiral,” *Physical Review Letters*, vol. 119, no. 16, p. 161101, 2017.
- [13] A. Vlasenko, G. M. Fuller, and V. Cirigliano, “Prospects for Neutrino-Antineutrino Transformation in Astrophysical Environments,” 2014.
- [14] A. Esteban-Pretel, R. Tomas, and J. W. F. Valle, “Probing non-standard neutrino interactions with supernova neutrinos,” *Phys. Rev.*, vol. D76, p. 053001, 2007.
- [15] A. Esteban-Pretel, R. Tomas, and J. W. F. Valle, “Interplay between collective effects and non-standard neutrino interactions of supernova neutrinos,” *Phys. Rev.*, vol. D81, p. 063003, 2010.

- [16] C. J. Stapleford, D. J. Vninen, J. P. Kneller, G. C. McLaughlin, and B. T. Shapiro, “Nonstandard Neutrino Interactions in Supernovae,” *Phys. Rev.*, vol. D94, no. 9, p. 093007, 2016.
- [17] A. Chatelain and C. Volpe, “Helicity coherence in binary neutron star mergers and non-linear feedback,” *Phys. Rev.*, vol. D95, no. 4, p. 043005, 2017.
- [18] A. Chatelain and M. C. Volpe, “Neutrino propagation in binary neutron star mergers in presence of nonstandard interactions,” *Phys. Rev.*, vol. D97, no. 2, p. 023014, 2018.
- [19] C. Giunti and W. Chung, *Fundamentals of Neutrino Physics and Astrophysics*. Oxford University Press, 2007.
- [20] S. Weinberg, *The Quantum Theory of Fields, Volume 1: Foundations*. Oxford University Press, 2005.
- [21] E. Majorana, “Teoria simmetrica dell’elettrone e del positrone,” *Nuovo Cim.*, vol. 14, p. 171, 1937.
- [22] S. Bilenky, *Introduction to the Physics of Massive and Mixed Neutrinos*. Springer-Verlag Berlin Heidelberg, 2010.
- [23] B. Pontecorvo, “Inverse beta processes and nonconservation of lepton charge,” *Sov.Phys.JETP*, vol. 7, p. 172, 1958.
- [24] S. Collaboration, “Direct Evidence for Neutrino Flavor Transformation from Neutral-Current Interactions in the Sudbury Neutrino Observatory,” *Physical Review Letters*, vol. 89, no. 1, 2002. arXiv: nucl-ex/0204008.
- [25] J. Serreau and C. Volpe, “Neutrino-antineutrino correlations in dense anisotropic media,” *Phys. Rev.*, vol. D90, no. 12, p. 125040, 2014.
- [26] C. Volpe, “Neutrino Quantum Kinetic Equations,” *Int.J.Mod.Phys.*, vol. E24, no. 09, p. 1541009, 2015.
- [27] A. D. Dolgov, “Neutrinos in the Early Universe,” *Sov.J.Nucl.Phys.*, vol. 33, p. 700, 1981.
- [28] L. Stodolsky, “On the Treatment of Neutrino Oscillations in a Thermal Environment,” *Phys.Rev.*, vol. D36, p. 2273, 1987.
- [29] S. Samuel, “Neutrino oscillations in dense neutrino gases,” *Phys.Rev.*, vol. D48, p. 1462, 1993.
- [30] G. Sigl and G. Raffelt, “General kinetic description of relativistic mixed neutrinos,” *Nucl.Phys.*, vol. B406, p. 423, 1993.
- [31] B. H. J. McKellar and M. J. Thomson, “Oscillating neutrinos in the early Universe,” *Physical Review D*, vol. 49, no. 6, pp. 2710–, 1994.
- [32] R. F. Sawyer, “Speed-up of neutrino transformations in a supernova environment,” *Phys.Rev.*, vol. D72, p. 045003, 2005.
- [33] A. B. Balantekin and Y. Pehlivan, “Neutrino-Neutrino Interactions and Flavor Mixing in Dense Matter,” *J.Phys.*, vol. G34, p. 47, 2007.

- [34] C. Volpe, D. Väänänen, and C. Espinoza, “Extended evolution equations for neutrino propagation in astrophysical and cosmological environments,” *Phys. Rev.*, vol. D87, no. 11, p. 113010, 2013.
- [35] A. Kartavtsev, G. Raffelt, and H. Vogel, “Neutrino propagation in media: Flavor-, helicity-, and pair correlations,” *Phys.Rev.*, vol. D91, no. 12, p. 125020, 2015.
- [36] S. Samuel, “Neutrino oscillations in dense neutrino gases,” *Phys.Rev.*, vol. D48, p. 1462, 1993.
- [37] S. P. Mikheev and A. \. Y. Smirnov, “Resonance Amplification of Oscillations in Matter and Spectroscopy of Solar Neutrinos,” *Sov. J. Nucl. Phys.*, vol. 42, p. 913, 1985.
- [38] H. A. Bethe, “Energy Production in Stars,” *Physical Review*, vol. 55, pp. 434–456, Mar. 1939.
- [39] C. Pena-Garay and A. Serenelli, “Solar neutrinos and the solar composition problem,” *arXiv:0811.2424 [astro-ph]*, 2008. arXiv: 0811.2424.
- [40] G. *et al.* Bellini, “Neutrinos from the primary proton–proton fusion process in the Sun,” *Nature*, vol. 512, no. 7515, p. 383, 2014.
- [41] J. N. Abdurashitov, *et al.*, “Measurement of the solar neutrino capture rate with gallium metal. III: Results for the 2002–2007 data-taking period,” *Phys.Rev.*, vol. C80, p. 015807, 2009.
- [42] P. Anselmann, *et al.*, “Implications of the GALLEX determination of the solar neutrino flux.,” *Phys.Lett.*, vol. B285, p. 390, 1992.
- [43] W. Hampel, *et al.*, “GALLEX solar neutrino observations: Results for GALLEX IV,” *Phys.Lett.*, vol. B447, p. 127, 1999.
- [44] M. Altmann, *et al.*, “Complete results for five years of GNO solar neutrino observations,” *Phys.Lett.*, vol. B616, p. 174, 2005.
- [45] K. S. Hirata, *et al.*, “Observation of B-8 Solar Neutrinos in the Kamiokande-II Detector,” *Phys.Rev.Lett.*, vol. 63, p. 16, 1989.
- [46] J. Hosaka, *et al.*, “Solar neutrino measurements in super-Kamiokande-I,” *Phys.Rev.*, vol. D73, p. 112001, 2006.
- [47] J. P. Cravens, *et al.*, “Solar neutrino measurements in Super-Kamiokande-II,” *Phys.Rev.*, vol. D78, p. 032002, 2008.
- [48] K. Abe, *et al.*, “Solar neutrino results in Super-Kamiokande-III,” *Phys.Rev.*, vol. D83, p. 052010, 2011.
- [49] B. Aharmim, *et al.*, “Measurement of the electron neutrino and Total 8b Solar Neutrino Fluxes with the Sudbury Neutrino Observatory Phase-III Data Set,” *Phys.Rev.*, vol. C87, no. 1, p. 015502, 2013.
- [50] G. Bellini, *et al.*, “First evidence of pep solar neutrinos by direct detection in Borexino,” *Phys.Rev.Lett.*, vol. 108, p. 051302, 2012.
- [51] W. C. Haxton, R. G. Hamish Robertson, and A. M. Serenelli, “Solar Neutrinos: Status and Prospects,” *Ann.Rev.Astron.Astrophys.*, vol. 51, p. 21, 2013.

- [52] G. Bellini, *et al.*, “Precision measurement of the ${}^7\text{Be}$ solar neutrino interaction rate in Borexino,” *Phys.Rev.Lett.*, vol. 107, p. 141302, 2011.
- [53] G. Bellini, *et al.*, “Neutrinos from the primary proton–proton fusion process in the Sun,” *Nature*, vol. 512, no. 7515, p. 383, 2014.
- [54] A. Gando, *et al.*, “ ${}^7\text{Be}$ Solar Neutrino Measurement with KamLAND,” *Phys.Rev.*, vol. C92, no. 5, p. 055808, 2015.
- [55] C. a. Patrignani, “Review of Particle Physics,” *Chin. Phys.*, vol. C40, no. 10, p. 100001, 2016.
- [56] M. Apollonio, *et al.*, “Search for neutrino oscillations on a long baseline at the CHOOZ nuclear power station,” *Eur.Phys.J.*, vol. C27, p. 331, 2003.
- [57] F. Capozzi, *et al.*, “Status of three-neutrino oscillation parameters, circa 2013,” *Phys.Rev.*, vol. D89, p. 093018, 2014.
- [58] M. C. Gonzalez-Garcia, M. Maltoni, and T. Schwetz, “Updated fit to three neutrino mixing: status of leptonic CP violation,” *JHEP*, vol. 1411, p. 052, 2014.
- [59] D. V. Forero, M. Tortola, and J. W. F. Valle, “Neutrino oscillations refitted,” *Phys.Rev.*, vol. D90, no. 9, p. 093006, 2014.
- [60] F. Capozzi, E. Lisi, A. Marrone, D. Montanino, and A. Palazzo, “Neutrino masses and mixings: Status of known and unknown 3 neutrino parameters,” *Nucl.Phys.*, vol. B908, p. 218, 2016.
- [61] P. Adamson, *et al.*, “First measurement of muon-neutrino disappearance in NOvA,” *Phys.Rev.*, vol. D93, no. 5, p. 051104, 2016.
- [62] P. Adamson, *et al.*, “First measurement of electron neutrino appearance in NOvA,” *Phys.Rev.Lett.*, vol. 116, no. 15, p. 151806, 2016.
- [63] K. Abe, *et al.*, “Measurements of neutrino oscillation in appearance and disappearance channels by the T2k experiment with 6.6×10^{20} protons on target,” *Phys.Rev.*, vol. D91, no. 7, p. 072010, 2015.
- [64] M. Ravonel Salzgeber, “Anti-neutrino oscillations with T2k,” 2015.
- [65] G. Mention, *et al.*, “The Reactor Antineutrino Anomaly,” *Phys.Rev.*, vol. D83, p. 073006, 2011.
- [66] F. Kaether, W. Hampel, G. Heusser, J. Kiko, and T. Kirsten, “Reanalysis of the GALLEX solar neutrino flux and source experiments,” *Phys.Lett.*, vol. B685, p. 47, 2010.
- [67] C. Giunti and M. Laveder, “Statistical Significance of the Gallium Anomaly,” *Phys.Rev.*, vol. C83, p. 065504, 2011.
- [68] C. Athanassopoulos, *et al.*, “Candidate events in a search for anti-muon-neutrino \rightarrow anti-electron-neutrino oscillations,” *Phys.Rev.Lett.*, vol. 75, p. 2650, 1995.

- [69] A. Aguilar-Arevalo, *et al.*, “Evidence for neutrino oscillations from the observation of anti-neutrino(electron) appearance in a anti-neutrino(muon) beam,” *Phys.Rev.*, vol. D64, p. 112007, 2001.
- [70] S. Gariazzo, C. Giunti, M. Laveder, Y. F. Li, and E. M. Zavanin, “Light sterile neutrinos,” *J.Phys.*, vol. G43, p. 033001, 2016.
- [71] A. Giuliani and A. Poves, “Neutrinoless Double-Beta Decay,” *Adv.High Energy Phys.*, vol. 2012, p. 857016, 2012.
- [72] J. D. Vergados, H. Ejiri, and F. Simkovic, “Theory of Neutrinoless Double Beta Decay,” *Rept.Prog.Phys.*, vol. 75, p. 106301, 2012.
- [73] F. An, *et al.*, “Neutrino Physics with JUNO,” *J.Phys.*, vol. G43, no. 3, p. 030401, 2016.
- [74] V. N. Aseev, *et al.*, “An upper limit on electron antineutrino mass from Troitsk experiment,” *Phys.Rev.*, vol. D84, p. 112003, 2011.
- [75] C. Kraus, *et al.*, “Final results from phase II of the Mainz neutrino mass search in tritium beta decay,” *Eur.Phys.J.*, vol. C40, p. 447, 2005.
- [76] J. Angrik, *et al.*, “KATRIN design report 2004,” 2005.
- [77] K. N. Abazajian, *et al.*, “Cosmological and Astrophysical Neutrino Mass Measurements,” *Astropart.Phys.*, vol. 35, p. 177, 2011.
- [78] P. A. R. Ade, *et al.*, “Planck 2013 results. XVI. Cosmological parameters,” *Astron.Astrophys.*, vol. 571, p. A16, 2014.
- [79] P. A. R. Ade, *et al.*, “Planck 2015 results. XIII. Cosmological parameters,” *Astron.Astrophys.*, vol. 594, p. A13, 2016.
- [80] H. Duan, G. M. Fuller, and Y.-Z. Qian, “Collective Neutrino Oscillations,” *Ann. Rev. Nucl. Part. Sci.*, vol. 60, p. 569, 2010.
- [81] S. Chakraborty, R. S. Hansen, I. Izaguirre, and G. Raffelt, “Self-induced flavor conversion of supernova neutrinos on small scales,” *JCAP*, vol. 1601, no. 01, p. 028, 2016.
- [82] A. Malkus, J. P. Kneller, G. C. McLaughlin, and R. Surman, “Neutrino oscillations above black hole accretion disks: disks with electron-flavor emission,” *Phys. Rev.*, vol. D86, p. 085015, 2012.
- [83] A. Malkus, A. Friedland, and G. C. McLaughlin, “Matter-Neutrino Resonance Above Merging Compact Objects,” 2014.
- [84] A. Malkus, G. C. McLaughlin, and R. Surman, “Symmetric and Standard Matter-Neutrino Resonances Above Merging Compact Objects,” *Phys. Rev.*, vol. D93, no. 4, p. 045021, 2016.
- [85] Y.-L. Zhu, A. Perego, and G. C. McLaughlin, “Matter Neutrino Resonance Transitions above a Neutron Star Merger Remnant,” *Phys. Rev.*, vol. D94, no. 10, p. 105006, 2016.

- [86] M. Frensel, M.-R. Wu, C. Volpe, and A. Perego, “Neutrino Flavor Evolution in Binary Neutron Star Merger Remnants,” *Phys. Rev.*, vol. D95, no. 2, p. 023011, 2017.
- [87] M. E. Burbidge, G. R. Burbidge, W. A. Fowler, and F. Hoyle, “Synthesis of the elements in stars,” *Rev. Mod. Phys.*, vol. 29, p. 547, 1957.
- [88] J. M. Lattimer, D. N. Schramm, and L. Grossman, “Supernovae, grains and the formation of the Solar System,” *Nature*, vol. 269, no. 5624, p. 116, 1977.
- [89] Y.-Z. Qian, “Diverse, massive-star-associated sources for elements heavier than Fe and the roles of neutrinos,” *J. Phys.*, vol. G41, p. 044002, 2014.
- [90] A. Arcones and F. K. Thielemann, “Neutrino-driven wind simulations and nucleosynthesis of heavy elements,” *J. Phys.*, vol. G40, p. 013201, 2013.
- [91] B. *et al.* Abbott, “GW170817: Observation of Gravitational Waves from a Binary Neutron Star Inspiral,” *Phys. Rev. Lett.*, vol. 119, no. 16, p. 161101, 2017.
- [92] E. *et al.* Pian, “Spectroscopic identification of r-process nucleosynthesis in a double neutron star merger,” *Nature*, vol. 551, p. 67, 2017.
- [93] D. Martin, *et al.*, “Neutrino-driven winds in the aftermath of a neutron star merger: nucleosynthesis and electromagnetic transients,” *Astrophys. J.*, vol. 813, no. 1, p. 2, 2015.
- [94] A. B. Balantekin and H. Yuksel, “Neutrino mixing and nucleosynthesis in core-collapse supernovae,” *New J. Phys.*, vol. 7, p. 51, 2005.
- [95] W. P. Wright, *et al.*, “Neutrinos from type Ia supernovae: The gravitationally confined detonation scenario,” *Phys.Rev.*, vol. D95, no. 4, p. 043006, 2017.
- [96] H. A. Bethe and J. R. Wilson, “Revival of a stalled supernova shock by neutrino heating,” *Astrophys.J.*, vol. 295, p. 14, 1985.
- [97] T. J. Loredo and D. Q. Lamb, “Bayesian analysis of neutrinos observed from supernova SN-1987a,” *Phys.Rev.*, vol. D65, p. 063002, 2002.
- [98] H.-T. Janka, “Explosion Mechanisms of Core-Collapse Supernovae,” *Ann.Rev.Nucl.Part.Sci.*, vol. 62, p. 407, 2012.
- [99] R. Fernández, B. Müller, T. Foglizzo, and H.-T. Janka, “Characterizing SASI- and Convection-Dominated Core-Collapse Supernova Explosions in Two Dimensions,” *Mon.Not.Roy.Astron.Soc.*, vol. 440, no. 3, p. 2763, 2014.
- [100] I. Tamborra, *et al.*, “Self-sustained asymmetry of lepton-number emission: A new phenomenon during the supernova shock-accretion phase in three dimensions,” *Astrophys.J.*, vol. 792, no. 2, p. 96, 2014.
- [101] H.-T. Janka, T. Melson, and A. Summa, “Physics of Core-Collapse Supernovae in Three Dimensions: a Sneak Preview,” *Ann.Rev.Nucl.Part.Sci.*, vol. 66, p. 341, 2016.

- [102] A. S. Dighe and A. Y. Smirnov, “Identifying the neutrino mass spectrum from the neutrino burst from a supernova,” *Phys.Rev.*, vol. D62, p. 033007, 2000.
- [103] I. Tamborra, B. Muller, L. Hudepohl, H.-T. Janka, and G. Raffelt, “High-resolution supernova neutrino spectra represented by a simple fit,” *Phys.Rev.*, vol. D86, p. 125031, 2012.
- [104] A. Mirizzi, *et al.*, “Supernova Neutrinos: Production, Oscillations and Detection,” *Riv.Nuovo Cim.*, vol. 39, no. 1-2, p. 1, 2016.
- [105] K. e. a. Hirata, “Observation of a neutrino burst from the supernova SN1987a,” *Physical Review Letters*, vol. 58, p. 1490, Apr. 1987.
- [106] E. N. Alexeyev, L. N. Alexeyeva, I. V. Krivosheina, and V. I. Volchenko, “Detection of the neutrino signal from SN 1987a in the LMC using the INR Baksan underground scintillation telescope,” *Physics Letters B*, vol. 205, p. 209, Apr. 1988.
- [107] F. Vissani, “Comparative analysis of SN1987a antineutrino fluence,” *J.Phys.*, vol. G42, p. 013001, 2014.
- [108] H. Duan and A. Friedland, “Self-induced suppression of collective neutrino oscillations in a supernova,” *Phys.Rev.Lett.*, vol. 106, p. 091101, 2011.
- [109] R. F. Sawyer, “The multi-angle instability in dense neutrino systems,” *Phys.Rev.*, vol. D79, p. 105003, 2009.
- [110] A. Banerjee, A. Dighe, and G. Raffelt, “Linearized flavor-stability analysis of dense neutrino streams,” *Phys.Rev.*, vol. D84, p. 053013, 2011.
- [111] D. Väänänen and C. Volpe, “Linearizing neutrino evolution equations including neutrino-antineutrino pairing correlations,” *Phys.Rev.*, vol. D88, p. 065003, 2013.
- [112] S. Galais, J. Kneller, and C. Volpe, “The neutrino-neutrino interaction effects in supernovae: the point of view from the matter basis,” *J.Phys.*, vol. G39, p. 035201, 2012.
- [113] S. Hannestad, G. G. Raffelt, G. Sigl, and Y. Y. Y. Wong, “Self-induced conversion in dense neutrino gases: Pendulum in flavour space,” *Phys.Rev.*, vol. D74, p. 105010, 2006.
- [114] G. G. Raffelt and A. Y. Smirnov, “Adiabaticity and spectral splits in collective neutrino transformations,” *Phys.Rev.*, vol. D76, p. 125008, 2007.
- [115] S. Galais and C. Volpe, “The neutrino spectral split in core-collapse supernovae: a magnetic resonance phenomenon,” *Phys.Rev.*, vol. D84, p. 085005, 2011.
- [116] A. Esteban-Pretel, *et al.*, “Role of dense matter in collective supernova neutrino transformations,” *Phys.Rev.*, vol. D78, p. 085012, 2008.
- [117] G. Raffelt, S. Sarikas, and D. de Sousa Seixas, “Axial Symmetry Breaking in Self-Induced Flavor Conversion of Supernova Neutrino Fluxes,” *Phys.Rev.Lett.*, vol. 111, no. 9, p. 091101, 2013.

- [118] H. Duan and S. Shalgar, “Flavor instabilities in the neutrino line model,” *Phys.Lett.*, vol. B747, p. 139, 2015.
- [119] S. Abbar, H. Duan, and S. Shalgar, “Flavor instabilities in the multiangle neutrino line model,” *Phys.Rev.*, vol. D92, no. 6, p. 065019, 2015.
- [120] R. F. Sawyer, “Neutrino cloud instabilities just above the neutrino sphere of a supernova,” *Phys. Rev. Lett.*, vol. 116, no. 8, p. 081101, 2016.
- [121] B. Dasgupta, A. Mirizzi, and M. Sen, “Fast neutrino flavor conversions near the supernova core with realistic flavor-dependent angular distributions,” *JCAP*, vol. 1702, no. 02, p. 019, 2017.
- [122] J. F. Cherry, J. Carlson, A. Friedland, G. M. Fuller, and A. Vlasenko, “Neutrino scattering and flavor transformation in supernovae,” *Phys.Rev.Lett.*, vol. 108, p. 261104, 2012.
- [123] H. Duan, A. Friedland, G. C. McLaughlin, and R. Surman, “The influence of collective neutrino oscillations on a supernova r-process,” *J.Phys.*, vol. G38, p. 035201, 2011.
- [124] K. Scholberg, “Supernova Neutrino Detection,” *Annual Review of Nuclear and Particle Science*, vol. 62, no. 1, p. 81, 2012.
- [125] B. P. Abbott, *et al.*, “Multi-messenger Observations of a Binary Neutron Star Merger*,” *The Astrophysical Journal Letters*, vol. 848, no. 2, p. L12, 2017.
- [126] A. Perego, *et al.*, “Neutrino-driven winds from neutron star merger remnants,” *Mon. Not. Roy. Astron. Soc.*, vol. 443, no. 4, p. 3134, 2014.
- [127] E. O’Connor, *et al.*, “Global Comparison of Core-Collapse Supernova Simulations in Spherical Symmetry,” *J.Phys.*, vol. G45, no. 10, p. 104001, 2018.
- [128] J. Lippuner and L. F. Roberts, “r-Process Lanthanide Production and Heating Rates in Kilonovae,” *Astrophys.J.*, vol. 815, p. 82, Dec. 2015.
- [129] O. L. Caballero, T. Zielinski, G. C. McLaughlin, and R. Surman, “Black hole spin influence on accretion disk neutrino detection,” *Phys.Rev.*, vol. D93, no. 12, p. 123015, 2016.
- [130] D. Väänänen and G. C. McLaughlin, “Uncovering the Matter-Neutrino Resonance,” *Phys. Rev.*, vol. D93, no. 10, p. 105044, 2016.
- [131] M.-R. Wu, H. Duan, and Y.-Z. Qian, “Physics of neutrino flavor transformation through matterneutrino resonances,” *Phys. Lett.*, vol. B752, p. 89, 2016.
- [132] S. Shalgar, “Multi-angle calculation of the matter-neutrino resonance near an accretion disk,” *JCAP*, vol. 1802, no. 02, p. 010, 2018.
- [133] M.-R. Wu and I. Tamborra, “Fast neutrino conversions: Ubiquitous in compact binary merger remnants,” *Phys. Rev.*, vol. D95, no. 10, p. 103007, 2017.

- [134] A. Vlasenko and G. C. McLaughlin, “Matter-neutrino resonance in a multiangle neutrino bulb model,” *Phys.Rev.*, vol. D97, no. 8, p. 083011, 2018.
- [135] M.-R. Wu, I. Tamborra, O. Just, and H.-T. Janka, “Imprints of neutrino-pair flavor conversions on nucleosynthesis in ejecta from neutron-star merger remnants,” *Phys.Rev.*, vol. D96, no. 12, p. 123015, 2017.
- [136] A. Vlasenko, G. M. Fuller, and V. Cirigliano, “Neutrino Quantum Kinetics,” *Phys.Rev.*, vol. D89, no. 10, p. 105004, 2014.
- [137] B. Dasgupta, A. Dighe, A. Mirizzi, and G. G. Raffelt, “Collective neutrino oscillations in non-spherical geometry,” *Phys.Rev.*, vol. D78, p. 033014, 2008.
- [138] A. Esteban-Pretel, S. Pastor, R. Tomas, G. G. Raffelt, and G. Sigl, “Decoherence in supernova neutrino transformations suppressed by deleptonization,” *Phys.Rev.*, vol. D76, p. 125018, 2007.
- [139] V. Cirigliano, G. M. Fuller, and A. Vlasenko, “A New Spin on Neutrino Quantum Kinetics,” *Phys.Lett.*, vol. B747, p. 27, 2015.
- [140] J. Y. Tian, A. V. Patwardhan, and G. M. Fuller, “Prospects for Neutrino Spin Coherence in Supernovae,” *Phys.Rev.*, vol. D95, p. 063004, Mar. 2017.
- [141] M. S. Bilenky and A. Santamaria, “‘Secret’ neutrino interactions,” in *Neutrino mixing. Festschrift in honour of Samoil Bilenky’s 70th birthday. Proceedings, International Meeting, Turin, Italy, March 25-27, 1999*, p. 50, 1999.
- [142] S. Davidson, C. Pena-Garay, N. Rius, and A. Santamaria, “Present and future bounds on nonstandard neutrino interactions,” *JHEP*, vol. 03, p. 011, 2003.
- [143] C. Biggio, M. Blennow, and E. Fernandez-Martinez, “General bounds on non-standard neutrino interactions,” *JHEP*, vol. 08, p. 090, 2009.
- [144] T. Ohlsson, “Status of non-standard neutrino interactions,” *Rept. Prog. Phys.*, vol. 76, p. 044201, 2013.
- [145] D. *et al.* Akimov, “Observation of Coherent Elastic Neutrino-Nucleus Scattering,” *Science*, vol. 357, no. 6356, p. 1123, 2017.
- [146] P. S. Amanik and G. M. Fuller, “Stellar Collapse Dynamics With Neutrino Flavor Changing Neutral Currents,” *Phys. Rev.*, vol. D75, p. 083008, 2007.
- [147] M. Blennow, A. Mirizzi, and P. D. Serpico, “Nonstandard neutrino-neutrino refractive effects in dense neutrino gases,” *Phys. Rev.*, vol. D78, p. 113004, 2008.
- [148] A. Das, A. Dighe, and M. Sen, “New effects of non-standard self-interactions of neutrinos in a supernova,” *JCAP*, vol. 1705, no. 05, p. 051, 2017.
- [149] H. Nunokawa, Y. Z. Qian, A. Rossi, and J. W. F. Valle, “Resonant conversion of massless neutrinos in supernovae,” *Phys. Rev.*, vol. D54, p. 4356, 1996.

- [150] M. Maltoni and A. Y. Smirnov, “Solar neutrinos and neutrino physics,” *Eur.Phys.J.*, vol. A52, no. 4, p. 87, 2016.
- [151] S. Pastor, G. G. Raffelt, and D. V. Semikoz, “Physics of synchronized neutrino oscillations caused by selfinteractions,” *Phys. Rev.*, vol. D65, p. 053011, 2002.
- [152] I. Tamborra, G. G. Raffelt, L. Hudepohl, and H.-T. Janka, “Impact of eV-mass sterile neutrinos on neutrino-driven supernova outflows,” *JCAP*, vol. 1201, p. 013, 2012.
- [153] N. Fornengo, C. Giunti, C. W. Kim, and J. Song, “Gravitational effects on the neutrino oscillation,” *Phys.Rev.*, vol. D56, p. 1895, 1997.
- [154] G. Lambiase, G. Papini, R. Punzi, and G. Scarpetta, “Neutrino optics and oscillations in gravitational fields,” *Phys.Rev.*, vol. D71, p. 073011, 2005.
- [155] C. Y. Cardall and G. M. Fuller, “Neutrino oscillations in curved space-time: An Heuristic treatment,” *Phys.Rev.*, vol. D55, p. 7960, 1997.
- [156] Y. Yang and J. P. Kneller, “GR effects in supernova neutrino flavor transformations,” *Phys.Rev.*, vol. D96, no. 2, p. 023009, 2017.
- [157] S. Nussinov, “Solar Neutrinos and Neutrino Mixing,” *Phys.Lett.*, vol. 63B, p. 201, 1976.
- [158] C. Giunti, C. W. Kim, and U. W. Lee, “When do neutrinos really oscillate?: Quantum mechanics of neutrino oscillations,” *Phys.Rev.*, vol. D44, pp. 3635–, 1991.
- [159] J. Kersten, “Coherence of Supernova Neutrinos,” *Nucl.Phys.Proc.Suppl.*, vol. 237-238, p. 342, 2013.
- [160] E. Akhmedov, J. Kopp, and M. Lindner, “Collective neutrino oscillations and neutrino wave packets,” *JCAP*, vol. 1709, no. 09, p. 017, 2017.
- [161] M. Beuthe, “Oscillations of neutrinos and mesons in quantum field theory,” *Phys.Rept.*, vol. 375, p. 105, 2003.
- [162] E. K. Akhmedov and A. Y. Smirnov, “Paradoxes of neutrino oscillations,” *Phys.Atom.Nucl.*, vol. 72, p. 1363, 2009.
- [163] J. Kersten and A. Y. Smirnov, “Decoherence and oscillations of supernova neutrinos,” *Eur.Phys.J.*, vol. C76, no. 6, p. 339, 2016.
- [164] D. V. Naumov, “On the Theory of Wave Packets,” *Phys. Part. Nucl. Lett.*, vol. 10, p. 642, 2013.
- [165] V. A. Naumov and D. S. Shkirmanov, “Covariant asymmetric wave packet for a field-theoretical description of neutrino oscillations,” *Mod. Phys. Lett.*, vol. A30, no. 24, p. 1550110, 2015.
- [166] C. Giunti and A. Studenikin, “Neutrino electromagnetic interactions: a window to new physics,” *Rev.Mod.Phys.*, vol. 87, p. 531, 2015.